Faculteit Wetenschappen

Departement Fysica

Mechanics of the middle ear: Optical measurements and finite-element modeling

---

Mechanica van het middenoor: Optische metingen en eindige-elementenmodellering,

Proefschrift voorgelegd tot het behalen van de graad van

Doctor in de Wetenschappen: Fysica

aan de Universiteit Antwerpen te verdedigen door

Kilian GLADINÉ

Promotor

Prof. Dr. Joris Dirckx

Antwerpen 2019

DOCTORAL COMMITTEE

Chair

Prof. Dr. Paul Scheunders: *Department of Physics, University of Antwerp*

Supervisor

Prof. Dr. Joris J. J. Dirckx: *Department of Physics, University of Antwerp*

Internal members

Prof. Dr. Bart Partoens: *Department of Physics, University of Antwerp*

Prof. Dr. Steve Vanlanduit: Department of Mechanical Engineering, Vrije Universiteit Brussel (Belgium); Departement of electromechanics, University of Antwerp (Belgium)

External members

Prof. Dr. Hanif Ladak: *Departement of Medical Biophysics, Electrical & Computer-Engineering, University of Western Ontario (Canada); Robarts Research Institute, Western University (Canada)*

Prof. Dr. Magnus von Unge: *Department of Otorhinolaryngology, Akershus University Hospital and University of Oslo (Norway); Department of Clinical Science, Intervention and Technology, Karolinska Institute, Stockholm (Sweden); Center for Clinical Research, University of Uppsala (Sweden)*

Private PhD defense

Monday, 26 August 2019, 14:30
Meeting room De Rede, office U.338
Campus Groenenborger, University of Antwerp

Public PhD defense

Tuesday, 17 September 2019, 16:00
Auditorium A.143
Campus Middelheim, University of Antwerp

PREFACE

Hearing is one of the five traditional senses which works by a marvelous biological design. In our daily life, pressure variations in the air about a million times smaller than the atmospheric pressure stimulate our hearing organ. The vibrations of our eardrum, which are only on the nanometer scale, are transported to the cochlea by the ossicles, which are just a few millimeters large. The ingenious construction of the cochlea enables it to analyze the different frequencies of the sound and produce the appropriate neural stimulation, allowing us to communicate, listen to music, and much more.

Unfortunately, our hearing is prone to several pathologies or self-inflicted damage, causing hearing loss. According to the world health organization, over 5% of the world's population has disabling hearing loss. Two main categories of hearing loss exist, sensorineural and conductive hearing loss. The origin of sensorineural hearing loss lies within the cochlea. In young individuals, sensorineural hearing loss is often caused by longtime exposure to loud sounds (or music) or short exposure to extremely loud sounds like gunshots. However, many elderly suffer from sensorineural hearing loss simply due to aging. This type of hearing damage is permanent but can be resolved using cochlear implants which directly stimulate the hearing nerves, and in less severe cases, a traditional hearing implant amplifying the sound can suffice. The root causes of conductive hearing loss lie within the middle ear where the eardrum and ossicles reside. Some types of conductive hearing loss are temporary and are caused by, for example, an ear infection or an excess of fluid in the middle ear cavity. Other types can involve calcification, fracturing, discontinuation of the ossicles. These types require either hearing aids, surgery or a prosthesis placement. This thesis focusses on the mechanics of the middle ear, thus any hearing loss related research concerns only conductive hearing loss.

Whether fundamental or applied middle ear research is performed, insights in either field can be retrieved. Traditional hearing aids amplify the sound tremendously, which leads to the question: does the middle ear function well at high-intensity sounds? When one of our colleagues investigated the best remedy for ossicle fractures, they observed that the human eardrum loses its shape and wrinkles and overall seems to have lost its elastic properties. Current models do not incorporate what seems to be eardrum pre-strain, as observed by our colleague. Can models, in turn, predict the best way to evaluate ossicular fixation? The list can go on.

The first four chapters function as an introduction to the research topics and measurement techniques, which will be used in the research of this PhD dissertation. The remaining five chapters go more into depth of each research topic and our obtained results. The majority of these chapters are strongly based on published material (chapter 6, 8, 9) or papers under review (chapter 7). Chapter 5 contains mostly unpublished material.

In **chapter 1**, we will give an introduction to sound and the morphology and physiology of the mammalian ear, with a focus on the human ear. In **chapter 2**, we briefly describe the research topics of chapters 5-9 and explain the type of required research tools. In **chapter 3**, we explain (visco-)elasticity and vibration theory, which helps us understand the middle ear as a mechanical system. In **chapter 4**, we describe the tools which we will use to evaluate certain variables of the middle ear and investigate the problems posed in chapter 2. In **chapter 5**, we dive into the first research topic and explore how high-intensity sounds affect the functionality of the middle ear using modeling and optical measurement techniques. In **chapter 6**, we use modeling to obtain a deeper understanding of what exactly causes hearing loss after fracturing one of the hearing ossicles. However, we will see that our models seem to be inadequate to replicate the same hearing loss curves obtained in the experimental work of our colleagues. In **chapter 7**, we try to find the missing piece in our modeling work of chapter 6. **Chapter 8** contains mostly experimental work in which we develop a measurement method to evaluate the severity and location of ossicular fixations. In **chapter 9**, we explore data manipulation methods, which can provide more accurate averaged data, which can in turn, be used to validate models.

For one published paper and another under review, I contributed by assisting with the measurements and processing the measurement data. Since my contribution was relatively small and the research topic of those papers was slightly off-topic, they are not included in this PhD dissertation. The references to these papers can be found in the **list of publications**.

CONTENTS

Chapter 1:
THE MAMMALIAN EAR AND SOUND

In this chapter, we will give an introduction to sound and the morphology and physiology of the mammalian ear, with a focus on the human ear. The content of this chapter is based on Aerts (2010), Muyshondt (2018b) and Puria and Steele (2008).

1.1 Sound

The air surrounding us consists of a mixture of molecules (N_2, O_2, Ar, ...), which are constantly moving and colliding with each other. Gravity pulls the atmosphere, and as a consequence, the air is pressurized. The pressure of the air at sea level is 101325 Pascal. This pressure is called atmospheric pressure. A sound is a periodical variation of this atmospheric pressure that propagates through the air. When an object vibrates, it causes the surrounding air molecules to compress and decompress sequentially. Such compression or decompression is a local pressure variation of the atmospheric pressure. This local pressure variation, *acoustic pressure*, propagates through the air and is what we perceive as sound. The amplitude or the magnitude of the acoustic pressure determines the loudness. The sound pressure level (L_p) is defined as

$$L_p = 20 \cdot \log_{10}\left(\frac{p_{rms}}{p_0}\right) dB \tag{1.1}$$

Where p_{rms} is the root mean square (RMS) value of the acoustic pressure at a point in space and p_0 is a reference pressure. The reference pressure is chosen to be $p_0 = 20\ \mu Pa$, the *hearing threshold*. It is about the smallest acoustic pressure a human can hear at 1 kHz, and it is about 5 billion times smaller than the atmospheric pressure. An acoustic pressure p_{rms} of 20 μPa matches a sound pressure level of 0 dB. The threshold of pain lies at 120 dB (or 20 Pa RMS) which is about a million times larger than the hearing threshold. The largest sound pressure level without distorting the sound is 191 dB SPL. At this sound pressure level, the acoustic peak pressure is 101325 Pa, and the generated underpressure of the sound wave results in a complete vacuum.

Humans can perceive sound over a frequency range of 20-20000 Hz. However, our hearing is not equally sensitive to different frequencies. Figure 1.1 shows a human audiogram measurement, which displays at which level the subject could hear a specific frequency. We can see that our hearing is less sensitive in the lower and higher frequencies. The most sensitive region lies between 1-4 kHz, which is also the frequency region in which speech occurs.

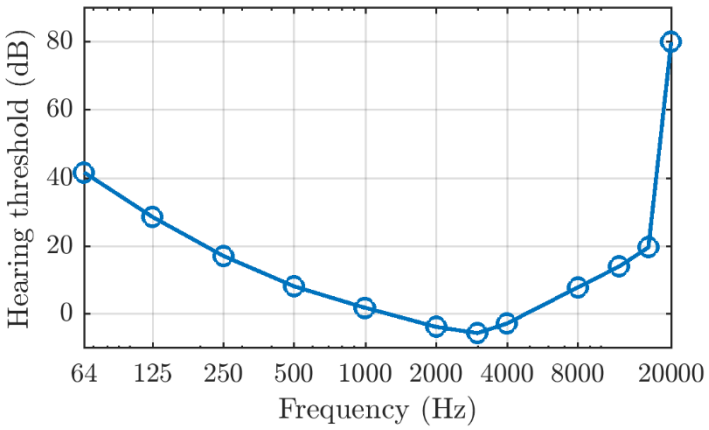

Figure 1.1: Hearing threshold in human. The reference pressure of 20 µPa RMS is based on the lowest observable acoustic pressure at 1000 Hz. Data taken from Sivian and White (1933).

Let us find out how these pressure variations are converted to brain stimulation by looking at the ear its three main parts: the outer, middle, and inner ear.

1.2 The mammalian ear

Before we dive into the different parts of the ear and its subcomponents, we will give a brief overview of the functionality of the ear.

The goal is to convert sound pressure variations in the air into electrical pulses which are sent to the brain. The electrical pulses are generated by the motion of the hair cells which reside in the fluid-filled cochlea (figure 1.2). To excite these hair cells, we have to stimulate the cochlear fluid acoustically. This means we have to convert sound waves in the air into sound waves into a fluid. The acoustic impedance (z), the resistance of passing an acoustic wave through a medium, of air and fluid are very different. If an acoustic wave has to pass a barrier between two media of different acoustic impedance, a part of the acoustic energy will be reflected. The amount of reflection (R) is determined by

$$R = \left(\frac{z_2 - z_1}{z_2 + z_1}\right)^2 \tag{1.2}$$

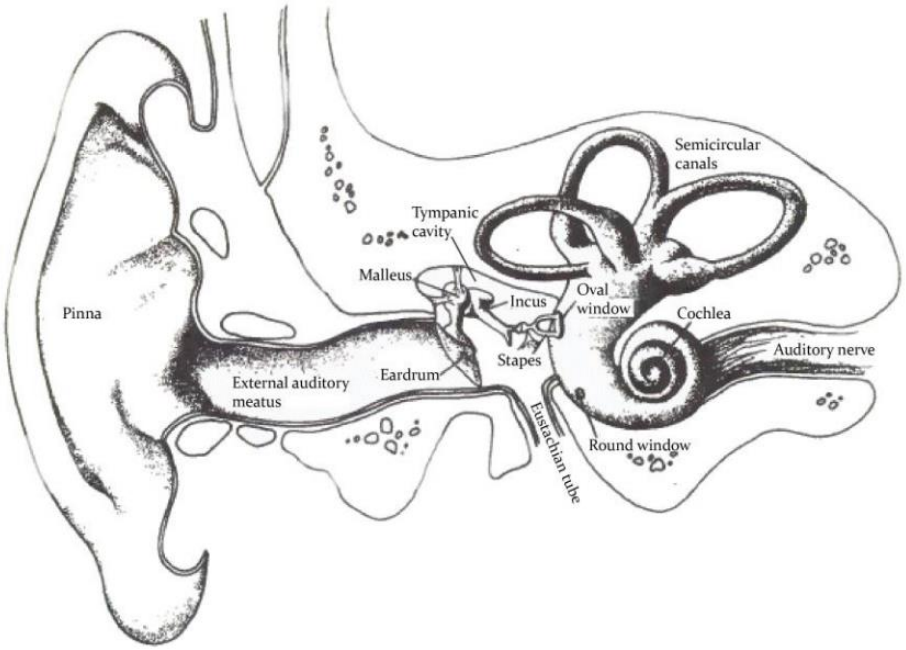

Figure 1.2: Overview of the outer, middle, and inner ear. Figure modified from Lindsay and Norman (1977)

If we use the values for the acoustic impedance of air $z_1 = z_{air} = 415\ Pa \cdot \frac{s}{m}$ and saline $z_2 = z_{saline} = 1.48 \cdot 10^6 Pa \cdot \frac{s}{m}$, we find that 99.89% of the sound energy would reflect at the air-fluid boundary. The equivalent hearing loss is 59 dB! A mechanism is needed to overcome this energy loss due to this acoustic impedance mismatch. The middle ear adds an additional step in between the conversion of acoustic waves in air to fluid. The ME converts the sound waves in the air into mechanical vibrations. These vibrations are passed along the ossicles to the input of the cochlea, the oval window. In turn, the vibration of this oval window stimulates the fluid inside the cochlea. The mechanical properties of the ME and geometrical construction of the outer ear will allow to make up for the 59 dB loss due to the acoustic impedance mismatch between the air and the fluid filled cochlea.

1.2.1 Outer ear

The outer ear consists of two main parts, the pinna or auricle, and the ear canal. The pinna is the visible part of the human ear residing outside the head. It has two main functions; boosting the sound, and conveying information about the directionality of the sound. How does the pinna achieve this?

Figure 1.3 shows a drawing of the human pinna. Sound is collected over the area of the pinna which is about 20 cm^2 and is projected onto the tympanic membrane which has a surface area of only 1 cm^2. This boosts the sound by 26 dB. However, the outer ear is

much more sophisticated than just a cone that simply collects and projects the sound from a large to a smaller area as we can see in figure 1.3. The pinna contains various geometrical features which boost the sound pressure in certain frequency regions. The largest feature is the concha which typically has a height of 19 mm, a width of 16 mm and a depth of 10 mm. A pressure gain of 10 dB is obtained in the 4-5 kHz range due to the depth-resonance mode of the concha. This pressure gain is independent of the incident angle of the sound.

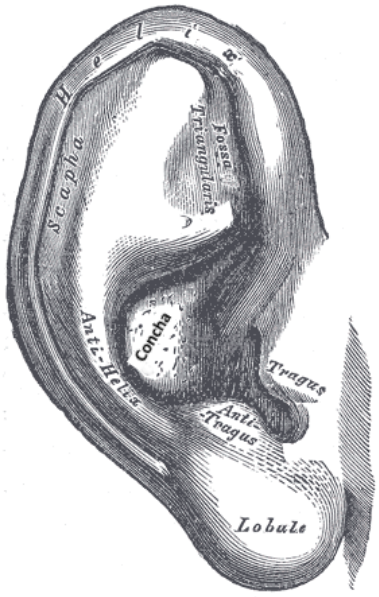

Figure 1.3: Drawing of the human pinna. Figure modified from Gray (1918) (public domain)

In contrast to the depth-resonance mode of the concha, the resonances produced by other of the pinna features are dependent on the angle of incidence. These features contribute to the pressure gain above 6-7 kHz. Depending on the direction of where the sound comes from, the pinna diffracts the sound differently, and we perceive slightly different sound amplitudes in specific frequency ranges, as shown in figure 1.4. The spectral cues as a result of the geometrical features of the pinna are one of the ways we can localize the sound source. While the spectral cues mainly allow us to determine the source elevation, either interaural time differences or interaural intensity differences allow us to find the source azimuth. The interaural differences occur due to the finite distance between both ears. A sound coming from our left will reach our left ear sooner than the right ear. Our brain can interpret this timing difference to determine where the sound comes from. Similarly, the interaction of the sound waves with our head and torso adjust the amplitude in certain frequency regions in one or both ears. The effects of interaural time and amplitude differences and spectral cues of the pinna combined can be summarized by a head-related transfer function (HRTF). This HRTF determines how a sound will be perceived by an individual based on their characteristic geometry of the head, torso and pinna.

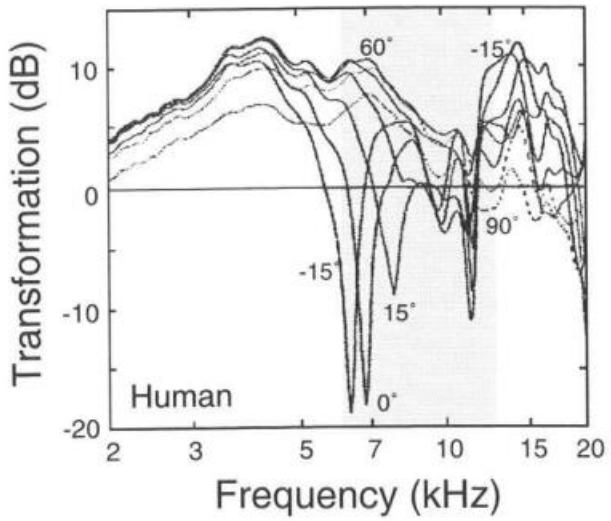

Figure 1.4: Transformation of the sound pressure for sound waves incident under different elevation angles. A positive angle corresponds to an incident wave from above the horizontal plane through the ears. Figure from Shaw (1982)

The ear canal also produces a pressure gain. The ear canal is 25 mm long and 7 mm wide. One-third of the canal consists of cartilage which is an extension of the pinna. The other two-thirds are called the bony ear canal, which is embedded in the skull bone. The ear canal has a quarter-wavelength resonance around 2.5 kHz, resulting in a pressure gain of about 10 dB.

1.2.2 Middle ear

At the end of the ear canal lays the TM (figure 1.5A), the boundary between the outer and middle ear. Sound energy is converted into vibrational energy when the sound waves from the ear canal impinge on the TM. The human TM is a thin semitransparent membrane. The TM has an inclination with respect to the ear canal. This inclination allows the TM cross-section to be larger than the cross-section of the ear canal itself, increasing sound transmission to the cochlea. We can discern two main parts of the TM: the *pars tensa* and *pars flaccida*. From above, the surface of the pars tensa looks elliptic with a long axis of about 8.5-10 mm and short axis of 8-9 mm and spans about 80% of the total surface of the TM. It has a conical shape of which the deepest point, called the *umbo*, points medially (inwards). The height difference between the cartilaginous annular ring and umbo is about 1.7 mm. The pars flaccida is much smaller and is located superiorly (above) to the pars tensa.

The pars tensa and pars flaccida both consist of three layers: a lateral epithelial layer, a fibrous layer in the middle, and a medial mucosal layer. The fibers in the pars tensa are organized in circular and radial fibers. In contrast, the pars flaccida does not have such highly organized fiber structure, and the stiffness is much lower, making it more elastic than the pars tensa.

The vibrational energy of the TM is passed along the three ossicles: malleus, incus, and stapes. The malleus, informally referred to as the hammer, contains a handle (*manubrium*), neck and head as shown in figure 1.5B. Two processes emerge from the malleus between the head and neck: the anterior and lateral process. The manubrium is connected to the pars tensa by a thin mucous fold, the *manubrial fold*. At the umbo and lateral process, a firm connection exists between the malleus and the pars tensa. The malleus is connected to the ME cavity by several ligaments. The anterior ligament is located close to the anterior process. The superior and lateral ligament are both connected onto the malleus head. A muscle, the *tendon tympani*, is connected to the manubrium. This muscle protects our hearing at high sound pressure levels. The tendon tympani pulls the TM inwards, which increases the stiffness and reduces the input to the cochlea.

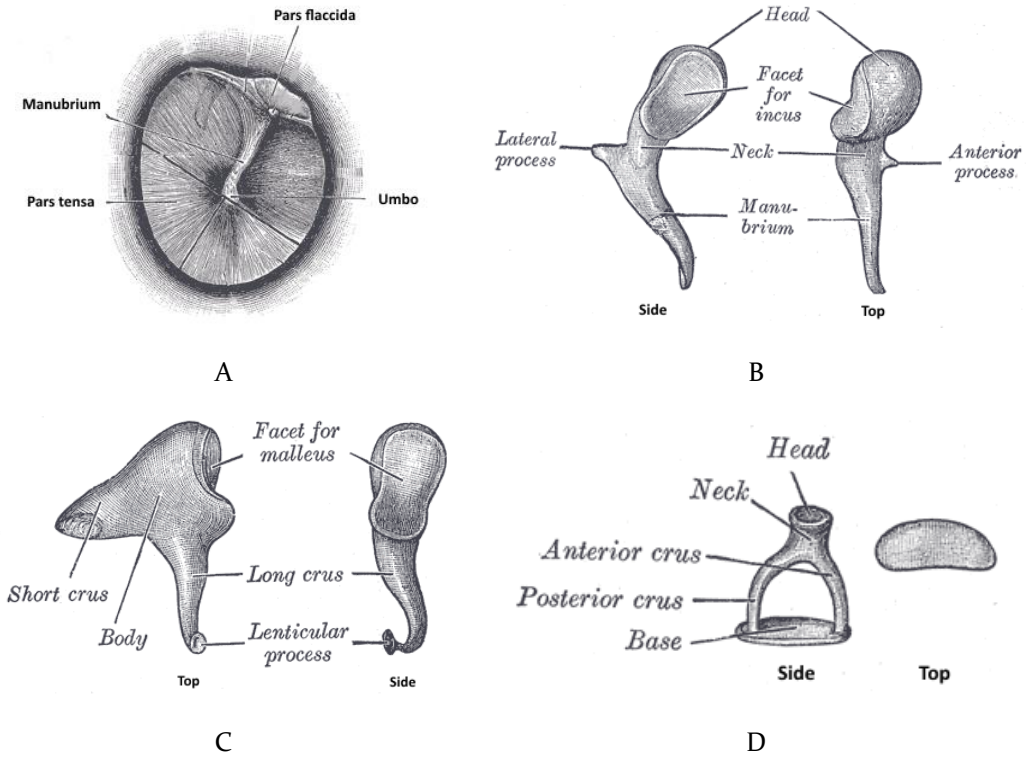

Figure 1.5: Drawing of the tympanic membrane (A), malleus (B), incus (C) and stapes (D). Figure modified from Gray (1918) (public domain)

The second ossicle, the incus or *anvil,* is connected to the malleus head by soft tissue forming the incudo-mallear joint (figure 1.5C). This joint is responsible for more complex movements at higher frequencies as slipping between both ossicles starts to occur. The incus contains one short and one long crus. The posterior incudal ligament is connected to the short crus, whereas the long crus connects to the third ossicle by the circular shaped lenticular process. Another ligament, the superior ligament, connects the top of the incus to the roof of the TM cavity, similar to the superior mallear ligament.

The third ossicle, the stapes or *stirrup*, is connected to the incus via the lenticular process (figure 1.5D). Further down the stapes neck, the stapes splits into two crura, a posterior and anterior one. The base of the stapes, an oval disk also called the stapes footplate, connects to the oval window of the cochlea by the annular ligament. Attached to the posterior side of the stapes is a muscle which also contracts at loud sound pressure levels. It pulls the stapes sideways. This behavior is called the acoustic reflex. It protects the inner ear by reducing the input at the oval window.

So how does the ME deliver the remaining gain to overcome the energy loss due to the impedance mismatch? The ME system achieves the most substantial increase in gain by transporting a force on a large surface (TM) to a small surface (stapes footplate). A similar process occurs in the external ear where the large surface is the pinna, and the small surface is the TM. The stapes footplate to TM area ratio is about 17, resulting in a gain increase of 25 dB. Additionally, the length difference between the manubrium and the long crus of the incus delivers a lever-effect. The manubrium is about 1.3 times larger than the long incus crus, which results in a 2.3 dB force increase at the level of the stapes due to the conservation of angular momentum.

Similarly, due to its shape, the areas of the TM next to the manubrium move more than the manubrium itself. The smaller displacement of the manubrium is accompanied by another 6 dB of increased force. This effect is often referred to as the *buckling effect*. So in total, we get a gain of about 33 dB. A similar amount of gain was achieved due to the area difference between pinna and TM and the resonance of the pinna substructures and ear canal. The 60 dB energy loss due to impedance mismatching is resolved.

High static pressures can degrade the efficiency of the ME. Such static pressures differences between the ME cavity and the ambient air can arise when taking an elevator, for example. The pressure difference can push the TM inward or outward, and this deformed configuration results in diminished hearing ability. However, the Eustachian tube which connects the ME cavity with the upper portion of the throat (*nasopharynx*) regulates the pressure difference. The pressure in the nasopharynx is equal to the ambient pressure. In normal conditions, the Eustachian tube is closed, but when swallowing it opens temporarily, removing the pressure difference between the ME cavity and ambient pressure.

1.2.3 Inner ear

The external and middle ear manage to efficiently transduce the sound to the oval window, the entrance of the cochlea. The vibration of the stapes footplate at the oval window converts the vibrations again into sound waves, but this time the sound waves propagate through a fluid. The cochlea is part of a larger structure, the *bony labyrinth of the inner* ear shown in figure 1.6. It is a coiled cavity which in humans makes two and three quarter turns around its axis. There are two fluid-filled partitions: the *scala vestibule* and the *scala tympani*. The oval window is the entrance to the scala vestibule. The basilar membrane almost completely separates both scala*e*. At the end of the basilar membrane, *the helicotrema*, the scala vestibule meets the scala tympani. At the end of the scala tympani, the round window is located. If this flexible window were not present, it would be hard to produce sound waves in the cochlea since the fluid is practically

incompressible. On the basilar membrane lies the *organ of Corti*, which contains the hair cells which produce the electrical pulses sent to the brain. In humans, between 17500 and 23500 hair cells can be found spread over the length of the basilar membrane. Different hair cells are assigned to generate electric pulses for specific frequencies. The cochlea is, in fact, also a frequency analyzer. Lower frequencies are detected at the end (apex) of the basilar membrane, while high frequencies are detected at the base of the membrane. How is this separation of frequencies achieved by the cochlea?

The pressure difference across the basilar membrane between the two scalas will cause the basilar membrane to vibrate. The shape of the basilar membrane is tapered. At the base, the membrane has a small width (0.08-0.16 mm) and high stiffness. At the apex, the membrane is wide (0.42-0.65 mm) and more flexible. As a consequence, the membrane its resonance frequency changes along the length of the membrane. A sound will induce membrane vibrations in certain regions depending on its frequency content. The membrane vibrations stimulate the hair cells, which produce the corresponding signal, which is sent to the brain.

Two types of hair cells exist: inner and outer hair cells. The outer hair cells also function as amplifiers. They increase the vibration level of the basilar membrane at low sound levels which increases frequency sensitivity and allows us to hear the great range of sound pressure levels of six orders of magnitude (0-120 dB SPL). Without this amplification, we would only be able to discern two orders of magnitude determined by the dynamic range of the auditory neurons. This amplification, however, is nonlinear. As a consequence, distortion products can arise. For example, a two-tone stimulation $(f_1, f_2; f_2 > f_1)$ can produce a distortion product $f_{dp} = f_2 - f_1$. This distortion product produced by the cochlea can propagate backward and be detected in the ear canal. Such observed tones are called *otoacoustic emissions*. Otoacoustic emissions are used to evaluate the hearing functionality in very young infants.

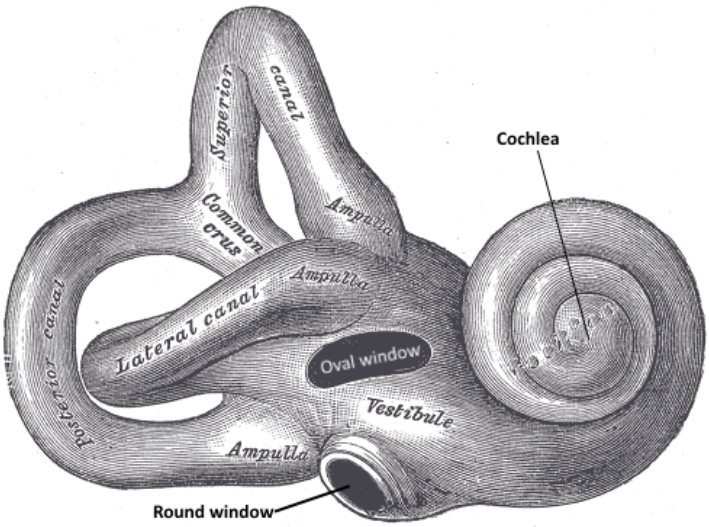

Figure 1.6: The bony labyrinth of the inner ear. The oval window connects to the stapes footplate. Figure modified from Gray (1918) (public domain)

The remaining structures of the bony labyrinth do not contribute to our perception of sound. The three semicircular canals also contain fluids and motion sensors, which provide us a sense of balance.

Chapter 2:
RESEARCH GOALS

In this chapter, we briefly describe the research topics of this thesis and what tools are needed to collect the necessary data.

2.1 How does the middle ear cope with loudness?

We saw that the ME functions as an acoustic-impedance matcher resolving the energy loss issue that would occur at an air-fluid boundary at the entrance of the cochlea. It performs well over a vast range of sound pressure levels, maintaining the temporal structure and shape of the incoming sound signal. We have seen that at low intensities the outer hair cells of the cochlea produce nonlinear distortion products, in contrast, it is generally accepted that the ME works perfectly linear at least up to 120 dB SPL. However, when subjected to large static pressures (>1000 Pa), the ME does not behave linearly at all. For this reason, we expect to be able to detect small nonlinearities at high sound pressure levels too (>20 Pa). Moreover, there exists an asymmetry in the nonlinear behavior at static pressures, which we believe is a result of the asymmetry of the conical shape of the TM.

To measure the nonlinear behavior of the ME, we will need a tool that can measure the vibration response over an acoustically relevant frequency range. Our measurement technique of choice will be laser Doppler vibrometry. We will describe this non-contact optical measurement technique in section 4.1.

To investigate the importance of TM shape on the nonlinear ME response, we must resort to modeling or substitute membranes as we cannot change the TM shape in a temporal bone. We will discuss the nonlinear behavior of the ME in more detail in chapter 5.

2.2 Help, I broke my malleus! How will my middle ear transfer sound?

Whether the human ME works perfectly linear at high sound pressure levels or not, we still have to find out. Nonetheless, every ME ossicle is crucial for a well-functioning ear. A quite uncommon injury, although it could happen to anyone, is the broken malleus handle. It can occur when inserting your finger in your ear after or during a shower. This action can create a vacuum, resulting in a large force pulling on the TM when retracting the finger. This force can be so large that the manubrium fractures, leaving with you a sudden but short pain and even worse, hearing loss.

It seems logical that the hearing loss caused by a malleus fracture is simply a result of the disconnection of a part of the manubrium from the ossicular chain. We will investigate if

this is the case by creating ME models with a fractured manubrium and comparing the results to experimental ME response measurements of TBs with fractured manubrium measured by our Swedish colleague Dr. Anders Niklasson. The results will be discussed in chapter 6.

2.3 Can we measure tympanic membrane (pre-)strain?

Without revealing everything all at once, let us say that our ME models, which only contained a malleus fracture, did not match the experimental results very well. The models lacked something. Experimentally it was observed that after a malleus fracture, the TM became wrinkly and became much less stiff. We, therefore, assumed that the TM is pre-strained and that this pre-strain is lost after fracturing the malleus. Current models do not take into account such pre-strain.

It would, therefore, be interesting to measure the TM strain when subjected to static pressures or the change in strain after fracturing the manubrium. Therefore we need a full-field method which can provide us information on the TM strain. We opted for digital image correlation (DIC), which we will introduce in section 4.3. The results of tympanic membrane strain measurements will be discussed in chapter 7.

2.4 How to locate the ossicular fixation

A more common pathology than the malleus fracture is the ossicular fixation. An ossicular fixation can come in different forms (soft tissue, calcification) and as a consequence of different diseases (otosclerosis, chronic adhesive otitis media, …). In general, an ossicular fixation is a reduction of the mobility of an ossicle due to the presence of unwanted tissue. Otosclerosis, for example, is the calcification of the ossicles their surroundings which usually connects the ossicle to the ME cavity, making them immobile.

Although there exist surgical techniques to resolve the hearing loss caused by ossicle fixation, the methods to detect which ossicle is fixated can be improved. In most cases, manual palpation of the ossicles is used to evaluate the mobility. This method relies on the experience of the surgeon and can be subjective. Therefore it would be useful to determine quantitatively which ossicle and how strong an ossicle is fixated.

We will again use laser Doppler vibrometry as it can return us the vibration response of the ossicles. Since laser Doppler vibrometry is an optical technique, we need visual access to the ossicles. The least invasive way to achieve this in live patients is to lift the TM, which is also done when the surgeon would use palpation to evaluate ossicular mobility. However, without a TM, we cannot let the ossicular chain vibrate using sound. Instead, we will use a *floating mass transducer* (FMT). A device we can stimulate using an electrical current, which in turn will displace the ossicular chain. More on the methods and results in chapter 8.

2.5 Improving the cross-sectional average of frequency response curves: maintaining individual curve characteristics

Many measurements of the ME vibration response have been performed over the years. The average of such vibration response measurements is often used to validate computer models. Such average can, however, be misleading too. We discussed that certain features cause the ear response to show different resonances. These resonances occur at similar, but different, frequencies for each ear. When calculating an average vibration response, we do not take these differences in resonance frequencies into account. As a consequence, the calculated average becomes a very broad indistinctive curve with a loss of the characteristics of the individual curves from which it is calculated.

We can improve this by aligning the individual curves such that the corresponding resonances of all vibration responses occur at the same frequency. If an average of the aligned curves is calculated, the resulting average will maintain the curve characteristics of all individual curves. In chapter 9, we explore the best way to achieve this.

Chapter 3:
ELASTICITY AND VIBRATION THEORY

In this chapter, we explain (visco-)elasticity and vibration theory, which helps us understand the middle ear as a mechanical system. The chapter contents are based on R. F. Coelho and Pyl (2014), Sadd (2005), Fletcher (1992), Banks et al. (2011), Muyshondt (2018a) and Aerts (2010).

3.1 Elasticity theory

The *Cauchy stress* is a mathematical concept that allows us to analyze the internal forces in the body caused by external forces ($\boldsymbol{P}$). Figure 3.1 shows a body through which a cutting plane (A) is defined by an external normal direction ($\boldsymbol{n}$). Since the body is in equilibrium, the imaginary cutting plane gives rise to internal forces[1]. The Cauchy stress is defined by the limit of the ratio between the resultant force ($d\boldsymbol{f}$) on an arbitrary surface (dS) and that arbitrary surface, dS:

$$\boldsymbol{t}^{(n)} = \lim_{dS \to 0} \frac{d\boldsymbol{f}}{dS} \tag{3.1}$$

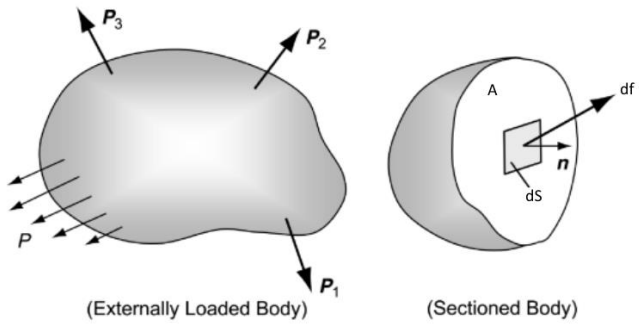

Figure 3.1: Body loaded by external forces (left). Body sectioned by imaginary cutting plane A defined by a normal vector $\boldsymbol{n}$ showing resultant force df over an arbitrary surface dS (right). Figures adjusted from Sadd (2005).

Because of Newton's third law, we know that $\boldsymbol{t}^n = -\boldsymbol{t}^{(-n)}$. We can construct a second order stress tensor $\bar{\bar{\boldsymbol{\tau}}}$ by defining all stress vectors to each of the three coordinate planes. We then get 9 different values. Any stress vector on any plane can be calculated using

[1] We make the hypothesis of the absence of couple-stress, meaning there is no moment.

these 9 values by the projection of the stress tensor onto the normal associated with that plane:

$$\bar{\bar{\boldsymbol{\tau}}} \cdot \boldsymbol{n} = \begin{bmatrix} \tau_{xx} & \tau_{xy} & \tau_{xz} \\ \tau_{yx} & \tau_{yy} & \tau_{yz} \\ \tau_{zx} & \tau_{zy} & \tau_{zz} \end{bmatrix} \begin{bmatrix} n_1 \\ n_2 \\ n_3 \end{bmatrix} \tag{3.2}$$

The diagonal components of $\bar{\bar{\boldsymbol{\tau}}}$ are the normal components ($\tau_{xx} = \sigma_x, \tau_{yy} = \sigma_y, \tau_{zz} = \sigma_z$). If a normal component is positive, the surface is under tension. Vice versa, a negative normal component represents compression. The non-diagonal components represent shear stresses. The first index always represents the direction of the normal of the cutting plane. In the absence of body moments, the shear components are symmetric ($\tau_{ij} = \tau_{ji}$).

When we are studying deformations, we need additional variables such as strains and displacements. Consider a one-dimensional rod which is elongated along its length L_0 by ΔL to obtain a length L_f. The strain (ϵ) can then be calculated as:

$$\epsilon = \frac{\Delta L}{L_0} \tag{3.3}$$

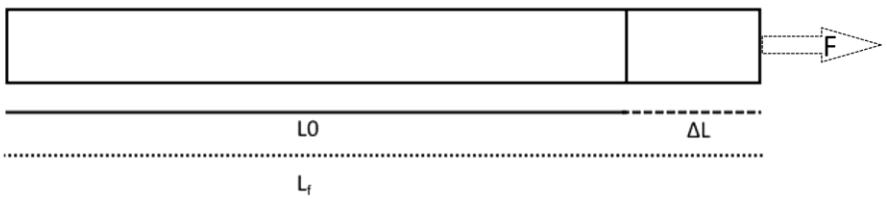

Figure 3.2: A rod of length L_0 which is elongated along its length by ΔL to obtain a final length L_f.

Equation (3.3) represents a normal strain. The elongation occurs in the direction of the applied normal stress/force. For ΔL is small, it does not matter whether L_0 or L_f is used in the denominator of (3.3). When one uses the initial configuration as the reference, we speak of the Green-Lagrangian strain. If the deformed configuration is used as a reference, the calculated strain is referenced as the Almansi-Eulerian finite strain tensor.

A three-dimensional body can deform and strain in multiple directions at the same time. To calculate the strain in a general manner, we need partial derivatives. Consider a body with initial configuration V and deformed configuration V' (figure 3.3). The deformed configuration was reached by the displacement $\boldsymbol{u}(x, y, z)$ at any point (x, y, z).

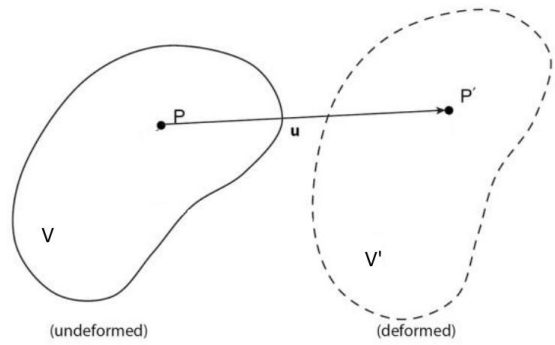

Figure 3.3: Undeformed body V with point P (left) and deformed body V' with point P' which is displaced by vector $\boldsymbol{u}$ (right).

The linear strain tensor $\bar{\bar{\boldsymbol{\epsilon}}}$ is then defined as

$$\epsilon_{ij} = \frac{1}{2}\left(u_{i,j} + u_{j,i}\right) \tag{3.4}$$

With $u_{i,j} = \frac{\partial u_i}{\partial j}$ with $i, j \in (x, y, z)$. In matrix form we have:

$$\bar{\bar{\boldsymbol{\epsilon}}} = \begin{bmatrix} \epsilon_{xx} & \epsilon_{xy} & \epsilon_{xz} \\ \epsilon_{yx} & \epsilon_{yy} & \epsilon_{yz} \\ \epsilon_{zx} & \epsilon_{zy} & \epsilon_{zz} \end{bmatrix} \tag{3.5}$$

The material law relates strain ϵ to stress τ. Let us return to our one-dimensional bar. For axial loading along the x-direction we have:

$$\epsilon_x = \frac{1}{E}\sigma_x \tag{3.6}$$

Where E is the *Young's modulus*, a material property which could be intuitively described as the stiffness of the material. Equation (3.6) is basically Hooke's law. However, when the bar is axially stretched, negative transversal strains will occur. This is called the *Poisson effect*:

$$\epsilon_y = \epsilon_z = -\frac{\nu\sigma_x}{E} \tag{3.7}$$

With ν the *Poisson ratio* which lies between 0 and 1. For most materials $\nu = \frac{1}{3}$, for incompressible materials such as rubber $\nu = \frac{1}{2}$. Considering all orthogonal contributions to each normal strain, we get that:

$$\epsilon_i = \frac{1}{E}\left(\sigma_i + \nu\left(\sigma_j + \sigma_k\right)\right) \tag{3.8}$$

For shear strains we have

$$\epsilon_{ij} = \frac{1}{G}\tau_{ij} \; for \; i \neq j \tag{3.9}$$

Where $G = \frac{E}{2(1+\nu)}$ is the shear modulus of elasticity.

For three-dimensional loadings, Hooke's law can be generalized to be

$$\tau_{ij} = C_{ijkl}\epsilon_{kl} \tag{3.10}$$

In which C_{ijkl} is a fourth-order elasticity tensor containing 81 components. For isotropic materials for which the material properties are independent of the orientation, the law can be simplified.

$$\tau_{ij} = \lambda\delta_{ij}\epsilon_{kk} + 2\mu\epsilon_{ij} \tag{3.11}$$

Where $\lambda = \frac{\nu E}{(1+\nu)(1-2\nu)}$ and $\mu = \frac{E}{2(1+\nu)} = G$ are Lamé constants. We can rewrite (3.11) to obtain the stress-strain relationship for isotropic elastic materials:

$$\epsilon_{ij} = \frac{1}{E}\left[(1+\nu)\tau_{ij} - \nu\delta_{ij}\tau_{kk}\right] \tag{3.12}$$

3.2 Viscoelasticity

A purely elastic material will not dissipate any energy during dynamic loading. In contrast, a viscoelastic material will. Figure 3.4 shows the stress-strain relation during dynamic loading of an elastic and viscoelastic material. The elastic material shows no hysteresis (the area between loading and unloading curve) during a loading cycle. Although viscoelastic materials return to their original state after one cycle (hence the elastic suffix), hysteresis is present meaning there is a net energy loss during a load cycle. In finite element modeling, we will often refer to the viscosity as damping.

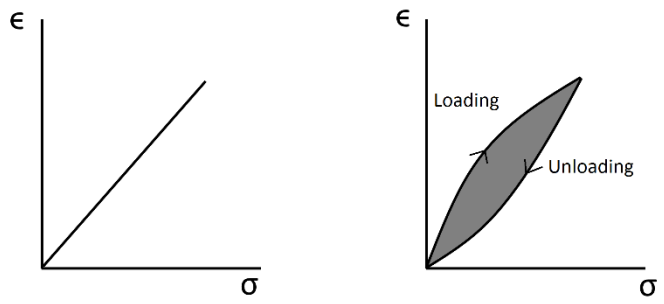

Figure 3.4: Stress-strain curve during loading and unloading of an elastic material (left) and viscoelastic material (right). A finite area between the loading and unloading curve means an energy loss exists during the loading cycle.

The viscoelastic property of solid materials is a result of the reorganization of molecules when the material is subjected to a change in stress. Viscosity is a time-dependent phenomenon. Several theoretical models exist to describe viscoelastic properties based on simple spring-dashpot systems. The spring is the elastic component, while the dashpot represents the viscous component.

The *Maxwell* model consists of a spring and dashpot in series (figure 3.5A). The time-dependent stress-strain relationship for a Maxwell model is

$$\sigma + \frac{\eta}{E}\dot{\sigma} = \eta\,\dot{\epsilon} \tag{3.13}$$

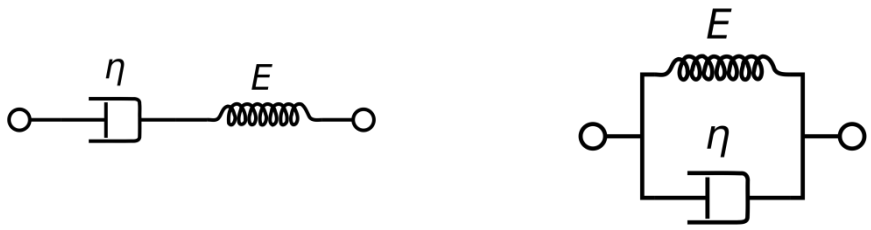

A B

Figure 3.5: Representations of two visco-elastic models consisting of a spring and damper. The Maxwell model (A) and Kelvin-Voigt model (B).

This model accurately describes the strain after a sudden stress release, a process called *relaxation*. The stress will decay exponentially with time. However, the model does not describe the strain for a sudden application of stress. The strain rate in polymers slows down after time, a process called *creep*. In contrast, the Maxwell model predicts a linear increase in strain.

Another model, the *Kelvin-Voigt* model (figure 3.5B), places the dashpot and spring in parallel. The relation then becomes:

$$\sigma = E\epsilon + \eta\dot{\epsilon} \tag{3.14}$$

This model predicts creep accurately but does not for relaxation. The most general model is the *generalized Maxwell* model, also known as the *Wiechert* model. This model is a spring in parallel with multiple Maxwell models. We then get

$$\sigma(t) = \left(R_0 + \sum_{j=1}^{m} \frac{R_j D}{D + \frac{R_j}{\eta_j}} \right) \epsilon(t) \quad with\ D = \frac{d}{dt} \tag{3.15}$$

This model takes into account that the relaxation occurs at different rates due to the different sizes in molecules that rearrange themselves after a sudden application/release of stress. This model allows characterizing the materials on different time scales and thus different frequency ranges.

3.3 Vibration theory

The behavior of structures, when subjected to harmonic loading, can be explained by vibration theory. With only three simple concepts, we can describe the behavior of a whole range of vibrational systems; Stiffness, mass, and damping. The harmonic oscillator is the go-to example which demonstrates the effect of these basic parameters on the vibration response.

3.3.1 The harmonic oscillator

The harmonic oscillator is a mechanical system that consists of a mass attached to a parallel setup of a spring and a dashpot (damper) which are connected to a rigid wall (figure 3.6). The stiffness (k) determines the restoring force based on the displacement of the mass (m). The damping (c) causes the system to exhibit energy loss. The equation of motion for the harmonic oscillator is:

$$m\ddot{x} + c\dot{x} + kx = F(t) \tag{3.16}$$

In which $F(t)$ is the driving force and $\ddot{x}$, $\dot{x}$ and x are respectively the acceleration, velocity, and displacement of the mass.

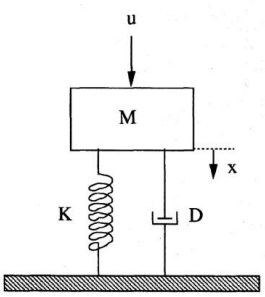

Figure 3.6: Sketch of a harmonic oscillator consisting of a mass attached to a spring and damper in parallel.

If the driving force $F(t)$ is harmonic, it can be written in the complex space as $F(t) = |F|e^{i\omega t}$ with $|F|$ the amplitude of the force and ω the angular frequency which equals to $2\pi f$ with f the stimulation frequency. The harmonic oscillator is a linear system. Thus we assume the solution to equation (3.16) to be a harmonic solution with the same frequency as the driving force

$$X(t) = Ae^{i\omega t+\phi} \tag{3.17}$$

Substituting (3.17) in (3.16) gives:

$$\begin{aligned} -m\omega^2 Ae^{i\omega t+\phi} + ic\omega Ae^{i\omega t+\phi} + kAe^{i\omega t+\phi} &= |F|e^{i\omega t} \\ -m\omega^2\tilde{X} + i\omega c\tilde{X} + k\tilde{X} &= |F| \end{aligned} \tag{3.18}$$

with $\tilde{X} = Ae^{i\phi}$. We then find that

$$\begin{aligned} \tilde{X} &= \frac{|F|}{-m\omega^2 + i\omega c + k} \\ \tilde{X} &= \frac{\frac{|F|}{m}}{\omega_0^2 - \omega^2 + i\omega\frac{c}{m}} \end{aligned} \tag{3.19}$$

Or

$$\begin{aligned} A &= \frac{\frac{F}{m}}{\sqrt{(\omega_0^2 - \omega^2)^2 + \left(\frac{c}{m}\omega\right)^2}} \\ \phi &= \operatorname{atan}\left(-\frac{\frac{c}{m}\omega}{\omega_0^2 - \omega^2}\right) \end{aligned} \tag{3.20}$$

Where $\omega_0 = \sqrt{\frac{k}{m}}$ is the undamped angular resonance frequency. We will often not refer to the angular resonance frequency but the resonance frequency defined as $f_0 = \frac{\omega_0}{2\pi}$. The term $\frac{c}{m}$ is often rewritten as $\frac{c}{m}\frac{2}{2}\frac{\sqrt{k}}{\sqrt{k}} = 2\zeta\omega_0$. The parameter ζ is the so called damping ratio. The frequency responses calculated as (3.20) for different parameters values are shown in figure 3.7. The lower frequencies are stiffness-governed, making the amplitude independent of the frequency. The displacements at low frequency occur in phase with the applied force. The high frequencies are mass-governed. The amplitude decreases with increasing stimulation frequency by power two. At the resonance frequency we find the maximal amplitude of the frequency response. The phase undergoes a phase jump of half a cycle (1π). If the damping decreases, the sharpness of the resonance peak increases, and the phase jump occurs more abrupt. If the stiffness increases, the resonance frequency increases, the amplitude at low frequencies and resonance frequency decreases. If mass increases, the amplitude at low frequencies and resonance increases.

The velocity response is calculated by multiplication of $\tilde{X}$ by $i\omega$. This implies that at low frequencies $A_v \sim \omega$ and at high frequencies $A_v \sim \omega^{-1}$. The phase shifts by $\frac{\pi}{2}$ or +0.25 cycles.

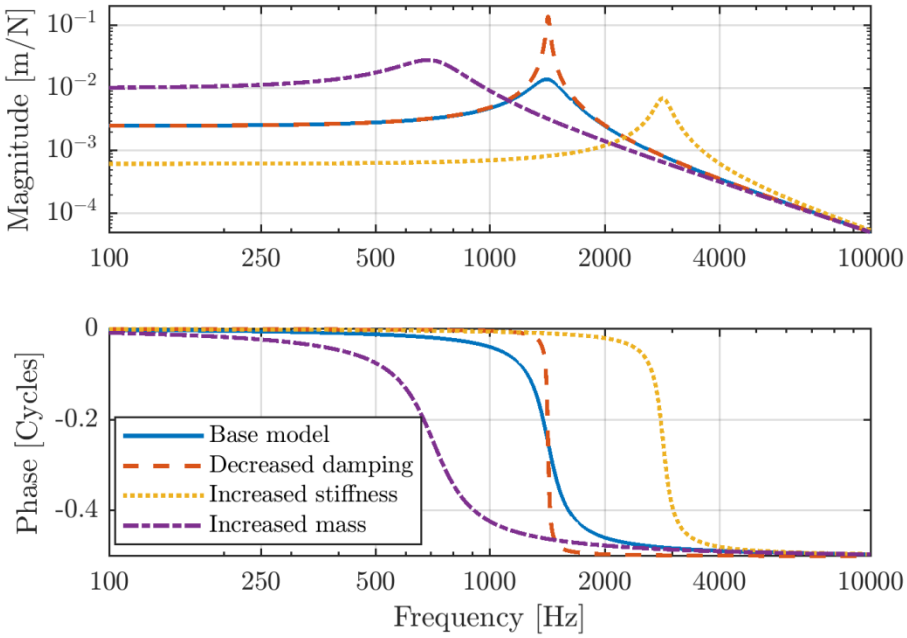

Figure 3.7: Frequency response of the harmonic oscillator for different parameter values. The base model (solid blue line) has a stiffness $k = 400\frac{N}{m}$, a mass of $5 \cdot 10^{-6} kg$ and damping $c = 8.13 \cdot 10^{-3} N \cdot s/m$. The applied force amplitude was $F = 10^{-3} N$.

3.3.2 Nonlinear harmonic oscillator (Duffing equation)

When we stimulate the linear harmonic oscillator using a sinusoidal force, the response will be sinusoidal with the same frequency. The normalized frequency response will be independent of stimulation amplitude. For a nonlinear system, these properties are not true. An extension on the linear harmonic oscillator is the so-called Duffing equation. The Duffing equation adds a nonlinear stiffness term to (3.16).

$$\begin{aligned} m\ddot{x} + c\dot{x} + k_1 x + k_2 x^3 &= F(t) \\ m\ddot{x} + c\dot{x} + (k_1 + k_2 x^2)\, x &= F(t) \end{aligned} \tag{3.21}$$

Due to this nonlinear term, the normalized frequency response at different excitation levels will not remain the same. If $k_2 > 0$ we see that the total stiffness increases as the displacements grow. If the system *stiffens*, we know that the resonance frequency increases and the overall displacement magnitude will reduce. If $k_2 < 0$, the opposite occurs. The system *softens* and the resonance frequency decreases. Both effects are presented in figure 3.8. The maximal amplitude as a function of a change in resonance frequency at different excitation levels is called a backbone curve is shown in figure 3.9. The backbone curve shows a negative change in resonance frequency, demonstrating the *softening behavior* ($k_2 < 0$).

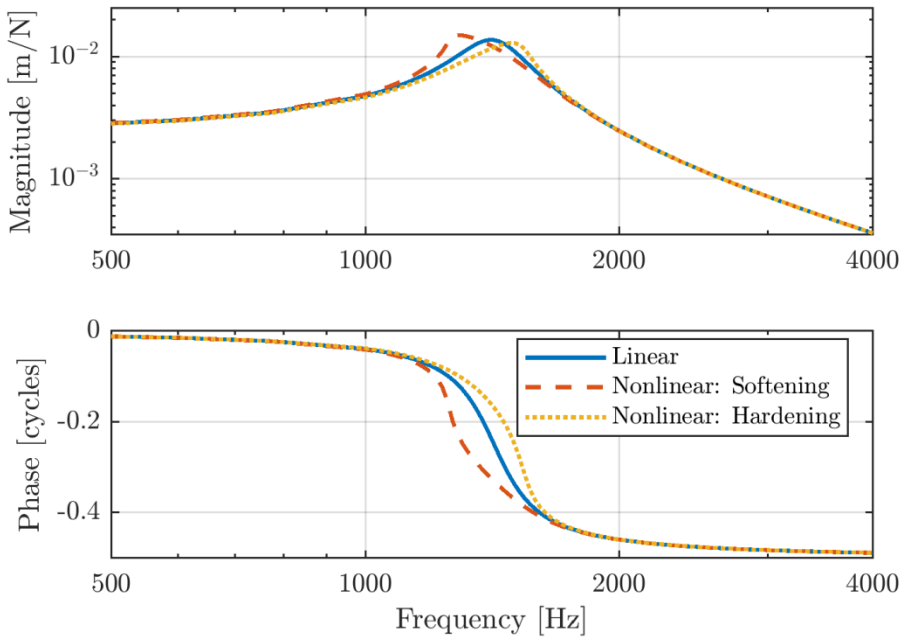

Figure 3.8: Solution of the Duffing equation for low stimulation amplitude (blue) and high stimulation amplitude with $k_2 < 0$ (red) and $k_2 > 0$ (yellow).

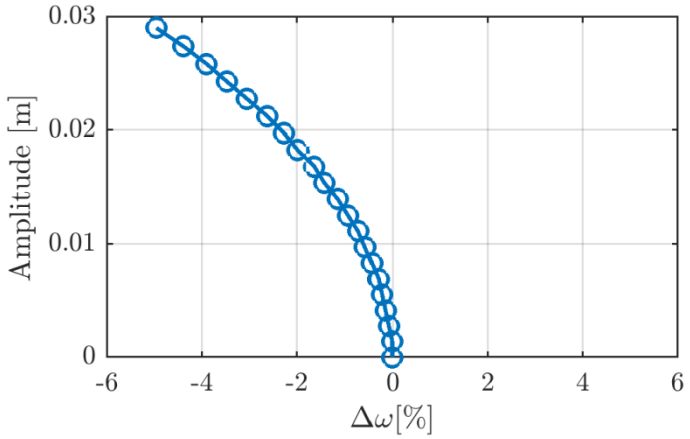

Figure 3.9: Backbone curve for a nonlinear harmonic oscillator with $k_2 < 0$. The oscillator's resonance frequency reduces as the stimulation level increases; this is typical for softening behavior.

The cubic term in (3.21) causes the system to respond at frequencies which are not contained in the stimulation signal. Figure 3.10 shows the spectrum of the displacement when the nonlinear oscillator was stimulated only at a single frequency of 100 Hz. We observe non-zero amplitude frequency content of the displacement signal at odd multiples of the stimulation frequency. These are called odd harmonics or odd degree nonlinear distortions. Even harmonics are absent. If (3.21) had contained a quadratic term instead of a cubic term, both even and odd harmonics would have been present. We can confirm the absence of the even harmonics over an entire frequency range by calculating the higher-order frequency responses.

$$H_n(\omega) = \frac{2^{n-1}X(\omega)}{F(\omega)} \tag{3.22}$$

For $n = 1$ equation (3.22) simply returns the normalized first order frequency response we have shown before. For $n = 2$ and $n = 3$, we get the responses representing the vibration response of respectively the second and third harmonic. These are shown in figure 3.11. The level of the second harmonic is indeed close to the computational noise. The curve representing the level of the third harmonic shows similarities to that of the first harmonic we saw in figure 3.8. At low frequencies, the response is independent of stimulation frequency. At high frequencies, the magnitude declines. A resonance peak is seen at about 1400 Hz. However, we observe that another resonance is present. Its resonance frequency is one-third of that of the linear resonance frequency. This means that the linear frequency response affects the nonlinear response. If we stimulate at a third of the linear resonance frequency, the level of the third harmonic will be higher than if nearby frequencies would be used. The fact that the oscillator moves “more easily” at its linear resonance frequency makes it easier for the nonlinear displacement component to move at that frequency. Similarly, when we stimulate at the resonance frequency, the oscillator displaces more. A larger displacement causes the nonlinear component to be larger. This is why the third harmonic also exhibits a resonance at the linear resonance frequency.

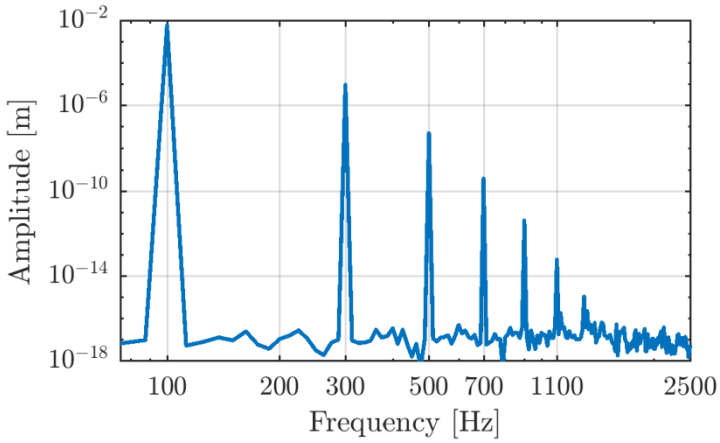

Figure 3.10: Spectrum of a nonlinear oscillator with a cubic stiffness term obtained using single frequency stimulation at 100 Hz. Odd degree nonlinearities are visible while even degree nonlinearities are absent.

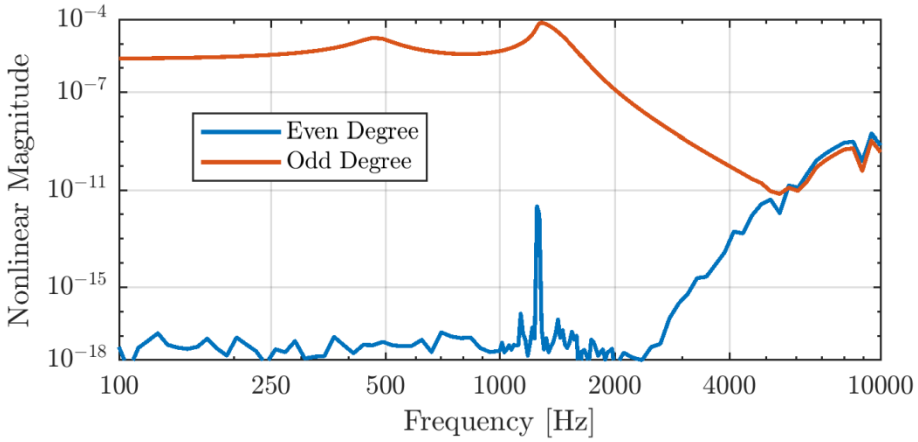

Figure 3.11: Higher-order frequency responses of a nonlinear oscillator with a cubic stiffness term. The vibration level of the second harmonic is negligible. The level of the third harmonic shows resonances at the linear resonance frequency ($\approx 1400\,Hz$) and a third of the linear resonance frequency.

Chapter 4:
FINITE ELEMENT MODELING AND MEASUREMENT TECHNIQUES

In this chapter, we describe the tools which we will use to evaluate certain variables of the middle ear and investigate the problems posed in chapter 2.

4.1 Laser Doppler vibrometry

In many cases, we want to evaluate the state of the middle ear. In TB studies, we want to determine whether a TB exhibits any hearing loss. Since we are working ex-vivo, we cannot use standard hearing tests which require the cooperation of the "patient". We need a different variable which can tell us something about the functionality of the TB. We can make use of the frequency response discussed in section 3.3.1. Previous studies have shown that the frequency response of the stapes footplate is an adequate substitute to evaluate hearing losses in TBs (Nakajima et al., 2005). In such TB studies, one starts out with a healthy ME after which a pathology is simulated (e.g. ossicle fixation by application of dental cement). By calculating the ratio of the response for the ME with simulated pathology to that of the healthy ME, the hearing loss induced by that simulated pathology is estimated. Laser Doppler vibrometry (LDV) is a non-contact optical measurement technique which we will use to measure the frequency response in MEs of TBs.

This section is based on Rothberg et al. (2016) and Muyshondt (2018b).

4.1.1 How does laser Doppler vibrometry work?

LDV is based on the Doppler effect. A common example is the frequency of the siren of an ambulance changes when it passes by. An illustration of this is shown in figure 4.1. We see that the frequency of the produced sound increases as it approaches us. Vice versa, it decreases when it moves away. Similarly, the frequency (f_0) decreases when the observer is moving away from the source (ambulance) and increases when moving towards the source. The frequency shift (Δf) is dependent on the relative velocity of the observer to the source (Δv):

$$\Delta f = \frac{\Delta v}{c} f_0$$

This quantity is positive when observer and source are moving towards each other. The speed of sound is denoted by c.

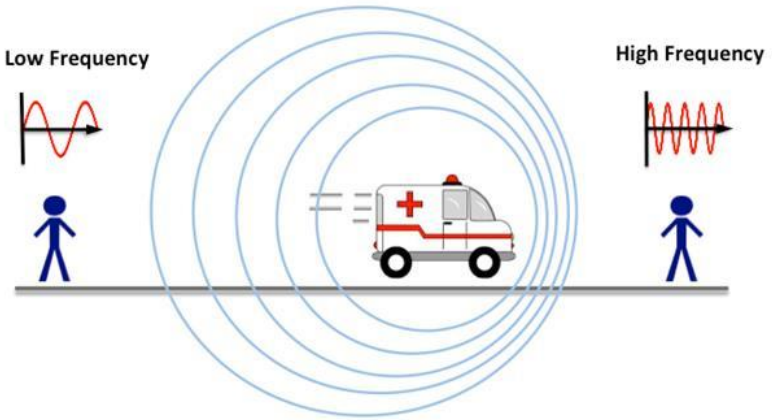

Figure 4.1: Sketch illustrating the Doppler effect which occurs for a relative movement between sound source and observer. If the distance between source and observer increases, the frequency of the sound is observed to be lower. This frequency shift is linearly dependent on the relative speed between source and observer.

In our case, we are not observing a moving sound source. Instead, we want to evaluate the sound-induced vibrations of an object. The Doppler effect also occurs when using light instead of sound.

When light impinges on a vibrating object, the light scatters in all directions. Some light reflects to the observer. The frequency of the light wave will shift due to the Doppler effect. The Doppler shift will be $f_d(t) = 2v(t)\cos\alpha\,/\lambda$. The time-dependent velocity of the vibrating object is denoted by $v(t)$. The direction of the vibration velocity might be under an angle α with the line of sight of the observer. The observed shift is dependent on this angle. This means we cannot evaluate the vibration velocity if the vibration occurs perpendicular to the viewing direction ($\cos 90° = 0$). The wavelength of the light is denoted by λ. In theory, we can determine the vibration velocity of the object if we can measure the frequency of the reflected light ($\frac{c_{light}}{\lambda}$). However, the frequency of light is very high ($> 10^{14} Hz$). Such frequency is not measurable by our photodetector. If we use a monochromatic light source (i.e. laser light), we could combine the original light beam (reference beam) with the reflected light beam (object beam). Both beams will interfere and the observed signal contains an amplitude modulation. The amplitude modulation frequency is the difference between the frequencies of both beams. This frequency is much lower than the carrier frequency (i.e. the original frequency of light) and detectable by the sensor. However, the modulation frequency is the same regardless of the object moving towards or away from the sensor. We thus only have knowledge about the vibration amplitude and not about the phase. This issue can be solved by adding a constant shift to the reference beam f_B by placing a *Bragg cell* in the path of the reference beam. The modulation shift then becomes $f_m(t) = f_b + f_d(t)$. The sensor records an intensity signal:

$$I(t) = I_r + I_o + \sqrt{I_r I_o}\cos(2\pi f_m(t) + \phi)$$

This is a frequency modulated signal with f_b as the carrier frequency and the Doppler shift $f_d(t)$ as modulation frequency. When the object moves towards the sensor the modulation frequency decreases, and when the object moves away from the sensor, the modulation frequency increases. By demodulation, we can determine the vibration velocity $v(t)$ of the object.

The above description involves splitting the original light beam into a reference and an object beam and eventually recombining them. This is achieved by using beam splitters. A sketch of the beam paths and used optical components is given in figure 4.2. A light beam exits the laser and passes through a first beam-splitter. We now have our separated object and reference beam. The reference beam passes through the Bragg cell generating the constant frequency shift f_b after which it reaches the detector. The object beam passes through another beam splitter and hits the vibrating object. A part of the reflected light bounces back to the beam splitter which redirects, so it is recombined with the reference beam at the sensor.

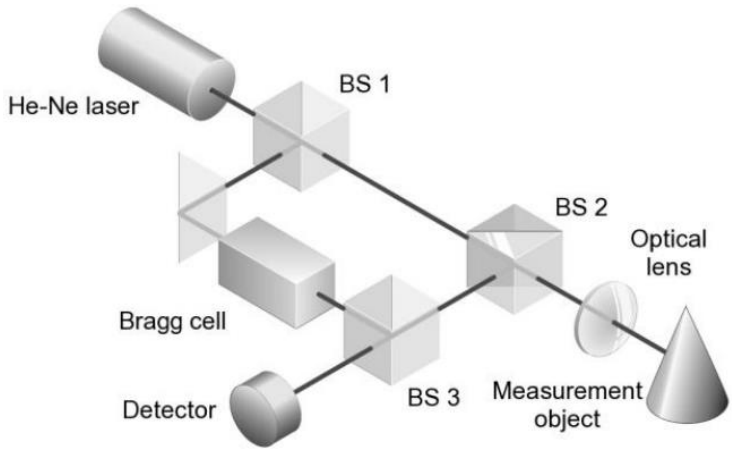

Figure 4.2: Path of the laser beam in a laser Doppler vibrometer setup. The original laser beam is split up (BS1) in an object beam and a reference beam. The reference beam passes along a Bragg cell which shifts the light frequency and then reaches the detector. The object beam hits the measurement object, which shifts the light frequency due to the Doppler effect. The Doppler-shifted reflected light is guided to recombine with the reference beam at the detector. Figure from Muyshondt et al. (2018).

4.1.2 Measurement setup

In the section above, we described how the vibrometer works internally. Here we will describe the part of the setup which allows for precise aiming of the object beam. The ME components are quite small, and the measured vibration response can vary depending on the exact measurement location. Figure 4.3 shows the vibration response of three points on the manubrium for a sound pressure level of 90 dB SPL. The measurement points are less than 5 mm separated from each other, but the response level is quite different due to the mechanical properties of the ME.

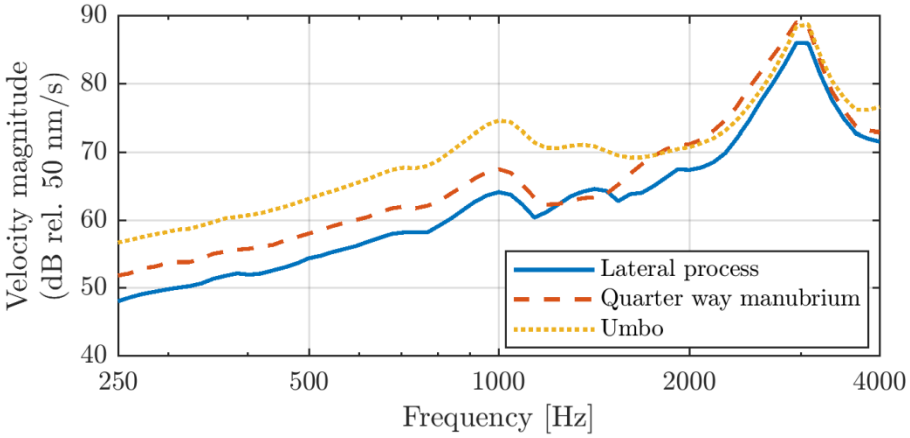

Figure 4.3: The effect of small changes in laser aiming (<5 mm) on the velocity magnitude of the tympanic membrane. This graph demonstrates the need for a setup which allows precise laser beam aiming.

For this reason, we mounted a vibrometer head, which emits the object beam, on a surgical microscope, as shown in Figure 4.4. The laser beam is reflected by a mirror and is aligned to the viewing direction. The orientation of this mirror can be micro-adjusted using piezo-motors, allowing for very precise positioning of the beam. Similarly, the focusing can be adjusted electromechanically. Reflective patches are used to enhance the signal of the reflected beam from the object. These patches are 0.16 mm^2 in size and weigh no more than 0.04 mg.

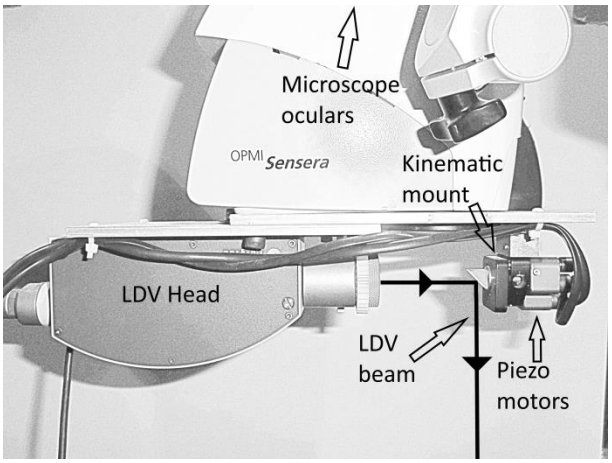

Figure 4.4: Operation microscope with mounted laser Doppler vibrometer head. The piezo motors and kinematic mount allow for precise aiming and focusing of the laser beam at small targets.

In many cases, we induce ME vibrations using sound. This can be done using a free-field speaker or a semi-closed cavity with a transparent window with non-reflective coating on top to let the laser beam through. We often use a semi-closed cavity because it is easier to obtain a sound pressure level of 90 dB at the level of the TM without exposing ourselves to loud sounds.

The sound has to be recorded to obtain an accurate velocity response function of the ME,. We saw this in section 3.3.1, where the velocity response function was defined as:

$$X(f) = \frac{x(f)}{F(f)}$$

Where $x(f)$ is the displacement and $F(f)$ is the applied force as a function of frequency. In our case, this is the applied sound pressure. The sound pressure level is preferably measured close to the TM (i.e. 2 mm distance) but is often also measured at the entrance of the ear canal (ANSI, 2014). When calculating the phase, the time delay caused by the distance from the microphone sensor to the measurement location should be incorporated. This is also true for time delays generated by the electronics.

All measurement data using LDV will be obtained utilizing the setup described above. The data will be recorded using a National Instruments an A/D-D/A conversion board with 16-bit resolution and a sampling rate of 50 or 500 kHz (National Instruments, USB-6251 BNC, Austin, TX, USA).

4.2 Sound stimulation and measurement

To measure the frequency response, we need to stimulate the ME. In almost any case, we will use sound stimulation except for measurements on MEs with ossicular fixations

(chapter 8). Many variants of stimulation signals exist. In this section, we will highlight two we make use of in our lab and how the sound is measured.

4.2.1 Stepped single sine stimulation

If we want to know the frequency response of the ME for N frequencies, we could stimulate the ME at each frequency separately and calculate the Fourier spectrum of the measured vibration and sound. Of each Fourier spectrum, we only keep the data point of the corresponding stimulation frequency. By combining all the relevant data points, we obtain the desired frequency response of the ME.

The main advantage is that you can measure a very large number of frequencies as the power the sound system has to deliver is independent of the number of frequencies if you want a fixed sound pressure level for each frequency.

The main disadvantage is that it is time-consuming. Each frequency requires a separate measurement, and each measurement requires some additional stimulation time to eliminate transients. To be sure we achieve this, we use 0.1 s as additional stimulation time. For 16 frequencies per octave using a frequency range of 125 to 8000 Hz, we have a total of 97 frequencies. When using 50 periods for each frequency, the additional stimulation time becomes about half of the total measurement time of 19 seconds. In addition, many authors use a fixed sound pressure level of 90dB SPL. To achieve a 90dB SPL for each stimulation frequency, we have to adjust the voltage sent to the speaker system using an iterative process. Often we use two correction cycles, and the third cycle then becomes the final measurement. So we have a total measurement time of about 1 minute. In some situations, this might be considered to be impractical, so let us look at a stimulation method that decreases measurement time.

4.2.2 Multisine stimulation

An alternative is to stimulate multiple frequencies at the same time. This can be achieved using multisine stimulation. Multisine stimulation $s(t)$ is simply a sum of sine functions:

$$s(t) = \frac{1}{\sqrt{N}} \sum_{i=1}^{N} A_{k_i} \sin\left(2\pi k_i f_{res} t + \phi_{k_i}\right) \qquad (4.1)$$

If we use harmonically related functions, we can fit a whole number of periods of each sine wave precisely for a chosen measurement time. For example, let us choose all stimulation frequencies (f) to be harmonically related to a single $f_{res} = 5\ Hz$ in equation (4.1) by choosing $f = kf_{res}$ with k a natural number. For a fixed measurement time of $T = \frac{1}{f_{res}} = 0.2\ s$, an exact number of periods of each sine wave will fit. As a consequence, there is minimal spectral leakage and no windowing required. The frequency resolution of our measurement is equal to f_{res}. It is clear that multisine stimulation allows for much faster measurements. If we include a 0.1 s additional stimulation time to eliminate transients and use two cycles to obtain the desired sound pressure level using $f_{res} = 5\ Hz$, we will have a total measurement time of about 0.9 s.

Depending on the number of stimulation frequencies, it will become hard to achieve 90dB SPL at each frequency. On top of that, each sine wave of the multisine contributes to the total sound pressure level. If we want to be certain of obtaining the linear response of the ME, we should keep this total sound pressure limited, preferably at 90dB SPL. If we want a total sound pressure level of 90dB SPL using $N = 97$ frequencies, we only have a sound pressure level $90 - 20\log_{10}(\sqrt{N}) = 70dB$at each frequency separately. The number of frequencies cannot be too large, or the vibration levels might disappear in the noise floor of the measurement equipment. For this reason, we prefer to use the stepped single sine stimulation in applications where measurement time is not important.

The phase ϕ_{k_i} should be chosen randomly. Because all stimulation frequencies are harmonically related, very large amplitude spikes would arise if all phases were equal.

4.2.3 Correct phase determination

We will always measure the sound pressure using a Bruel & Kjaer type 4182 probe microphone unless specifically mentioned otherwise. The determination of the sound pressure level is straight forward. In contrast, the calculation of the phase requires some additional knowledge of the setup. The metal probe on the microphone generates a distance between the microphone membrane and the actual measurement point. Sometimes another flexible rubber tube is added to reach down the ear canal and get close to the TM, increasing the distance between the microphone membrane and measurement point. The phase of the sound wave at the measurement point will not be the same as at the microphone membrane because the sound still has to travel through the tubes to reach the microphone membrane. The phase shift $\Delta\phi$ is determined by the distance between the measurement point and the microphone membrane Δx, by frequency f and the speed of sound c and the sound which we will consider to be a constant (343 m/s):

$$\Delta\phi(f, \Delta x) = \frac{\Delta x}{\frac{c}{f}} 2\pi \tag{4.2}$$

For a frequency of 1 kHz and a tube length of 250 mm, a phase shift of 4.58 radians is observed. This example demonstrates the necessity of correcting for this phase shift due to the distance between the microphone membrane and the measurement point.

4.2.4 Effect of measurement point

In section 1.2.1, we saw that the pinnae and ear canal produce resonances, increasing the sound pressure level in certain frequency bands at the level of the TM. Since the frequency response $X(f)$ is calculated as $X(f) = \frac{vibration(f)}{sound(f)}$, the placement of the probe microphone influences the calculated frequency response. Ideally, the sound is measured about 2 mm from the TM since most finite element models will not include an ear canal and apply a pressure load directly on the TM ANSI (2014). In some TB experiments described in this thesis, the sound will be measured at the entrance of the ear canal instead. The location of the probe microphone will always be mentioned for each experiment separately.

4.2.5 Speaker nonlinearities at high sound pressure levels

In chapter 5, we will investigate the nonlinear behavior of the TM at high sound pressure levels ($\approx 120dB$). In a small closed cavity, it is fairly easy to produce high sound pressure levels. As soon as a sound leak is present, the speaker system will have to push hard to attain these high sound pressure levels. This causes the speaker to distort and to produce sound at unwanted frequencies. Two solutions will be discussed in detail in chapter 5.

4.3 Digital image correlation

The LDV technique we described above is a single-point measurement technique and allows us to measure the vibration velocity in a single direction in a single measurement point at a time. Adjustments to the LDV technique can allow it to measure multiple points on a surface and expanding to 3D velocity measurements. However, to obtain full-field 3D displacement, strain, and shape data of ME components, we will need to use a different non-contact optical technique called digital image correlation. This section is based on Cheng et al. (2007) and Palanca et al. (2016) and Guillermo et al. (2017).

4.3.1 How does digital image correlation work?

The principle consists of tracking stochastic intensity patterns, present on the object surface. Suppose we placed two markers on a surface. If the surface deforms, we can extract information from the new positions of the markers. First, we can calculate the displacements of each marker since we have knowledge of its original and current position in the image. Second, we can also measure the strain which depends on the relative position of both markers which respect to each other. Figure 4.5 shows a stochastic intensity pattern on a surface before and after deformation of the surface. Since the pattern is stochastic, the surface can be divided into unique sections called facets. For each facet, we can calculate the displacement and strain, which is based on the distortion of the facet after deformation. Alternatively, the strains can be determined by calculating the gradient of the displacement maps.

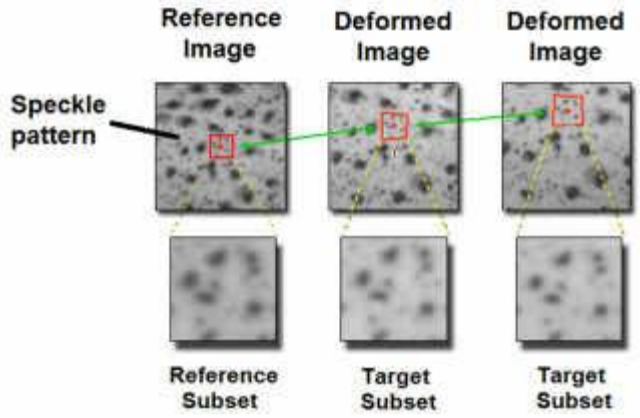

Figure 4.5: Example of a stochastic intensity pattern on a surface before and after two sequential deformation steps. Figure from Guillermo et al. (2017).

Once a stochastic intensity pattern is present on the object surface, a reference image has to be made. The unique facets are constructed using this reference image. The DIC-algorithm then tries to find each unique individual facet in subsequent images of the deformed surface. This search is achieved by employing a least-square optimization to determine the parameters of the displacement mapping of each facet between the reference image and deformed image.

A single camera allows for measuring in-plane displacements. Two cameras also allow for out-of-plane displacement and 3D shape measurements. A large angle between the cameras results in high accuracy of the out-of-plane displacements. However, for steeply curved objects, a trade-off has to be made between the accuracy of out-of-plane displacements and visibility of the entire object surface on both cameras.

A stochastic intensity pattern needs to fulfill certain conditions to be suited to be useable for DIC measurements. Evidently, the pattern needs to be stochastic. This is usually achieved by spraying some kind of paint on the surface. The eardrum surface texture is not suited to be used as a stochastic intensity pattern on its own. It is too smooth and thus does lack contrast variation. The surface should be treated by the application of an artificial pattern. By spraying droplets of paint, we can generate a random distribution of speckles on the surface. A high level of contrast is necessary. The individual speckles or surface structure need to generate distinct grey values when recorded by a camera. Ink or toner naturally gives a high contrast pattern. Ideally, the size of the individual speckles is about 5 pixels. Larger speckles would be inefficient in terms of accuracy because the surface could have been divided into smaller facets with smaller speckles. Smaller speckles make it more difficult to distinguish them. Controlling the speckle size, especially on small surfaces like the eardrum, takes some trial and error. Image coverage should lie between 40-70%. Sparser distributed speckles would again be an inefficient use of pixels. Denser patterns are too difficult to correlate. Again, the image coverage is not easy to control for small objects.

4.4 Finite element modeling

Measurement techniques allow us to evaluate different variables and improve our understanding of the ME. However, the amount of information we can obtain and predictions we can make based on our findings remains limited due to various factors. TB studies are expensive. The amount of manipulations that can be done to a single TB is very limited and usually irreversible. For example, an evaluation of the effect of different malleus fractures on sound transmission requires a TB for each fracture type. Optical measurement techniques require visible access to the desired area of interest. Other technical difficulties can arise due to the available equipment.

To circumvent many of these burdens, analytical or numerical models can offer relief. For simple geometries, analytical models are still feasible. However, for complex geometries such as the ME one has to resolve to different techniques to solve the governing partial differential equations describing the mechanics. We will make use of finite element modeling (FEM). This numerical technique is often used in industry to overcome all the above issues and perform cost-efficiently research and development. Let us dive into the works of FEM and discover how it can be used in ME research.

4.4.1 How does finite element modeling work? Theory for static analysis

The complex geometry of the ME does not allow for an analytical approach to solving the partial differential equations describing the mechanics of the ME. However, if we divide our domain into many small subdomains, *finite elements*, the calculations become much more feasible to solve.

Principle of virtual work

This section is based on R. F. Coelho and Pyl (2014).

The equilibrium equations of an elastic solid subjected to body forces b_j and contact forces τ_{ij} are:

$$b_i + \tau_{ij,j} = 0 \tag{4.3}$$

This equality must be satisfied for any point of the elastic solid with domain V. Thus when multiplying by any displacement function $\hat{u}_i$ and integrating over the entire volume V the result remains zero:

$$\int_V (b_i + t_{ij,j})\hat{u}_i dV = 0 \quad \forall \hat{u}_i \tag{4.4}$$

We now see that the required conditions to solve the equations are reduced. Equation (4.3) had to hold for every point in volume V. Equation (4.4), however, only demands a global quantity to be zero when integrated over the volume V. The displacements $\hat{u}_i$ are

virtual displacements as they can take on any form. Partial integration of the second term in equation (4.4) returns:

$$\int_V b_i \hat{u}_i dV + \oint_S \tau_{ij} n_j \hat{u}_i dS - \int_V \tau_{ij} \hat{\epsilon}_{ij} dV = 0 \ \ \forall \hat{u}_i \tag{4.5}$$

$$\int_V b_i \hat{u}_i dV + \oint_S t_i^{(n)} \hat{u}_i dS - \int_V \tau_{ij} \hat{\epsilon}_{ij} dV = 0 \ \ \forall \hat{u}_i \tag{4.6}$$

The left-hand-side represents the total virtual work determined by real forces and virtual displacements. The total virtual work of a body in equilibrium is zero for any virtual displacement.

We can restrict the choice of virtual displacements to kinematically homogeneous displacements and kinematically admissible displacements. Kinematically admissible displacement fields satisfy the geometric boundary conditions. These are the prescribed displacements on portion S_u from surface S. Homogeneous displacements vanish on the surface portion S_u. The motivation for using a kinematically homogeneous field is to get rid of the surface integration over S_u which contains unknown reaction forces due to the boundary conditions. We then get:

$$\int_V b_i \hat{u}_i dV + \int_{S_t} t_i^{(n)} \hat{u}_i dS - \int_V \tau_{ij}(\boldsymbol{u}) \hat{\epsilon}_{ij} dV = 0 \ \ \forall \hat{u}_i \tag{4.7}$$

For a kinematically admissible displacement field $\boldsymbol{u}$ is the solution of the equilibrium problem if and only if the above statement holds for all kinematically homogeneous virtual displacement fields $\hat{u}_i$. Notice how (4.7) only requires first-order derivatives and integral quantities over the entire domain instead of second-order derivatives and pointwise calculations as in equation (4.7).

A variational formulation of equation (4.7) can be constructed by replacing the virtual fields by small variations $\delta u_i$of the real displacements.

$$\int_V b_i \, \delta u_i dV + \int_{S_t} t_i^{(n)} \delta u_i dS - \int_V \tau_{ij} \delta \epsilon_{ij} dV = 0 \ \ \forall \delta u_i | \, \delta u_i = 0 \, on \, S_u \tag{4.8}$$

The first two terms form the opposite of the potential energy of the external loads ($-\delta U$). The third term equals the strain energy W. We can rewrite equation (4.8) to be:

$$\delta \Pi = \delta(\mathrm{U} + \mathrm{W}) = 0 \tag{4.9}$$

with Π the total potential energy. So the solution has been rewritten such that it is the minimization of a functional, the potential energy.

Local approximation

As stated earlier, we will divide our total domain into subdomains, finite elements V^e. Each finite element will be defined by a number of nodes. In the end, we want to predict the value of a variable at any point in our domain. To achieve this we will use a nodal

approximation by subdomains. The nodes are the points of the finite elements where the approximation coincides with the exact values. The interpolation functions are called shape functions and will be denoted by $N_i(x)$ where i is the node index. A simple shape function can be constructed using linear interpolation. An illustration for a one-dimensional problem is given in figure 4.6.

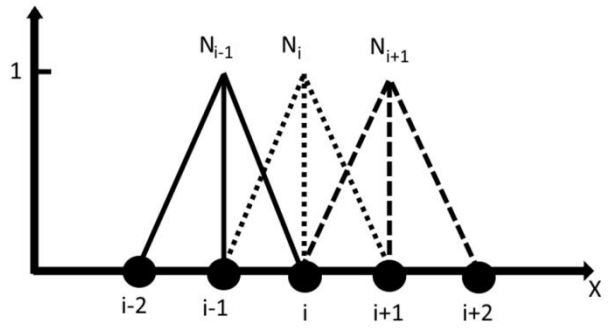

Figure 4.6: Illustration of shape functions in 1D.

Any approximation of the variable u position in the first finite element is given by:

$$u_{approx}^{V_1}(x) = N_1(x)u_1 + N_2(x)u_2 \tag{4.10}$$

We stated before that at the nodes the approximation $u_{approx}^{V_1}(x_j)$ should equal the value in the node u_j meaning that $N_i(x_j) = \delta_{ij}$ must hold. For linear shape functions we can construct:

$$N_1(x) = \frac{x - x_2}{x_1 - x_2} \;\&\; N_2(x) = \frac{x - x_1}{x_2 - x_1} \tag{4.11}$$

By using this finite element approximation, we have enforced local behavior as the function of an element can only influence the elements in its neighborhood. The shape function of an element only differs from zero within that element. Thus the approximation can be written in vector form as follows:

$$\begin{aligned} u_{approx}(x) &= \boldsymbol{N^e(x)q^e} \\ &= \boldsymbol{N(x)q} \end{aligned} \tag{4.12}$$

With $\boldsymbol{q^e}$ containing nodal values of u on the element and $\boldsymbol{q}$ the nodal values of u for the whole domain.

Galerkin method and static analysis

The Galerkin method utilizes the weak integral formulation (equation (4.7)) and the finite element approximation for the displacements to convert our continuous problem into a discrete problem. We will need to plug in the approximation of the displacements by use of the finite element shape functions (equation (4.12)) into the weak integral

formulation. To do this, we still need a way to define the strains and stresses in matrix form based on the shape functions. For the displacements we have (in 2D):

$$\boldsymbol{u^h}(\boldsymbol{x}) = \begin{bmatrix} u^h(x,y) \\ v^h(x,y) \end{bmatrix} \tag{4.13}$$

While for strains we have

$$\boldsymbol{\epsilon^h}(\boldsymbol{x}) = \begin{bmatrix} \epsilon_x^h(x,y) \\ \epsilon_y^h(x,y) \\ \gamma_{xy}^h(x,y) \end{bmatrix} = \begin{bmatrix} \frac{\partial}{\partial x} & 0 \\ 0 & \frac{\partial}{\partial y} \\ \frac{\partial}{\partial y} & \frac{\partial}{\partial x} \end{bmatrix} \begin{bmatrix} u^h(x,y) \\ v^h(x,y) \end{bmatrix} \tag{4.14}$$

However, we can apply the derivative matrix onto the shape functions, so equation (4.14) becomes:

$$\boldsymbol{\epsilon^h}(\boldsymbol{x}) = \boldsymbol{D}\boldsymbol{u^h}(\boldsymbol{x}) = \boldsymbol{DN}(\boldsymbol{x})q = \boldsymbol{Bq} \tag{4.15}$$

For homogeneous isotropic and linear elastic materials, Hooke's law holds true and the stresses $\boldsymbol{\tau^h}(\boldsymbol{x})$ can be obtained by multiplication of the strains by Hooke's matrix $\boldsymbol{H}$. For 2D problems this, Hooke's matrix is different depending on the type of problem. For problems of plane stress and plane strain, we get respectively

$$\begin{aligned} H_{plane\ stress} &= \frac{E}{1-\nu^2} \begin{bmatrix} 1 & \nu & 0 \\ \nu & 1 & 0 \\ 0 & 0 & \frac{1-2\nu}{2} \end{bmatrix} \\ H_{plane\ strain} &= \frac{E}{1+\nu}(1-2\nu) \begin{bmatrix} 1-\nu & \nu & 0 \\ \nu & 1-\nu & 0 \\ 0 & 0 & \frac{1-2\nu}{2} \end{bmatrix} \end{aligned} \tag{4.16}$$

In general, we can write $\boldsymbol{\tau^h}(\boldsymbol{x}) = \boldsymbol{H}\boldsymbol{\epsilon^h}(\boldsymbol{x}) = \boldsymbol{HB}(\boldsymbol{x})\boldsymbol{q}$. By using the same finite element shapes functions as trial functions for the virtual displacements $\widehat{\boldsymbol{u}}^{\boldsymbol{h}}(\boldsymbol{x}) = \boldsymbol{N}(\boldsymbol{x})\widehat{\boldsymbol{q}}$ the discretized version of the weak form becomes:

$$\int_V \boldsymbol{\epsilon}^{\boldsymbol{hT}} \widehat{\boldsymbol{\tau}}^{\boldsymbol{h}} dV - \int_V \widehat{\boldsymbol{q}}^T \boldsymbol{N}^T \boldsymbol{b} dV - \int_{S_t} \widehat{\boldsymbol{q}}^T \boldsymbol{N}^T \boldsymbol{t}^n dS = 0 \quad \forall \widehat{\boldsymbol{q}} = 0 \ on \ S_U \tag{4.17}$$

or

$$\underbrace{\int_V \widehat{\boldsymbol{q}}^T \boldsymbol{B}^{\boldsymbol{T}} \boldsymbol{HBq} dV}_{Stifness\ term} - \underbrace{\int_V \widehat{\boldsymbol{q}}^T \boldsymbol{N}^T \boldsymbol{b} dV - \int_{S_t} \widehat{\boldsymbol{q}}^T \boldsymbol{N}^T \boldsymbol{t}^n dS}_{Force\ terms} = 0 \quad \forall \widehat{\boldsymbol{q}} = 0 \ on \ S_U \tag{4.18}$$

and eventually

$$\boldsymbol{Kq} = \boldsymbol{f}^V + \boldsymbol{f}^S = \boldsymbol{f} \tag{4.19}$$

For which $\boldsymbol{K}$ is the Q by Q stiffness matrix and $\boldsymbol{q}$, and $\boldsymbol{f}$ are vectors with Q elements with Q corresponding to the number of degrees of freedom. The number of degrees of freedom is equal to the number of degree per freedom per node multiplied by the number of nodes. We now have a linear algebraic system which we can solve.

4.4.2 Dynamic analysis

We will not be performing any static analysis. Instead, we are more interested in the dynamic behavior of the ME. If we want to perform a dynamic analysis we have to include additional terms in (4.19). In dynamic analysis, time-dependent terms such as inertia and damping become important. Adding these terms to equation (4.19) gives

$$\boldsymbol{M}\frac{d^2\boldsymbol{q}(\boldsymbol{t})}{dt^2} + \boldsymbol{H}\frac{d\boldsymbol{q}(\boldsymbol{t})}{dt} + \boldsymbol{K}\boldsymbol{q}(\boldsymbol{t}) = \boldsymbol{f}(\boldsymbol{t}) \tag{4.20}$$

with $\boldsymbol{M}$ and $\boldsymbol{H}$ respectively the mass and damping matrix.

Frequency domain modeling

If we assume the system is linear, and we consider harmonic load cases, (4.20) does not have to be solved for every single time step. Instead, we can calculate the stationary harmonic solution by assuming the solution is of the form $\boldsymbol{q} = |\boldsymbol{q}|e^{i(\omega t+\boldsymbol{\phi})}$. We obtain the solvable set of equations:

$$(-\omega^2\boldsymbol{M} + i\omega\boldsymbol{H} + \boldsymbol{K})\boldsymbol{q} = |\boldsymbol{f}| \tag{4.21}$$

Time-domain modeling

In the case of non-harmonic load cases or nonlinear systems, the above assumptions cannot be used. Instead, the time-dependent equations can be discretized using a finite-difference scheme, and the set of equations can be solved for each time step. Time-domain models can exhibit transient behavior when suddenly subject to a load. This transient behavior would distort the simulated frequency response of the model. The transient effects can be diminished by applying so-called *load ramping*. Such load ramping is achieved by slowly increasing the load over time instead of beginning the stimulation with a high amplitude stimulation. Figure 4.7 shows the effect of load ramping on the Fourier spectrum of the displacement of an object when using single sine stimulation.

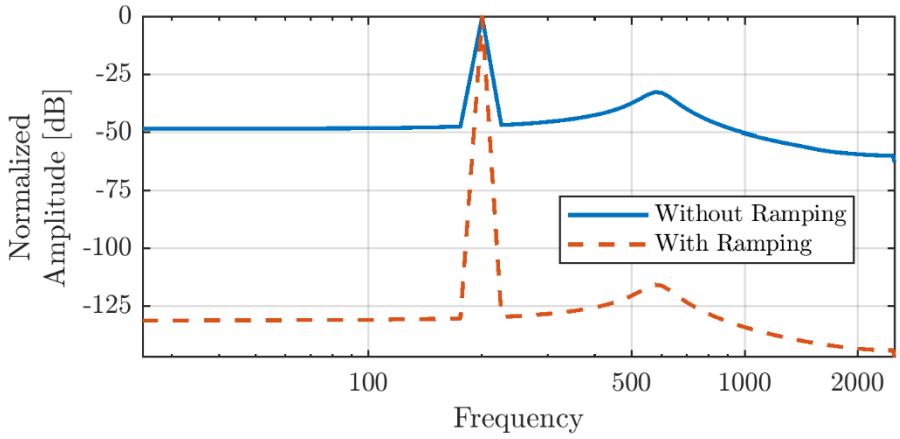

Figure 4.7: Effect of load ramping on the Fourier spectrum for single sine stimulation of 200 Hz. Transient effects (e.g. resonance at 600 Hz) contaminate the spectrum much more when no load ramping is used.

Without load ramping, the calculated Fourier spectrum figure 4.7B is contaminated with the full frequency response of the system due to the transients. Load ramping reduces this contamination. If the system exhibits high damping properties, the transients will disappear after a certain time even without load ramping. Another solution is to use extremely small time steps. However, this approach is very time-consuming.

For accurate simulations, the time step Δt is chosen to be $\Delta t = \frac{1}{25 \cdot f_{MAX}}$ or smaller with f_{MAX} the highest stimulation frequency of the harmonic stimulation. To obtain a detailed frequency spectrum, a total simulated time (transient time excluded) of at least $t = \frac{8}{f_{MIN}}$ is used with f_{MIN} the lowest stimulation frequency of the stimulation signal. For a single sine stimulation $f_{MIN} = f_{MAX} = f$ and the simulation time is not so dependent on the stimulation frequency. For multisine stimulation, however, the simulation time can become very large depending on the range of frequencies that is used. For this reason, we will only use single sine stimulation.

Damping

In this work, we will use two different types of FE damping implementations: *loss factor damping and Rayleigh damping*.

Loss factor damping is only applicable in a frequency domain analysis. It uses a complex Young's modulus.

$$K^c = (1 + in_s)K \tag{4.22}$$

The imaginary term is the damping term, similar to that in (4.21). The factor n_s is called the loss factor. The equality $n_s = \frac{\Im(K^c)}{\Re(K^c)}$ holds. We can construct a complex Young's modulus, which replicates a standardized Maxwell model using equation (3.15):

$$R_0 + \sum_{j=1}^{m} \frac{R_j i\omega}{i\omega + \frac{R_j}{\eta_j}} \tag{4.23}$$

For time-domain models, we will use Rayleigh damping. The damping matrix H in (4.21) is will then be proportional to the mass and stiffness matrix as:

$$H = \alpha M + \beta K \tag{4.24}$$

Where α and β are the Rayleigh damping coefficients. Rayleigh damping is not directly linked to any material property. It is mainly a numerically attractive way to implement damping and works both in the frequency- and time-domain.

4.4.3 Geometric nonlinearities

We discussed in section **Fout! Verwijzingsbron niet gevonden.** that we want to learn more about the dynamic nonlinear behavior of the ME at high sound pressure levels. Two types of nonlinear behavior exist: material and geometric nonlinearity. As the name implies, material nonlinearity is related to the material's properties. Such materials have nonlinear stress-strain curves. This means the nonlinear behavior only arises when the object exhibits large strains. We assume this will not be the case for the ME. Even at considerable static pressures (>1 kPa), Ladak predicted strains of maximally 4% using nonlinear FE models of a cat's ear. A sound pressure level of 140 dB SPL only equals 200 Pa, resulting in even smaller strains.

For this reason, only geometric nonlinearity is considered in this work. This type of nonlinearity rather occurs for large displacements or rotations instead of large strains. Considering geometric nonlinearities means we take into account the deformation. Boundary normals are updated, and area changes due to stretching affect how pressure loads work on the object. The Green-Lagrange strain will be used instead of engineering strains, eliminating strain artifacts due to rigid body motions or large rotations.

4.4.4 Finite element model of the human middle ear

Our lab has built human ME FE models in the past. We will use and/or adapt these models in several parts of this work. For this reason, we will describe the base models here.

Geometry

An accurate representation of the geometry is needed to create an FE model of the ME. Our lab achieved this by using micro-computed tomography (μCT). Two TBs (1: male 73y, right – 2: male 73y, left) were imaged using μCT after they were stained with phosphotungstic acid (PTA). The isotropic voxel size of the datasets was 22.8 μm. The reconstructed images were segmented into different materials and converted into surface models in Amira® 6.1 (FEI Visualization Sciences Group, Hillsboro, Oregon, USA). The surface models were then imported into Comsol Multiphysics® 5.2 (Comsol, Burlington,

MA, USA), where they were converted into volume meshes of approx. 120,000 tetrahedral elements. A surface mesh is illustrated in figure 4.8.

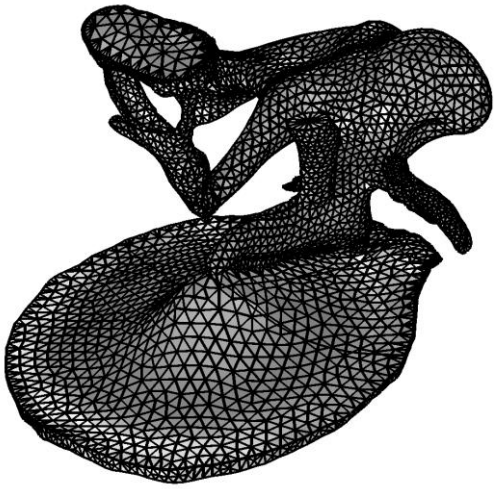

Figure 4.8: The finite element geometry as exported from Amira.

Boundary conditions

Without boundary conditions, an FE modeling problem cannot have a unique solution. The boundary conditions in the ME are called fixed boundaries. They exist where the ME ligaments touch the ME cavity. We assume that at these locations the displacements are zero ($\boldsymbol{u} = 0$). A contiguous selection of triangles at the periphery of the TM, as well as the end surfaces of the anterior mallear ligament (AML), lateral mallear ligament (LML), posterior incudal ligament (PIL), stapedial annular ligament (SAL), tensor tympani (TT) tendon and stapedius muscle (SM) tendon were all fixed.

The influence of the cochlea was modeled as an acoustic complex impedance, acting on the medial surface of the SFP and the SAL. The frequency-dependent values of this impedance were taken from Puria et al. (1997).

Material properties

All materials except for the interior of the incudo-stapedial joint (ISJ) were modeled as solid materials. The Young's moduli of all structures are listed in table 4.1. In some works, we have used a non-isotropic TM elasticity as described in De Greef et al. (2017) while in others, we assigned an isotropic TM elasticity. The choice will be highlighted in each work specifically.

If a non-isotropic TM elasticity was used, then the TM was subdivided in an attempt to represent the arrangement of collagen fibers, similar to Tuck-Lee et al. (2008),. The Young's moduli of all sub-regions were orthotropic, but their coordinate systems were

different. The inferior region was modeled as an orthotropic material within a polar coordinate system with its origin in the umbo. Similar to Tuck-Lee et al. (2008), the radial Young's modulus decreased away from the umbo:

$$E_{rad}(r) = \min\left(40\ \text{MPa} * \frac{2 \cdot 10^{-3}\ \text{m}}{r}, 100\ \text{MPa}\right). \tag{4.25}$$

The superior region was subdivided into three regions, all orthotropic in a Cartesian system. In the region overlying the manubrium of the malleus, the y-axis was defined as lying along the manubrium and the x-axis perpendicular to it. In the anterior and posterior regions, the x and y-axes were rotated 30° and -30° respectively. The Poisson ratios and shear moduli were calculated as $\nu_{ij} = \nu\sqrt{\frac{E_i}{Ej}}$ and $\mu_{ij} = \frac{\sqrt{E_i E_j}}{2(1+\nu)}$ as suggested by Li and Li et al. (2014). The value for ν was set to 0.3 and the indices i and j denote the different components of the Poisson ratio and Young's modulus (r, c, t or x, y, z).

If an isotropic TM elasticity was assigned, the Young's modulus was 10 MPa, and the Poisson ratio was set to be $\nu = 0.3$.

For all soft tissue structures, the mass density was 1200 kg/m³ (Homma et al. 2009). The densities of the ossicles were 2390 kg/m³ (malleus), 2150 kg/m³ (incus), and 2200 kg/m³ (stapes) (Homma et al., 2009). The interior of the ISJ was modeled as a fluid, with a bulk modulus of 2.2 GPa (De Greef et al., 2017). The damping of soft tissues is modeled as Rayleigh damping ($\alpha = 0, \beta = 0.0001$) except for the TM and TMC damping which was modeled as an isotropic loss factor ($\eta = 0.25$). More details can be found in (De Greef et al., 2017).

Structure	**Young's modulus (MPa)**	**Source**
Tympanic membrane – pars tensa inferior	$E_r = E_{\text{rad}}(r)$ (eq. 1) (radial)	(De Greef et al., 2017)
	$E_c = 20$ (circumferential)	(De Greef et al., 2017)
	$E_t = 5$ (transverse)	(De Greef et al. 2017)
Tympanic membrane – pars tensa superior	$E_x = 40, E_y = 20, E_z = 5$	(De Greef et al. 2017)
Tympanic membrane – pars flaccida	6.7	E_c/3, similar to many sources, see Volandri et al. (2011)
Tympano-mallear connection	2	E_c/10, (De Greef et al., 2016)
Malleus, incus and stapes	$14.1 \cdot 10^3$	(Cai et al., 2010; Homma et al., 2009)
Incudomallear joint	7	(Homma et al., 2010)
Incudostapedial joint capsule	6	(Koike et al., 2002)
Anterior mallear ligament	21	(Homma et al. 2009)
Lateral mallear ligament	5	(Gan et al., 2004) (6.7 MPa)
Posterior incudal ligament	4.8	(Homma et al. 2009)
Stapedial annular ligament	0.15	(De Greef et al. 2017)
Tensor tympani tendon	5	(Homma et al. 2010)
Stapedius muscle tendon	0.38	(Homma et al. 2010)

Table 4.1: Material properties of the intact middle ear model.

Convergence analysis

We now have all ingredients for our FE simulations: a geometry, defined material properties, and boundary conditions. We can now perform a convergence analysis. A convergence analysis consists of evaluating a variable for a reducing element size until further reduction does not seem to alter the value of that variable. We then obtain a mesh which can be considered suitable to use for our research. Figure 4.9 shows the stapes footplate velocity magnitude evaluated in a single point for an increasing amount

of degrees of freedom (DoF). We see that the magnitude changes less as the DoF keep increasing. The change between the coarsest and finest mesh is about 14% (1.15 dB difference). The change between the latest two meshes is only about 1%. We consider further mesh refinement unnecessary as we have reached mesh convergence for 417127 DoF. Now we have a proper mesh; we can validate our model by comparing FE results to experimental data.

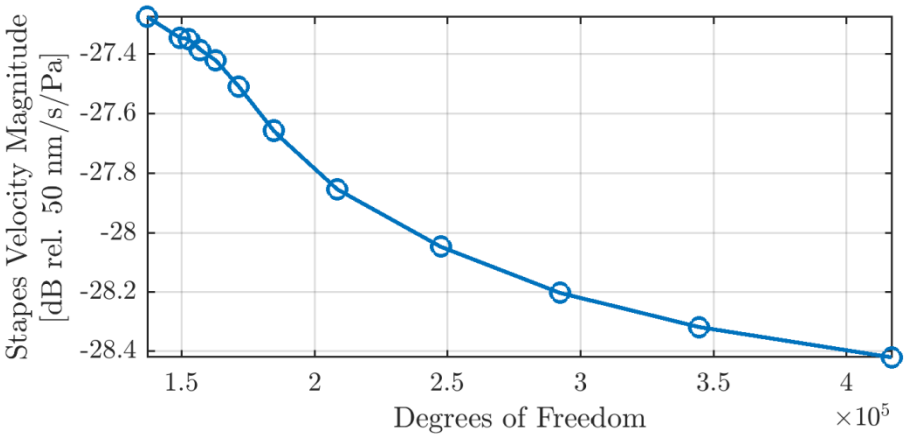

Figure 4.9: Stapes footplate velocity magnitude as a function of degrees of freedom. The velocity was evaluated in a single point in the center of the footplate. We see that the change in magnitude decreases with increasing degrees of freedom, which is equivalent to mesh refinement.

Validation

To validate our model, we performed a frequency-domain analysis. A uniform load of 1 Pa was applied at the lateral side of the TM. The stapes velocity magnitude was evaluated for 75 frequencies within a range of 0.1-10 kHz with and without a cochlear load. The result is shown in figure 4.10 along with experimental data from literature. At frequencies below 1 kHz, all four curves match very well. At higher frequencies, some fundamental differences are observed. The FE model shows two more resonances at about 1.8 and 2.5 kHz respectively. The experimental average of TBs without cochlea obtained in our lab (Gladine and Dirckx, 2018b) contains small resonances at 1.5, 5 and 6 kHz and a very large resonance at about 3.8 kHz which is clearly absent in the FE model. However, the TBs used to obtain the data in Gladine and Dirckx (2018b) still contained a partially intact ear canal. We saw that the ear canal has a resonance frequency of about 3-4 kHz. The sound was measured at the entrance of the ear canal instead of close to the TM. For this reason, we observe the 4 kHz resonance in the experimental data and not in the model. Apart from this ear canal resonance, the results are very similar. In contrast, the average stapes velocity of Rosowski et al. (2007) does not show significant resonances above 1 kHz. This might indicate the FE model lacks damping. However, the average calculated by

Rosowski, is an average of 13 averages of other works. This affects the shape of the curve as we will discuss in chapter 9.

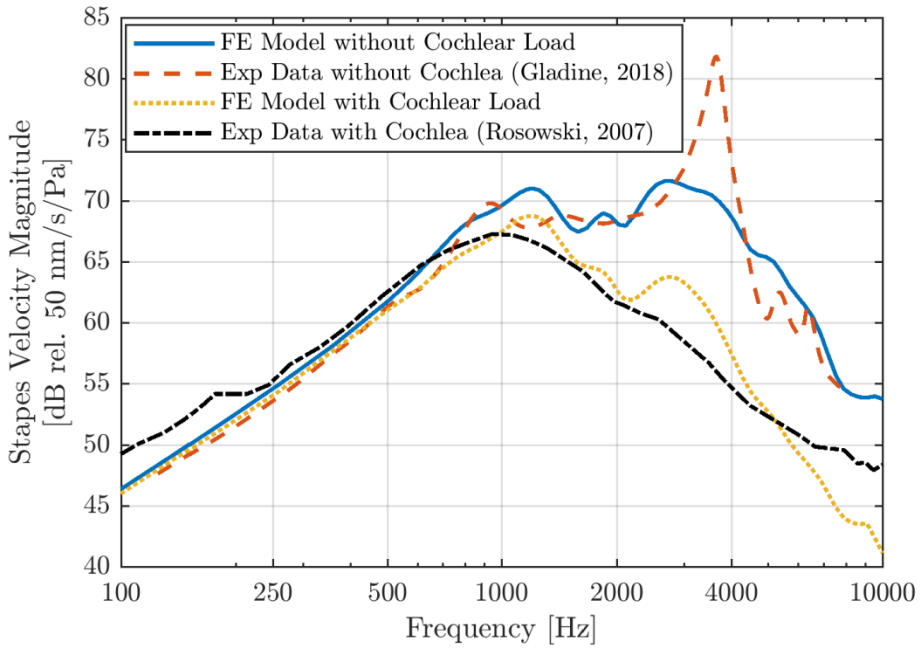

Figure 4.10: Stapes footplate velocity magnitude as a function of frequency for our FE model with and without cochlea and experimental data with and without cochlea.

In figure 4.11, we show a comparison of between the phase data of the model without cochlear load and experimental data. The model data agrees well except for frequencies above 4 kHz since the experimental data shows an additional phase jump due to the ear canal resonance. Overall, we can state that the FE model matches the experimental data quite well. We demonstrated the importance of comparing FE models with experimental results obtained in the exact same conditions (e.g. exclusion of ear canal). We also pointed out that one has to be careful using averages of ME frequency responses when comparing to a single FE simulation result.

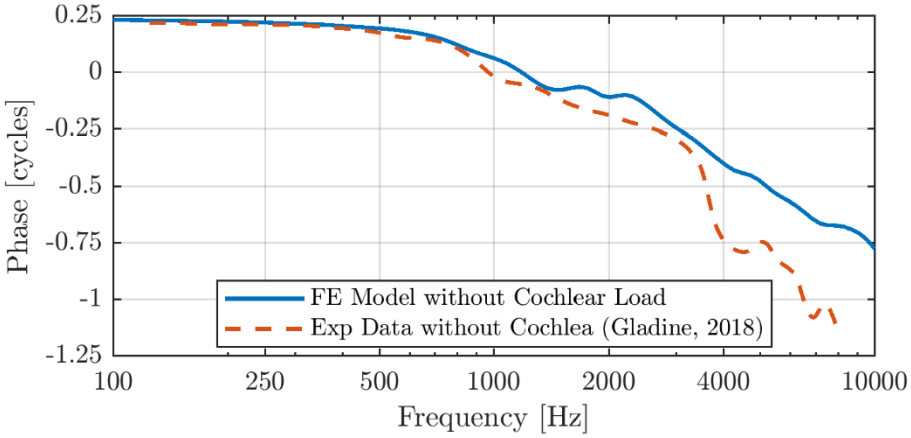

Figure 4.11: Phase of the stapes footplate velocity as a function of frequency of our finite element model compared to that of experimental data. The model agrees well with the experimental data up until 4 kHz. However, the experimental data was obtained in temporal bones with partially intact ear canal which is different of the model, resulting in a phase jump at around 4 kHz due to the ear canal resonance.

We now have a validated ME FE model. Although we only demonstrated the simulated frequency response of the stapes footplate, we have access to many more variables (umbo velocity, membrane strains, stresses). We now also have the ability to alter the models to investigate the effect of pathologies, geometry changes. For this reason, FE is a very powerful tool.

Chapter 5:
(NON)LINEARITY OF THE HUMAN MIDDLE EAR

Abstract

In this chapter, we will look into how the ME reacts to high-intensity sounds. Will the ME maintain the temporal structure of the incoming sound, or will the sound become distorted? Experimental data found in literature suggests that the ME remains linear up until 130 dB SPL. However, at static pressures, the ME behaves highly nonlinear, and thus we can expect some small nonlinearities to be found when acoustically stimulating the TM. We will see that the nonlinear behavior at static pressures displays some characteristics which can possibly be attributed to the curvature of the TM. Therefore, we try to determine if the human ME is nonlinear and, if it is, we try to find out if the shape of the TM is responsible for the nonlinear behavior in the dynamic regime. As we will see, nonlinear behavior is likely due to the TM shape when the following characteristics are observed: First, the TM is easier to move laterally (towards ear canal) than medially (towards ME cavity). Second, the produced distortions consist mainly of even degree nonlinearities. And lastly, the ME displays softening behavior. To predict and demonstrate these qualities based on membrane shape, we will discuss measurement data from literature and perform measurements and modeling on flat and curved membranes. To verify such behavior in the human ME, we will use different optical measurement techniques and acoustical stimulation methods. Lastly, we will evaluate our on human ME FE model and compare it to our measurement data.

This chapter is based on:

Gladine, K., Muyshondt, P.G.G., Dirckx, J.J.J. 2017. Human middle ear nonlinearity measurements using laser Doppler vibrometry. Opt Laser Eng 99, 98-102.

Gladiné, K., Muyshondt, P., Dirckx, J. 2016. LDV measurement of small nonlinearities in flat and curved membranes. A model for eardrum nonlinear acoustic behaviour. AIP Conference Proceedings Vol. 1740, 050005.

and additionally contains work which has not yet been published.

5.1 Introduction

In section 1.2.2, we described the function of the ME as a mechanical impedance transformer that converts relatively large motions with little force into smaller motions with higher force to make up for the acoustic impedance difference of about a factor 1000 between air and water. Previous measurements have led to the assumption that the mammalian ME is functionally linear. This statement is supported by the work of Guinan and Peake (1967), Nedzelnitsky (1980), Dalhoff et al. (2007) and Voss et al. (2000), who measured ME input-output functions at varying stimulus levels. That linearity is generally a good approximation has been pointed out by others (Rosowski et al., 1984). In conclusion, the ME was regarded as a mainly linear system at least up till sound pressure levels of 120 dB.

However, stapes velocity measurements at different sound pressure levels by Voss et al. (2000) show something peculiar (figure 5.1). Up till 125 dB, one of the resonances consistently occurs at about 1430 Hz regardless of the sound pressure level. This is exactly what is to be expected from a linear system. However, at 135 dB SPL, this resonance frequency has shifted to about 1280 Hz. This negative frequency shift implies a decrease in system stiffness. Since this effect seems to occur due to an increase in stimulation level, it can be considered as nonlinear behavior. It resembles what was discussed in section 3.3.2; *softening behavior*.

The stapes velocity phase displays coherent behavior; a shift in the phase jump associated with the resonance to lower frequencies as seen in figure 5.2. Intuitively, softening implies the system deforms more easily, resulting in higher normalized displacement or velocity magnitudes. However, measurements by Voss show that the maximal magnitude decreases at higher sound pressure levels (figure 5.2). At frequencies lower than the resonance frequency, the magnitude has increased slightly.

So as of about 135 dB SPL, the nonlinear behavior of the human ME appears to be strong enough to be detected by observing the stapes velocity response. Can we evaluate these nonlinearities differently at lower sound pressure levels? And which ME components cause these nonlinear effects? To gain more understanding, we will first have a look at a more obvious case of ME nonlinearity; displacements of ME components subjected to high (quasi-)static pressures.

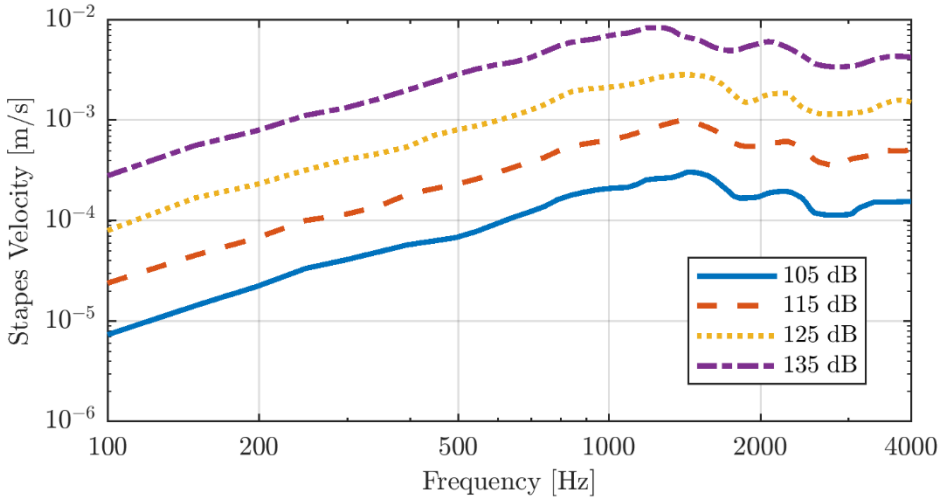

Figure 5.1: Stapes velocity response at different sound pressure levels (Voss et al., 2000). At 135 dB SPL the first resonance frequency shifts slightly to lower frequencies displaying the nonlinear behavior of the ME at high sound pressure levels.

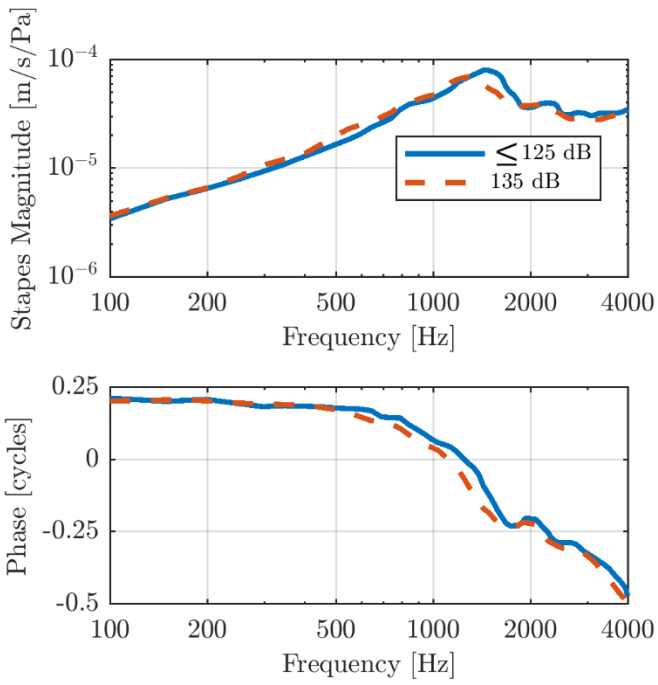

Figure 5.2: Normalized stapes velocity magnitude and phase for different sound pressure levels (Voss et al., 2000). The shift in resonance frequency at higher sound pressure levels can be observed from both the magnitude and phase data. The maximal achieved normalized magnitude is seen to be smaller for higher sound pressure levels. ≤

5.2 Quasi-static ME nonlinearity

ME nonlinearity in the (quasi-)static regime has been a much more investigated topic (Aernouts et al., 2012; Claes et al., 2018; Dirckx and Decraemer, 1992; Dirckx and Decraemer, 2001; Dirckx et al., 2006; Ladak et al., 2004; Muyshondt et al., 2018). The observed nonlinearity is quite strong and occurs in physical relevant situations. Daily occurrences such as taking an elevator cause significant pressure differences between the ME cavity and the ambient atmosphere (i.e. 1 kPa for 100 meters). As a result of these pressure differences, the TM undergoes large (nonlinear) deformations.

Figure 5.3 shows an umbo displacement as a function of pressure measured in a human temporal bone using phase-shift moiré topography (Dirckx and Decraemer, 1991). A positive pressure represents an overpressure in the ear canal. A positive displacement represents a medial displacement of the umbo. A few things stand out. The aforementioned nonlinear behavior is clearly present. As the pressure levels increase, the displacements show asymptotic behavior. Additionally, the pressure-displacement relation is very asymmetric. The TM seems to be much more resistant to displace medially at overpressures than move laterally at underpressures.

Nature provides us a hint of the origin of this asymmetry in umbo displacement. The displacement of the tip of the extrastapedius, the bird's equivalent of the umbo, shows an inverse asymmetry compared to mammals when the ear is subjected to large static pressures as shown by Claes et al. (2018) (figure 5.4). The bird's TM is also orientated differently than mammals. In mammals, the conical shape of the TM points medially (inwards). For birds, the opposite is true; the TM points laterally (outwards). This suggests that the origin of asymmetry (and nonlinearity) stems from the shape of the TM. What about other ME structures?

Dirckx and Decraemer (2001) showed the effect of ME components on quasi-static TM deformation in gerbils. They dissected MEs in different stages, removing ME components and measuring the shape deformation and umbo displacements. They found that in gerbils, removing the cochlea, the tensor tympani, and stapes, does not affect static deformation. Further dissection stages increased deformation magnitudes, but these deformations still maintained their nonlinear characteristics, suggesting that the TM is a source of nonlinearity. However, this does not state whether these nonlinearities are of geometric origin or due to material nonlinearities.

Ladak et al. (2006) created a geometric nonlinear model of finite-element model of the cat TM. Such model incorporates the effects of the deforming geometry on the stiffness matrix, but it does not account for nonlinear material properties. The malleus was fixed, thus any nonlinearities would stem directly from the TM. They achieved displacement curves similar to measurements. Their model predicted TM strains of maximally 4%, which led to the conclusion that the incorporation of nonlinear material models was unnecessary.

All of these findings suggest that the quasi-static nonlinearity in mammal MEs is geometrical and that the TM and its shape have a significant role in it. What if the nonlinearity in the dynamic case has similar origins? Is it possible to get an idea of the nonlinear distortions that would arise based on what we know from quasi-static nonlinearities?

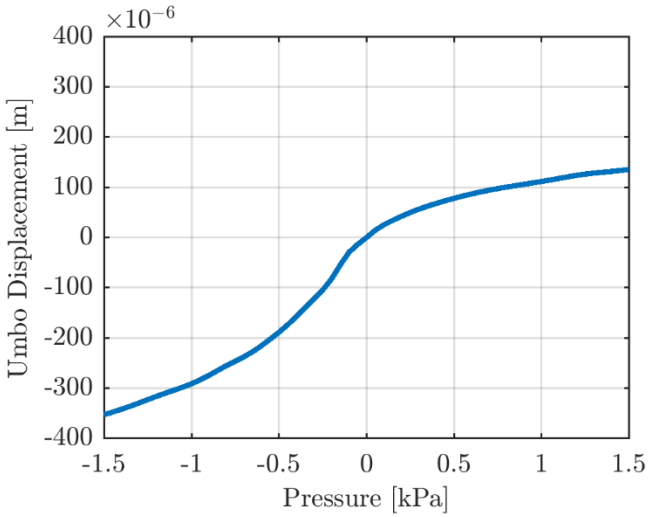

Figure 5.3: Umbo displacement of a human ME subjected to high static pressures. The pressure-displacement curve shows the nonlinear behavior of the ME when subjected to static pressures.

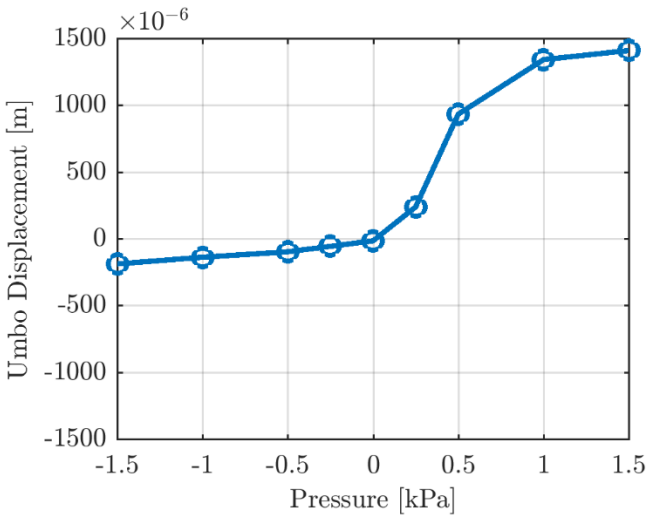

Figure 5.4: The asymmetry of the pressure-displacement relationship in a bird ear is opposite to that of human. The cone shape of the bird TM is oppositely orientated to that of human. This suggests the nonlinearity originates from the shape of the TM (Claes et al., 2018).

5.2.1 Nonlinear distortions based on quasi-static nonlinearities

In section 3.3.2, we saw that harmonic stimulation as an input to a nonlinear system results in additional harmonic content in the output of that system. More specifically, if the nonlinear system is stimulated by a sine wave of a single frequency, it will react at the same frequency, but also at harmonics, integer multiples of that single frequency. These harmonics are usually categorized into two types; even and odd harmonics. Even harmonics are just the even multiples of the ground frequency (first harmonic). Similarly, odd harmonics are odd multiples of that first harmonic. Why this distinction?

In case of nonlinearity, the second harmonic, which is even, originates from a quadratic nonlinearity. Suppose the input is a single sine wave, $\sin(2\pi f)$, the quadratic nonlinear component returns $\sin^2(2\pi f) = \frac{1-\cos(2\cdot 2\pi f)}{2}$. This term contains a DC-component, which makes the function asymmetrical. Any nonlinear pressure-displacement function which is asymmetrical, results in even harmonics when a harmonic stimulation is applied. A perfectly symmetrical nonlinear pressure-displacement function would produce only odd harmonics.

If the nonlinear behavior of the TM at high sound pressure levels is similar to that when subjected to large quasi-static pressures, we should expect both even and odd harmonics when applying a single frequency harmonic sound. Figure 5.5A and 5B show respectively a hypothetical symmetrical and asymmetrical nonlinear pressure-displacement relationship roughly based on the human quasi-static displacement shown in figure 5.3. Figure 5.5C and 5D show the corresponding harmonic content when a single sine pressure wave would be presented to both systems which obey these pressure-displacement relationships. The symmetrical pressure-displacement function returns only odd harmonics. The magnitudes of these harmonics are all less than the first harmonic, which represents the linear component. The asymmetrical relationship returns both the even and odd harmonics and a DC-component. This means that on average, the TM displaces in a single direction compared to its rest state. The direction of this net displacement is determined by the movement which requires less effort. In the case of the human TM this is the lateral displacement.

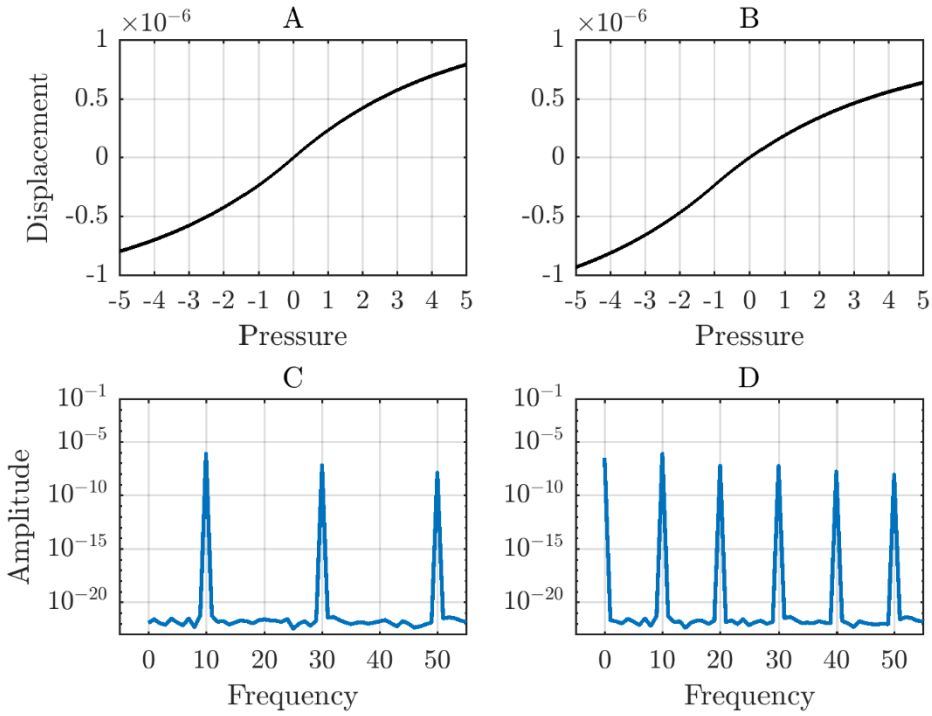

Figure 5.5: A nonlinear symmetrical (A) and asymmetrical (B) pressure-displacement relationship causes an object to have only odd degree nonlinearities (C) or odd and even degree nonlinearities and DC-component (D) respectively.

In conclusion, assuming that the origin of dynamic ME nonlinearity is the same as quasi-static nonlinearity, being geometric nonlinearity highly governed by the conical shape of the TM, we can expect even and odd nonlinearities and a net lateral displacement of the TM when subjected to high sound pressure levels.

5.3 Gerbil and rabbit nonlinearity measurements

Previous research performed at our lab reported ME nonlinearities in gerbil (Aerts and Dirckx, 2010) and rabbit (Peacock et al., 2015). These authors used random phase multisine stimulation to measure nonlinear distortions simultaneously at different frequencies. This technique will be explained in detail in section 5.4 where we will use the same technique to measure nonlinear distortion in human MEs.

5.3.1 Gerbil

Aerts and Dirckx (2010) reported nonlinearities exceeding the noise floor in gerbil as from 96 dB SPL (figure 5.6). At 120 dB SPL, the nonlinear distortion levels were 40 dB below the linear velocity levels. A faster increase in distortion levels were observed than for the linear velocity levels. Nonlinear distortions increased about two decibels for each decibel in sound pressure level. In contrast, the linear velocity increased only one decibel, as expected of a linear system. However, technically one would expect the linear component to rise more slowly as a fraction of the energy is distributed across the nonlinear distortions. A deviation on this linear increase was not observed according to Aerts and Dirckx (2010). They claimed this is due to the fact that the nonlinear distortions are so small. In addition, they state that other authors could not observe ME nonlinearity to 130 dB since they do not observe changes in the linear component. We would like to stress that the assumption of ME linearity is still valid for many applications since the distortion levels are so low but it is clear that the ME is not a perfectly linear system.

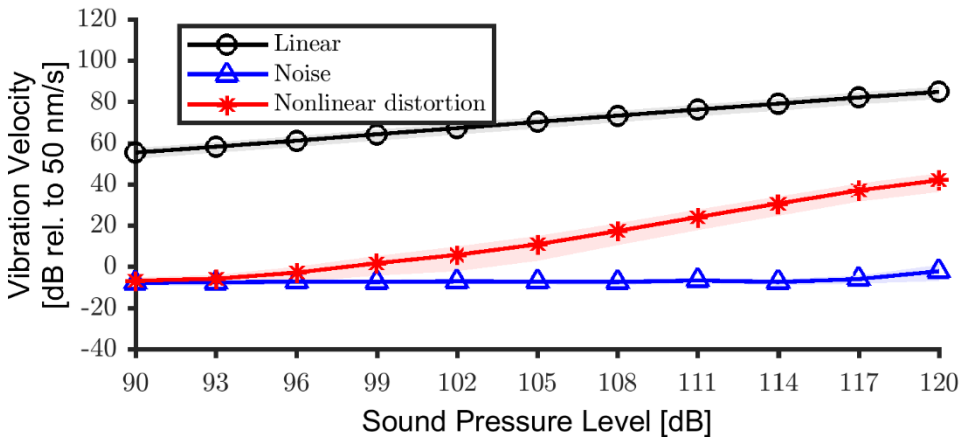

Figure 5.6: Linear and nonlinear vibration level in gerbil as a function of sound pressure level. From 96 dB, the nonlinear distortion levels surpass the noise.

5.3.2 Rabbit

Peacock et al. (2015) found very similar results when using the same technique on rabbit MEs. In midrange frequencies (1-2 kHz), umbo nonlinearities were detected as of 96 dB SPL. The nonlinearities increased at a faster rate than the linear component when the sound pressure level was increased.

Peacock et al. (2015) reported that frequency dependence of the nonlinear distortions was different to that of the linear component. The average linear vibration response had a resonance at about 2 kHz. At higher frequencies, there was a decay in magnitude. At 7 kHz there was another resonance visible followed by additional decay of velocity magnitude. In contrast, the average nonlinear vibration response was fairly flat up to 2 kHz. At higher frequencies there is a decline in magnitude which was stronger than that of the linear velocity response. Since the nonlinear vibration response did not exhibit resonances, the authors concluded that a higher linear vibration response does not imply a high nonlinear vibration amplitude.

In the same work, Peacock et al. (2015) measured stapes velocities as well. They found the ratio of the umbo response to stapes response was constant for the linear levels at all frequencies. For frequencies between 1 and 2 kHz, the ratio of the umbo to stapes nonlinear distortion levels was also constant and equals 10 dB. However, the authors do not mention that for lower and higher frequencies the ratio mainly increased for higher sound pressure levels, meaning the nonlinear distortions at the umbo grew faster compared to the stapes. This seems to suggest the nonlinearities occur at the level of the TM and are not properly transmitted through the ME to the stapes for frequencies below 1 kHz and above 2 kHz.

5.4 Human ME nonlinearity measurements (part 1)

In this section, we will describe how we used the same technique as Aerts and Dirckx (2010) and Peacock et al. (2015), to measure nonlinearity in human temporal bones. The measurement technique and adjustments made to the data analysis process will be described in detail further on.

This section is based on:

Gladine, K., Muyshondt, P.G.G., Dirckx, J.J.J. 2017. Human middle ear nonlinearity measurements using laser Doppler vibrometry. Opt Laser Eng 99, 98-102.

5.4.1 Materials and methods

Temporal bones

Seven cadaver temporal bones were used. The bones were removed from the skull within 24 hours after death, and were immediately frozen. Prior to the measurements, the bones were left to thaw for 24 hours at 4°C, and one hour before measurement they were left to accommodate to room temperature. It has been shown that the freezing process does not

have a significant influence on the vibration response of the ME system (Rosowski et al., 1990).

Laser Doppler Vibrometry setup

The laser Doppler vibrometry setup has been described in section 4.1.2. A polytec OFV-5000 was used.

The ear canal was reduced in length to obtain good visible access to the TM. A small cavity (about 1 ml volume) was placed over the ear canal and was acoustically sealed to the temporal bone using silicone paste. The cavity had an anti-reflection coated window at one side to allow access by the laser beam. Two earphone speakers (Sennheiser type MX170) were glued in holes at both sides of the cavity. Sound pressures were measured using a probe microphone (Bruel&Kjaer 4182) of which the needle was inserted in the sound generating cavity through a tightly fitting hole

Nonlinearity detection using multisines

In order to measure small nonlinearities, multisine stimulation was used. This type of stimulation permits an excitation of the specimen with a broad frequency range in a short time frame. In addition, the number of frequencies at which the nonlinear distortions can occur is much higher compared to using single sine stimulation. The multisine stimulation signal $s(t)$ can be described as

$$s(t) = \frac{1}{\sqrt{N}} \sum_{i=1}^{N} A_{k_i} \sin\left(2\pi k_i f_{res} t + \phi_{k_i}\right) with\, k_i \in S_f$$

which consists of a sum of *N* harmonically related sine functions because the frequencies of these sine functions are all an integer multiple k_i of the fundamental frequency f_{res}. The choice of these integers k_i belonging to the set S_f is described below. The fundamental frequency f_{res} determines the period of the signal $s(t)$ and subsequently the minimal duration of the measurement to avoid spectral splatter. Since multisine stimulation can be used to excite the specimen in a broad range of frequencies, it is convenient to use a quasi-logarithmically spaced frequency grid as opposed to a linear one. The amplitudes A_{k_i} are often chosen equal. To realize this, a correction is needed for the frequency-dependence of the speaker. The phases ϕ_{k_i} are chosen randomly as described in Pintelon (2001).

Unwanted nonlinear distortions produced by the speaker in the experimental setup were eliminated using a first order correction (Aerts et al., 2007). The correction method assumes that the nonlinear system which is investigated is weakly nonlinear. The TM will respond linearly to the undesired nonlinear distortions of the speaker. As we can measure the sound pressure level of the distortions and measure the linear vibration response of the TM. We can estimate the vibration levels of the TM induced by the speaker nonlinearities. We can then subtract these levels from the measured TM vibration levels. After this subtraction, only nonlinear vibration levels produced by the TM itself remain.

If the input presented to a linear system is a multisine signal, the output will be a multisine signal with the same frequency content as the input, but with different amplitudes and phases depending on the frequency response function of the system. In contrary, a nonlinear system will also vibrate at unexcited frequencies (figure 5.7).

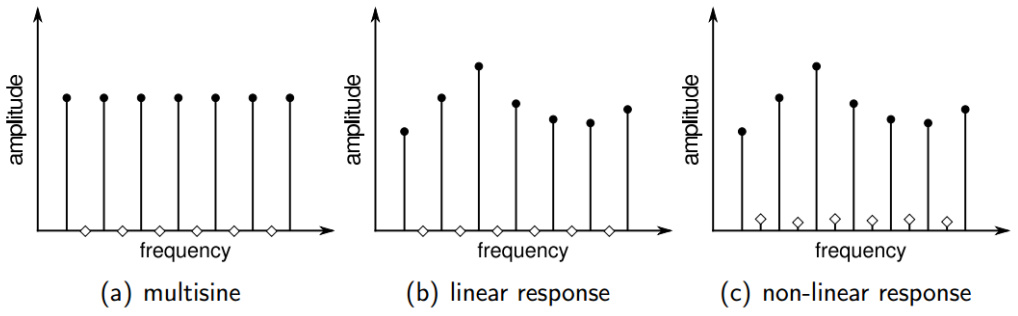

Figure 5.7: Frequency domain representation of a multisine (a), the response of a linear system (b) and a nonlinear system (c) with black circles representing the excited frequency components and diamonds the non-excited harmonics. Figure taken from Aerts and Dirckx (2010)

When using single sine stimulation, the nonlinear distortion frequencies are integer multiples of the stimulation frequency. This is also true for multisine stimulation, but additional nonlinear distortions arise at frequencies which are combinations of stimulation frequencies. We calculated the set of frequencies $(f_{quadratic}, f_{cubic})$ at which the stimulation frequencies can produce quadratic distortions

$$\left[(\alpha k_I + \beta k_{II}) \cdot f_{res} \in f_{quadratic}\ with\ \alpha, \beta \in \{-1,0,1,2\}\ \&\ |\alpha + \beta| = 2\ \&\ k_I, k_{II} \in S_f\ \right]$$

or cubic distortions

$$[(\alpha k_I + \beta k_{II} + \gamma k_{III}) \cdot f_{res} \in f_{cubic}\ with\ \alpha, \beta, \gamma \in \{-2, -1,0,1,2,3\}\ \&\ |\alpha + \beta + \gamma| = 3\ \&\ k_I, k_{II}, k_{III} \in S_f]$$

within the range of stimulation frequencies. Only the frequencies of the set $(f_{quadratic}, f_{cubic})$ within 5 Hz (i.e. f_{res}) or 10 Hz (i.e. $2f_{res}$) from a stimulation frequency were considered. For these frequencies the first-order correction to remove nonlinearities of the earphone speakers is the most accurate as it uses interpolated data from the frequency response function measured with those stimulation frequencies (Aerts and Dirckx, 2007). Secondly, for each stimulation level, only frequency components with vibration levels which exceed the noise were used. Finally, the sum of these nonlinear distortion levels was divided by the number of frequency components that satisfy this criterion.

The calculation of the plausible nonlinear quadratic and cubic distortion frequencies is the main difference between this work and Aerts and Dirckx (2010) and Peacock et al. (2015). In Peacock et al. (2015) and Aerts and Dirckx (2010), the assumption was made that within f_{res} and $2f_{res}$ of a stimulation frequency respectively an even or odd degree nonlinear distortion would be present. However, higher degrees of nonlinearity are less likely to produce significant vibration amplitudes in a weakly nonlinear system. Calculating the plausible quadratic and cubic distortion frequencies revealed that certainly not all stimulation frequencies were surounded by nonlinear distortions within $2f_{res}$. As a consequence, noise contributed to the level of nonlinear distortions in Aerts and Peacock. In this work, nonlinear distortions were only evaluated at plausible distortion frequencies within $2f_{res}$ of the stimulation frequencies. Much more distortion components are present in the recorded vibration spectrum but we cannot accurately correct for distortions present in the sound signal for frequencies further than $2f_{res}$ of the stimulation frequencies. The total level of nonlinear distortions is therefore larger than we can evaluate using this technique. Therefore, we calculated the average nonlinear distortion amplitude by dividing the sum of evaluated nonlinear distortion levels by the number of plausible distortion frequencies. Additionally, this allows for a normalized comparison between even (quadratic) and odd (cubic) degree nonlinearities. After all, there exist more plausible cubic distortion frequencies since they are linear combinations of three stimulation frequencies instead of just two as we have seen for quadratic combinations. This issue would not exist when using single sine stimulation as there is only one stimulation frequency.

Only by including strictly odd multiples of f_{res} (i.e. $k_i \in S_f$ are odd) in the stimulation signal s(t), a distinction can be made between even (quadratic, …) and odd (cubic, …) degree nonlinearities in the output. The contribution of even (resp. odd) nonlinearities to the output will be only visible at even (resp. odd) multiples of f_{res}.

Vibration responses were measured for a frequency range of 255 to 7645 Hz, using approximately 4 stimulation lines per octave and f_{res} was chosen to be 5 Hz. This gives a total number (N) of 19 stimulation frequencies (example in table 5.1). The amplitudes A_{k_i},

which in our case represent the sound pressure levels, were chosen to be equal. Measurements were done at total sound pressure levels between 99 and 120 dB, in steps of 3 dB. The sound pressure level at each stimulation frequency is lower than the total sound pressure level. For example, a total sound pressure level of 99 dB SPL requires $99 - 20\,log10(\sqrt{N}) = 86.2\,dB\,SPL$ at each stimulation frequency.

f_1	f_2	f_3	f_4	f_5	f_6	f_7	f_8
255	315	385	465	565	685	905	1095
f_9	f_{10}	f_{11}	f_{12}	f_{13}	f_{14}	f_{15}	f_{16}
1195	1555	1705	2035	2435	3185	3795	4145
f_{17}	f_{18}	f_{19}					
4935	5875	7645					

Table 5.1: Example of used stimulation frequencies in a multisine signal.

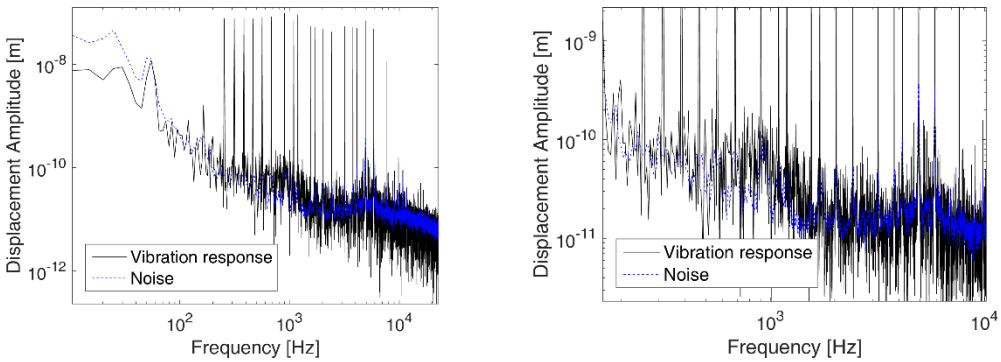

Figure 5.8: Human umbo vibration response and noise level at 111 dB SPL (A) and a close up showing the nonlinear frequency components above the noise floor.

5.4.2 Results

One of the seven ears showed erratic behavior and was excluded from the results. In two other ears one data point was an outlier, and was therefore removed to calculate averages.

Figure 5.8 shows a typical measured vibration spectrum at a stimulation level of 111 dB SPL and a zoomed view on the low-intensity levels revealing the nonlinear responses above the noise.

Starting from a sound pressure level of about 99dB, the measured nonlinearities exceeded the noise floor. As shown in figure 5.9, the mean level of the nonlinear distortions averaged over 6 TBs grows as a function of sound pressure level. At 99dB SPL the mean amplitude of the nonlinear vibration response is only 0.014 nm. At 120dB SPL it has grown to 0.281 nm. The total vibration response (averaged over the available five data points and the number of stimulation frequencies) at this pressure level is 203.7 nm, or a

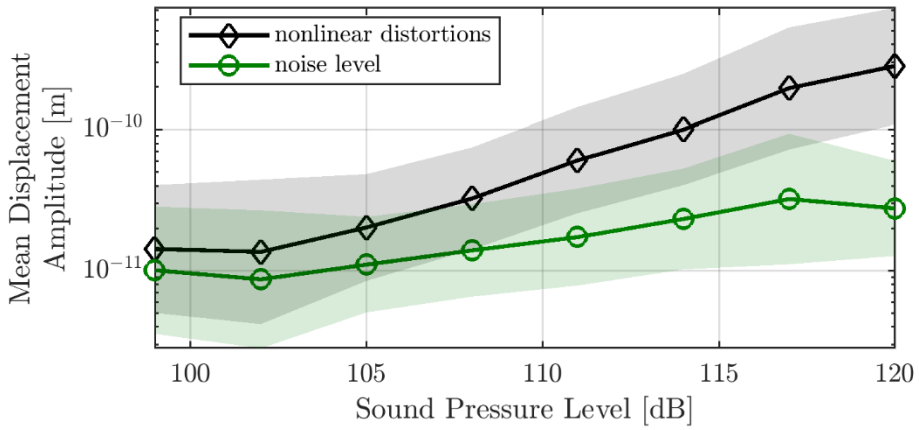

Figure 5.9: Mean nonlinear displacement amplitude as a function of sound pressure level.

factor of 57dB larger than the nonlinear response.

The even and odd nonlinearities can also be measured separately. At all stimulation levels the odd nonlinearities were found to be slightly smaller than the even nonlinearities. The ratio of the amplitudes of even to odd nonlinearities has a nearly constant value of 1.56 over the entire stimulation range but the uncertainty bands are quite large. Figure 5.10 shows the mean amplitude of even and odd nonlinearities as a function of stimulation level, again averaged over the six specimens. These amplitudes grow with a power of about 1.5 as a function of stimulus level.

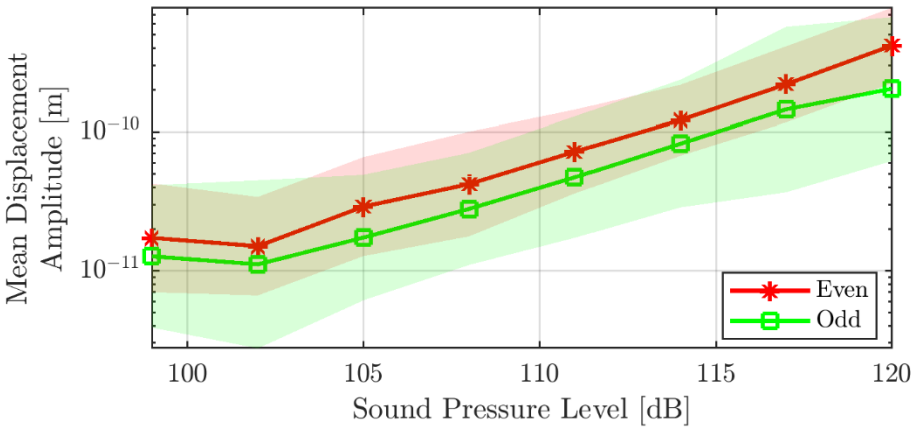

Figure 5.10: Mean nonlinear displacement amplitude for even and odd degree nonlinearities as a function of sound pressure level. The mean level of even degree nonlinearities is slightly higher than the mean level of odd degree nonlinearities. However, a large overlap in standard deviation bands is present.

It was not possible to observe the nonlinear behavior directly from the vibration response curves. As seen in figure 5.11, the response curve divided by the expected linear growth as function of stimulation level of each specimen deviates so little from a constant line that no nonlinear behavior can be quantified. The figure also shows that the vibration response can vary over about a factor of 10 between different specimens. This range of variability has also been observed in previous studies (Volandri et al., 2011).

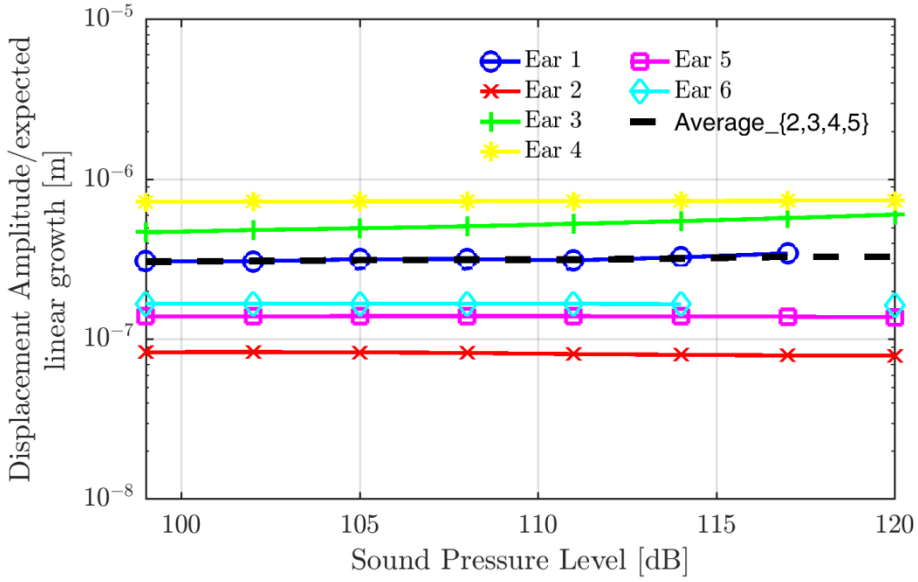

Figure 5.11: The linear displacement amplitude as a function of sound pressure level divided by the expected linear growth. Although we were able to measure the nonlinear distortions at unexcited frequencies, the effect of the nonlinearity on the linear vibration is almost absent.

5.4.3 Discussion and conclusions

With the LDV technique, it is possible to detect and to quantify the presence of nonlinearities in the vibration response of the human ME. The level of nonlinear distortions is however very small: even at a sound pressure level of 120 dB, which is the pain threshold, the mean level of nonlinearity is still 57 dB below the mean linear vibration level. These extremely low levels are probably the reason why nonlinearity remained largely unobserved using other techniques as pointed out in the introduction. LDV makes it possible to detect the nonlinearities and to quantify their level.

It is demonstrated that the odd multisine stimulation allows for separate detection of even and odd degree nonlinearities. This is illustrated in figure 5.10. The level of the even degree nonlinearities seems to be a little higher than the odd degree nonlinearities. However, statistical testing showed that the difference is not significant, due to the large variability and the limited number of specimens. Further investigation on a larger data set will be needed to determine if the difference between the levels is a significant feature.

The results show that even and odd distortions grow with stimulus level at a power of about 1.5 which is less than expected a power of two for quadratic and power of three for cubic distortions. One possible reason is that we assumed that the nonlinear frequency components we examined were produced by only quadratic or cubic type of nonlinearities. Higher-order nonlinearities will also produce these very same frequency components and they might have a different phase. It might be the case that the higher-

order distortions interfere with the lower-order distortions. In this way the growth rate of these frequency components can be smaller than expected.

Another contribution might be due to the fact that at high pressure levels, the frequency response of the system might change by small amounts (softening behavior). When the frequency response of the system changes, the nonlinear frequency response also changes and this might in turn decrease the growth rate of the nonlinearities.

The paper by Rosowski et al. (1984) also shows a decrease in growth rate of the nonlinearities: At first, the level of the third harmonic grows as a function of sound pressure level with a power of three, which is to be expected. For higher stimulation levels, the growth rate decreases significantly as pointed out by Rosowski et al. (1984).

Figure 5.11 suggests that only examining the total vibration response divided by expected linear growth as a function of sound pressure is an inadequate method to detect the nonlinear behavior of the ear. The vibration response will closely resemble a constant line, not revealing the extremely low level of the nonlinear component. One ear shows a small increase in growth rate for higher sound pressure levels. The opposite is often expected as a part of the energy is distributed over the distortion products. As mentioned before, the frequency response function of a system can change by small amounts at high pressure levels. Depending on the chosen stimulation frequencies, the total vibration level can exceed linear growth. This is possibly the case for TB3. This case further supports the necessity to measure the level of nonlinear distortions themselves instead of the effects of nonlinearity on the expected linear growth at stimulation frequencies.

Due to ethical reasons, it is extremely difficult to obtain fresh human cadaveric material. Therefore, studies in hearing often need to be performed on specimens which have been harvested and frozen immediately after death on locations other than the lab where they are investigated. Elaborate studies have been performed to investigate the effect of freezing (Rosowski et al., 1990), and it was found that the process does not influence vibration behavior significantly. It can however not be fully excluded that some changes in tissues occur, and that also the time post-mortem before freezing may have an effect. The LDV technique is minimally invasive since only a small reflective patch needs to be placed on the eardrum. Therefore, measurements can also be performed in vivo, but in this case the strongly nonlinear contribution of the inner ear will influence the results. Therefore, in-vitro studies seem the best choice to quantify the contribution of passive ear mechanics to the nonlinear response, but it should be noted that additional variability caused by time-dependent post-mortem artifacts cannot be fully excluded.

The driving sound signal also contains nonlinearities, especially at the higher sound pressure levels. These nonlinearities could erroneously be interpreted as nonlinearities generated by the ear. Aerts and Dirckx (2007) have shown that this effect can be reduced by applying a first order correction in which the measured vibration response is being corrected for the actual sound input signal. The authors showed that for a sound generation system similar to the one used in the current experiments, no distortions were detected in the vibration of flat metal membranes which are indeed expected to have a near to perfect linear vibration response.

Rosowski et al. (2008) have demonstrated the use of LDV in a clinical setting. To estimate the noise, they evaluated the response at non-excited frequencies. This is the same way how we evaluated non-linear components in this work. However, Rosowski used only 9 stimulation frequencies and presented this sound signal to the ear at sound pressure levels between 50 and 90 dB SPL. Since the nonlinear distortions at 120 dB SPL is still about 50-60 dB below the linear response, the noise estimation of Rosowski can still be considered valid between 50-90 dB.

In conclusion, the LDV technique has made it possible to detect and quantify nonlinear response in the human eardrum. Nonlinearities can be detected at sound pressure levels starting from 99 dB and at 120 dB the mean level of the nonlinearities is more than 50 dB below the mean linear vibration response. It is possible to discriminate between even and odd degree nonlinearities, which can help to pinpoint the source of nonlinear behavior.

5.4.4 In retrospect

Source of nonlinearity

In section 5.2, we concluded that based on the asymmetrical quasi-static nonlinear behavior of the human ME, both even and odd degree nonlinearities should be present. Measurements in Gladine et al. (2017) have shown this to be correct. We did not measure the linear and nonlinear stapes vibration levels as was done in Peacock et al. (2015). Such additional would have been valuable as they could reveal if the nonlinearities mainly exist at the level of the TM as was shown in rabbits.

Multisine versus single sine

We already touched lightly upon a few of the drawbacks of using random phase odd multisine stimulation for detection of nonlinearities.

Firstly, a lot of data remains unused. We can only properly evaluate nonlinear distortions at frequencies close to the stimulation frequencies. This is a consequence of the correction method for the nonlinearities present in the sound. This correction method requires interpolation at the unexcited frequencies of the vibration response of the TM which was only measured at the stimulation frequencies. Since the stimulation frequencies are sparsely distributed over the measured frequency range, such interpolation is only accurate close to the stimulation frequencies. This limits the number of usable frequencies in the distortion analysis tremendously since distortions occur across the whole spectrum. A further reduction in usable frequencies occurred by only considering quadratic and cubic nonlinear behavior. This can be avoided by measuring the linear vibration response at all plausible distortion frequencies beforehand. This might be impractical due to the high amount of frequencies. Up to what degree of nonlinearity would be taken into account? A higher degree of nonlinearity causes more plausible distortion frequencies. This also holds for single sine stimulation, but the nonlinear distortions only occur at harmonics of the stimulation frequency. As a consequence, a correction of the sound can be easily performed for high degrees of nonlinearity since this requires only a measurement of the vibration response at a few frequencies (e.g. 4 frequencies for 5th degree of nonlinearity).

Second, if only quadratic and cubic nonlinearities are considered, the plausible number of cubic distortion frequencies is much larger than quadratic. This can easily provide a false view on which type of distortion is more prominent. On top of that, higher-order nonlinearities can coexist at the same frequencies as quadratic and cubic nonlinearities. Depending on the phase difference between these higher-order nonlinearities and quadratic or cubic nonlinearities, it is not unimaginable that higher-order nonlinearities are able to reduce the distortion levels at the evaluated frequencies.

The multisine stimulation was said to be great since it produces much more nonlinear components than single sine stimulation. However, it is clear that most of these nonlinear components were not evaluated and that it makes interpretation more complicated.

And finally, the amount of energy per stimulation frequency is much lower using multisine stimulation compared to single sine stimulation. Has this an effect on the magnitude of the nonlinearity?

For these reasons it seems interesting to explore what single stimulation might reveal.

5.5 Measurement of small nonlinearities in flat and curved membranes using single sine stimulation

In this section, we explore what information high sound pressure level single sine stimulation can provide about the influence of shape on nonlinear behavior in silicone membranes. We also investigated a way of compensating for nonlinearities generated by the sound source different to the first order post-processing correction which was used in Gladine et al. (2017), Peacock et al. (2015) and Aerts and Dirckx (2010).

This section is based on work presented at the A.I.V.E.L.A. conference of 2016 in Ancona.

This work has been published as a conference paper:

Gladiné, K., Muyshondt, P., Dirckx, J. 2016. LDV measurement of small nonlinearities in flat and curved membranes. A model for eardrum nonlinear acoustic behaviour. AIP Conference Proceedings Vol. 1740, 050005.

5.5.1 Methods and materials

Flat and curved membrane

To investigate the importance of the shape of a membrane with regard to nonlinearity, two different shapes were used in this work. One membrane was flat and another resembled the tent-like shape of a TM. Figure 5.12 shows a cross-section along the diameter of the curved membrane. Membranes were clamped at their circumference

between a metal ring and the supporting cylinder. The thickness of the flat and curved membrane were 500 µm and 350µm respectively. The freely vibrating part of the membranes had a diameter of 18 mm. A small piece of reflective tape was attached to the surface to increase the reflection of the laser beam directed to the LDV.

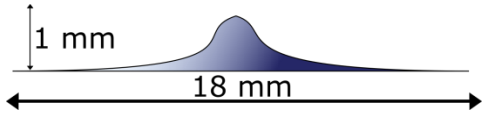

Figure 5.12: Cross-section of the curved membrane

Experimental setup

The experimental setup consists of an LDV (Polytec OFV-5000), Bruël and Kjær probe microphone (type 4182) and earphone speakers. These three elements are connected to a National Instruments card (USB 6251) which is controlled using Matlab scripting. The NI acquisition card its sampling rate is set at 50 kHz and can deliver an output signal with maximal amplitude of 10V.

A closed metal cylindrical cavity was used. The earphone speakers were located at opposite sides of the cylinder and perpendicular to them the probe microphone was inserted. The upper part of the cylindrical cavity was closed by the sample membrane itself. The laser beam of the LDV reached the sample on the outside boundary of the sample membrane. Figure 5.13 shows a sketch of the experimental setup.

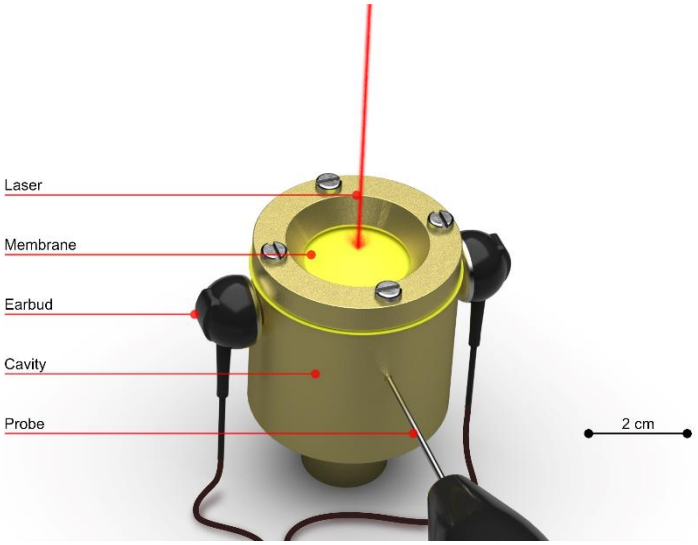

Figure 5.13: Sketch of the measurement setup.

Nonlinear sound source correction methods

Stimulus correction

A method to avoid nonlinear artifacts at the stimulus is to modify the signal sent to the speaker. Let us suppose that the speaker behaves as nonlinear system which can be described as:

$$y(x) = x(t) + 0.01\,x^2(t) \tag{5.1}$$

$x(t)$ is the voltage sent to the speaker and y is the pressure output recorded by the probe microphone. This pressure output is the stimulus for the vibration measurement done later in the experiment. For simplicity, we assume that the frequency response function (FRF) of the speaker is constant as a function of frequency. If $x(t) = \sin(2\pi f t)$ is a sinusoidal function of time, then we get:

$$y(t) = \sin(2\pi f t) + \frac{0.01}{2} + \frac{0.01}{2}\sin\left(2\pi(2f)t - \frac{\pi}{2}\right) \tag{5.2}$$

Thus, $y(t)$ is a signal with frequency components f and $2f$ which have different phases. The additional signal with frequency $2f$ is unwanted and should be removed from the pressure output. This is done by modifying the voltage signal x as shown in (5.3). If the amplitude and phase of y at frequency $2f$ are known, the signal x can be changed such that the linear component of y produces an additional term that is in antiphase with the 2f component. In this way, the $2f$ term produced by the quadratic component of $y(t)$ is annihilated.

$$x_1(t) = x_0(t) + \frac{0.01}{2}\sin\left(2\pi(2f)t + \frac{\pi}{2}\right) = \sin(2\pi ft) + \frac{0.01}{2}\sin\left(2\pi(2f)t + \frac{\pi}{2}\right) \quad (5.3)$$

The modified voltage signal $x_1(t)$ eliminates the production of the $2f$ component but gives rise to undesired higher-order components. These higher-order components have lower amplitudes than the original 2f component, and the same procedure can be repeated to eliminate them. This iterative method will result in a stimulation signal $y(t)$ of which the linear component remains at its original amplitude, and the nonlinear components are greatly reduced.

The assumption that the speakers FRF is constant as a function of frequency is of course not true. When the voltage signal (x(t)) that is sent to the speaker is converted to pressure waves (y(t)), the phase and amplitude of these waves will be determined by the FRF of the speaker. The amplitude and phase used in $x_1(t)$ should be accommodated using the speakers FRF at the frequency of the harmonic that is being corrected.

Post-Processing Correction

If no modification is done of the signal that is sent to the speaker, the stimulation signal will contain frequency components which are not intended. The membrane will vibrate at these frequencies, and this can be misinterpreted as membrane nonlinear response. If the stimulation signal and the FRF of the membrane at the harmonics of the stimulation frequency are known, a first order post-processing correction can be done. To remove the nonlinearities caused by the stimulus, the Fourier transform of the stimulation signal is multiplied with the FRF of the membrane at the unwanted frequency components and is subtracted from the vibration spectrum. This is a first order correction that works under the assumption that the nonlinearities of the system are small.

Comparison of Membrane Behaviour

To compare the nonlinear behavior of a flat and a curved membrane, several measurements were performed. The vibration amplitudes of the harmonics were compared as a function of stimulation amplitude (i.e. SPL), for a fixed stimulation frequency. Alternatively, the vibration amplitude of the membrane at the stimulation frequency was used (not shown).

Vice versa, the SPL or vibration amplitude at the stimulation frequency can be fixed and we can sweep over a range of frequencies. Only the data for a fixed sound pressure level is shown.

General Outline of a Measurement and Signal Creation

The following procedure was used to generate the stimulation signal and perform a measurement.

1. A sinusoidal voltage signal with frequency f is sent to the earphone speakers
2. A correction factor is calculated to correct either
    a. the effective SPL to the desired SPL
    b. the effective vibration amplitude to the desired vibration amplitude at the stimulation frequency
3. A measurement is done of the FRF at the harmonics of f of
    a. the membrane at a constant SPL for all harmonics (in case of post-processing correction method)
    b. the speakers by sending a constant voltage amplitude for all harmonics (in case of stimulus correction method)
        i. The speaker is corrected by modifying the voltage signal as described above
4. Fifty measurements are performed, each with a length of 0.1 s
5. The mean value of these fifty measurements is calculated
    a. Data-correction is applied if no stimulus correction was done

This is done for every frequency/amplitude level separately.

All signals sent to the earphone speakers were single sine signals. Each signal is extended with 0.05 seconds to eliminate transient effects. When processing the data, the data during this transient time is removed. The frequency f is chosen to be a multiple of 10. This way an integer number of periods fit into the measured time of 0.1 seconds. As a consequence, the Fourier transform can be evaluated exactly at f and its harmonics.

5.5.2 Results

Correction methods

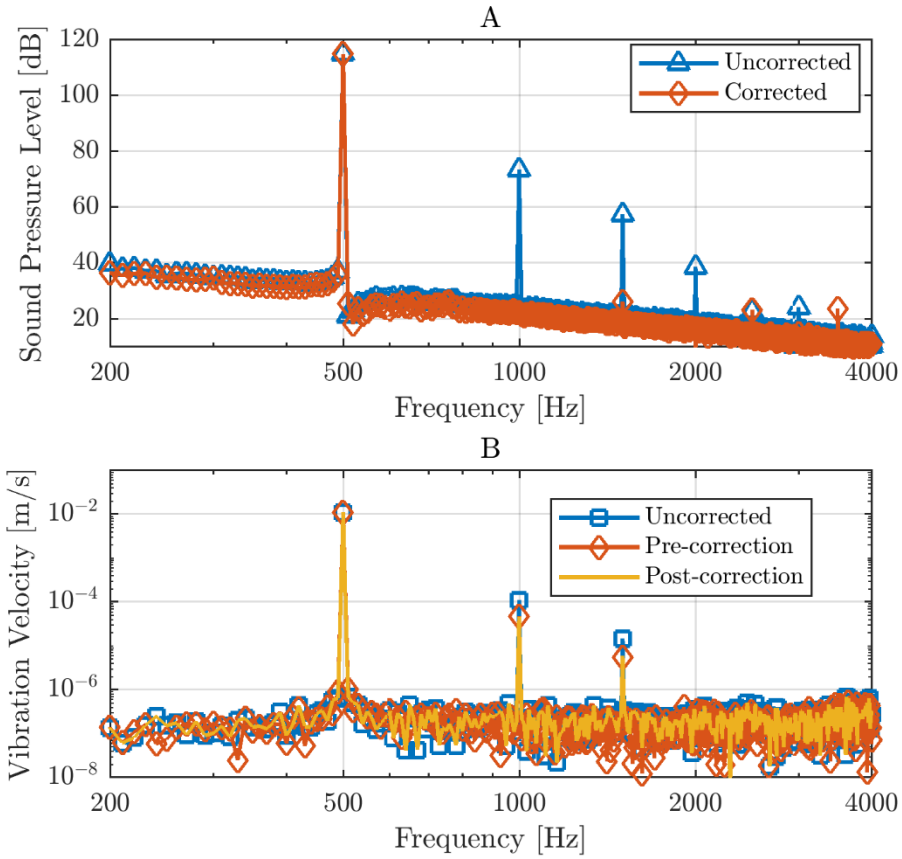

Figure 5.14: Comparison of the two proposed correction methods, in which corrections were performed for the harmonics of the stimulus frequency of 500 Hz. (A) Measured frequency spectrum of the stimulation signal without and with modification of the signal sent to the speaker. (B) Frequency spectrum of the vibration response of the membrane without any correction (□), with correction of the stimulus (◊) and with correction in post-processing (-).

Figure 5.14A shows the spectrum of the stimulation signal without and with modification of the signal sent to the speaker as described in section *stimulus correction*. The sound pressure level at the stimulation frequency of 500 Hz is 110 dB. As expected, the amplitude of the stimulation frequency is the highest peak in the spectrum. The uncorrected stimulus signal also has significant amplitudes at integer multiples of the stimulation frequency. A few other peaks are visible but with small amplitudes. The corrected stimulus signal has the same amplitude at the stimulation frequency but much

lower amplitudes at the harmonics. For higher frequency components, the amplitude has increased after correction. However, these amplitudes are very small as compared to the amplitude at the stimulation frequency and the harmonics of the uncorrected stimulus signal.

Figure 5.14B shows the spectrum of the vibration velocity of the membrane without and with using stimulus correction and using post-processing correction. For all spectra, the vibration velocity amplitude is the highest at the stimulation frequency and the first two higher harmonics. With stimulus correction, the peak at the stimulus frequency remains unchanged, but the amplitudes at the higher harmonics are reduced. Similar results are obtained with post-processing correction. The remaining amplitude at the harmonics is now due to the nonlinear response of the object, and not caused by nonlinearities in the stimulation signal.

Membrane comparison

Figure 5.15 shows the membrane vibration amplitude of the stimulation frequency (figure 5.15A), second harmonic (figure 5.15B) and third harmonic (figure 5.15C) as a function of stimulation frequency at a fixed sound pressure level of 110 dB. Figure 5.15B and 15C should be interpreted as followed:

> The x-axis always displays the stimulation frequency. This means that a vibration amplitude of the second harmonic, for a stimulation frequency of 500 Hz, is the vibration amplitude evaluated at 1000 Hz when the membrane was stimulated at 500 Hz. Similarly, the vibration amplitude of the third harmonic was evaluated at 1500 Hz.

A clear resonance is observed for both membranes (figure 5.15A). The resonance frequency of the flat membrane is lower compared to that of the curved membrane. The curvature contributes geometrically to the stiffness of the membrane and thus increases the resonance frequency. Similar observations were made in ME models in which the depth of the TM was altered (Koike et al., 2001). A shallow TM causes the frequency of the ME to be lower compared to a normal conical shaped TM (Koike et al., 2001). Multiple peaks are visible in figure 5.15B. One peak occurs at the resonance frequency of the linear vibration response, but also at half of that frequency. The curved membrane shows an additional peak at a frequency of about 500 Hz. Similarly, figure 5.15C contains a peak at the linear resonance frequency but also at a third of that frequency although no measurements using sufficiently low stimulation frequencies were performed to clearly visualize this for the flat membrane.

Figure 5.16 shows the membrane vibration amplitude at the stimulation frequency (A), the second harmonic (B) and third harmonic (C) as a function of the pressure, using a stimulation frequency of 500 Hz. In this case, the vibration amplitude at the stimulation frequency is not the same for both membranes (figure 5.16A) as it depends on the membrane FRF. At 500 Hz, the vibration amplitude of the flat membrane is larger than that of the curved membrane. Figure 5.16B shows that the amplitude of the second harmonic is almost equal for both membranes. From figure 5.16C we see that the vibration amplitude of the third harmonic is also similar for both membranes.

A

B

C

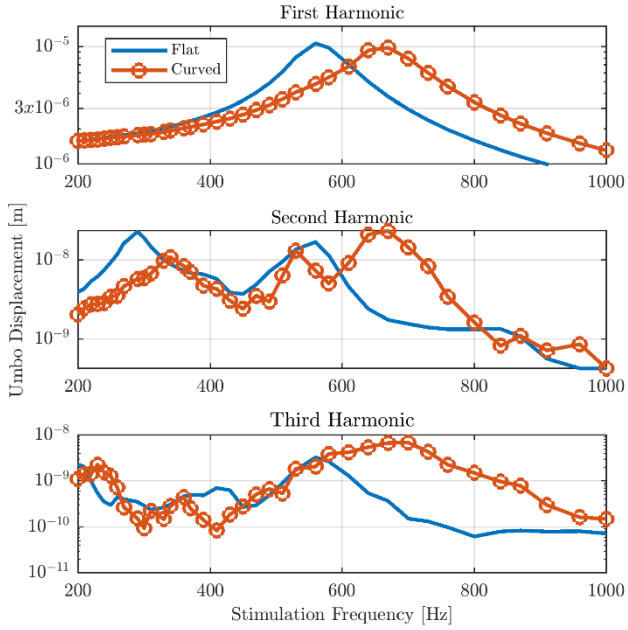

Figure 5.15: Umbo displacement as a function of stimulation frequency for the first harmonic (A), second harmonic (B) and third harmonic (C) at a sound pressure level of 110 dB SPL.

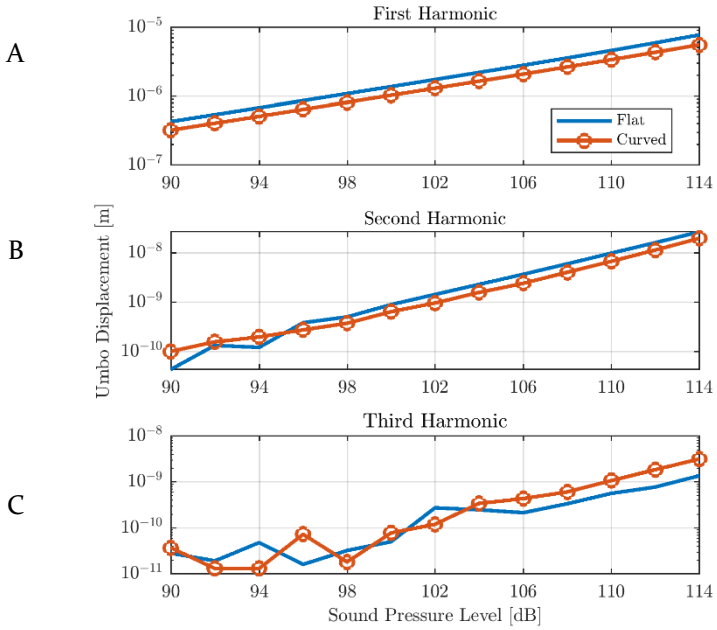

Figure 5.16: Umbo displacement as a function of sound pressure level for the first harmonic (A), second harmonic (B) and third harmonic (C) using a stimulation frequency of 500 Hz.

5.5.3 Discussion

Correction methods

From figure 5.14A, it is clear that sending a modified voltage to the speaker as described in section *5.5.1* strongly reduces the amplitude of the harmonics of the stimulation frequency. It works very well for the first higher harmonics, but as mentioned before, other higher-order nonlinearities are created. The amplitudes of these nonlinearities are very small and have little influence on the vibration of the membrane.

The harmonics present in the uncorrected stimulus signal contribute to the vibration amplitude of the membrane. This is apparent in figure 5.14B, in which the data with corrected stimulus signal and the data corrected using post-processing show a reduced amplitude at the harmonics. The results of the stimulus correction method and the post-processing method are in good agreement with each other.

It is very important to determine the phase of the stimulation signal at the harmonics as correct as possible. It is the key ingredient to the stimulus correction method because it makes it possible to send an anti-phase signal that annihilates the unwanted frequency components. At higher frequencies, the phase changes very rapidly, and a small delay can make a big difference in the results of the correction. In this work, not one but two

speakers are driven simultaneously. A single microphone captures the sound at approximately an equal traveling distance from both speakers. The phases of both speaker signals measured at the tip of the microphone might deviate a bit from one another. For higher frequencies, this is more likely to happen, and the correction method will work less well than for low frequencies.

Membrane comparison

Peacock et al. (2015) observed that the nonlinear distortions did not show a peak at the resonance frequency of the ME. This is different from the observations made here. The second harmonic and third harmonic showed a small peak when stimulating at half and a third of the resonance frequency respectively. This means that the nonlinear distortions actually are larger at the resonance frequency of the membrane.

The second and third harmonic curves also show a peak when stimulating the membrane at the resonance frequency, which means that due to the larger vibration amplitude at the resonance frequency, higher levels of nonlinearities are achieved.

We assume this difference in observations with Peacock et al. (2015) is due to the type of stimulation. The observations using single sine stimulation are similar to those used for the calculations of the theoretical models like the Duffing equation seen in section 3.3.2. The nonlinear response is partly similar to the linear response. The behavior of the second harmonic when stimulating between 200-400 Hz is a "copy" of that of the first harmonic when stimulating between 400-800 Hz. We also saw that the level of distortions is dependent on the vibration amplitude. Because of this, such similarity between nonlinear and linear response would be less obvious if the membrane's linear response at 200-400 Hz was not as flat as it is. When using multisine stimulation, the nonlinear distortions are generated by a combination of frequencies. The linear response at the frequencies that will generate nonlinear distortions around the resonance frequency will not be as flat, and thus the frequency dependence of the distortion levels will not resemble the linear response as much.

The goal of this experiment was to evaluate the effect of geometry on the nonlinear behavior. The hypothesis was that a flat membrane would show a low level of even degree nonlinearity (second harmonic). However, the flat membrane did show significant even degree nonlinear distortions, and the difference between the flat and curved membrane is very small. These results seem to debunk our hypothesis, or did we miss something?

The flat and curved membranes have a diameter to thickness ratio of about 36 and 51, respectively. This is very small compared to the TM, which holds a ratio of about 140. The membranes in this experiment are thus very thick. In the next section, we will use a modeling approach to investigate if the membrane thickness can also contribute to the nonlinearities of a membrane and which degrees it influences the most.

5.6 Finite element modeling of flat and curved membranes

This section is not based on published material, but work was performed by us.

5.6.1 Methods

Geometry

Finite element models of two geometrically different membranes were constructed: A flat and curved(figure 5.17). Membrane diameter was always set to 18 mm. All membrane thicknesses were 500 µm. Additional models were made for the flat membrane with an adjusted thickness of 100, 250, and 1000 µm. The membranes were considered perfectly symmetrical so that an axisymmetric model could be used.

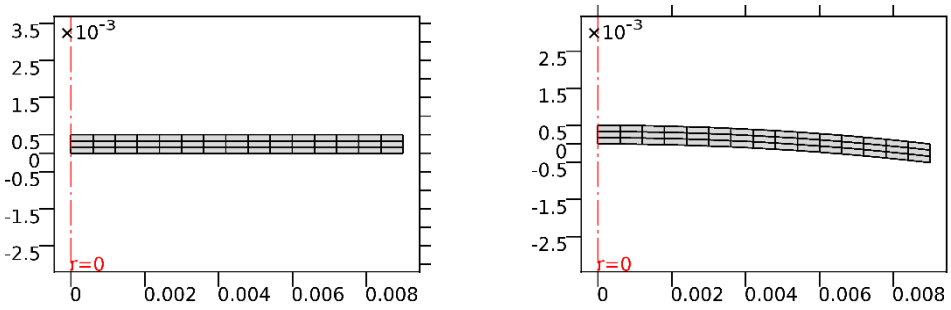

Figure 5.17: Geometry and mesh of the finite element models of a flat membrane (A) and curved membrane (B).

Material properties

The purpose of these models is merely to investigate the effect of the membrane shape and thickness on nonlinear behavior. Therefore, the material properties such as density, Young's modulus, Poisson ratio, and material damping are not based on the materials used in section 5.5. The material properties were chosen to be isotropic and linear. Only geometric nonlinearities were considered.

Mesh

A mapped quad mesh was generated. Five element layers were distributed over the membrane thickness (figure 5.17).

Study type

Since we are studying dynamic nonlinear behavior, we cannot use a frequency domain study. Such frequency domain study assumes a linear harmonic solution. Instead, a time domain study is performed. Single sine stimulation was used. In section 5.5, we noted that the level of nonlinearity is dependent on the vibration amplitude of the first harmonic. For this reason, we either adjusted the amplitude of the sine stimulation to obtain the same linear vibration amplitude for all membranes or chose the stimulation frequency to be very low in comparison to the first resonance frequency of the membrane to avoid the influence of the membrane response on the nonlinearities. The amplitude of the single sine stimulation was slowly increased over time, a process called ramping. Ramping up the stimulation amplitude allows for a smooth transition of the time-dependent solver to a steady state solution. In total 16 periods were calculated using a time step of $\Delta t = \frac{1}{25f}$. A Fourier transform was then used to obtain the frequency spectrum of the response. All data was evaluated in the center of the membrane.

5.6.2 Results

Influence of membrane thickness

All flat membrane models showed even and odd degree nonlinearities (figure 5.18). However, decreasing the thickness affected the ratio of odd to even degree nonlinearities. For thinner membranes, the ratio of odd to even degree nonlinear distortion levels was higher than for thick membranes.

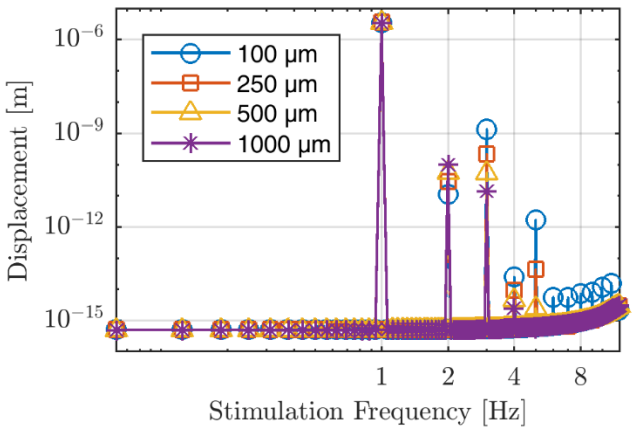

Figure 5.18: Effect of thickness on the nonlinear response of a flat membrane to single sine stimulation for equal linear displacements. The odd-to-even degree ratio increases as the membrane gets thinner.

Influence of membrane shape

Figure 5.19 shows the response of the first 3 harmonics of both membranes at 1 Hz. The linear response of the flat membrane exceeds that of the curved membrane by 6dB. However, the response of the flat membrane at the second harmonic is 38dB lower compared to the curved membrane. The response of the flat membrane at the third harmonic is 10dB higher than the curved membrane.

The backbone curves shown in figure 5.20 display different behavior for the flat and curved membrane. The resonance frequency of the flat membrane increases by 7.5% when increasing the sound pressure level up to 144dB SPL. The amplitude at the resonance frequency increases slower than linear growth. In contrast, the resonance frequency of the curved membrane decreases by 1.84%. The amplitude at resonance surpasses the expected linear growth by less than 5%.

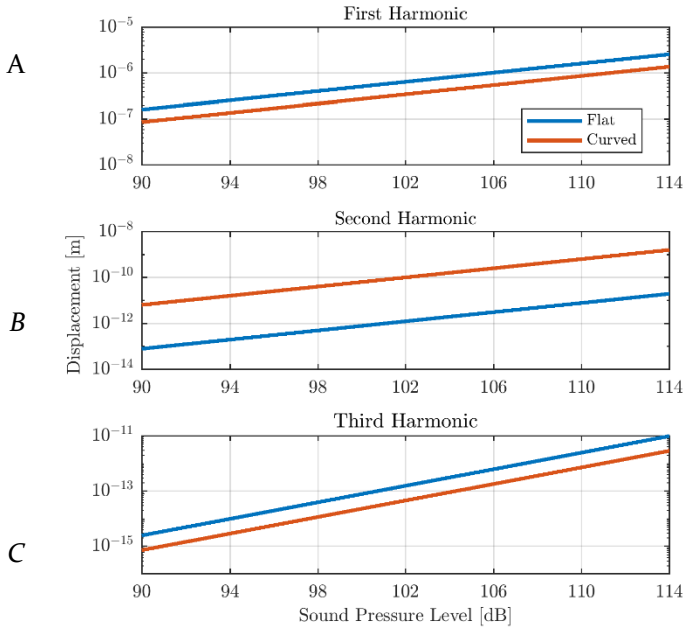

Figure 5.19: Response of the first harmonic (A), second harmonic (B) and third harmonic (C) to a single sine stimulation of 1 Hz.

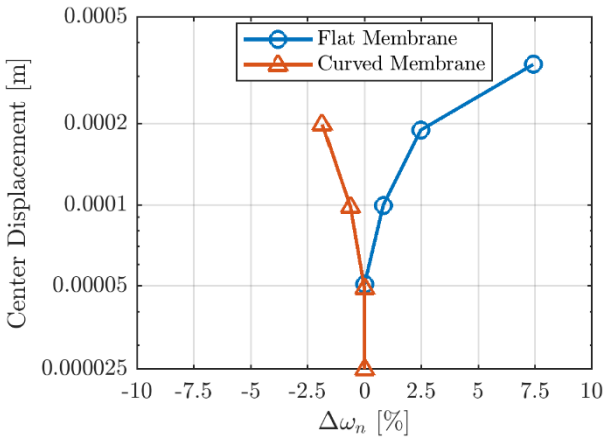

Figure 5.20: Backbone curves for small and flat membrane. The used sound pressure levels range is 126-144dB SPL in steps of 6dB SPL. A flat membrane exhibits hardening behavior and its maximal amplitude increases slower than the expected linear growth. A curved membrane exhibits softening behavior and its maximal amplitude rises slightly (<5%) faster than the expected linear growth.

At 144 dB SPL, the curved membrane shows a net displacement of about -50 μm while the linear displacement amplitude is 200 μm. The net displacement of the flat membrane is negligible.

5.6.3 Discussion

Influence of membrane thickness

For thick membranes, the top and bottom surface do not deform exactly the same when subjected to sound at high sound pressure levels. This asymmetry causes the membrane to deform nonlinearly. The nonlinear components contain even degree distortions. The level of these distortions decreases as the diameter to thickness ratio increases. We can conclude that our original hypothesis that flat membranes only show odd degree distortions only holds for an infinitely thin membrane. Thus, the even degree nonlinearity observed in TM vibrations at high sound pressure levels exists partly due to through-thickness nonlinear behavior. However, a flat membrane with a diameter to thickness ratio of 70, similar to the TM, has a higher ratio of odd to even degree nonlinearities. TM measurements showed that the even degree nonlinearities were larger than the odd degree, implying that other mechanisms contributed to the even degree nonlinearities.

Influence of membrane shape

We observe from the nonlinear response that the curved membrane exhibits more even degree nonlinearities than the flat membrane. Vice versa, the flat membrane shows a higher level of odd degree nonlinearities. This is partially in agreement with the measurements we made of the human ME. The nonlinearity of the TM was governed (slightly) by even degree nonlinearities.

The backbone curves suggest that the nonlinear behavior of the TM indeed originates from its shape. The curved membrane shows softening behavior just like the ME. In contrast, a flat membrane shows hardening behavior.

5.7 Human ME nonlinearity measurements (part 2) and FE modeling

In this section, we will apply some of the knowledge we gathered in the preceding sections. We will discuss measurements of the ME backbone curve and investigate if the ME consistently exhibits softening behavior. We will discuss single sine measurements and the level of even and odd degree nonlinear distortions.

This section is not based on published material, but all measurements and data analysis was performed by us.

5.7.1 ME softening behavior and backbone curve using multisine stimulation

Methods

Two cadaver temporal bones were used. The bones were removed from the skull within 24 hours after death and were immediately frozen. Prior to the measurements, the bones were left to thaw for 24 hours at 4°C, and one hour before measurement they were left to accommodate to room temperature.

Laser Doppler vibrometry was used to measure the velocity of the umbo. We described the setup already in section 4.1. A reflective patch was placed on the umbo in order to increase the amount of light reflecting to the vibrometer sensor.

The ME system was stimulated using earphone speakers mounted in a small semi-closed cavity mounted on the ear canal. A multisine sound signal was employed. In contrast to the multisine signal described in section 5.4, this multisine signal was designed to accurately measure the umbo velocity response instead of evaluating the level of nonlinear distortions at non-stimulated frequencies. For this reason, much more frequencies were included in the multisine. Different multisines were used for each temporal bone[2]. For TB1 the 1576 stimulation frequencies spanned a range of 125 to 8000 Hz. TB2 was stimulated using a multisine of 191 frequencies ranging from 200 to 4000 Hz.

The sound pressure level was measured using a probe microphone connected to a small tube which fitted through a small hole in the cavity. The tube was placed 2 mm from the TM. Sound pressures were used ranging from 90 to 120 dB with intervals of 6 dB. For TB1, the individual sound pressure levels at each frequency were all increased equally to obtain the total requested sound pressure level. As a consequence, the sound pressure level is not equal for all frequencies. For TB2, the sound pressure level was set equal for all frequencies.

[2] The measurements described here were tests while performing another study. For this reason, there was a lack of coherence of the used stimulation signals.

Results

Figure 5.21 shows the umbo velocity magnitude and phase at different sound pressure levels. A small shift in resonance frequency is detected by observing both variables. On the magnitude graph, we see that the resonance peak shifts to lower frequencies and increases very slightly in magnitude. On the phase graph, we observe a shift to lower frequencies of the phase jump associated with that same resonance. Data at higher frequencies was not shown as no changes were observed at different sound pressure levels.

The backbone curve shows that the resonance frequency decreases 7.5-9% while the resonance magnitude increases about 3.5% for both TBs (figure 5.21).

Discussion

The data presented here displays the softening behavior of the ME. At high sound pressure levels, the first resonance frequency decreases, and the magnitude slightly increases. The amount of change is very similar for both temporal bones, although the sound stimulation was not so similar. The total of 120 dB SPL was divided over the number of stimulation frequencies that were used. As the amount of stimulation frequencies increases, the sound pressure level per frequency decreases. Overall, the sound pressure level per frequency is lower for TB1. Sound pressure levels are similar for both temporal bones up to 700 Hz (figure 5.23). At 1000 Hz, the resonance frequency of TB1, the sound pressure level is 10 dB below to that of TB2. This seems to imply that the energy of mainly the lower frequencies seems to contribute the softening behavior. This seems reasonable as all frequencies below the first resonance frequency contribute to the first mode and thus increase the vibration levels of the same mode.

The backbone curves do not take the exact form of the backbone curves in section 3.3.2 in which we discussed softening behavior using the Duffing equation. However, due to the limited number of data points and the fact that the change in magnitude is so small that a small alteration of a single data point could result in a different shape of the backbone curve.

In conclusion, our measurements show that the ME exhibits softening behavior at high sound pressure levels. This measurement data confirm those of Voss et al. (2000). This behavior is associated with curved membranes as we saw in section 5.6. This suggests again that the TM is the source of the ME nonlinear behavior.

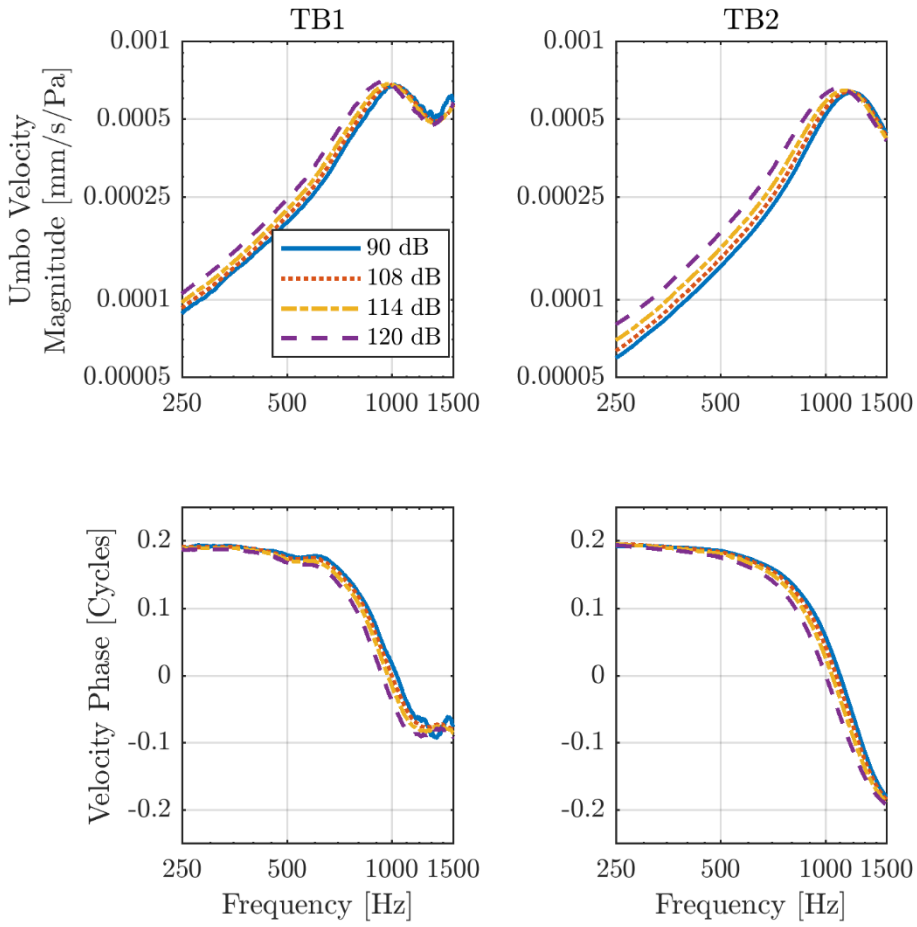

Figure 5.21: Umbo velocity magnitude (top) and phase (bottom) for TB1 (left) and TB2 (right) at different sound pressure levels. A negative frequency shift of the first resonance frequency is observed as the sound pressure level increases.

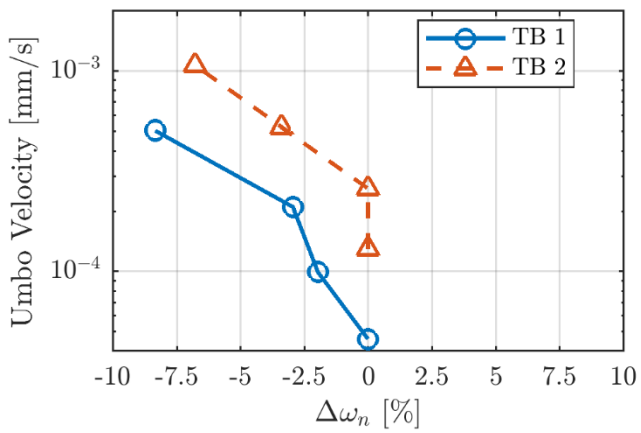

Figure 5.22: Backbone curves of both temporal bones. Softening behavior is observed as sound pressure level increases.

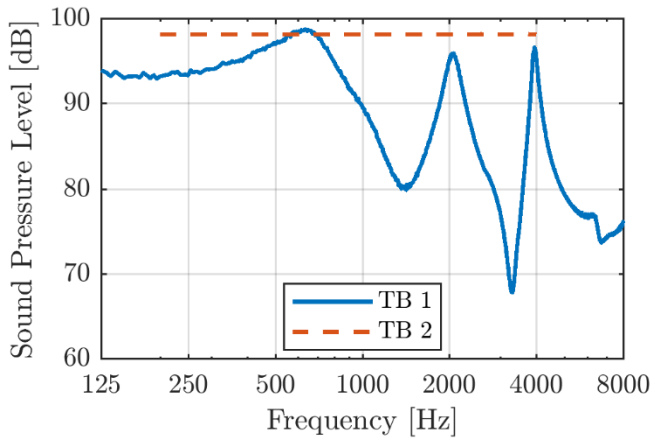

Figure 5.23: Measured sound pressure level of the multisine stimulations used for TB1 (blue) and TB2 (red). Although the stimulations were so different, the nonlinear behavior was very similar.

5.7.2 Measurement using single sine stimulation

In section 5.4.4, we discussed some of the disadvantages of using multisine stimulation regarding detection of nonlinear distortions of the human ME. We suggested the usage of single sine stimulation and tested this on rubber membranes in section 5.5. We discussed using a correction scheme to linearize the speaker output at high sound pressure levels. This correction scheme is compatible with weakly nonlinear systems. We were able to

make the setup described in section 5.5 to be airtight using a closed cavity. It is easier for the speaker to generate large sound pressure levels than in open air.

We tried the same approach for ME measurements. However, due to improper sealing, the speaker sound correction scheme failed. In fact, the correction scheme added more harmonics to the sound signal during the iterations.

We could have resorted to the post-processing correction; however, we did not save the frequency response data at the harmonics. The last option we have is to evaluate the level of nonlinear vibrations with respect to the level of the linear vibrations and compare this to the ratio of linear to the nonlinear sound. Such an approach has been used by others (Greene et al., 2017).

The experimental setup was the same as described in section 5.7.1.

Results

Three TBs were used. However, in only one TB were the nonlinear components of the sound source significantly lower than the observed nonlinear components of the TM vibration. We will focus on the results obtained using this TB.

Figure 5.24 shows the linear and nonlinear response of the umbo at different sound pressure levels alongside the noise. The noise was calculated by evaluating the vibration level at non-excited frequencies, which were not harmonics of the stimulation frequency. At 96 dB SPL, the nonlinearities do not surpass the noise level. At 114dB, the response at the second harmonic is far above the noise level. The curve shows two resonances; at 1200 Hz and at about 600 Hz, which are the resonance frequency and half the resonance frequency of the linear response respectively. The third harmonic levels are slightly above the noise, but no clear resonances are presented yet. At 120dB SPL, the curve of the second harmonic looks similar but is shifted to higher levels. The third harmonic levels now show resonances at 1200 Hz and about 400 Hz, which are respectively the resonance frequency and a third of the resonance frequency of the linear response.

We calculated the mean sound pressure level and mean velocity amplitude over all frequencies for different each sound pressure level (figure 5.25). The linear component of the sound behaves as expected. The mean linear component of the sound pressure level was the requested sound pressure level. We see that as of 108dB SPL, the sound becomes nonlinear. At 120dB SPL, the difference between the linear and nonlinear components of the sound is 55dB. In contrast, the difference between the first and second harmonic of the vibration response is only 36dB. Between the first and third harmonic a 53dB difference was measured.

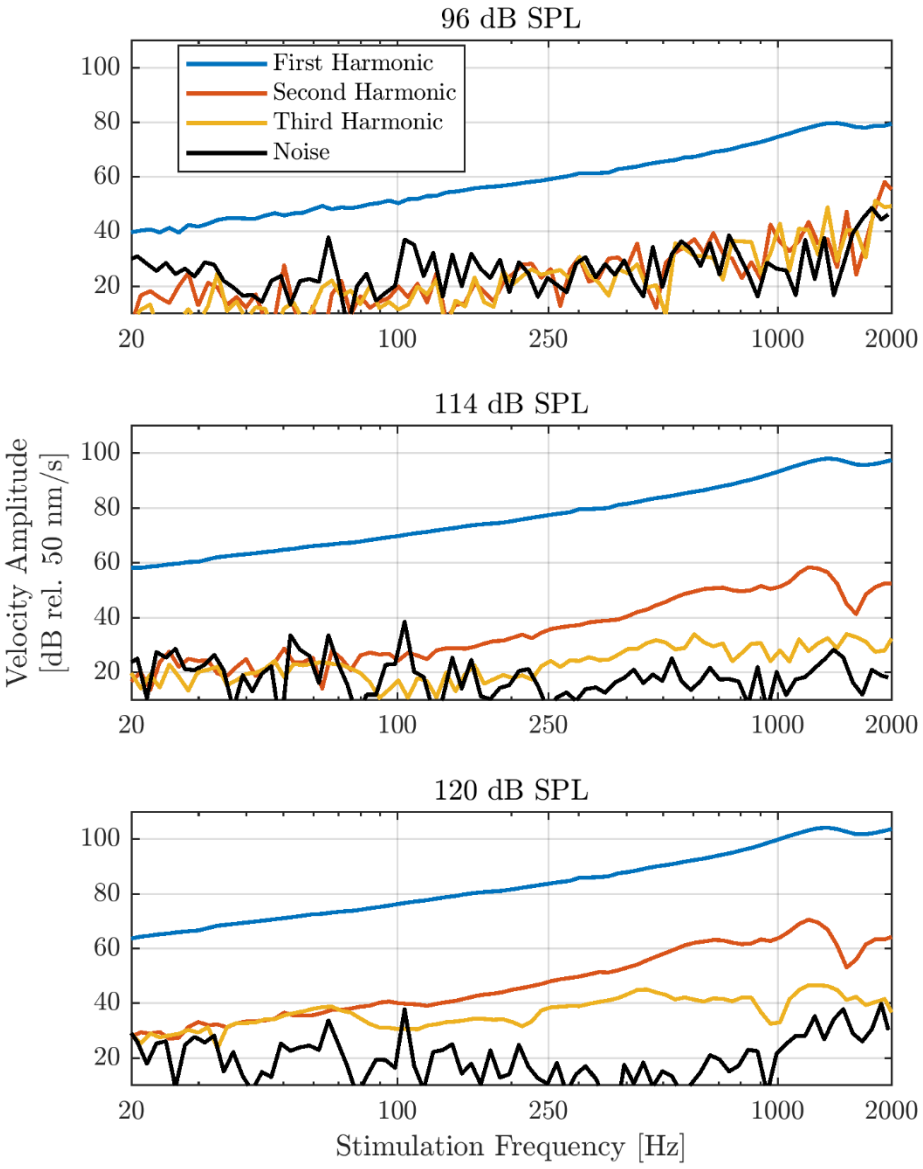

Figure 5.24: Linear and nonlinear response as a function of frequency for different sound pressure levels.

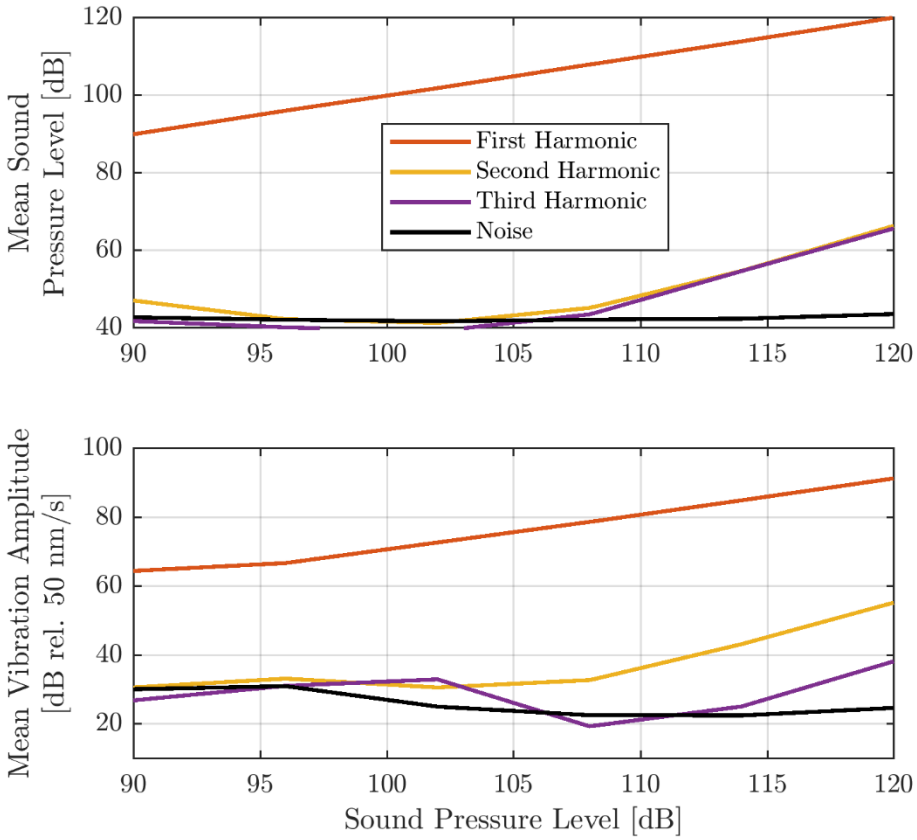

Figure 5.25: Sound pressure level (TOP) and vibration amplitude (BOTTOM) averaged over all stimulation frequencies (blue), second harmonics (red) and third harmonics (yellow).

Discussion

Even though the sound stimulation contains nonlinearities at high sound pressure levels, the vibration level at the second harmonic originates shows that the ME behaves nonlinearly. We observe again that the even degree nonlinearities are larger than the odd degree nonlinearities. This confirms the measurement results on the curved rubber membrane (section 5.5) and the simulations on the curved membrane (section 5.6).

The frequency resolution in this experiment is low compared to that of the multisine measurements in section 5.7.1. In those experiments, we found a negative shift of the resonance frequency of about -7.5 to -9% at about 120 dB SPL. Here we observe a negative shift of about -5.6399% as from 114 dB (figure 5.26). Due to the limited resolution, the backbone curve has a very discrete character. We have an inaccuracy of about 2.5%,

which means the values measured here could fall within the range of the values measured using multisine stimulation.

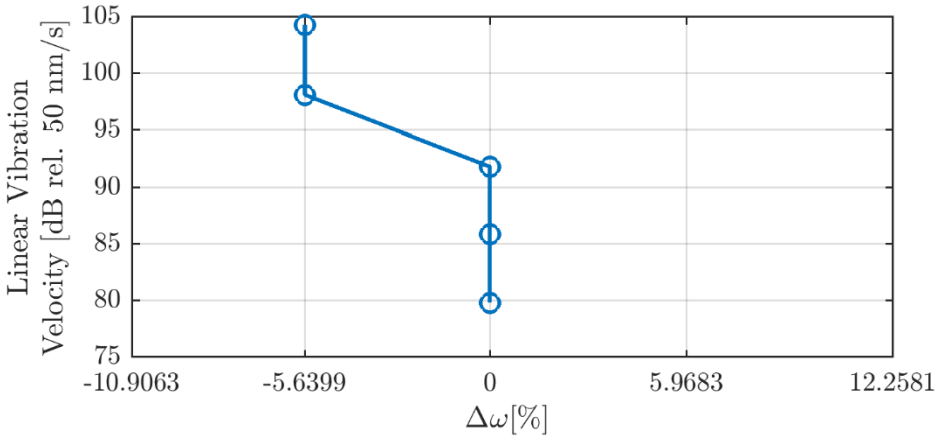

Figure 5.26: Backbone curve of the human ME measured using single sine stimulation. The vertical gridlines are determined by the frequency resolution used during measurements.

In conclusion, independent of the stimulation type, the same observations are made regarding the nonlinear behavior of the ME. The ME softens with increasing sound pressure level, resulting in a reduction of the first eigenfrequency. The abundance of even degree nonlinearities is larger than those of odd degree nonlinearities. This correlates well with nonlinear behavior observed for curved membranes.

5.7.3 Measurement using digital image correlation

Whole chapter 7 will be dedicated to digital image correlation and strain measurements. However, with the same technique, we acquired displacement measurements in a human TB at high sound pressure levels. For this reason, we will discuss the results of those measurements here. Details on the experimental setup will be described in chapter 7 instead.

Measuring displacements instead of velocities allows us to evaluate the DC-component of the TM when subjected to high sound pressure levels. In section 5.2.1, we hypothesized that if the dynamic nonlinearities obey similar pressure-displacement relationships as for static behavior, we should be able to detect a net lateral displacement.

Measurements will be performed at 10 and 1000 Hz at 140 and 145 dB SPL respectively.

Results & discussion

The displacement at a frequency of 10 Hz as a function of time shows that the umbo does not oscillate around its resting position as shown at the top of figure 5.27. Instead, it oscillates around -46 µm. This means that at high sound pressure levels, the TM shows a net lateral displacement. We discussed in section 5.2.1. that at static pressures it easier to displace the TM laterally than medially. Therefore, we concluded that if the dynamic nonlinear behavior would be similar to static that the TM at high sound pressure levels would center its oscillation around a lateralized position. This is exactly what we observe.

We were not able to achieve a clean sound signal as seen on the bottom graph of figure 5.27. However, the ratio between the linear and nonlinear components of the measured sound pressure level is larger than for the measured displacement. This proves that the TM generated nonlinear distortions itself and that the vibration components at the higher harmonics are not merely an artifact due to the nonlinearity of the speaker. If we evaluate the ratio of the vibration amplitude at the harmonics to that of the first harmonic and subtract this by the ratio of the sound amplitude at the harmonics to that of the first harmonic (stimulation frequency), we get an estimate of the relative nonlinearity of the TM. This is illustrated in figure 5.28. We observe again that the even degree nonlinearities are larger than the odd degree nonlinearities. This suggests again that the nonlinear behavior stems from the curved shape of the TM.

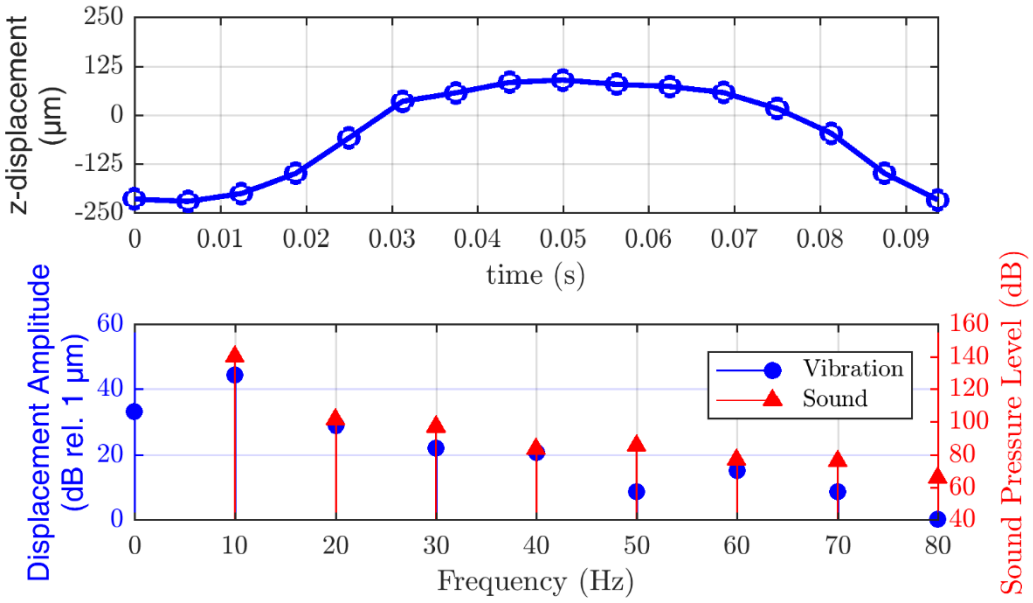

Figure 5.27: Displacement of the umbo as a function of time (top). Frequency spectrum of the measured displacement (bottom – blue) and applied sound pressure level (red). The applied sound pressure level was 140 dB SPL at a frequency of 10 Hz.

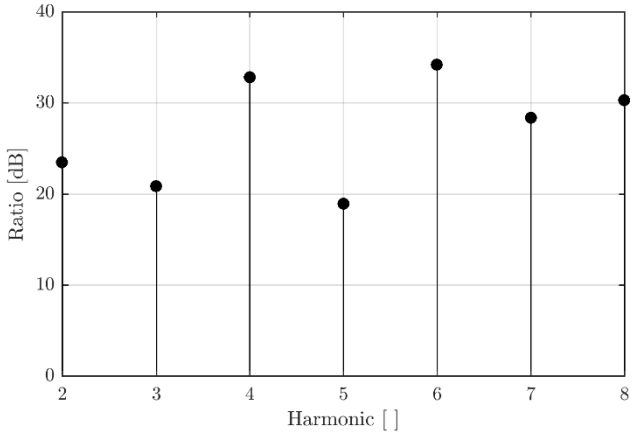

Figure 5.28: The ratio of the vibration amplitude at each harmonic to that of the first harmonic subtracted by the ratio of the sound amplitude at each harmonic to that of the first harmonic (stimulation frequency). A positive value indicates that the nonlinearity of the TM was larger than that of the speaker. The even degree nonlinearities are systematically higher than odd degree nonlinearities.

Figure 5.29 shows the z-displacement as a function of time and its frequency spectrum for a stimulation frequency of 1000 Hz at 145 dB SPL We see again that the oscillation of the umbo occurs around a lateralized position (-25 μm) compared to the resting state. Only a small preference for even degree nonlinearities is observed.

In conclusion, the DIC method allowed us to verify another quality of nonlinear behavior of the TM at high sound pressure levels; the oscillation of the TM around a lateralized position. We assume that the behavior at frequencies above the ME's first resonance frequency can be different. Additional measurements in such frequency regions would be interesting.

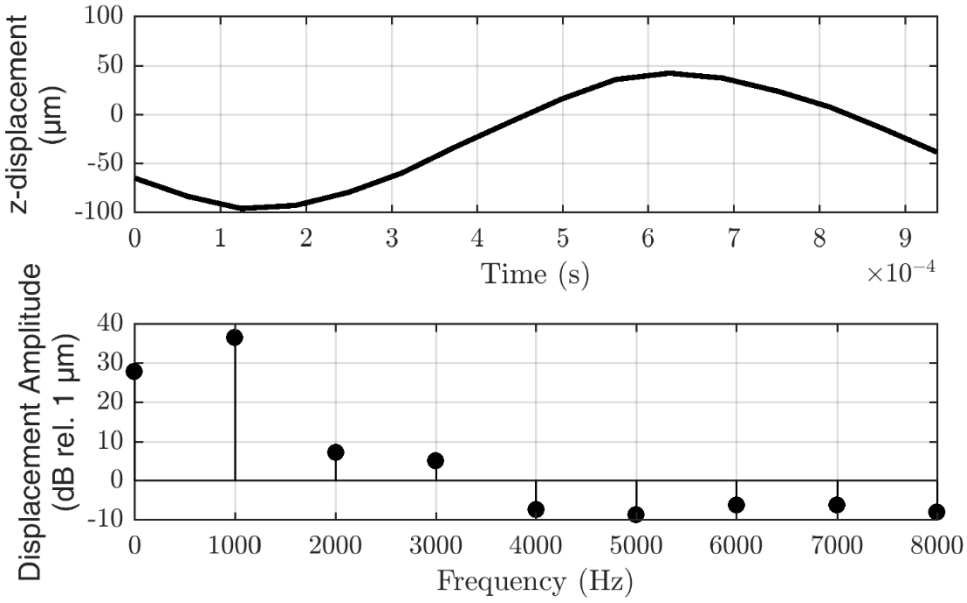

Figure 5.29: Displacement of the umbo as a function of time (top) and frequency spectrum of the measured displacement (bottom). The applied sound pressure level was 145 dB SPL at a frequency of 1000 Hz.

5.7.4 Human ME nonlinearity modeling

We will now replicate the experiment in the previous section using the FE model we described in section 4.4.4. A uniform load will be applied with an equivalent sound pressure level of 145 dB at a frequency of 1000 Hz. And the frequency response will be calculated for different sound pressure levels ranging from 91 dB (1 Pa peak) to 163 dB (4000 Pa peak). The model will only include geometric nonlinearity.

Results and discussion

When simulating at 1000 Hz at 145 dB SPL, we immediately observe that the umbo oscillation is much more symmetrical compared to the experimental data from the previous section (figure 5.30). The level of medial displacement is very similar, but the lateral displacement deviates about a factor 2 from the experimental result. The vibration spectrum shows that the net lateral displacement is almost 20 dB smaller, which is a factor 10! The second and fourth harmonics are larger than the experimental case, but all the other harmonics are smaller.

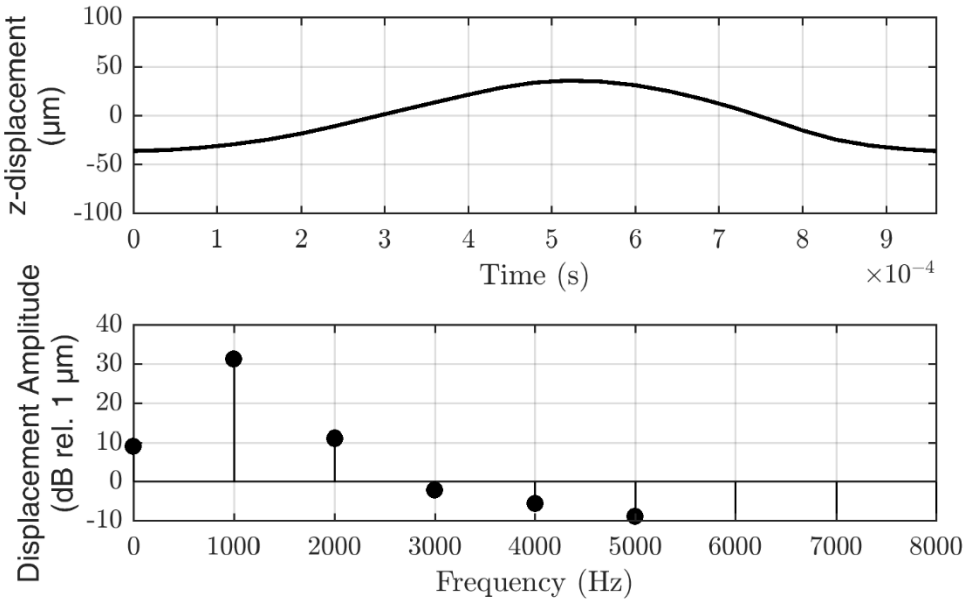

Figure 5.30: Displacement of the umbo as a function of time (top) and frequency spectrum of the measured displacement (bottom). The applied sound pressure level was 145 dB SPL at a frequency of 1000 Hz.

If we calculate the frequency response and backbone curve for different sound pressure levels, we see a deviation from the experimental results once again (figure 5.31). The magnitude of the FRF diminishes with increasing SPL, which is unexpected, and although the shape of the frequency response changes, there is no clear trend showing softening behavior as seen on the backbone curve.

In summary, we find that the TM of our FE model does not displace as easily laterally compared to experiments. This reduces the amplitude of the linear component of the oscillation. It also reduces the DC-component and higher harmonic content. On top of that, it means there is no softening behavior. We hypothesized that the shape of the TM would be the main factor that would result in the aforementioned nonlinear behavior. However, there must be another reason why the TM is allowed to displace so easily in the lateral direction.

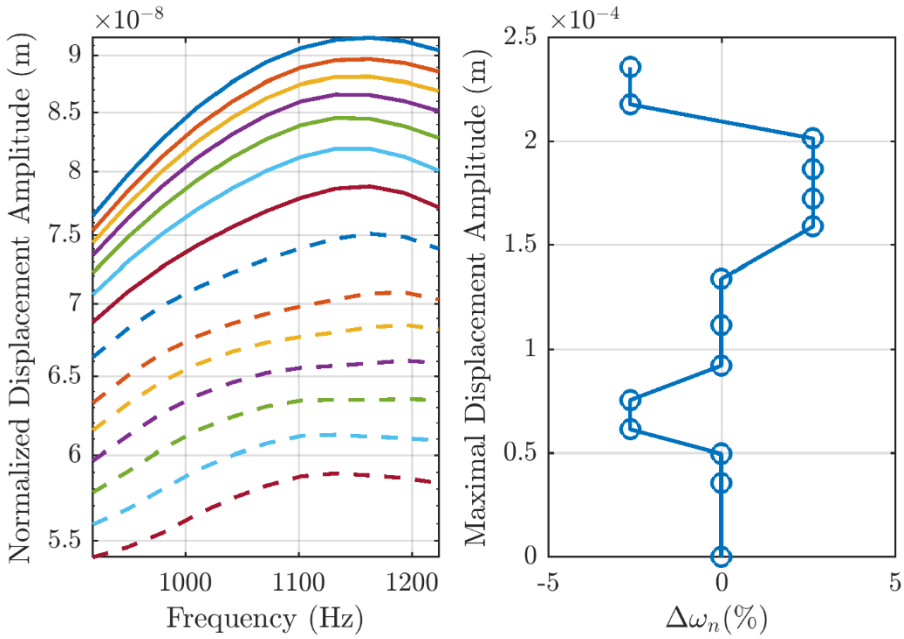

Figure 5.31: Normalized frequency response (left) and backbone curve (right) of the finite element model of the human middle ear. The top frequency response curve was retrieved using a 1 Pa acoustic pressure. The bottom curve used a 4000 Pa acoustic pressure.

5.8 Other sources of ME nonlinearity & stimulation methods

In section 5.2, we concluded that the TM was a probable source of nonlinearity based on the observations by Dirckx and Decraemer (2001). Nonlinear behavior is still present after removing the cochlea, stapes and incus. However, this does not mean that these removed components cannot contribute to the nonlinearity of the ME. In fact, there exists an upper limit to the movement of the stapes (Price, 1974). Such a hard limit on stapes displacement introduces a high level of nonlinearity at very high sound pressure levels. However, this limit occurs at about 25µm. Such stapes displacement magnitudes require much higher sound pressure levels than those used in our experiments. It would be interesting to conduct a similar experiment to Dirckx and Decraemer (2001) but for dynamical nonlinearity.

In this chapter, we made use of single and multisine stimulation to evaluate nonlinear behavior. Another option is Gaussian white noise. To describe the nonlinear system, Wiener series are used. Such Wiener series are closely related to Volterra series which are able to describe nonlinear systems with memory effects. It is similar to Taylor series, only Taylor series can predict the output of a nonlinear system at one specific time based on

the input, Volterra series can predict the output at any requested time. However, according to Johnson (1980) it is tedious to apply this method to the auditory system.

5.9 Conclusion

In this chapter, we discovered the human ME does not behave linearly at high-intensity sounds. However, it is only weakly non-linear, and the assumption of linearity can still be used in many applications. We found three main characteristics of the dynamic nonlinear behavior of the ME:

1. The TM will displace more easily laterally than medially. As a consequence, the TM oscillates around a lateralized position instead of its resting position when subjected to high-intensity sounds.
2. Due to the asymmetric motion of the oscillation, the distortion components contain more even degree nonlinearities than odd degree nonlinearities.
3. The ME is a softening system. The resonance frequency decreases as the displacement magnitude increases.

Such properties can all be attributed to the curvature of a membrane. A lack of curvature will cause symmetric oscillations at high sound pressure levels. The mechanical system will harden instead of soften. For this reason, it seemed obvious that the shape of the TM would be the cause of this nonlinear behavior. However, the FE model lacks all the properties we discovered using our experimental techniques. There must be another factor that facilitates lateral displacements of the TM.

Chapter 6:
MALLEUS FRACTURES

Abstract

In this chapter, we have another modeling case of which the results will not match up with experimental data. Cases of isolated malleus handle fractures are rare and easily missed, making clinical studies difficult to organize. Recently, an ex-vivo study on malleus handle fracture was published. In the present study, numerical modeling is used to expand our understanding of this injury. Different finite element models were developed based on two human temporal bones. In each model, a fracture was introduced in the malleus handle at one of three different positions. Stapes footplate (SFP) velocity ratios predicted by the models with only a fracture do not match up well with the experimental data. Therefore, we made alterations of the model to try and find what was missing from the model. Interestingly, this missing link could be the same property our model was lacking in chapter 5.

This chapter is based on:

Gladine, K., Muyshondt, P., De Greef, D., Dirckx, J. 2018. Effect of Malleus Handle Fracture on Middle Ear Sound Transmission: Laser Doppler Vibrometry Measurements and Finite Element Simulations. Proceedings of The International Conference on Experimental Mechanics2018 2, 1-5.

6.1 Introduction

With less than 80 reported cases since 1855 (Blanchard et al., 2011), it can be said that isolated malleus handle fractures (in literature) are fairly uncommon. The diagnosis appears to be difficult as the symptoms vary a lot (Niklasson et al., 2016). For this reason, it is highly probable that a lot of malleus fracture cases are missed or misdiagnosed. Due to the limited amount of clinical cases and difficult diagnosis, it is hard to perform a clinical study to investigate the effectiveness of different treatment methods. Despite the low abundance of patients, the consequences of malleus fractures on those individuals should not be disregarded as hearing losses up to 45 dB can occur (Chien et al., 2008).

Even though the amount of reported clinical cases of malleus fractures is limited, a great number of them have the same cause: digital manipulation of the ear canal during or after a shower (Chien et al., 2008; Hato et al., 2007; Iurato and Quaranta, 1999; Niklasson and Tano, 2010; Pedersen, 1989; Punke and Pau, 2006). Presumably, inserting a finger in and retracting it from a wet ear canal suddenly creates a high negative pressure in the ear canal. This negative pressure exerts a large lateral force on the tympanic membrane and malleus handle. It is hypothesized that the tendon tympani counteracts with a force in the medial direction. This sudden combination of forces exerted on the malleus handle causes it to fracture. Immediately after, a pain is felt, and a decreased hearing ability is observed. The pain disappears but the hearing loss remains. In almost every case, the tympanic membrane does not rupture. However, it does not fully retain its shape either. The TM can show an irregular contour of the manubrium (Blanchard et al., 2011; Chien et al., 2008; Hato et al., 2007; Ozturk and Uneri, 2009)and sometimes the tympanic membrane becomes wrinkled (Hato (2007), Chien (2008), Niklasson[3]). When using pneumatic otoscopy, a hypermobile umbo is observed. In some cases, high-resolution CT showed that both fragments of the fractured malleus were displaced with respect to one another and their original anatomical position. The superior fragment was lateralized, while the inferior fragment was medialized (Blanchard et al., 2011; Delrue et al., 2015; Sy A., 2017; Tan M., 2015). This suggests the existence of a force pulling on the malleus (and tympanic membrane) from the medial side. Once the malleus is broken, the force on the malleus fragment disconnected from the middle ear chain is lost, and it displaces to a new resting position for which the TM is wrinkled. This suggests a loss in TM pretension after a fracture. However, to our knowledge, there is no data available in literature on the amount of TM pretension and its source for an intact human middle ear.

[3] Confirmed in personal communication by A. Niklasson on 14th of April 2017. Including the cases for which the fractures were made in a controlled manner in temporal bones.

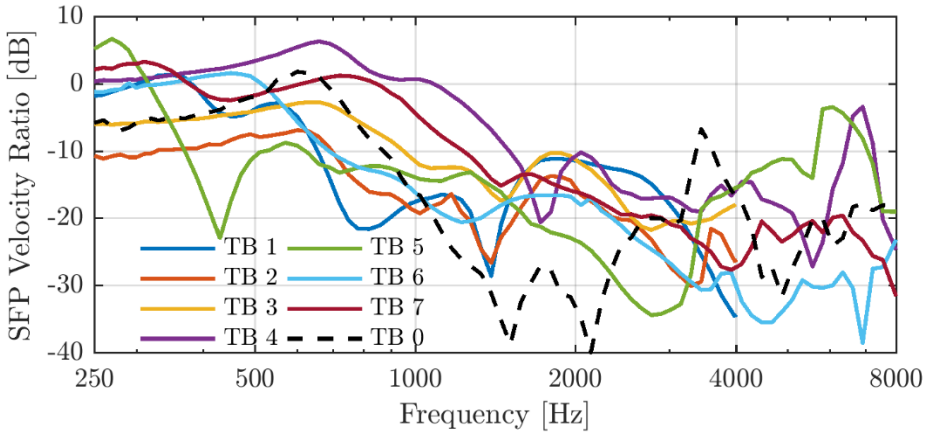

Figure 6.1: Ratio of the stapes footplate velocity amplitude of middle ears with malleus fracture to healthy ears. TB0 has had three consecutive fractures; all the other TBs only had one fracture just inferior to the tendon tympani.

As clinical trials to investigate the optimal treatment procedures in case of malleus fracture are difficult to organize due to the limited amount of clinical cases, Niklasson et al. (2016) performed a temporal bone study. In this study, the stapes footplate velocity was measured from the medial side using laser Doppler vibrometry, before and after creating a malleus fracture using a back-biting forceps. They showed that cementing the fracture resulted in a slightly better recovery than a partial ossicular replacement prosthesis. We will try to increase our understanding of malleus fractures by a comparison of finite element modeling results to this study. But first, let's look at what else we can discover from the study itself.

For TB0, fractures were made at three different positions. The ratio of the SFP velocity before fracture to that of after the fracture correlates to the hearing loss and is shown in figure 6.5. We see that velocity loss increases when the fracture is placed more superiorly. However, keep in mind that all fractures were performed on a single TB; when the distal fracture was made, only one fracture was present. When the proximal fracture was made, three malleus handle fractures were present. The minimal loss for superior fractures occurs at lower frequencies. In fact, a gain is observed for some frequencies. In clinical cases, umbo velocity measurements have shown to be larger at lower frequencies in case of malleus fractures (Chien et al., 2008). It is as if the middle ear system's stiffness has been reduced and therefore the resonance frequency has decreased and consequently the ME has become more mobile at lower frequencies. Our hypothesis is that a higher stiffness reduction is achieved for more superiorly located fractures.

Based on these findings, we can adjust our available ME FE models to investigate the effect of malleus fractures on the stapes velocity response. We can then compare our results to those found experimentally by Niklasson. The data by Niklasson was obtained on TBs without cochlea. We will also simulate the clinical case for which a cochlear load is present.

6.2 Methods

6.2.1 Malleus handle fracture models

The base models which will be adapted to include malleus handle fractures were described in section 4.4.4. In the two models, malleus handle fractures were simulated by removing a small volume of material from the malleus. This was done after importing the geometry of the intact middle ear model into Comsol. Two planes perpendicular to the manubrium and 10 μm apart from each other were used to partition the malleus geometry. After partitioning the domain, the small volume with a length of 10 μm along the manubrium was removed from the model. The effect of decreasing gap width was tested using gap widths between 10 and 2 μm. Stapes footplate velocity changed less than 6% at all frequencies, with a change of about 1% on the average. As some clinical cases of malleus fractures were detected using clinical CT scans, we can assume the gap width is larger than the displacements and possible mechanical contact should not be taken into account. The fracture was positioned at three locations (Figure 6.2): either at 1 mm from the umbo, at 2 mm from the umbo, or just inferior to the location of attachment of the TT tendon (infTT). The distance from the infTT fracture to the umbo differed between the two models: 2.20 mm (model 1) and 2.45 mm (model 2). In any model, either no or one fracture was introduced, never more than one.

The deformation and occasional wrinkling of the TM observed in clinical cases was not taken into account directly. The geometry the tympanic membrane was unaltered. However, as mentioned in the introduction, such deformation and wrinkling suggest a release in TM tension. Additional models were made by crudely mimicking this tension release utilizing a lower TM Young's modulus. For 1 mm, 2 mm and infTT fractures, the Young's modulus of the pars tensa (PT) was reduced by a factor of 2, 2.5, and 3, respectively.

Note:

> *As no data about TM pretension, lowering the TM's Young's modulus is nothing more than a reasoned guess. The reduction factors of 2, 2.5, and 3 for 1 mm, 2mm, and infTT fracture, respectively, were chosen arbitrarily. However, it is interesting to see if these models including a crude mimicking of TM tension release correlate more with the experimental data than the models with only a fracture.*

The SFP velocity ratio of the fractured model to the intact model was compared to experimental results from Niklasson et al. (2016). In that study, laser Doppler vibrometry was used to determine the effect of malleus handle fracture and different reconstructive interventions on the SFP velocity. In these experiments, the cochlear fluid was drained from the inner ear for practical reasons, so that the cochlear impedance was essentially eliminated. Therefore, the model was evaluated without a cochlear impedance so that a meaningful comparison with the experiments could be made. After this, a cochlear impedance was added to the model in order to investigate clinically relevant scenarios.

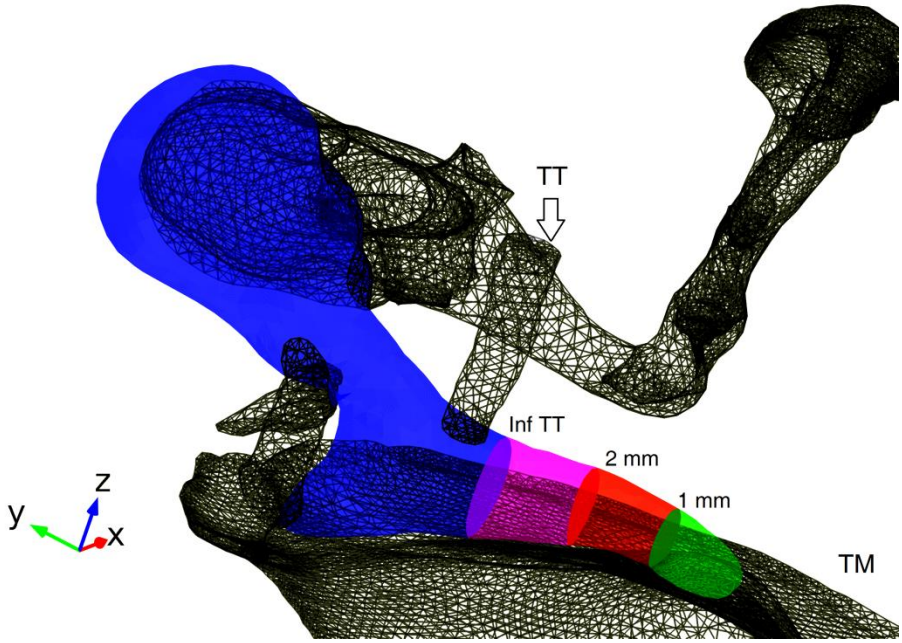

Figure 6.2: Finite element model of the human middle ear. The colored parts indicate at which locations fractures were simulated.

6.2.2 Stimulation

In all scenarios, the stimulating load on the model was a direct, uniform, harmonic pressure of 1 Pa peak amplitude on the lateral side of the TM to simulate incident acoustic waves. A frequency-domain analysis was carried out, sweeping over 74 frequencies between 0.1 and 10 kHz. The 74 frequencies were divided into three frequency ranges ([100,500]; [500,1260]; [1260,10000] Hz) with each a number of 6, 25 and 43 quasi-logarithmically spaced frequencies rounded up or down to a multiple of 10 Hz.

6.3 Results

6.3.1 Fracture just inferior to the tensor tympani tendon

Stapes footplate velocity ratios without cochlear impedance

The SFP velocity loss due to an infTT malleus handle fracture was measured for eight different TB's in Niklasson et al. (2016). Above 4 kHz, data for only five of the eight TB's were obtained (figure 6.1). This data is compared to the model results for the infTT fracture models.

We included the data of sample 3 and 4 in figure 2, which we will compare to the simulation data. The fractured models without pre-strain reduction (1A and 2A) show an

SFP velocity ratio of about -8.5 dB below 500 Hz (Figure 6.3) which is lower than most experimental data. The first local maximum occurs at around 1100 Hz with ratio values of -2.5dB and -4.3dB for model 1A and 2A respectively. The experimental data exhibits maxima at lower frequencies. Above 1100 Hz, a steep decrease is observed. At around 2000 Hz, the velocity ratio increases again, almost reaching the same levels as the first local maximum. Between 2000 Hz and 4000 Hz, the ratio is about -10dB, which is a higher ratio than seen for the TB data. A dip occurs at around 5 kHz, after which the ratio increases again, such dip and increase are also visible for TB4 around 5 kHz. The SFP velocity ratio is negative at all frequencies, which is not the case for TB4-7.

The fractured models with pre-strain reduction (1B & 2B) have a higher SFP velocity ratio at low frequencies of about -6dB. The local maximum occurs at around 700 Hz. At this local maximum the velocity ratio becomes positive, showing ratios of about +2dB. At higher frequencies, a steep decrease is observed to values of -16 to -20dB for model 1B and 2B respectively. After this dip, the ratio increases again to a new local maximum at around 1600-1750 Hz to ratio values of -2.5 and -7.5dB (model 1B and 2B respectively). Above 1600-1750 Hz, the ratio drops further to values of about -20dB.

Without going too far in-depth, we can conclude that the models without mimicking pre-strain reduction do not match the experimental data very well. The loss at low frequencies is too high. The frequency of the least change in SFP velocity ratio is too high. In fact, it occurs at the resonance frequency of the model. For this reason, the models without pre-strain reduction will not be shown in further graphs.

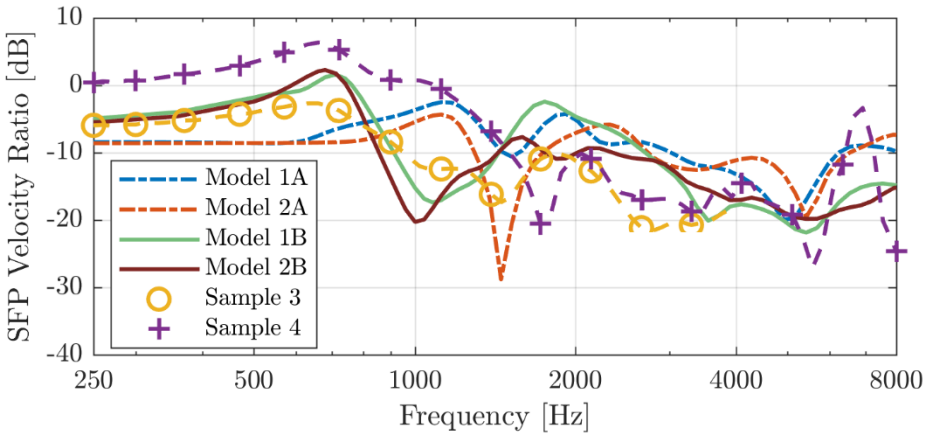

Figure 6.3: Stapes footplate velocity ratio of middle ear models and temporal bones with fractured malleus to that of middle ears without fracture.

Umbo hypermobility: Umbo velocity response (with cochlear impedance)

A common feature of ears with malleus handle fracture is that the umbo is hypermobile. The umbo velocity of the models with an infTT fracture and with cochlear impedance is

compared to experimental data (Chien et al., 2008) in figure 6.4. The in-vivo results are very diverse, but the majority shows an increase in umbo velocity below 2 kHz. Case 2 of the in-vivo study resembles the models the most. Maximum umbo velocity is reached at a frequency of 0.7 kHz. After this maximum, a decrease in velocity is present. For most frequencies, umbo velocity is greater for the fractured model compared to the intact model. This is not the case for the experimental data, which is compared to an average umbo velocity curve in patients with intact middle ears. For these cases, umbo velocity drops below the intact curve starting from 3 kHz or lower.

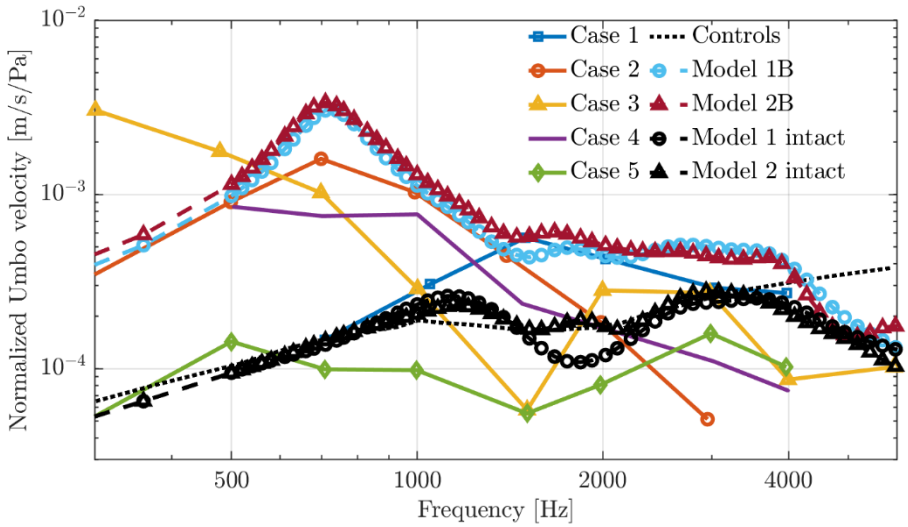

Figure 6.4: Comparison of umbo velocity amplitude of clinical data of intact middle ears and cases of malleus fractures and our models.

6.3.2 Different fractures

Stapes footplate velocity ratios without cochlear impedance

For one TB, Niklasson et al. (2016) reported SFP velocity ratios for three different fracture positions: 1 mm from the umbo, 2 mm from the umbo and just inferior to the TT (infTT). Therefore, we calculated the SFP velocity for our two models for these three fracture positions. For these simulations, no cochlear impedance was included in the model, similar to the experimental conditions. Unlike the experiment, the models exhibit only one fracture at a time. In the experiment, all measurements were done sequentially, meaning that the infTT result was obtained from a TB with three fractures. A comparison of the SFP velocity loss between experiment and simulation is presented in figure 6.5.

The experimental data are available from 0.25 to 8 kHz, whereas the model results were evaluated from 0.1 to 10 kHz. For all curves, at most frequencies, a velocity loss is observed after fracturing the malleus.

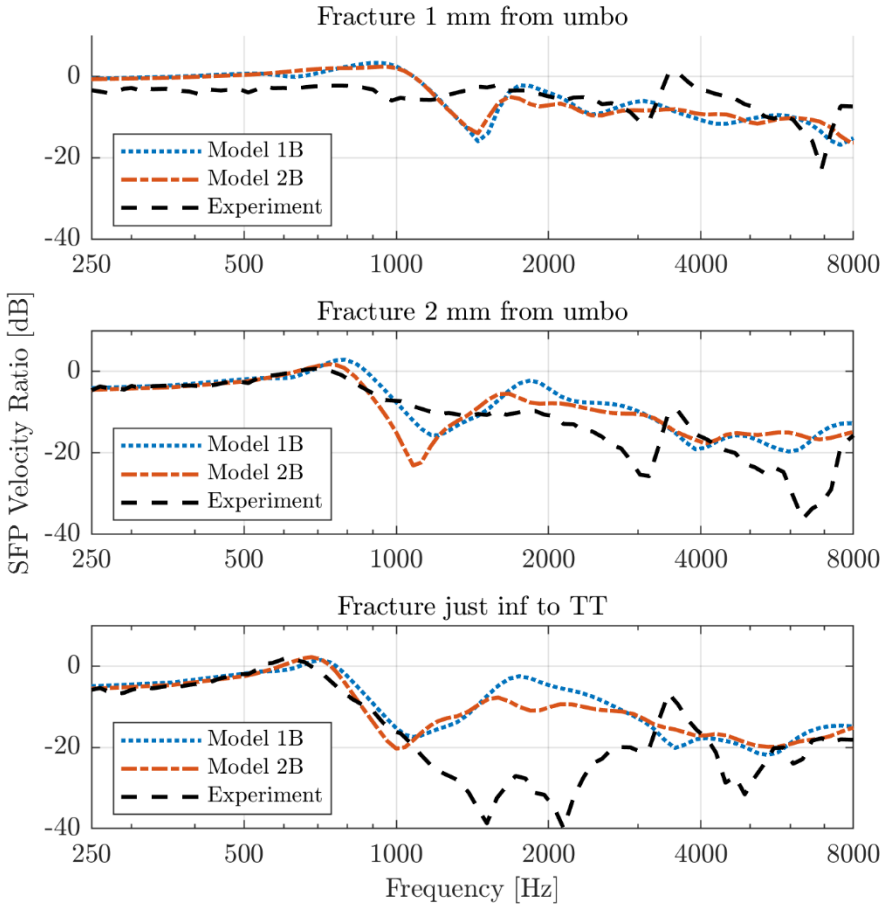

Figure 6.5: Stapes footplate velocity ratio of middle ear models and temporal bones with fractured malleus to that of middle ears without fracture for different fracture positions.

For a fracture at 1 mm from the umbo, the experimental curve has a constant velocity ratio of about -3 dB below 0.8 kHz. The models show a velocity ratio between -1 dB and 2 dB. Between 1-3 kHz, the experimental velocity ratio stays fairly smooth and constant within a range of -3 to -10 dB. In contrary, the models show a minimum at 1.5 kHz. Between 3-4 kHz, the experimental curve shows a local maximum, which is not present in the model curves. At higher frequencies, the velocity ratio decreases again until 7-8 kHz. Over the range of 0.25-8 kHz, all model curves stay within +3.3 to -16.8 dB. The SFP velocity ratio of the experimental curve ranges from 0.9 dB to -22.7 dB.

For the 2 mm fracture, the experimental data exhibits a velocity ratio of -5 dB below 0.75 kHz. A global maximum is seen at 0.75 kHz, and the velocity ratio becomes positive, reflecting a boost in this frequency region. The models show a velocity ratio of -5 dB at

the lowest frequencies and a maximum at 0.8 kHz. After the maximum, all curves show a roll-off as a function of frequency. However, the roll-off of the experimental curve is more subtle. The experimental curve shows a plateau between 1.2-2 kHz, while the model curves recover from their local minimum. Both experiment and model show a dip at 3 and 4 kHz, respectively. At higher frequencies, the experimental data shows a roll-off until another dip is reached around 6 kHz, after which the velocity ratio rises again. In contrary, the model SFP ratio remains fairly constant.

For the infTT fracture, the experimental curve remains similar to the curve of the 2 mm fracture for frequencies between 0.25-0.8 kHz. The maximum is slightly higher in amplitude and slightly lower in frequency compared to the 2 mm fracture. For the models, the frequency of the maximum also decreases compared to the 2 mm fracture, while an increase of the corresponding amplitude is only observed for Model 2. After its maximum, the experimental curve now shows a roll-off and reaches a value of -38 dB. A small increase is present at 1.5-2 kHz. Just beyond 2 kHz, the SFP velocity ratio decreases to a minimum value of -40 dB. The models show a strong roll-off just after the maximum but then show a local maximum between 1.5-3 kHz. The local maximum can reach values of almost -2 and -7 dB (model 1 and 2 respectively), and the ratios are not less than -20 dB in this frequency range. The experimental data shows a local maximum between 3.5-4 kHz with an amplitude of about -10 dB as with the 2 mm fracture. After this local maximum, the behavior of the infTT curve is similar to the 2 mm curve. The models have a small local maximum at about 4 kHz and resemble the experimental data at higher frequencies.

Quantification of the difference between the experimental and model results is done by calculating the mean absolute difference between model results and measured values of SFP velocity ratios for different frequency bands (table 6.1).

Fracture type	**Frequency band**	**Model 1**	**Model 2**
1 mm	0.25 – 0.5 kHz	3.3 dB	3.1 dB
	0.5 – 4 kHz	4.4 dB	4.4 dB
	4 – 8 kHz	4.2 dB	3.9 dB
	Overall (0.25 – 8 kHz)	4.2 dB	4.1 dB
2 mm	0.25 – 0.5 kHz	0.3 dB	0.3 dB
	0.5 – 4 kHz	4.7 dB	4.3 dB
	4 – 8 kHz	8.4 dB	9.2 dB
	Overall (0.25 – 8 kHz)	4.4 dB	4.3 dB
InfTT	0.25 – 0.5 kHz	1.0 dB	0.6 dB
	0.5 – 4 kHz	11.3 dB	9.9 dB
	4 – 8 kHz	4.5 dB	4.4 dB
	Overall (0.25 – 8 kHz)	7.8 dB	6.8 dB

Table 6.1 Mean absolute difference between model results and measured values of SFP velocity ratios for different frequency bands.

Stapes footplate velocity ratios with cochlear impedance

When running the models with (as opposed to without) a cochlear impedance, the absolute values of the SFP velocity magnitude changed substantially for certain frequencies (up to 14 dB difference), but the velocity loss after malleus handle fracture changed on average less than 0.4 dB for all fracture positions and at the most 2.8 dB for the 2 mm fracture.

Figure 6.6 shows a comparison between the SFP velocity ratios with and without cochlear impedance for the model (with intact malleus and infTT fracture) and the experimental data obtained by Gan et al. (2004). In the low-frequency range between 250Hz and 500 Hz the model gives nearly no difference between intact and removed cochlea, while the measurements show a small increase in SFP mobility of about 2 dB after cochlea removal, but the differences between model and measurement are very small. In the higher frequency range, similar trends are seen between model and measurement when the cochlea is removed: in the frequency band between 2kHz and 4kHz removal of the cochlea leads to increased SFP vibration amplitude. For the model, the average increase in this frequency band is 7.65 dB, in the experiments this increase is about 7.72 dB. The ratio of the models starts to increase faster at a lower frequency of 1.5 kHz compared to the measured data (2 kHz). Overall, the effect of the cochlear impedance is very similar for experiments and all models, including the fractured models.

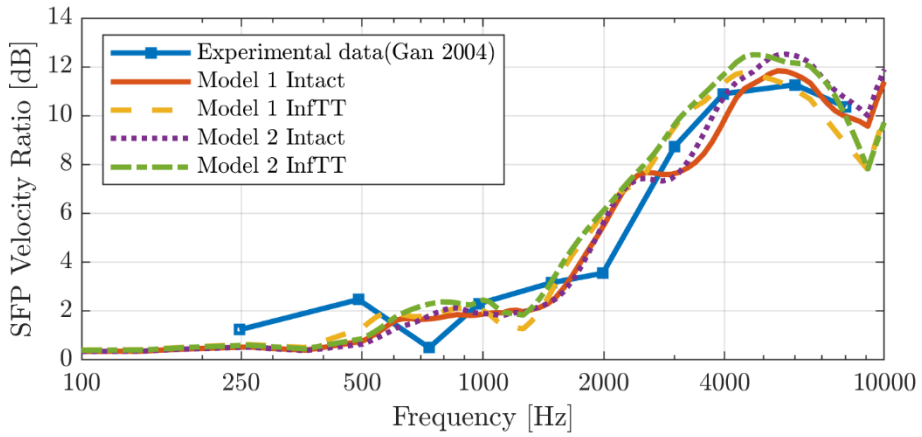

Figure 6.6: Comparison of experimental and simulation data of stapes footplate velocity ratios of ears with removed cochlea to that of ears with intact cochlea.

Tympanic membrane motion (without cochlear impedance)

The effect of fracture on the TM displacement patterns is presented in figure 6.7. The largest difference occurs at low frequencies where the maximal displacement shifts from the posterior region to the inferior region. This shift becomes more evident when the fracture is located further from the umbo. At higher frequencies, the TM displacement

pattern becomes more complicated for the 2 mm and infTT fractures due to lowered stiffness of the PT.

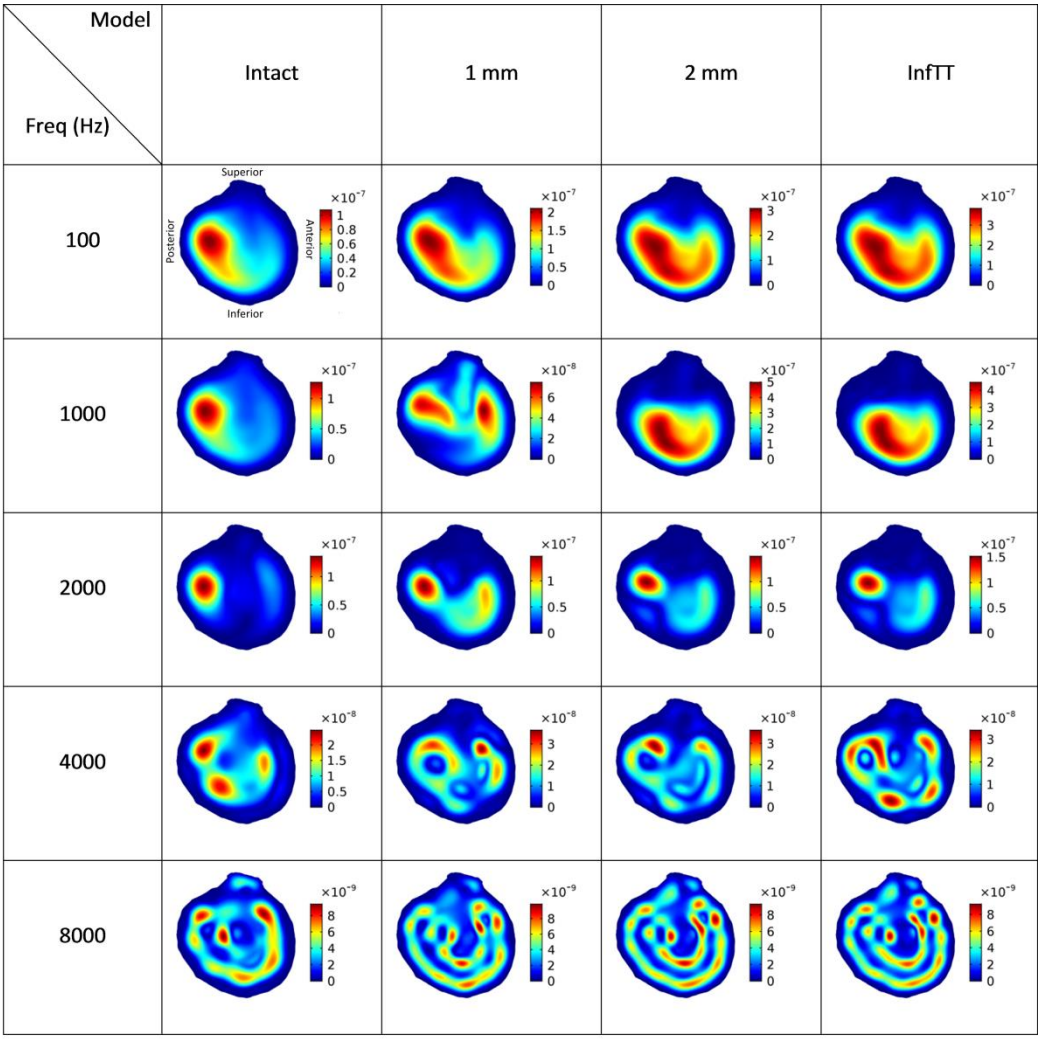

Figure 6.7: Tympanic membrane displacement patterns at different frequencies for models with intact and malleus fractures at various positions on the manubrium.

6.4 Discussion

In De Greef et al. (2017), the FE model of the ME with malleus intact was validated and compared to experimental data from TB measurements. It was concluded that the model represented the measured vibration response adequately at most frequencies, with the largest discrepancy between 2 and 4 kHz.

6.4.1 Fracture just inferior to the tensor tympani tendon

The measurements presented in figure 6.1 have shown that malleus fractures can cause tremendous hearing losses almost up to -40dB at some frequencies. The losses are minimal at low frequencies and mainly increase with increasing frequency. Two things stand out:

1. The global maximum usually occurs at a few hundred Hertz below the middle ear resonance frequency, which is typically around 1-1.2 kHz.
2. The SFP velocity ratio can be positive and is close to 0dB for most samples at low frequencies.

Both of these observations seem to be due to a shift of the middle ear resonance frequency to lower frequencies after a fracture. If the resonance frequency is lowered, the local velocity ratio maximum will be present at this new resonance frequency, and a steep decrease will occur at higher frequencies. The velocity ratio will also be boosted at frequencies below this new resonance frequency. The lack of contact between the broken malleus parts will thus produce an overall loss in transmission which can be (partly) countered at low frequencies by this resonance shift.

Simulations without the mimicking of pre-strain reduction do not show such properties. The maximal velocity ratio occurs at the original resonance frequency of the model. The velocity ratio at low frequencies is also comparable to the lowest observed in the experimental study. No resonance shift is present for this model. This suggests that the resonance shift present in the experimental data is a consequence of something else than just the separation of the two malleus handle pieces. The most likely possibilities are then the change in TM pre-strain and or TM shape change. Additionally, the local maximum at 2 kHz is too large and decrease at higher frequencies is too small.

Simulations with pre-strain reduction mimicking show an increased SFP velocity ratio at lower frequencies and a global maximum below the original resonance frequency due to a resonance shift to lower frequencies. However, the local minimum occurs at a too low frequency, and the local maximum at around 2 kHz is still too large. At frequencies higher than 2 kHz, the achieved velocity ratios resemble the experimental data a bit more, reaching levels of -15 and -20dB before 4 kHz.

It is clear that the models are not yet in good agreement with the experimental data. However, it has been shown that the effect of a malleus fracture on the sound transmission is caused by more than just the separation of the two broken parts of the malleus handle. A slightly better agreement was achieved by crudely mimicking release of TM pretension. It is possible that the change in shape after fracture also plays an important role.

6.4.2 Different fracture positions

A comparison was made between simulations and experiments for different types of fractures (figure 6.3). A reasonably well agreement was found for the 1 and 2 mm fracture, with an average absolute difference of 4.1-4.4 dB between experiment and simulation. For the infTT fracture, the discrepancy between the SFP velocity ratios of the model and

experiment was higher, with an average absolute difference of 6.8-7.8 dB. Especially in the frequency range of 1.5-3 kHz, the model does not predict equally high velocity loss. Note that the experimental data for the three fracture types was retrieved from one single TB, which could be a reason for the discrepancy. This is suggested by figure 6.1, in which the velocity loss is more severe for the sample with three successive fractures (sample 0) compared to all single infTT fracture samples. However, results of simulations with all three fractures simultaneously did not differ a lot to that of a single infTT fracture.

Despite the limitations of experimental data for different fracture types, some important ideas can be extracted from the comparison. The maximum velocity ratio shifts from mid to lower frequencies as the location of the fracture moves further away from the umbo, and the velocity ratio can be positive. These two characteristics of the models exist largely due to the mimicking of TM pre-strain reduction for the 2 mm and infTT fracture. Without the mimicking of TM pre-strain reduction, the maximum velocity ratio would be observed around the same frequency (1.2 kHz) for all three fractures.

In contrary, without mimicking the reduction of TM pre-strain, the velocity ratio at low frequencies would always decrease when increasing the umbo-fracture distance. With the mimicking of TM pre-strain reduction, the losses at low frequencies are roughly the same for the different type of fractures, similar to what was observed experimentally.

A few of these explanations can be confirmed by examining the absolute SFP velocity curves (Figure 6.8). The reduction in PT stiffness lowers the resonance frequency. It also reduces the velocity loss for the 2 mm and infTT fractures by boosting the velocity response in this frequency range.

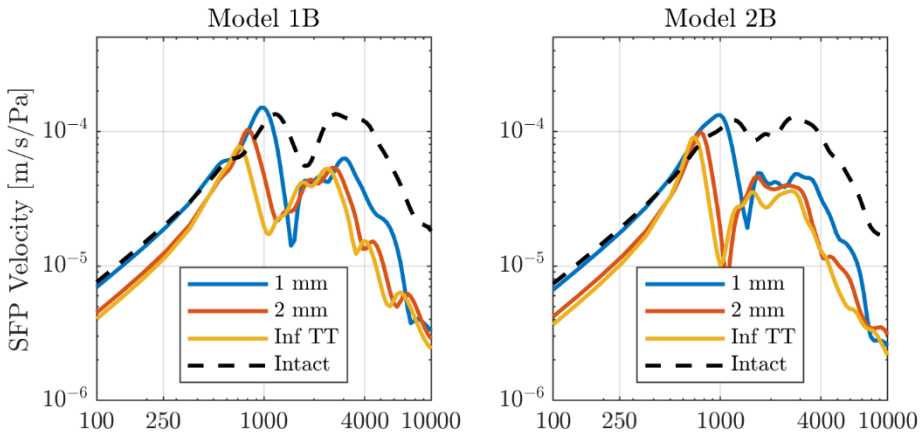

Figure 6.8: Stapes footplate velocity as a function of frequency for intact and fracture models.

6.4.3 Tympanic membrane motion

The TM motion patterns showed that at low frequencies, the maximal displacement shifts from the posterior to the inferior region. The maximal displacement amplitude also increased. These two observations support the experimental observations of umbo hypermobility. For high frequencies, the patterns became more complex for the 2 mm and infTT fracture due to the reduced PT stiffness. Due to lack of experimental data of TM motion patterns on TBs with a fractured malleus handle, no comparison can be made.

6.4.4 Effect of cochlear impedance on SFP velocity ratios

Using our models, it was shown that the velocity loss when the simulations were carried out with a cochlear impedance differed on average less than 0.2 dB compared to simulations without a cochlear impedance. The reason for this is that the cochlear impedance has little to no influence on the motion at the level of the TM or manubrium. The effect on the SFP velocity response will, therefore, be almost the same for the intact and fractured models (figure 6.6). Since velocity ratios are used, the influence of the cochlea mostly cancels out. This suggests that the removal of the cochlea for ex-vivo experiments, such as by Niklasson et al. (2016), influences the velocity ratio between pre- and post-manipulation of the TB very little.

6.4.5 Hypermobility of the umbo

Although the influence of cochlear impedance on the losses is negligible, the flexibility of modeling to include it can be appreciated. It allows us to compare the models to both ex-vivo and in-vivo measurements. The hypermobility of the umbo in the models is shown to agree with the experimental data (Chien et al. 2008) for frequencies below 3 kHz. The infTT fracture model velocity amplitude at first resonance is higher than for the intact

model and occurs at a frequency a few hundred Hertz lower than for the intact model. These two observations were also made for most of the in-vivo cases. At higher frequencies, the model umbo velocity was higher than that of the experimental data. The change in resonance frequency confirms once more that the stiffness of the middle ear has been reduced, most likely by the reduction of pre-strain in the membrane.

6.4.6 Contact modeling and other remarks

Typical audiometry results in clinical cases of an isolated malleus handle fracture indicate an air-bone gap across all frequencies and a conductive hearing loss that is larger at the higher frequencies (above on average 1 kHz) (Chien et al., 2008; Farahmand et al., 2016). It was hypothesized by Chien et al. (2008) that there might be "still sufficient contact between the fractured ends of the manubrium to permit sound transmission at low frequencies, with progressively greater dissipation (shunting) of sound energy away from the ossicular chain at the fracture site at higher frequencies". This hypothesis cannot be evaluated with the current models as contact is not included. Blanchard (2011) reported that in the three cases investigated in his study, the fracture was visible on clinical high-resolution CT. This indicates that the parts are separated wide enough so the gap is resolved by clinical CT, and that contact can be neglected. However, the possible existence of fractured malleus cases where both parts are still in contact is not excluded by this. So, it needs to be noted that the findings of the present study are only valid in the case of non-contacting broken malleus parts. In cases of a very small gap, mechanical contact could occasionally exist, leading to variable hearing thresholds.

Several observations in clinical cases reported deformation of the PT after malleus handle fracture. The effect of the geometrical deformation itself was not taken into account. The different shape of the PT may lead to an altered velocity response, which will, in turn, influence the SFP velocity response.

The mimicking of TM pre-strain reduction in the simulations was applied isotropically. In reality, it is possible that merely the pre-strain of the inferior part is released as this is the only part which is no longer connected to the ossicular chain.

6.5 Conclusions

We constructed finite element models simulating intact middle ears and middle ears with malleus fractures. Fractures at different positions on the manubrium were modeled. The lack of agreement between the experimental data and the models with only a fracture showed that the effect of a malleus fracture on the sound transmission is caused by more than just the lack of contact between the two broken parts of the malleus handle. Other important effects of malleus fractures on sound transmission are assumed to be due to release in pretension and the change in the shape of the tympanic membrane. However, experimental data on the existence of pretension in (human) tympanic membranes is currently non-existent. More experimental data has to be gathered to further understand the effect of malleus fractures on middle ear mechanics.

Chapter 7:
STRAIN AND PRE-STRAIN OF THE TYMPANIC MEMBRANE

Abstract

In the previous chapter, we discovered our FE models were not able to reproduce the velocity response measured on TBs with a fractured malleus. Due to the wrinkling after fracture, we hypothesized that the TM might be pre-strained. To investigate this, we built a digital correlation setup. To our knowledge, only one paper has reported strain fields measured in intact (cat) eardrums (Hernandez-Montes et al., 2015) using 3D digital interferometry. For this reason, we first tried to measure strain distributions in intact rabbit TMs subjected to static pressures. Next, we did similar measurements on human tympanic membranes. Finally, we tried to pinpoint the source of pre-strain in TMs of rabbits.

This chapter is based on:

Gladine, K., Dirckx, J. 2019. Strain distribution in rabbit eardrums under static pressure. Hear Res 381, https://doi.org/10.1016/j.heares.2019.107772.

7.1 Introduction

Non-contact optical techniques are commonly used to measure eardrum displacement and velocity. Some of these techniques are single-point measurements techniques such as Laser Doppler Vibrometry (LDV) and interferometry (Buunen and Vlaming, 1981; Dirckx et al., 2006; Rosowski et al., 2008; Vlaming and Feenstra, 1986) while others return full-field displacement maps (e.g. holography, moiré profilometry) (Dirckx and Decraemer, 2001; Khaleghi et al., 2015). Data gathered using these experimental techniques is used to validate finite element (FE) models. Comparisons of response curves, eigenfrequencies, eigenmodes, displacement, and phase maps are made between experimental data and modeled results.

In this work, digital image correlation (DIC) will be used to measure strain directly. Unlike holography, the coordinate system of the measurements is linked to the object surface and not to the reference frame of the measurement system, which allows determining strain distribution unambiguously.

In the field of hearing research, DIC has been used before to measure stress-strain curves of several ligaments and isolated eardrum strips (Cheng and Gan, 2007; Cheng and Gan, 2008a; Cheng and Gan, 2008b; Cheng et al., 2007). These allowed the authors to calculate the nonlinear material properties of these middle ear (ME) structures.

The majority of ME FE models assume linear material properties. To justify this assumption, strain measurements are needed. For dynamic ME behavior, this approximation is likely to be valid, although it has been shown that small nonlinearities are present in gerbils, rabbits and human ME response (Aerts and Dirckx, 2010; Gladine et al., 2017; Peacock et al., 2015). These small nonlinearities might mainly exist due to geometric nonlinearities. For quasi-static ME behavior, physical relevant pressure levels and deformations are much higher, and nonlinearity is more evidently present. Ladak et al. reported strains of 2-4% in an FE model of a cat eardrum with immobile malleus subjected to static pressures of $\pm$2.2 kPa. They suggested that for these strain magnitudes a linearized material model is a reasonable approximation. However, there is currently no experimental data to validate the simulated strains.

Another debated topic in ME modeling is the incorporation of the eardrum fibers in FE models (De Greef et al., 2017; Volandri et al., 2011). In a first approximation, this can be done by implementing an anisotropic Young's modulus based on the fiber directions (circumferential and radial) and fiber densities. This means that the stiffness of the eardrum would vary locally. Local strain measurements are then useful to compare to the local strain calculated by these FE models. This might resolve the issue of having such a wide variety of reported Young's moduli values of eardrum tissue in literature.

7.2 Setup, software and speckle pattern

A stereoscopic camera setup was used. The cameras (Manta G-507, Allied Vision) had a resolution of 2464 x 2056 pixels. For most measurements the angle between both cameras was about 35° unless mentioned otherwise. A larger angle between the cameras

results in better accuracy of out of plane movements but for curved objects like the TM a large angle between cameras will mask certain regions. The distance between the camera and lens depends on the object size. The image field size was adjusted optically by adding or removing tubes between the camera and the lens.

Commercial available DIC software was used (Dantec Dynamics, ISTRA 4D 4.4.6, Skovlunde, Denmark) for camera calibration, image acquisition, and digital image correlation. Cameras were calibrated using a checkerboard pattern printed on glass with a single square size of 0.5 mm on glass (Dantec Dynamics, KL501005, Skovlunde, Denmark).

When static pressures were applied, a custom made pressure generator was used. The pressure measurement was done by either an internal or external pressure sensor. The external pressure sensor will return a more reliable pressure value as it can be placed closer to the TM. We will mention which sensor was used for each set of measurements in the upcoming sections. For sound stimulation, a horn driver (TOA, TU-651, Japan) was utilized, a more detailed description will be given in the appropriate section. The applied pressure (or sound), as well as the camera triggering, was controlled from Matlab. The pressure ranges, pressure change rate, sound pressure levels, stimulation frequencies, and trigger rate will be described in each separate measurement section.

In section 4.3, we discussed the different requirements of a speckle pattern for DIC. We tested two different materials to generate a speckle pattern. We made solvents of toner and fluorescent powder mixed with ethanol. A custom made airbrush was used to spray the solvent on the tympanic membrane. The ethanol evaporated shortly after the application of the solvent, leaving only the toner or fluorescent powder on the TM. Both patterns are shown in figure 7.1[4]. It was harder to obtain a consistent speckle size using toner compared to the fluorescent powder.

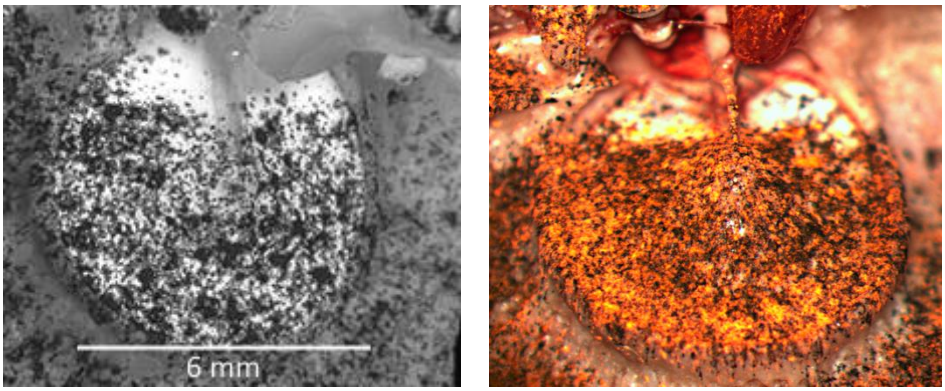

(a) (b)

Figure 7.1: Speckle patterns using (a) toner, (b) fluorescent powder

[4] In this section, the DIC method was tested. For this reason, some inconsistencies may be present such as facet size and other variables. Another example is that the fluorescent powder here is applied on top of the toner pattern. This will not be the case in further experiments.

White light was used to illuminate the toner speckle pattern from the medial side. Since the eardrum is semi-transparent, the light goes through. The light can then reflect back from the ear canal, resulting in a bright spot in the image. This is dependent on the viewing angle and curvature of the TM. As a consequence, different bright spots are seen by both cameras (figure 7.2). The DIC method relies on comparing the local gray values of the speckle pattern. The light reflected from behind the eardrum alters the local gray values and differently for both cameras. This interferes with the DIC method and will result in a failed correlation. This is clearly visible in figure 7.3, which shows the correlation result. The correlation failed for the bright spots seen in figure 7.2.

Moreover, the locations of the reflections perceived by each camera change during TM deformation. The change does not correlate with the pattern movement. Thus the gray values are altered during deformation (figure 7.4). As a result, the DIC method will fail in different areas of the TM for different deformation steps.

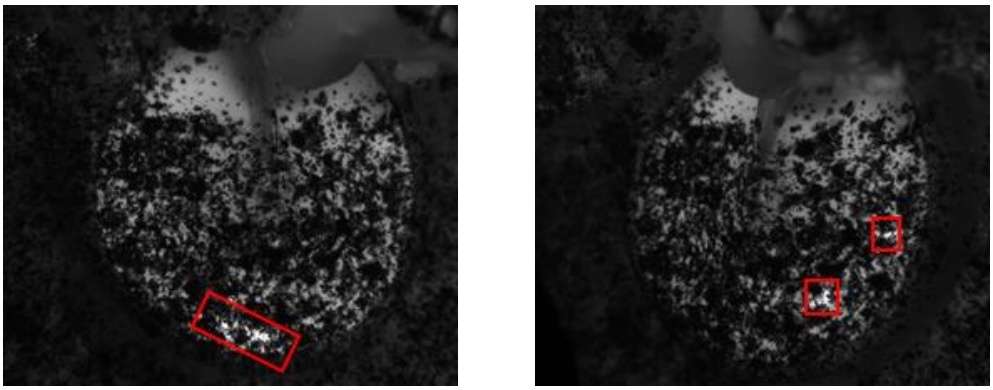

Figure 7.2: Different reflections are observed by each camera.

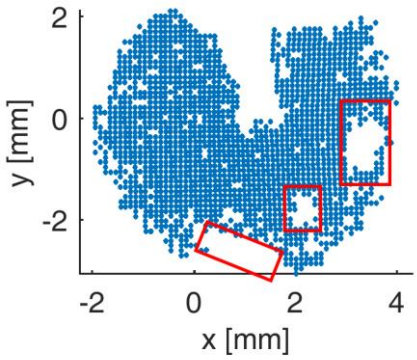

Figure 7.3: The point cloud illustrates at which coordinates the digital image correlation algorithm succeeded to locate the facet in both images. The red rectangles indicate failure of the algorithm due to the light reflected from behind the tympanic membrane which alters the gray values of the facets differently for each camera.

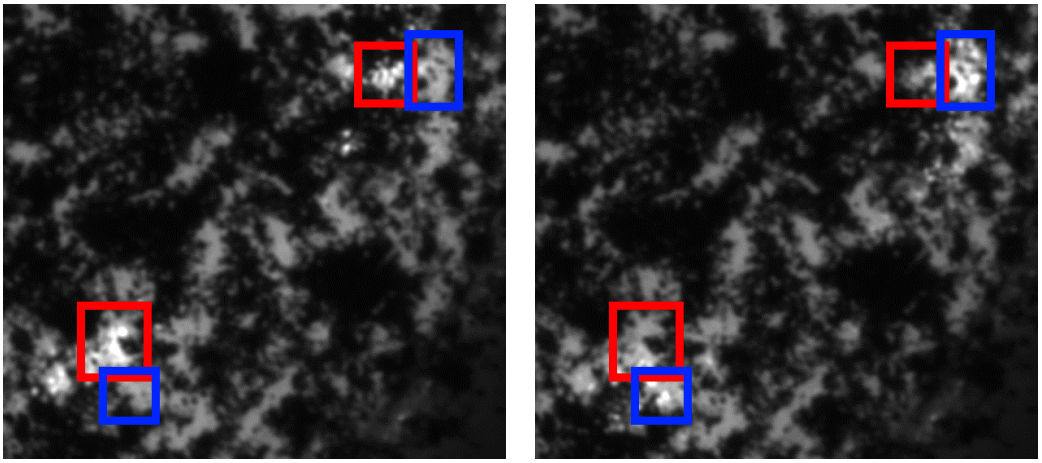

(a) (b)

Figure 7.4: Relative movement of reflections originating from behind the eardrum to the toner speckle pattern between pressure steps (a) +1 kPa and (b) +2 kPa (Camera 2).

These problems can be avoided by using fluorescent powder instead. The pattern is then illuminated by a green laser (532 nm). The fluorescent pattern will radiate light of different wavelength. Filters mounted on the camera lenses will then block the laser light. As a consequence, only light radiated directly from the surface of the TM is perceived by the camera. This solves the aforementioned problems regarding reflected light from behind the TM. All subsequent measurement results were obtained using a fluorescent speckle pattern.

7.3 Strain distribution in rabbit eardrums under static pressure

In this work, we measured displacements and strains in rabbit eardrums subjected to quasi-static pressures between ±2 kPa. Displacement results are compared to existing data (Dirckx et al., 2006).

7.3.1 Methods

Rabbit heads were obtained from the food supply chain and were stored at 4°C prior to measurements. No animals were sacrificed specifically for this research.

The ME bullas were removed from the heads and were kept in wet cloths to prevent dehydration of the ME. The soft ear canal was cut away, exposing the bony ear canal. A plastic tube, glued (Henkel, Loctite 401, Düsseldorf, Germany) onto the bony ear canal, was used to apply static pressures via the ear canal using a custom-built pressure generator. The connection of the tube and bony ear canal was reinforced by gluing a strip of paper tissue around it. Additionally, two-component hardening paste (Dreve Otoplastik GmbH, Otoform Akx, Unna, Germany) was used to make sure the connection was airtight. The internal pressure sensor of the generator was used to measure the applied pressure.

The bulla was opened, and bone was cut away, giving a medial view on the ME. For 10 ears, measurements were performed using an intact cochlea. The presence of the cochlea limits the medial view on the eardrum (figure 7.5A). Removing additional bone and the cochlea in order to increase the field of view (figure 7.5A), while keeping all structures intact, proved to be complicated. We succeeded to do this for five ears. In the remaining ears, the bone surrounding the oval window was fractured. For three ears (S8-10), measurements were performed with and without cochlea. For two ears (S11-12), only measurements without cochlea were made.

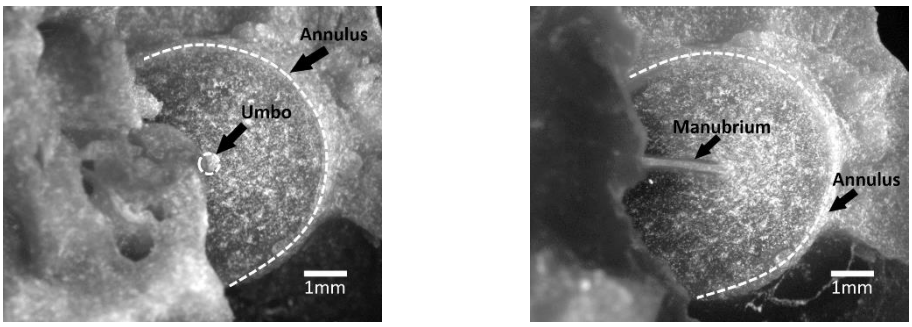

A B

Figure 7.5 Medial view of the tympanic membrane with intact cochlea (A) and removed cochlea (B)

Dehydration of the ME restricts the mobility of ossicles and eardrum (von Unge et al., 1993). This was also shown in dynamic measurements (Niklasson et al., 2016). The authors also showed that after dehydration, rehydrating the eardrum restores the mobility fairly well. It is therefore important to hydrate the MEs before each measurement. The ears could not be hydrated during the pressure cycles as an excessive amount of moisture could alter the applied speckle pattern during pressure cycles. The stochastic pattern needs to be the same for each step after the reference step (first photo). Otherwise, the correlation is rendered impossible. For this reason, the MEs were moistened sufficiently just before each measurement. Dehydration of the eardrum during measurement could be monitored by observing the umbo displacement. Figure 7.6 shows measurements of umbo displacement over five pressure cycles when the specimen was not well hydrated as well as when it was adequately hydrated. Well-hydrated ears had a stable pressure-displacement relationship after one or two pressure cycles. Drying ears showed a decreasing range of displacement amplitudes.

7.3.2 Results

Umbo displacement

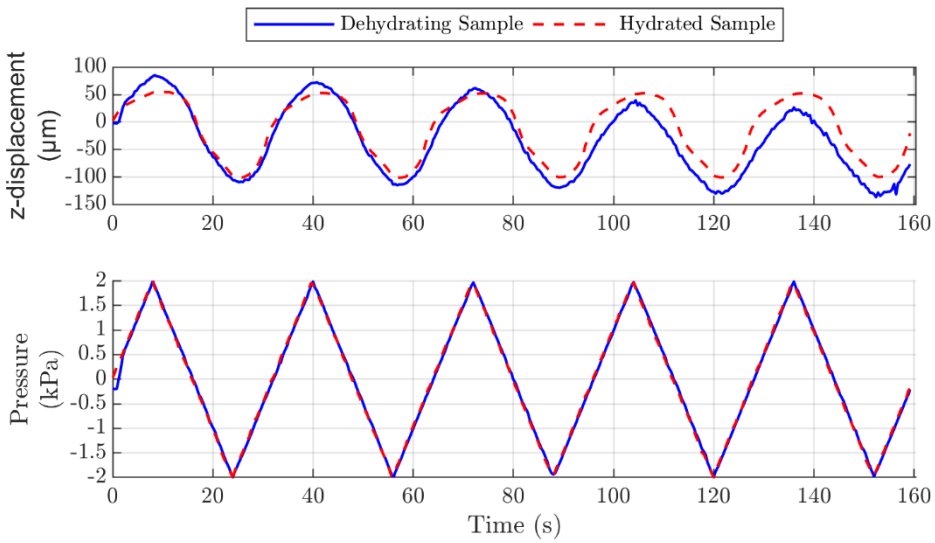

Figure 7.6: Umbo z-displacement for a specimen (top) when it was adequately moistened (red) and when it showed signs of dehydration (blue) and applied middle ear pressure (bottom) as a function of time.

From here on, we refer to an overpressure in the ear canal as a positive pressure. This positive pressure causes a medial displacement of the umbo, which we will refer to as a positive displacement. Similarly, a negative pressure corresponds to an underpressure in

the ear canal. This negative pressure causes a lateral displacement of the umbo and will be referred to as a negative displacement.

Specimens with intact cochlea were positioned in such a way that the umbo was visible for both cameras. The cochlea and surrounding bone sometimes visually obstructed the umbo when looking perpendicularly at the plane defined by the TM annulus. For this reason, the specimen was sometimes placed under an oblique angle when the cochlea was intact. A transformation matrix was calculated to correct the z-displacements for this oblique angle placement.

Figure 7.7 shows umbo displacement as a function of pressure. The curves are highly non-linear and show hysteresis. The displacements scale fairly linearly for pressures from -0.5 to 0.25 kPa. For pressures outside of this range, displacements change slower with respect to pressure changes. The average and standard deviation of the peak-to-peak amplitude was 153 ± 14 μm for intact cochlea (figure 7.7A) and 174 ± 12 μm when the cochlea was removed (figure 7.7B). The ratio of the maximal displacement at +2 kPa and minimal displacement at -2 kPa is on average approximately a factor of 2. Medial displacements are smaller than lateral displacements.

After preconditioning of the TM, we observed a mean net displacement with respect to the rest state of 8.2 μm at 0 kPa for decreasing pressures and -11.8 μm for increasing pressures. By calculating the area enclosed by the displacement-pressure curve, we obtain the hysteresis which scales with energy loss. On average we found a hysteresis of 89 ± 23 μm kPa for intact cochlea and 83 ± 31 μm kPa when the cochlea was removed.

For three samples (S8-10), umbo displacement was measured with intact and opened cochlea. After opening the cochlea, the peak-to-peak displacements increased 13% on average.

Strains

Multiple ways of visualizing the strains are possible. One can show the individual strain components in the Cartesian axis (ϵ_{xx},ϵ_{yy},ϵ_{xy}) or the principal strains (ϵ_{p1},ϵ_{p2}). The latter two show the *most positive* strain and *least positive* strain, respectively. This means that ϵ_{p1} can be negative, but for the same facet, ϵ_{p2} will be even more negative. Vice versa, ϵ_{p2} can be positive but then ϵ_{p1} will be more positive. The orientations of the principal strains are always perpendicular to each other. In our measurements, it often occurred that when one of the two principal strain values has a significant magnitude, the other principal strain value is close to zero. Figure 7.8A-C shows strain distributions (ϵ_{p1}, ϵ_{p2},ϵ_{pmax}) in one sample at +2 kPa. For this reason, it is more interesting to visualize the principal strain of each facet which has the highest absolute magnitude, whether it is positive or negative. In subsequent figures, we will use this representation and refer to it as ϵ_{pmax} or the "maximal absolute principal strain".

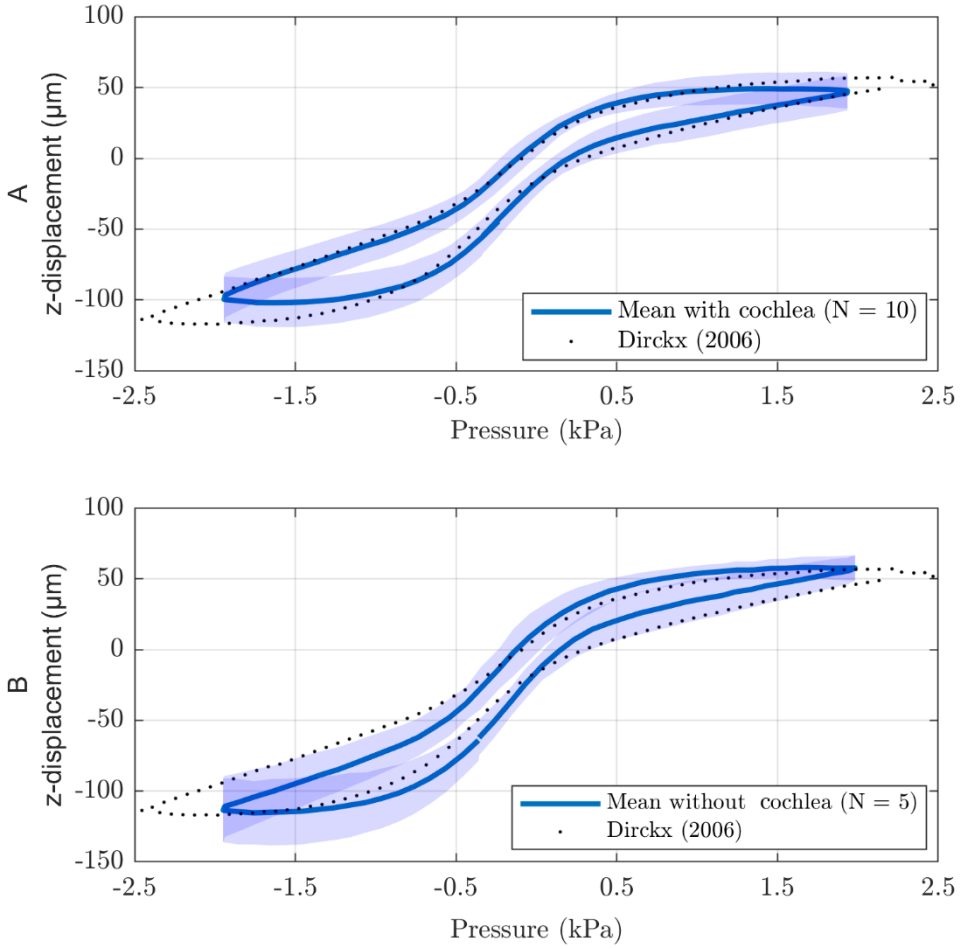

Figure 7.7: Umbo z-displacement as a function of pressure with (A) intact cochlea and (B) cochlea removed. A positive pressure value represents an overpressure in the ear canal. A positive displacement represents a medial displacement of the umbo. Measurements are compared to laser Doppler vibrometry data obtained in rabbits (Dirckx 2006). Averages and standard deviation bands are given in (C) and (D) for intact cochlea and cochlea removed respectively.

The strains can be calculated directly from the deformation of the facets (Figure 7.8A-C). However, ISTRA4D allows calculation of strains by using spatial derivatives of the displacements together with smoothing. This provides smoother results, as shown in figure 4D. Subsequent strain maps will show maximal absolute principal strains (ϵ_{pmax}) calculated using smoothed spatial derivatives of the displacements.

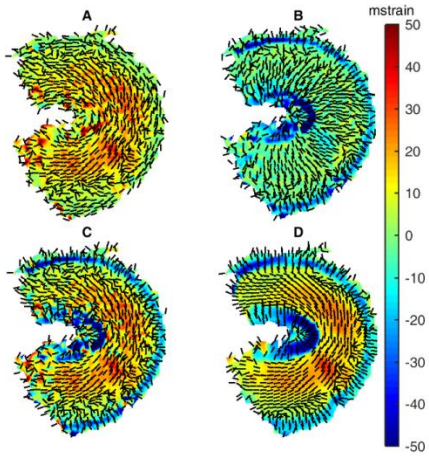

Figure 7.8: Example of strain visualization. (A) First principal strain (ϵ_{p1}), (B) second principal strain (ϵ_{p2}), (C) Maximal absolute principal strain (ϵ_{pmax}) and (D) ϵ_{pmax} calculated using both deformation of facets and displacement derivatives. For A-C, only facet deformation was used to calculate the strains. Strain magnitude is represented by color while the principal strain direction is visualized by black vectors.

Figure 7.9 shows strain distribution at +2 kPa and -2 kPa in the three ears where we succeeded to make measurements with both intact and removed cochlea. For positive pressures, ϵ_{pmax} is positive and circumferential in most areas of the tympanic membrane. In these areas strains vary from 10 to 35 millistrain. Close to the manubrium ϵ_{pmax} is negative and radially orientated. The strains in this area can reach values down to -130 millistrain. Similarly, ϵ_{pmax} is negative and orientated radially at the annulus with values ranging mostly from -25 to -10 millistrain.

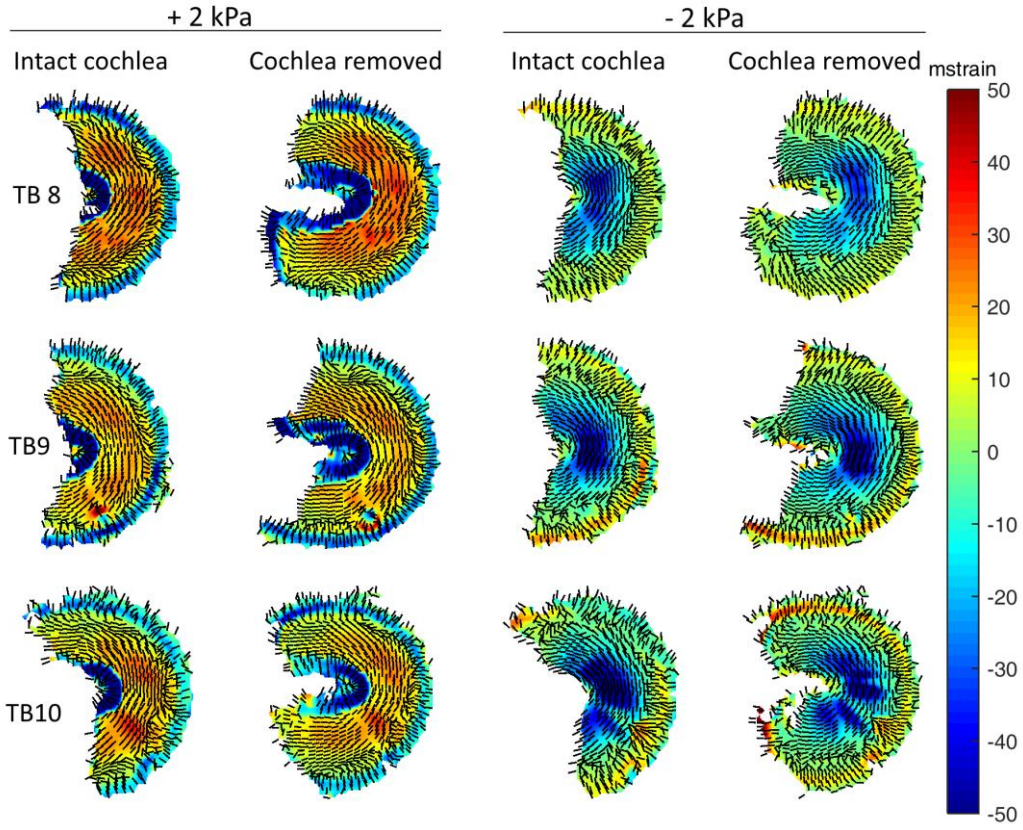

Figure 7.9: Maximal absolute principal strains (ϵ_{pmax}) of S8-10 for +2 kPa and -2 kPa with intact and removed cochlea. Strain magnitude is represented by color while the principal strain direction is visualized by black vectors.

For negative pressures, ϵ_{pmax} is negative but still circumferential. The most negative values are concentrated just inferior to the umbo, with ϵ_{pmax} hovering mostly around -30 to -50 millistrain. Posterior and anterior from the manubrium the values are closer to -10 millistrain. Close to the annulus ϵ_{pmax} is positive and again orientated radially. In most cases, the values do not exceed 15 millistrain.

Little difference is observed between the strains observed with and without presence of the cochlea.

Figure 7.10 shows ϵ_{pmax} as a function of pressure, averaged over a zone of 0.50 mm² central in the inferior region between umbo and tympanic annulus. We observe again that the magnitude of the strains is greater at negative pressures.

For positive pressures, the strain increases almost linearly at a rate of 10 millistrain/kPa and shows a small area in the hysteresis loop. In contrary, for negative pressures, there is strong non-linear behavior and much larger hysteresis.

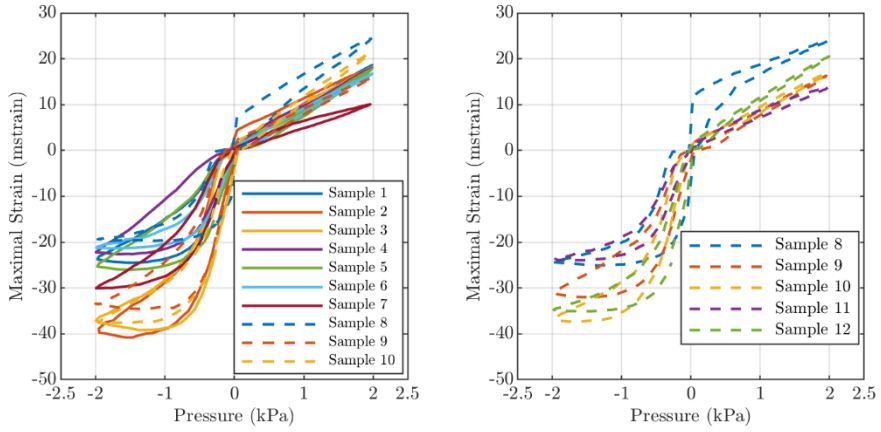

Figure 7.10: Maximal absolute principal strain (ϵ_{pmax}) averaged over an area of 0.50 mm² located in the middle of the inferior region between umbo and tympanic annulus with cochlea intact (left) and cochlea removed (right).

7.3.3 Discussion

Dehydration and specimen condition

Dehydration was evaluated by monitoring the umbo displacements over time. After two or three pressure cycles the pressure-displacement hysteresis is stable. In case of dehydration this is not true and the displacement magnitudes keep diminishing.

When removing the cochlea to enhance the view on the tympanic membrane we experienced some technical difficulties. The bone surrounding the cochlea is very hard. Sometimes, when cutting or drilling this bone, cracks would appear and propagate to the annular ring of the stapes, resulting in a less constraint stapes. The experiments showed that in cases where the annular ligament was damaged, umbo displacement as a function of pressure strongly increases. Umbo displacements of -300 to 250 µm were observed, which equals a peak-to-peak displacement more than three times the range of a specimen with an intact stapedial annular ring. The visco-elastic properties of the TM itself may contribute to the protection of the inner ear for quasi-static and extremely low-frequency pressure variations, together with other factors such as the elastic properties of the annular ligament.

The five specimens with removed cochlea presented in this work were carefully examined, and no fractured stapedial annular ring was detected.

Umbo displacement

Figure 7.7 shows the umbo displacement measurements are in good agreement with data found in literature (Dirckx et al. 2006), although the measurement conditions were not exactly the same.

The pressure-rate in this work was 250 Pa/s for a range of -2 to 2 kPa (31.3 mHz). The data from Dirckx et al. shown in figure 7.7 was measured at a pressure-rate of 200 Pa/s for a range of -2.5 to 2.5 kPa (20 mHz) and always with removed cochlea.

Peak to peak amplitude

We found a peak-to-peak amplitude of 153 ± 14 μm for intact cochlea and 174 ± 12 μm when the cochlea was removed. Dirckx et al. reported an average peak-to-peak amplitude of 165 ± 19 μm. However, in 4 out of 6 ears they found a value of about 180 μm.

Hysteresis

We calculated an average hysteresis of 89 ± 23 μm kPa for intact cochlea and 83 ± 31 μm kPa when the cochlea was removed. Performing the same calculations on the pressure-displacement curve of Dirckx et al. (figure 7.7) returns a hysteresis of 92 μm kPa. . The variation of hysteresis is large compared to that of the peak-to-peak amplitude. The standard deviations are 25% and 37% of the average value for intact and removed cochlea respectively. While for the peak-to-peak displacements they are only 9% and 7%. Such larger variation in hysteresis was also observed in previous work (Dirckx et al., 2006). Gaihede (1999) measured the pressure-volume-displacement relationship in 39 human subjects with a median pressure range of 4 kPa at 140 mHz equaling pressure change rate of 1.1 kPa per second. They found a median hysteresis of 20.33 μJ. Multiplication of this number by the surface area of a human eardrum (60 mm^2) returns an estimate of the hysteresis calculated using the pressure-displacement relationship we measured in this work. This estimate of hysteresis of human eardrums then gives a value of 250 μm kPa. Dirckx et al. (2006) showed that hysteresis is inversely proportional with the pressure change rate. This suggests that the hysteresis of human eardrums is even higher for a pressure change rate of 0.250 kPa per second which we used in this work. Hysteresis of rabbit eardrums is therefore much smaller than human.

Strains

Asymmetry

An asymmetry was found in TM strain as a function of pressure. The strains at +2 kPa are smaller in magnitude than those at -2 kPa (figure 7.9 and figure 7.10).

This correlates well with the umbo displacements. Positive pressures cause smaller umbo displacements and smaller strains than negative pressures (figure 7.7). The main difference between strains at positive and negative pressures is the sign of the strain. At positive pressures, the strains are mostly positive, meaning that the membrane mainly stretches. At negative pressures, strains are negative meaning that the TM shrinks. A flat membrane would show positive strains for both positive and negative pressures. This asymmetry in sign can be attributed to the cone shape of the TM.

The dependence of strains on pressure is very different for positive and negative pressures (figure 7.10). For positive pressures, the strain centrally located between umbo and the inferior part of the annulus was almost linearly proportional to the pressure at a rate of 10 millistrain/kPa. Hysteresis is almost absent. For negative pressures, the strain behaves more non-linearly, resembling the pressure-displacement curves more. The proportionality of negative strain with negative pressure is much larger, resulting in a steep strain-pressure curve. At -0.5 kPa, the curves start to saturate and grow more slowly. A larger hysteresis is observed.

Another difference between strains at positive and negative pressures is the strain just around the umbo. For negative pressures, the strain around the umbo is close to zero. At positive pressures, the largest part of the membrane shows positive strains, but close to the umbo, the strain is negative and very large (figure 7.9). This negative strain seems to be caused by the umbo movement, which stalls before the membrane does. This decreases the distance from the surrounding TM tissue to the umbo, resulting in negative strains.

In all samples, the annulus strains were of opposite sign as compared to the strain in between TM annulus and manubrium, which seems counterintuitive. For medial displacements, positive strains are to be expected as most of the TM moves further away from the annulus and vice versa. We assume that this effect is caused by the thickness of the membrane, which increases at its border in gerbils and humans (Kuypers et al., 2006; Kuypers et al., 2005; Van der Jeught et al., 2013). For the major part of its surface, TM thickness is of the order of 10 μm, so it can be regarded as a thin membrane. As a consequence, medial and lateral side will have nearly the same strain. At the borders however, the membrane becomes thicker and then medial and lateral surfaces will behave different due to bending and through-thickness compression. As a demonstration, we performed measurements on a 500 μm thick 20 mm diameter rubber membrane with the shape of a Chinese hat with an apex height of 1.4 mm. The ratio of thickness to diameter is much larger compared to most areas of the eardrum so it can be regarded as a thick membrane. Additionally, we made an FE model of this membrane. The results are shown in figure 7.11. The border of the membrane was not entirely visible in the experimental setup. But we see a strong resemblance between the measurement and the FE results. We see that on the borders and the center, strain of opposite sign is measured at the side where the cone is pointing towards (top). The corresponding strain directions are orientated radially, as we saw for the eardrum. Between the center and border, the strain directions are different compared to the eardrum. The other side of the membrane (bottom) behaves as we would expect; the strains show no change in sign and all strains are circumferential except at the borders. This is how the eardrum behaves in the thinner regions. Unfortunately, it is impossible to completely visually expose the lateral side of the rabbit TM to measure strain distribution on that side.

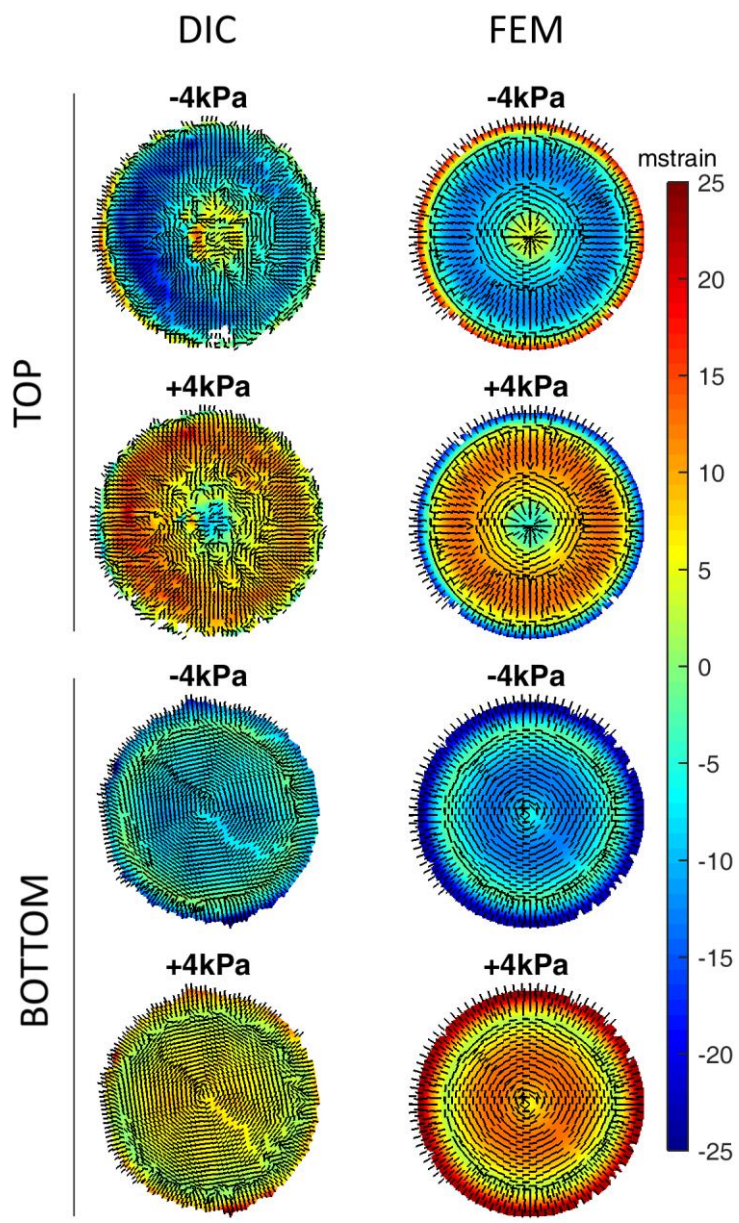

Figure 7.11: Maximal absolute principal strain of the top and bottom of a Chinese hat-shaped thick rubber membrane and corresponding finite element model at -4 and 4 kPa. The top surface shows changes in strain sign at the center point and border similar to the medial surface of the eardrum (Figure 7.9).

Strain directions

The maximal absolute principal strain directions were orientated circumferential in most parts of the tympanic membrane, regardless of whether negative strains occurred at negative pressures or positive strains were induced at positive pressures.

Intuitively, radial strains could be expected. When pulling at or pushing on a cone's tip, one observes radial strains. However, a force distributed over the entire surface makes the cone bulge towards the shape of a spherical shell. This bulging deformation causes the cone mainly to have circumferential strains. Only at the very edges, the strains are radial as there is no other strain direction possible at this fixed boundary. The radial strains at the TM annulus cover a larger area at negative pressures.

This same bulging causes negative strains at the umbo for positive pressures, as mentioned earlier. These negative strains are caused by the tissue around the umbo displacing more than the umbo, decreasing the distance of this tissue to the umbo. This strain obviously occurs in the radial direction.

Effect of removing the cochlea

Peak to peak umbo displacements became on average 13% larger when the cochlea was removed. Hysteresis (figure 7.7) and peak-to-peak strain (figure 7.10) only differed 7% and 3% respectively.

In gerbils, it was shown that the cochlea did not have a significant effect on the pressure-displacement curves (Dirckx and Decraemer, 2001). The difference we observed in the current results is not much larger than the variation between different samples. However, the measurements of S7-10 with intact and removed cochlea clearly show an increase in peak-to-peak amplitude.

The effect on peak-to-peak strain is much smaller, which can be expected as the strains for positive pressures were shown to increase slowly, and the strains at negative pressures started to saturate below -0.5 kPa.

Mass loading

The mass loading effect of the applied speckle pattern is so small that it cannot be measured directly. We, therefore, coated a 2100X2970mm paper surface with the speckle pattern, and found a mass increase of 0.091 grams, yielding a mass loading of 0.015 micrograms per square millimeter. We conclude that the mass loading of the entire eardrum is certainly less than 1.5 microgram ($1.5\ 10^{-9}$ kg).

7.3.4 Conclusion

Literature on intact eardrum strain data is very sparse. The availability of full-field eardrum strains maps could facilitate further validation of finite element models and understanding of the middle ear. We measured full-field strain maps of intact rabbit eardrums subjected to large static pressures with intact and removed cochlea using a stereoscopic digital image correlation setup. In general, we found that for ear canal over- and underpressures, the largest absolute principal strain was orientated circumferential between the manubrium and the tympanic annulus. At the tympanic annulus, the strain directions were radial. For ear canal overpressures, the strain direction around the manubrium was also found to be radial. Between manubrium and annulus, overpressures induced positive strains (up to about 25 millistrain) and underpressures generated negative strains (up to about -45 millistrain). At the annulus a change in sign was observed. For overpressures, such change of sign of the strains was also seen around the manubrium. This change of sign was speculated to be the consequence of the larger eardrum thickness at the annulus (and manubrium). We saw that for overpressures, the strain almost increased linearly, while for underpressure, a nonlinear relationship was observed. The effect of the removal of the cochlea on the strains was found to be smaller than on the umbo displacements.

7.4 Full-field deformation and strain distribution in the human eardrum subjected to static pressure and high-intensity sounds

This part is not based on any published paper. The measurements were performed during the writing of this thesis. Since the subject fits the thesis well, I thought it would be interesting to include it. However, we used one TB, making the data set very small. For this reason, we will be careful when drawing any conclusions based on these measurements.

7.4.1 Setup and temporal bone preparation

The same method was employed, as described in section 7.3. A few things were different in comparison with the experiments on rabbits. First off, the TM was observed from the lateral side instead of the medial side. This allows for a larger coverage of the TM. In rabbits, the DIC method would not work on the malleus itself when recording the medial side. Measuring the lateral side resolved this issue. To achieve visual access of the TM for both cameras, the ear canal was drilled away as close to the TM as possible (figure 7.12 [right]). The TB was placed against a cavity which contained a window providing a view of the lateral side (figure 7.12 [left]).

Dynamic measurement setup

Elastic paste was used the acoustically seal the connection between the TB and the cavity. A speaker was mounted on top of the cavity. A probe microphone was placed through a tight hole inside the cavity. Single sine stimulation was used at very low (10 Hz) and higher frequencies (1000 Hz) using a sound pressure level of about 145 dB.

Static measurement setup

The pressure was applied at the medial side instead of the lateral side. The pressure tube was placed through a tight-fitting hole drilled in the middle ear cavity. An external pressure probe was connected parallel to this tube, allowing for accurate measurement of the pressure close to the cavity.

Three consecutive pressure cycles were applied with pressures ranging from −2.5 to 2.5 kPa at a pressure change rate of 0.250 kPa/s. Images were recorded every 0.1 kPa or equivalently every 0.4 seconds. A total of 300 images were captured in 120 seconds. Stroboscopic laser light was used to prevent dehydration. The laser illuminated the TM for a brief time of 20 ms only when the cameras were triggered.

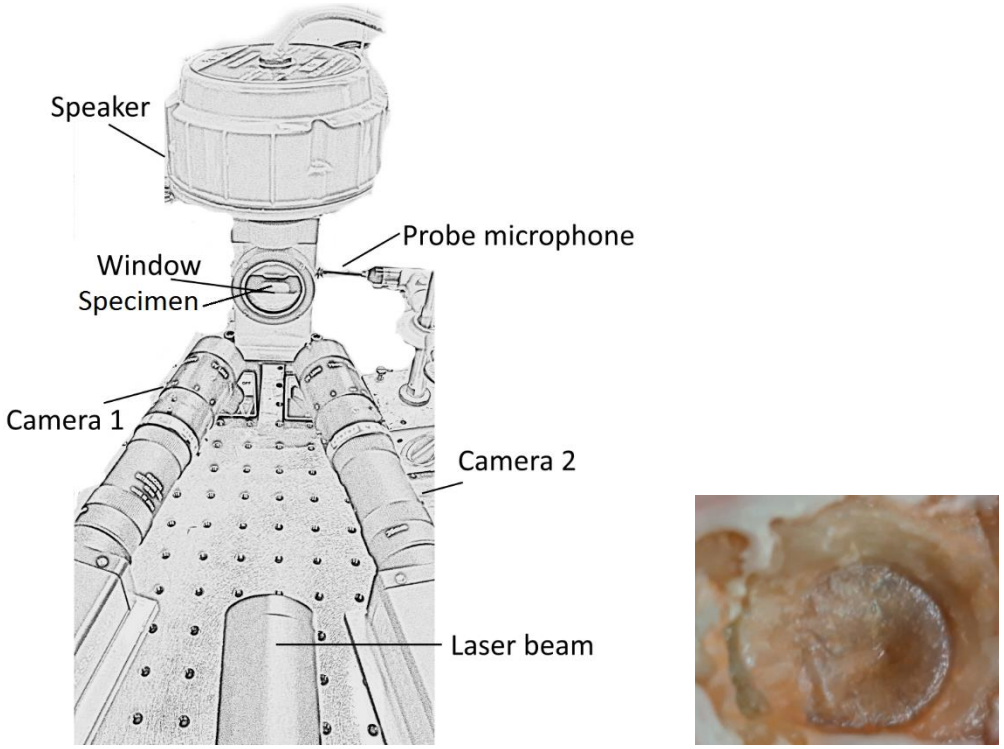

Figure 7.12: Illustration of the measurement setup (left) and close-up demonstrating the view on the tympanic membrane.

7.4.2 Results

Static measurements

Figure 7.13 shows the umbo displacement as a function of pressure. We observe higher displacements than observed by Dirckx and Decraemer (1991), especially when applying an ear canal underpressure. The maximal principal strains maps (figure 7.14) show mainly positive strains for positive pressure, and negative strains for negative pressures. Most of the strains show a circumferential character. Only at the TM border, the majority of strains are orientated radially. The sign of strain is the same on the TM borders as the majority of the TM. The largest strains occur on the manubrium and just inferiorly to the umbo. For positive pressures the sign of strain at the umbo is opposite to the majority of the rest of the TM. The area inferiorly to the umbo exhibits larger negative strains at negative pressures than positive strains at positive pressures. This is also observed when calculating the average strain in that area (figure 7.15).

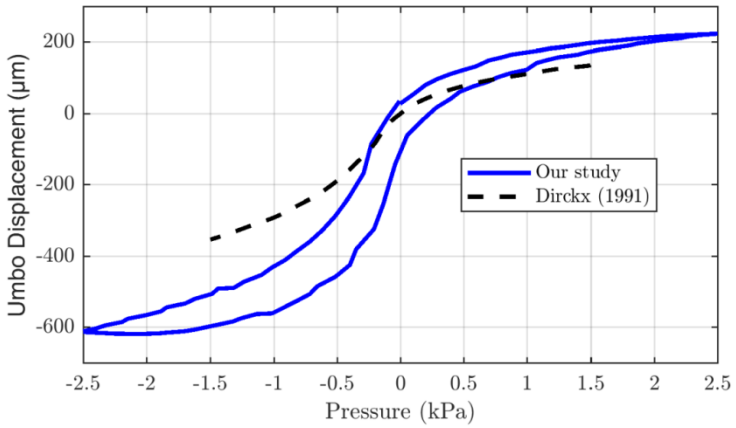

Figure 7.13: Umbo displacement as a function of ear canal pressure.

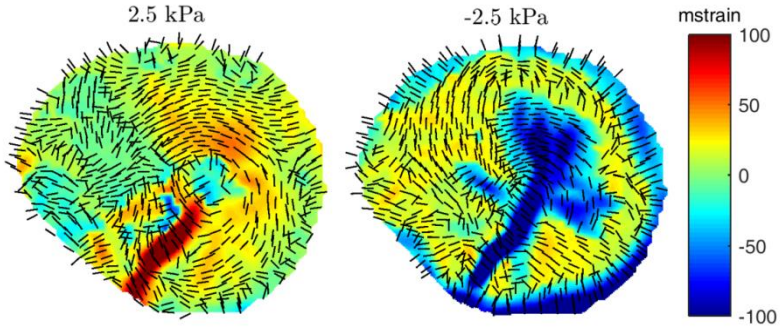

Figure 7.14: Maximal principal strain at positive and negative ear canal pressure.

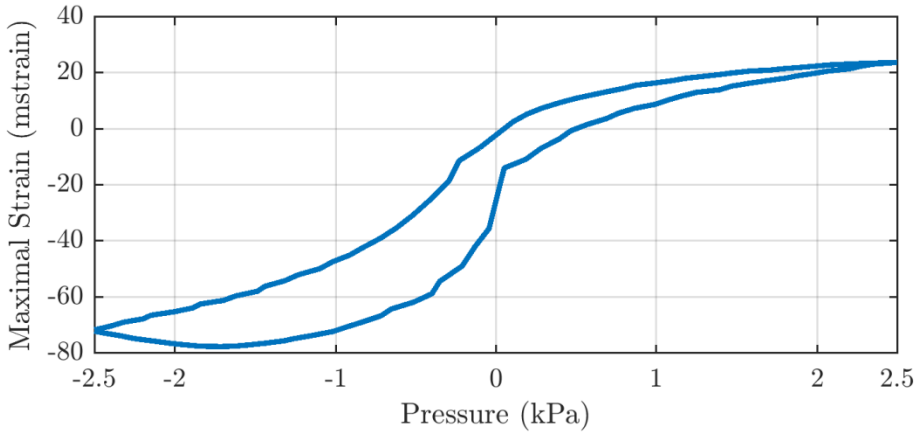

Figure 7.15: Strain averaged over an area of 3.14 mm² close to the umbo as a function of pressure.

Dynamic measurements

We already discussed the DIC displacement measurements in section 5.7.3. So we will focus on the strain maps here. Figure 7.16 shows the maximal principal strain during a harmonic loading cycle using a frequency of 10 Hz at 145dB SPL. The strain distribution is very similar to the case of static measurements. The values are smaller; however, we are only utilizing pressures of 500 Pa peak instead of 2.5 kPa.

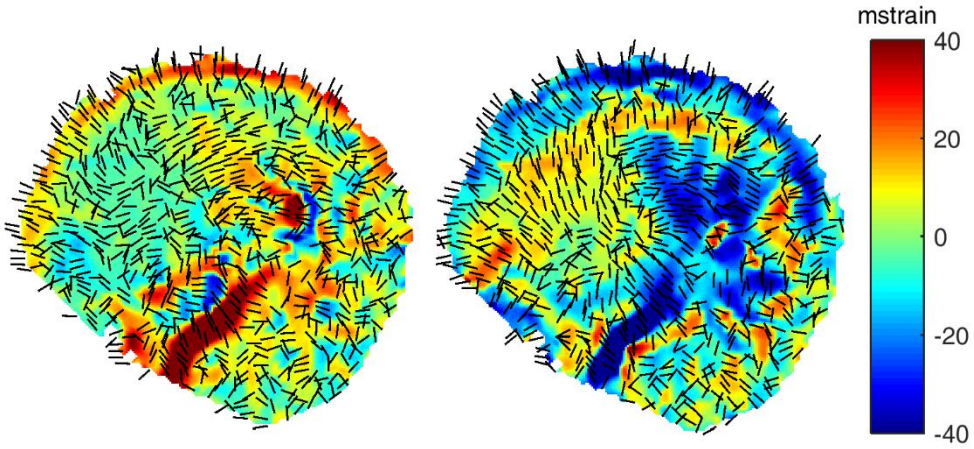

Figure 7.16: Maximal principal strain at pressure maximum (left) and minimum (right) during harmonic loading using a frequency of 10 Hz at 145dB SPL.

7.4.3 Discussion and conclusions

First, we want to stress the differences between the experimental setup of the measurements performed in humans and rabbits. The main difference is that in humans, we measured the lateral side of the TM, while in rabbits, we measured the medial side. We see that now we can evaluate the area covering the manubrium, which was not the case in rabbits. Another difference is that in humans, we applied the pressure from the medial side instead of the lateral side. However, this should not have any effect on the results.

Static measurements

We did not observe anything unusual about the used TB. However, the umbo displacements are quite large in comparison to those measured by Dirckx and Decraemer (1991), which is another reason to be careful about any conclusion made based on the measurements reported here.

The human TM strain maps show some similarities to those obtained in rabbits. The largest strains (disregarding those on the manubrium), occur just inferiorly to the umbo. They are orientated circumferentially. Negative pressure or lateral TM displacement causes higher absolute strain values than a positive pressure or medial TM displacement. The opposite sign in the strain at the umbo for positive pressures compared to the rest of the membrane.

A striking difference is the sign of strain at the TM borders. In rabbits, the medial side of the TM showed a different sign in the strain at the border compared to the rest of the membrane. This is not the case for the measurements of the lateral side in humans. This is, however, what we expected as discussed in section 7.3.3. We hypothesized that the increased thickness at the borders caused the effect on the sign of strain by means of through-thickness compression. The test on the rubber membrane showed that this change in sign would only occur on the "top" side (figure 7.11), in our case, the medial side of the membrane. We expected that this change in sign would be absent on the lateral side, which seems to be true. However, we have no measurements of both sides of either the rabbit or human TM, so we cannot be 100% sure whether this hypothesis is correct.

Dynamic measurements

At low frequencies, we observe that the TM dynamic behavior is very similar to its static behavior. In section 5.2.1, we hypothesized that the small nonlinearities at high sound pressure levels could be a consequence of the same nonlinearity we observe when subjecting the ear to high static pressures. Indeed, in section 5.7.3, we found that a net lateral displacement occurs at a stimulation of 10 Hz as we predicted. We also found that the TM exhibits both odd and even degree nonlinearities as predicted from the nonlinear static behavior. And now, we observe that the strains are quite similar too, once again reassuring us that the membrane behaves very similarly. This probably changes for frequencies above the first resonance frequency.

7.5 Pre-strain in rabbits

7.5.1 Introduction

In this section, we try to find the source of the TM pre-strain and measure the change in strain caused by malleus fractures. The pretension source probably lies beyond the TM, presumably in one or more of the ME ligaments. Once a malleus fracture occurs, the distal part of the fracture is disconnected from the rest of the ossicular chain, removing the TM pretension. As a consequence of this decrease in tension, the TM fails to retain its shape and becomes hypermobile as we have discussed in chapter 6.

7.5.2 Method

To find the source of the pre-strain, we sequentially remove parts of the ossicular chain such as ligaments or ossicles. We can then observe the shape and measure the change in strain after each dissection stage of the ME. Additionally, we can monitor the mobility of the TM by measuring its response to quasi-static pressures similar to section 7.3.

In dissection stage A, the TB was kept intact as much as possible. Only the cochlea was removed to improve the view of the TM. In stage B, the tendon tympani was removed. Stage C involved removing the stapes. In stage D, E, F, and G, we removed the anterior mallear ligament, posterior incudal ligament, superior mallear ligament, and superior incudal ligament respectively.

The TB may undergo rigid body motions due to replacing the sample after each dissection stage. We will correct for the rigid body out of plane rotations and displacements but not for the in-plane displacements and rotations since we will be only observing principal strains and out of plane displacements which are both independent of in-plane rigid body motions.

7.5.3 Results

Figure 7.17 shows photographs of the TM at each dissection stage (A-G). No apparent change occurred during stages A to E. Only when the superior mallear and incudal ligament were removed a clear change in TM appearance happened. Wrinkling close to the umbo was seen. We also observed the conical shape of the membrane was lost and was overall fairly flat. At the site of the wrinkles, the speckle pattern appears to be very bright and vastly different than the speckle pattern of the TM of the intact middle ear.

Figure 7.18 shows the strain difference between dissection stage A and the others. We see that no correlation was found for the facets on the wrinkly sites of the TM. No remarkable strain differences occurred up until stage D and E. The principal strain directions are randomly orientated in B and C. In stage D, the strain directions are becoming more circumferential, and a small buildup of positive radial strains at the TM border is seen. At stage E, the circumferential strains become more obvious. These circumferential strains are negative, with values ranging from -10 to -30 millistrain. The positive radial strains at the border have increased too. In stage F, mainly the strains

just around the manubrium have been increased in magnitude. Values of −45 up to −80 millistrain in some regions were measured. The strain directions are again more randomized than before. In stage G, the DIC method failed to correlate many facets at the sites of the TM wrinkling.

From the pressure-displacement curves, we see that our "intact" TB probably had a fractured stapedial annular ring since negative displacements go up to −300 μm. In section 7.3, we saw that a normal TB has negative displacements of about −150 μm at −1.5 kPa. The mobility had not changed at dissection stage B and C. Only from stage D; the lateral displacement amplitude increases slightly. A much larger increase occurs at stage E. In further stages, the TM can be considered hypermobile. Peak to peak displacements of 1 mm or more were measured. The largest displacements occur within −250 and 250 Pa range. We observed that in stages E and F, there could exist more than one rest state. If pressure were applied and subsequently be removed again, the TM would retain a very similar shape as when it was subjected to that pressure. We noticed that this could shift the total pressure-displacement curve up or down as the calculated displacements are in reference to the resting state.

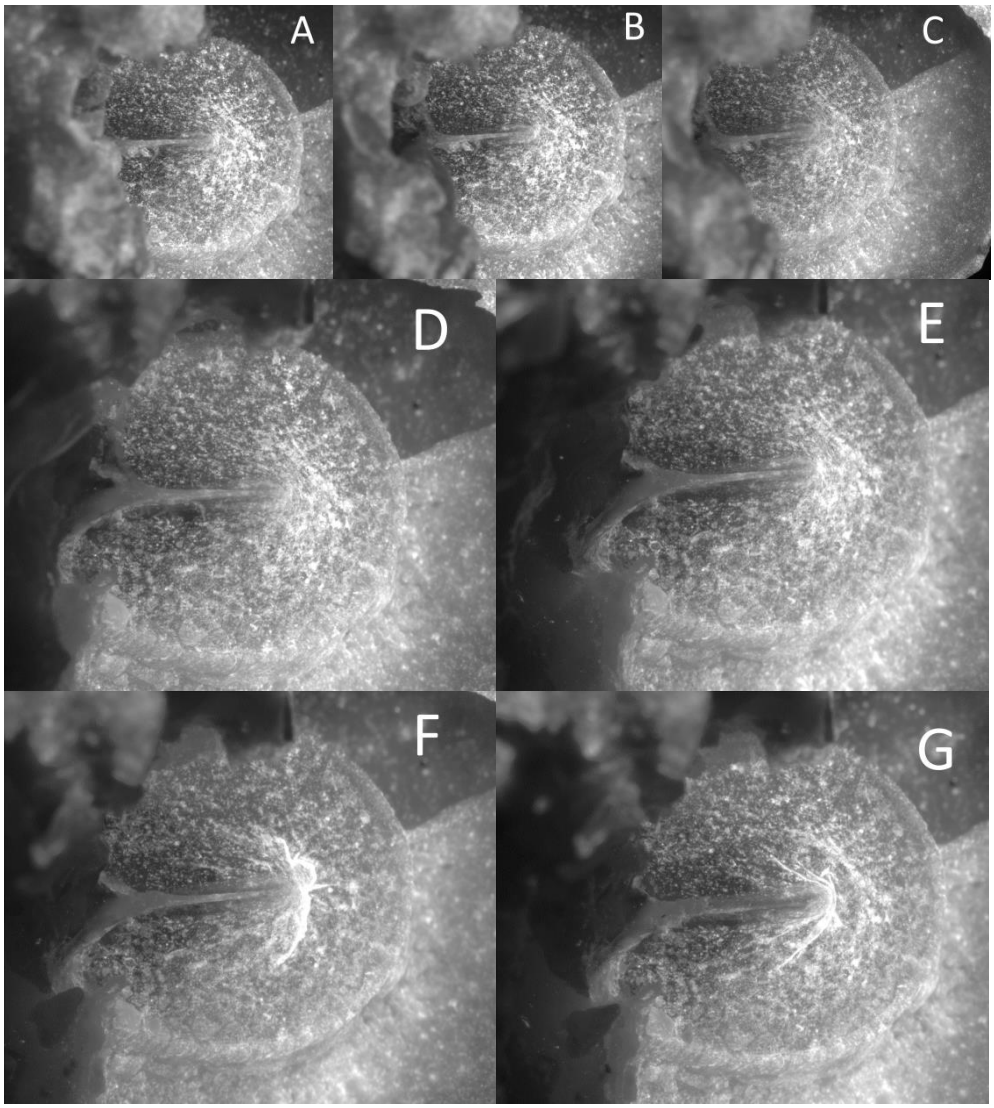

Figure 7.17: Photographs of a tympanic membrane during dissection of the middle ear. (A) middle ear as intact as possible. Presumably, the stapes footplate was not fully attached to the oval window. (B) Removal of tendon tympany,(C) stapes, (D) anterior mallear ligament, (E) posterior incudal ligament, (F) superior mallear ligament, and (G) superior incudal ligament. No real changes can be observed until stage F.

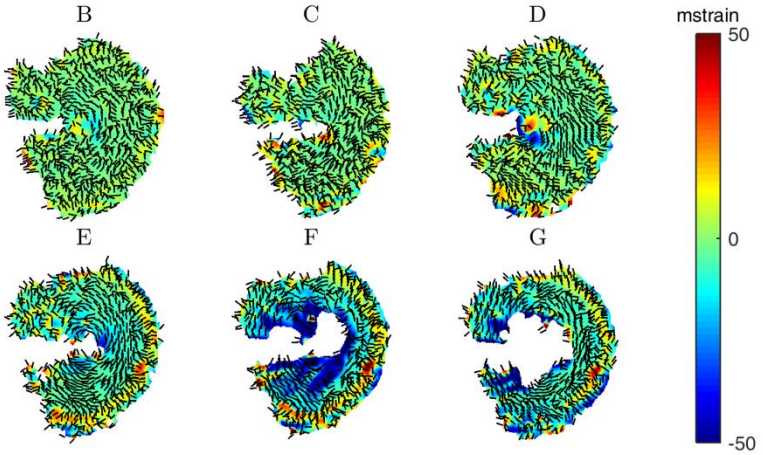

Figure 7.18: Tympanic membrane strain of stages B-G in comparison to stage A.

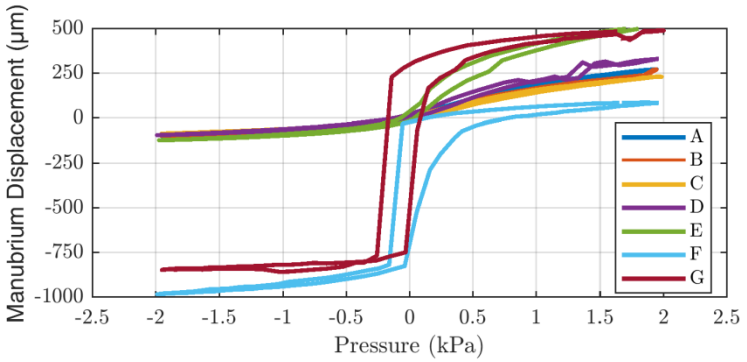

Figure 7.19: Displacement of the manubrium as a function of ear canal pressure for different dissection stages.

7.5.4 Discussion

Pre-strain

From all observations, we see that the removal of the tendon tympani and stapes do not affect the TM shape, strains, or displacements. However, note that the stapedial annular ring was probably fractured. Thus, we can only state that no change has been observed between a TB with loose stapes and removed stapes and tendon tympani. Only a small change was observed when removing the anterior mallear ligament. The principal strains got more aligned in the circumferential direction but the strain values were still very

small. Only when removing the posterior incudal ligament a large increase in lateral displacements was observed. Strain values increased with clear negative circumferential strains around the manubrium and positive radial strains at the inferior edge of the TM. The largest shape, displacement, and strain change occurred when removing the superior mallear ligament. Wrinkling of the tympanic membrane occurred, similar to the cases of malleus fractures. The elasticity of the TM seemed to be absent as the TM did not seem to return to a single state after being subjected to pressure. Only at pressures below or higher than -250 and 250 Pa respectively the ME showed some resistance against static pressures. These observations suggest that the TM is under pretension and that the source of this pretension lies in the superior mallear ligament. Presumably, the superior mallear ligament holds the malleus in a certain orientation and the TM simply holds onto the malleus and is therefore pre-strained. Removing the superior incudal ligament increased the peak-to-peak displacements a little more but the effect on TM strains could not be measured in the area around the manubrium due to the wrinkling of the TM.

So, do we know the amount of pre-strain in the rabbit TM? As mentioned before, the TM did not have a single resting state after removal of the superior mallear ligament. The measured strain difference was the strain when the TM was nearly flat and wrinkly. However, when a positive pressure was applied and subsequently removed, the TM shape would more or less recover. Presumably this would have been the best state to determine the amount of pre-strain in the TM.

TM wrinkling and correlation failure

The wrinkling of the TM after removing the superior mallear ligament caused the DIC method to fail. The wrinkles are very strong local deformations. The negative strains show that the speckle pattern has been squeezed together. At the location of the wrinkles, the pattern is squeezed so tight that the pattern becomes unrecognizable. We can already see this on the photographs (figure 7.17). The wrinkles are represented by the very bright lines in the image. The density of speckles is very high in these areas since the only light that is captured by the cameras originates from the speckles because we used the fluorescent powder. In dissection stage G, the malleus also seemed to be rotated towards the anterior side. The sharp edge of the malleus handle was never able to be correlated. The rotation of the malleus handle increased the area, which could not be correlated.

7.5.5 Summary

We found significant TM shape, mobility, and strain changes when removing the superior mallear ligament. After removal of the ligament, the TM showed no elasticity for pressures smaller than 250 Pa, positive or negative. These observations strongly suggest that the rabbit TM is pre-strained and that its source lies at the site of the superior mallear ligament.

7.6 Conclusion

In this chapter, we found that the rabbit TM is pre-strained. The TM is likely being pulled by the malleus due to a force applied by the superior mallear ligament. This can explain

why the negative strains for lateral movements of the TM is so much larger than the positive strains for medial movements. By pushing the TM laterally, the TM pre-strain is removed, which seems to be a large portion of the overall stiffness of the TM. In chapter 5, we hypothesized that the lateral displacements were easier due to the conical shape of the TM. This is not wrong. However, it might be that the pre-strain plays a more significant role in this story than the shape of the TM. It would be interesting to perform additional experiments in the human ME to see if the superior malear ligament performs the same function as in rabbits. Maybe the nonlinear behavior of the human ME is mainly caused by TM pre-strain instead of the shape of the TM.

Chapter 8:
QUANTIFICATION OF OSSICULAR FIXATIONS USING MINIMALLY INVASIVE VIBROMETRY (MIVIB)

Abstract

In previous chapters, we evaluated the functionality of the middle ear after a malleus fracture and the nonlinearity at high sound pressure levels. We were able to make observations at the level of the tympanic membrane. For some pathologies, measurements of the umbo mobility are insufficient, and the mobility of the individual ossicles has to be evaluated instead. In this chapter, we try to develop a clinical method for quantification of the effect and determination of the location of ossicular fixations based on TB experiments. A significant number of adults suffer from conductive hearing loss due to chronic otitis media, otosclerosis, or other pathologies. An objective measurement of ossicular mobility is needed to avoid unnecessarily invasive ME surgery and to improve hearing outcomes. Minimally invasive intraoperative laser vibrometry (MIVIB) provides a method that is compatible with ME surgery, where the tympanic membrane is elevated. The ossicles were driven by a floating mass transducer and their mobility was measured using a laser Doppler vibrometer. Utilizing this method, we assessed both the absolute velocities of the umbo and incus long process as well as the incus-to-umbo velocity ratio during artificial fixation of the incus alone, incus and malleus together or stapes. The change in incus velocity was shown to be the most suitable parameter to distinguish between incus, incus-malleus, and stapes fixation. MIVIB provides a promising objective analysis of ossicular mobility that would be useful intraoperatively.

This chapter is mainly based on:

Wales, J., Gladine, K., Van de Heyning, P., Topsakal, V., von Unge, M., Dirckx, J. 2018. Minimally invasive laser vibrometry (MIVIB) with a floating mass transducer - A new method for objective evaluation of the middle ear demonstrated on stapes fixation. Hear Res 357, 46-53.

Gladine, K., Wales, J., Silvola, J., Muyshondt, P., Topsakal, V., Van de Heyning, P., Dirckx, J., Von Unge, M. 2019. Evaluation of artificial fixation of the incus and malleus with minimally invasive intraoperative laser vibrometry (MIVIB) in a temporal bone model. Otol Neurotol (accepted).

8.1 Introduction

A significant number of adults suffer from a conductive hearing loss due to reduced mobility of the ME ossicles. The hearing loss is due to multiple pathologies such as otosclerosis, tympanosclerosis, malformations, and the sequelae of otitis media. In the case of ossicular fixation, hearing aids can partly alleviate the problem, but surgical treatment is often the best option to improve a patient's hearing. The best surgical result is based on knowledge of which ossicles are fixed and the degree that they are fixed. Traditionally, ossicle mobility is assessed by manual palpation. More recently, laser Doppler vibrometry was proposed as an objective alternative to assess the mobility of the ossicular chain (Peacock et al., 2013; Peacock et al., 2016; Rosowski et al., 2008; Zahnert et al., 2016)

Laser Doppler Vibrometry has shown promise to accurately measure the vibrational response of the ossicles. During ossicular surgery, the tympanic membrane (TM) must be (partly) elevated which renders sound-driven vibrometry impossible. To overcome this problem, our group has previously published work where the vibrational response of the umbo, the long process of the incus and posterior crux of the stapes was measured with laser vibrometry after the elevation of the tympanic membrane (Peacock et al., 2014, 2015, 2016). In this method, a small super magnet was attached to the manubrium, and an electromagnetic excitation coil was used to vibrate the ossicles (Figure 8.1). However, the clinical applications of this method were limited as attaching the super magnet with luting cement could be considered too invasive and time-consuming and the positioning of the driving magnetic coil difficult (Zahnert et al., 2016).

A clinically relevant alternative could be the use of the Med-El ® floating mass transducer with a suitable audio connector to vibrate the ossicles during measurement with laser vibrometry. This alternative is less invasive and less time consuming for the surgeon while providing valuable intra-operative information on the site and extent of fixation. This, in turn, would help surgical planning and therefore optimize surgical outcomes. It could also provide information on the outcome the surgeon might expect from an ossicular reconstruction, and the immediate perioperative feedback may give the surgeon a chance to revise the reconstruction to the patient's benefit (Zahnert et al., 2016). Therefore, we investigated the use of the floating mass transducer to drive ossicular vibration and assessed the changes in response to fixation of the stapes as seen in otosclerosis and incus and incus-malleus fixations

We coined the method MIVIB (minimally invasive laser vibrometry) and will be discussed thoroughly in section 8.2.1.

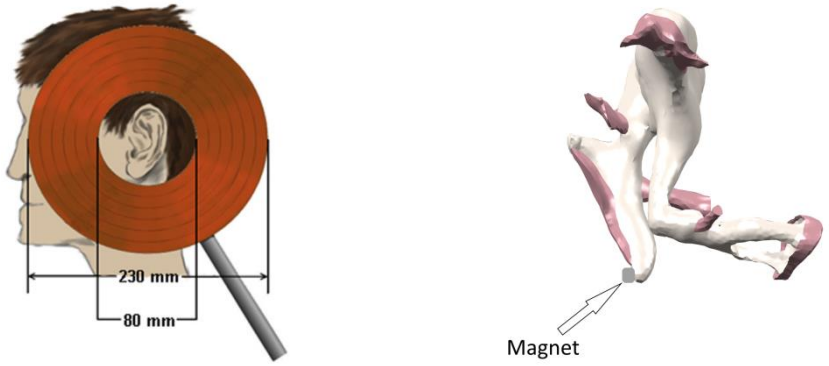

Figure 8.1: Sketch of electromagnetic excitation coil (A) used to excite small super magnet placed on the umbo after elevating the tympanic membrane (B) (Peacock et al., 2014, 2015, 2016)

8.2 Quantification of stapes, incus, and incus-malleus fixations

8.2.1 Materials and methods

Fifteen fresh-frozen human TBs were allowed to defrost at room temperature before the measurements and were examined for signs of abnormality such as external acoustic canal malformation or tympanic membrane abnormalities. Five TBs were used for stapes fixations while ten TBs were used for incus and incus-malleus fixations. Thirteen of the fifteens TBs were considered normal. In one TB, a large exostosis was observed which obscured the stapes and was therefore excluded from the study. One TB had a small exostosis, but this did not obscure the TM. Another TB was seen to have a shallow and narrow attic above the head of the malleus and the body of the incus. There was some connective tissue adherence, but no bony fixation between the ossicles and the tegmen bone. Both of these TBs were included in the study. One bone was excluded from the study as it was seen to have a TM which was severely retracted against the malleus, incus LP, crura of the stapes and promontory. Therefore 13 TBs were included in this study of which 4 TBs (referenced TBA-D) were used for stapes fixations and the remaining 9 TBs (referenced TB1-9) incus and incus-malleus fixations.

The LDV measurement set up is described in section 4.1. In some bones, aluminum foil from suture packaging was used instead of reflective tape. The mass of the patches is less than 0.04 mg and are about 0.4 mm x 0.4 mm in size (Niklasson et al., 2016).

For stapes fixation measurements, a free-field speaker positioned at 30 cm away from the temporal bone was used to generate the acoustic stimulus during measurements with an intact TM. Sound pressure was measured using a probe microphone (Bruel & Kjær probe

microphone, type 4182, Nærum, Denmark) with its probe needle positioned immediately above the entrance of the ear canal. In the case of incus and incus-malleus fixations, a small acoustic chamber (10ml volume) was placed over the ear canal opening, after removal of the pinna and cartilaginous canal, and was acoustically sealed to the temporal bone using silicone paste (Dreve Otoplastik GmbH, Otoform AK, Unna, Germany). An anti-reflection coated window at one side allowed visual access to the ossicles by the laser beam. The sound pressure at the level of the TM was measured using a probe microphone connected to a 25 mm long flexible tube which was put through a tightly fitting hole in the acoustic chamber. Sound pressure in the cavity was generated using a horn driver speaker (TOA, TU-650, Surrey, United Kingdom), which was connected to the cavity via a tube of 300 mm length. The signal was designed in a computer using MATLAB and generated using an A/D-D/A conversion board with 16-bit resolution, and a sampling rate of 50 kHz was used (National Instruments, USB-6251 BNC, Austin, TX, USA).

For the excitation, pure sine waves were used with frequencies ranging from 0.5-4 kHz and 0.25-4 kHz for stapes and incus(-malleus) fixations respectively. A sound pressure level of 90dB SPL was used. At each frequency, the stimulation signal contained 50 periods of that frequency and was extended with 0.1 s in order to exclude any transient effect. Measurements were taken at 16 lines per octave.

After performing the acoustic stimulation measurement, the TM was completely elevated (myringectomy), and reflective patches were placed on the umbo, the lateral surface of the distal (inferior) end of the incus long process (LP) and on the bony ear canal (as a negative control). An FMT with a suitable audio connector (Med-El, Innsbruck, Austria) was clipped onto the manubrium of the malleus using a left Incus-LP coupler that was manipulated so that the transducer was positioned in such a way that the longitudinal axis of the transducer body was parallel to the piston axis of the stapes (Figure 8.2A-C). Therefore, the transducer's main component of motion was aligned with the direction of the piston-motion of the stapes.

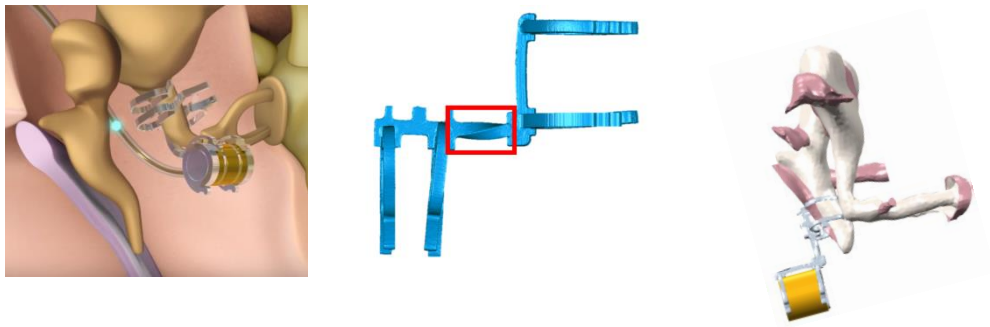

A B C

Figure 8.2: Sketch of the middle ear with incus-coupler attached to the incus (A) picture from MEDEL website, our adjustment of incus-coupler to make the floating mass transducer vibrate in the longitudinal direction of the stapes (B), sketch of the middle ear with the adjusted incus-coupler attached to the manubrium (C).

The signal to the transducer was again generated in MATLAB and amplitudes were adjusted until it produced an umbo velocity equivalent in level to the velocity produced by a 90 dB SPL acoustic stimulus in the intact ear (within 2dB). Measurements were then made at the three locations discussed above.

The FMT was rated for a maximal input voltage of 300mV. To make sure not to damage the device, the input was limited to 200mV. The signal coming from a D/A converter was sent to a custom-made current amplifier to drive the FMT.

Subsequently, the mobility of the ossicles was reduced by applying a few drops of glass ionomer luting cement (GC, Tokyo, Japan). The cement was applied using a syringe connected to an ear suction tube. Partial footplate fixation was achieved by placing one drop of the ionomer cement on the posterior stapes footplate. Full stapes fixation was achieved by placing ionomer cement around the whole of the stapes footplate. This was removed by lifting the cement with a small hook. Figure 8.3 shows one specimen before and after the application of the cement.

The TBs for incus and incus-malleus fixations were rotated 90 degrees superiorly with a custom-built clamp to expose the middle fossa for a straight angle access to the tegmen tympani. An otologic drill (W&H Dentalwerk, Bürmoos, Austria) was used to open the tegmen tympani sufficiently to expose the incudo-malleolar joint and surrounding structures, however, enough bone remained to allow fixation of the ossicles to the wall. In three TBs, the incus and malleus were both fixed in one step before measurement. In the 6 remaining TBs, the incus was fixed independently before measurement, and subsequently, the malleus was fixed in a second step before measurement of both fixations. The temporal bone was then rotated back 90 degrees so as to have exactly the same angle of the TB to the laser beam as with previous measurements. Both types of fixation are illustrated in figure 8.4. Due to technical reasons, the cement was not removed as could be done for stapes fixations. At each fixation stage, measurements were

again made at all measurement points. The ratio of the velocity amplitude with fixation to that of a TB without fixation of each ossicle was evaluated.

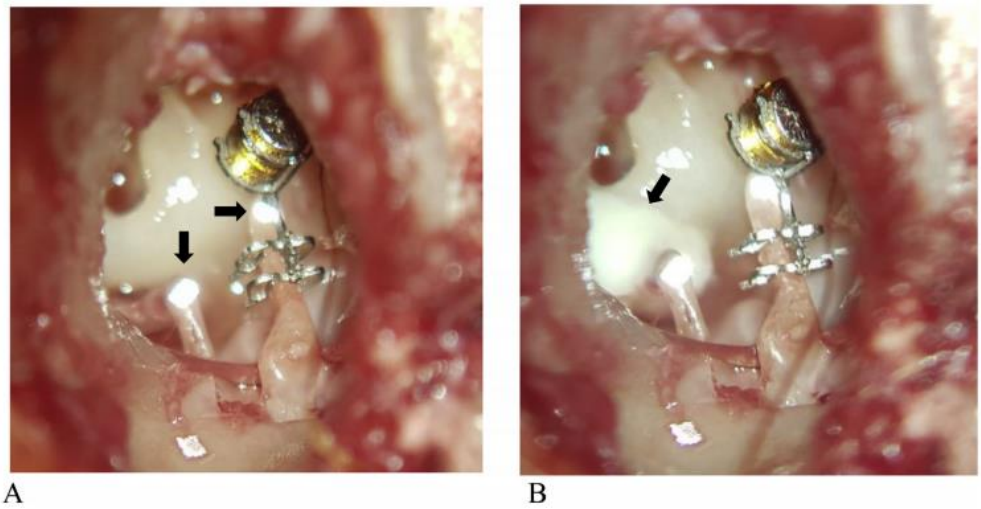

Figure 8.3: Photographs of TB4 obtained through the operating microscope. 1A, placement of the floating mass transducer and reflective tape (arrows). 1B, fixation of the stapes with ionomer luting cement seen as white material (arrow).

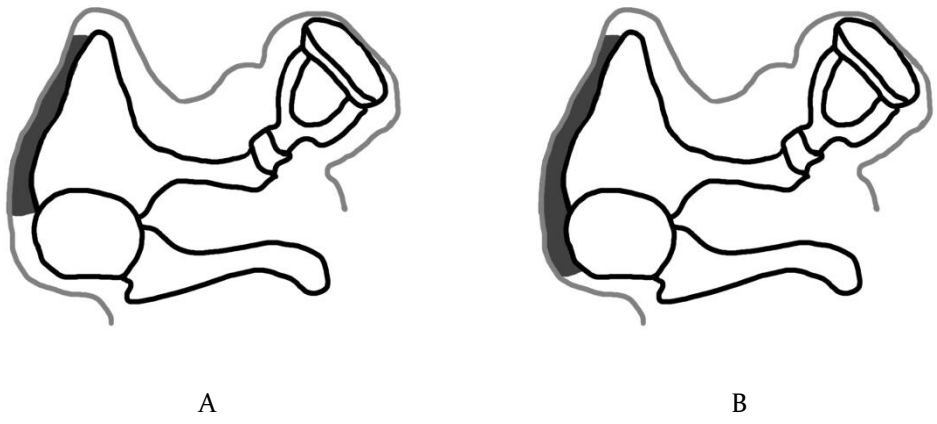

Figure 8.4: Illustration of incus fixation (A) and incus-malleus fixation (B).

8.2.2 Results

TB7 was accidentally lifted before performing the acoustic measurement. Therefore, the acoustic measurement could only be performed on 12 TBs. However, TB7 was still used in subsequent FMT measurements, as will be described in the next paragraph. Figure 8.5 shows the acoustically induced mean normalized umbo velocity of the remaining 12 intact temporal bones compared to other temporal bone measurements (Nakajima et al., 2005) and clinical measurements (Rosowski et al., 2012).

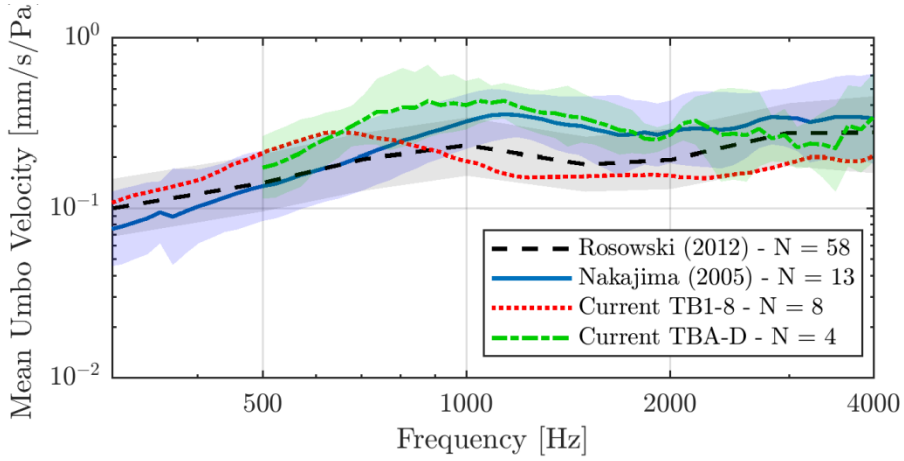

Figure 8.5: Comparison of the mean normalized umbo velocity of the intact temporal bones in this study to clinical measurements (Rosowski et al., 2012) and temporal bone measurements (Nakajima et al., 2005). A section of the annulus of the TM of TB7 was accidentally lifted prior to acoustic measurements and was therefore not included, hence only 8 out of 9 were used to calculate the mean umbo velocity.

The FMT was able to match (within 2dB) the umbo velocity produced by a 90dB SPL stimulus with the exception of sample D for three frequencies between 2.7 and 3.3 kHz, 250-284, 1542-1681, 1915 Hz and 250-310 Hz for respectively TB 2 and 6. Data acquired at these frequencies for this sample were therefore excluded from the study. Since a section of the annulus of the TM of TB7 was accidentally lifted before performing the acoustic measurement, the FMT input voltage was adjusted to match the acoustically induced umbo response of TB8 as this TB was of similar anatomy.

Change in umbo velocity amplitude

Figure 8.6 shows the average change in umbo velocity amplitude for different states of stapes fixation. Partial fixation caused a change of about -5dB up to 1.7 kHz. A net change up to -10dB occurred after full fixation. After fixation removal, an increase in umbo velocity occurred, bringing the net change close to 0dB at some frequencies or at the level of partial fixation at all other frequencies.

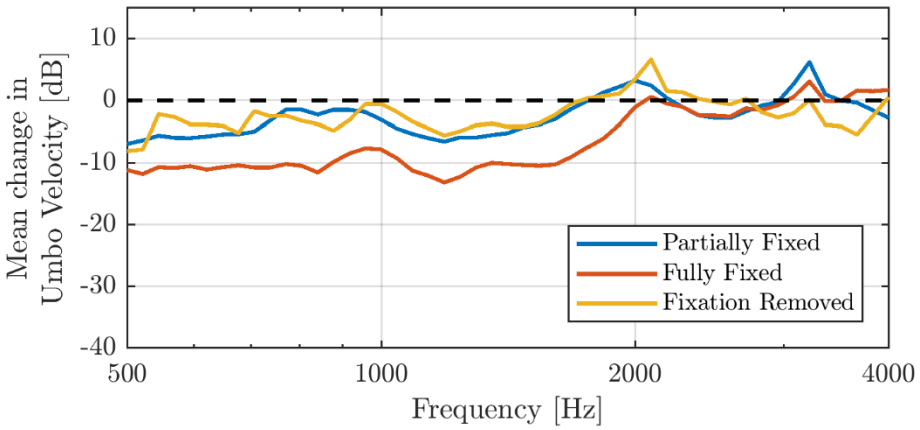

Figure 8.6: The mean change in umbo velocity amplitude in different stapes fixation states.

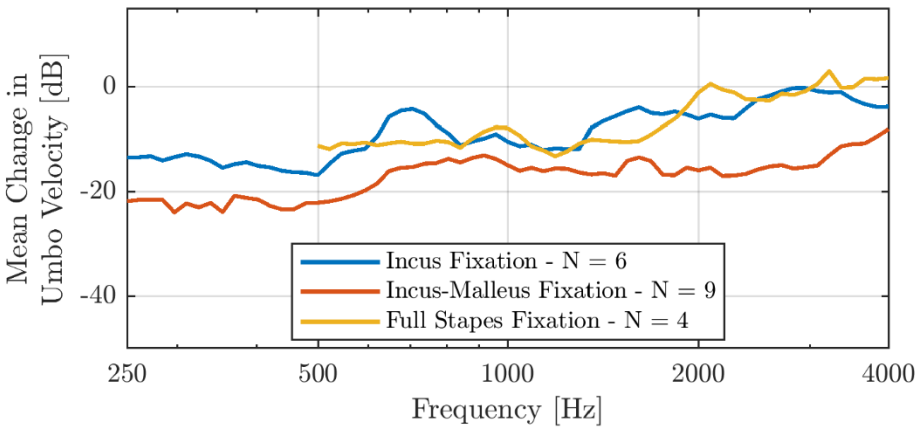

Figure 8.7: The mean change in umbo velocity amplitude for different fixation types.

Figure 8.7 shows the mean change in umbo velocity amplitude for a fixation of the incus alone (incus) or both the incus and malleus together (incus-malleus) together with full stapes fixation. In general, a reduction in the absolute velocity of the umbo was seen after fixation. The incus fixation caused a change in umbo velocity amplitude, which was on average -14.5±7.1dB below 0.5 kHz, -9.4±7.6dB between 0.5-1.5 kHz and -3.3±7.9dB above 1.5 kHz. The incus-malleus fixation showed higher reductions, on average -22.2±8.4dB below 0.5 kHz, -17.4±9.1dB between 0.5-3 kHz, and -16.3±9.8dB above 3 kHz. On average, the reduction in umbo velocity of an incus-malleus fixation was 8.4±3.1dB greater than for an incus fixation. This difference is most noticeable at the lower (<0.5 kHz) and higher frequencies (>1.5 kHz).

Change in incus velocity amplitude

On average, partial fixation caused a change of -10 dB up to 2.5 kHz with a local minimum difference seen at 2 kHz. After full fixation, the change reached values of -25 dB up to 1.6 kHz. At higher frequencies, the incus velocity change was closer to -15 dB. After fixation removal, an increase in incus velocity occurred, bringing the net change close to 0dB or at the level of partial fixation (Figure 8.8).

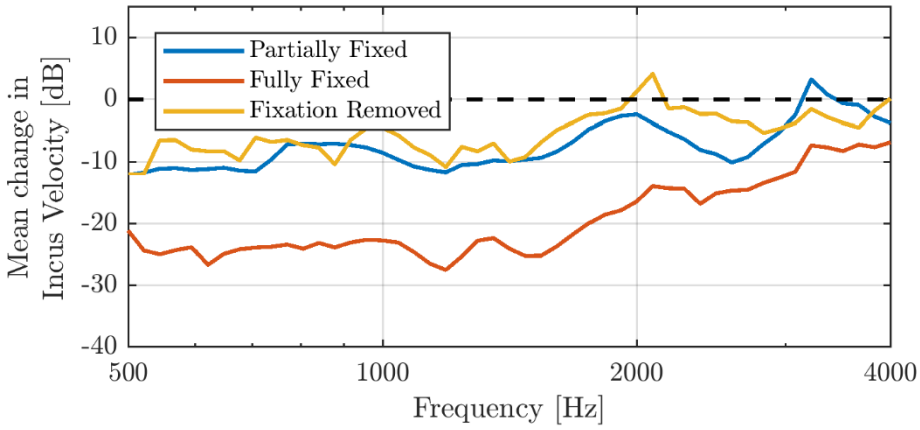

Figure 8.8: The mean change in incus velocity amplitude in different stapes fixation states.

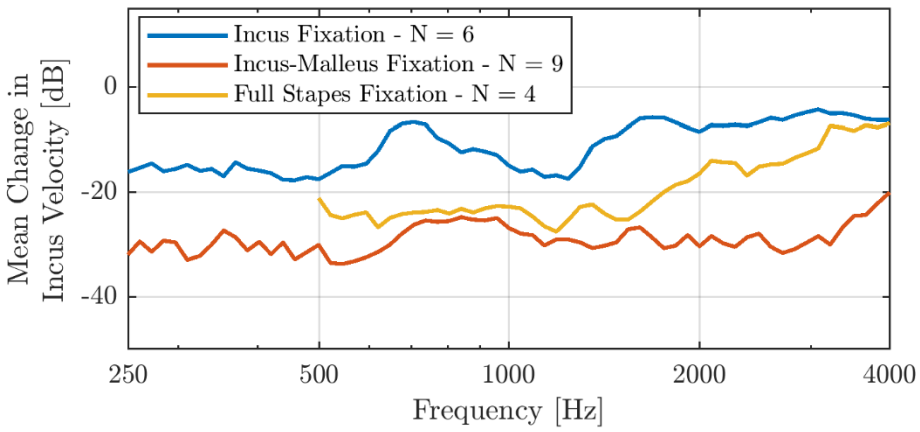

Figure 8.9: The mean change in incus velocity amplitude for different fixation types.

Figure 8.9 shows the mean change in incus velocity amplitude for an incus, incus-malleus, and full stapes fixation. Again, a reduction in incus velocity was seen for all types of fixation. After incus fixation, this decrease was on average -16.0±7.6dB below 0.5 kHz, -12.5±8.1dB between 0.5-1.5 kHz and -6.2±7.0dB above 1.5 kHz. The mean change in

incus velocity after malleus-incus fixation was fairly constant and was -30.0±11.5dB, except between 0.7-1 kHz for which it was -25.5±9.1dB and above 3 kHz for which the average was -25.1±10.8dB. On average, the reduction in incus velocity of an incus-malleus fixation was 17.7±4.3dB greater than for an incus fixation. This difference was smallest between 0.8-1.2 kHz (12.8±1.0dB) and, as with umbo velocity, the lower and higher frequencies were affected the most.

Change in incus-umbo velocity amplitude ratio

On average, a partial fixation caused a net change in the incus-to-umbo ratio of -5dB up to 3 kHz. A full fixation resulted in a net change of -15dB. The removal of the fixation resulted in a movement towards zero but was nearer the level of the state of partial fixation (Figure 8.10).

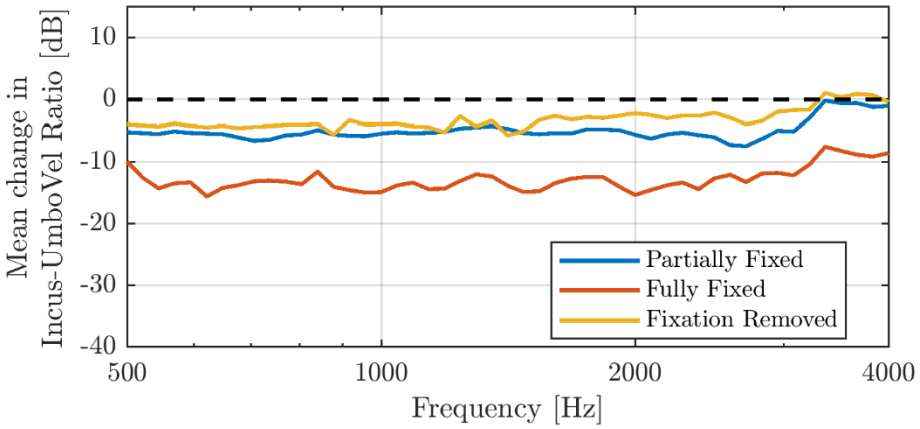

Figure 8.10: The mean change in incus-umbo velocity amplitude ratio in different stapes fixation states.

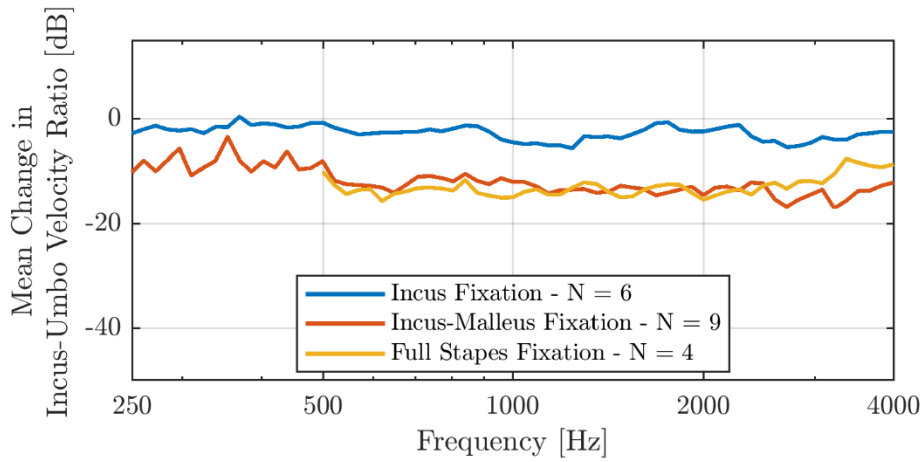

Figure 8.11: The mean change in incus-umbo velocity amplitude ratio for different fixation types.

Figure 8.11 shows the mean change in incus-umbo velocity amplitude ratio for an incus and incus-malleus fixation and their SDs. After incus fixation, the average change in incus-umbo velocity ratio was fairly constant across all frequencies. This change ranged from -5.6dB to 0.4dB with a mean value of -2.6±6.4dB. The mean change in incus-umbo velocity ratio after a malleus-incus fixation ranged from -16dB to -3.4dB with a mean value of -11.9±10.4dB. The reduction was seen to be the smallest below 0.5 kHz. On average, the reduction in incus-umbo velocity ratio of an incus-malleus fixation was 9dB higher than for an incus fixation. This difference was smallest below 0.5 kHz.

8.2.3 Discussion

The mean normalized umbo velocity was compared to other temporal bone measurements (Nakajima et al., 2005) and clinical measurements (Rosowski et al., 2012) (figure 8.5). Our data is in good agreement with the referenced data. Our data did not differ more than 3.5dB from clinical measurements, confirming that the TBs were normal. The largest deviations were seen around the resonance frequency of 1 kHz.

As previously reported by us and others (Merchant et al., 2016; Nakajima et al., 2005; Peacock et al., 2016), this work confirms that a fixation in the attic can be simulated by utilizing cement to fix the malleus or incus to the tegmen. MIVIB was able to show that this fixation led to a significant reduction in the absolute velocities of both the umbo and incus.

The FMT driving voltage differs between each ear, especially in the lower frequency region where the differences could be large. For instance, the driving voltage in the region between 0.5 kHz and 0.8 kHz differed with a factor of 10 between sample B and C. For sample D, in the frequency region between 2.7 kHz and 3.3 kHz, the maximal driving voltage of 200mV was insufficient to obtain the same umbo response as with acoustic

stimulation. The differences between the needed stimulation voltages are maybe due to the differences in umbo response for the different specimens, but can also be partly due to the inevitable differences in the exact placement of the FMT on the manubrium.

As measurements were taken through the ear canal, little liberty was available in choosing the incidence angle of the laser vibrometer. As the orientation of the ossicles concerning the ear canal is largely constant over different subjects, the measurement angle will also be mainly the same, but it cannot be controlled or measured precisely. For this reason, we did not apply a cosine correction to the measured data. As the ossicles are very close together, moving from one ossicle to the other would change the beam angle by less than a few degrees and not affect the results in a significant manner. Although the motions of the ossicles become more complicated in the higher frequency region, the main motion component remains in one direction (Hato et al., 2003) and the effect of the measurement angle is constant. The inevitable variability in laser vibrometer measurement angle will, therefore, have a limited effect on the measured response ratios.

For sample B, the umbo velocity amplitude was not affected after partial/full stapes fixation. For the other samples, the effect of stapes fixation was less for the umbo velocity than for incus velocity. The net change in umbo velocity was only negative up to about 2 kHz. This indicates that using only umbo velocity measurements to determine stapes fixation is unreliable.

On average, the net change in incus velocity was below zero for frequencies below 3 kHz in the case of partial stapes fixation. The frequency range for which the net change in velocity was below zero is thus broader for incus velocity than for umbo velocity. For all samples with full stapes fixation, the change in incus velocity was well below zero and easy to perceive over the entire frequency range.

Removal of the cement increased incus and umbo velocity amplitudes and their ratio for most frequencies. For two samples (B and D), the removal was less successful as there was some residual cement left in the TB. The umbo velocity data of sample B does not show this, as the umbo velocity was not affected by the stapes fixation in the first place. However, the changes in incus velocity and incus-to-umbo velocity ratio do reflect this unsuccessful removal of cement. Although samples A and C showed proper restoration based on their incus-to-umbo ratios, incus and umbo velocity amplitudes were on average about 3dB lower compared to those of the unfixed TBs with peak differences of about -9dB.

For an incus fixation, the reduction of incus velocity was similar to that of the umbo velocity. This was reflected by the change in incus-umbo velocity ratio, which was close to 0dB.

An incus-malleus fixation resulted in a larger reduction of incus and umbo velocity, but the amount of incus velocity reduction was greater. For an incus-malleus fixation, the change in incus-umbo velocity ratio was, therefore, larger (-11dB). In some cases of incus-malleus fixation, the incus velocity magnitude coincided with the noise floor. This

implies a completely immobile incus, although we cannot guarantee this because of the noise floor limit.

Once we placed cement in the attic, the incus was fixated on the lateral and superior surfaces of its corpus incudis, as compared to the malleus which was fixated at the attic. If the malleus head is fixed extensively, the transmission to the incus is reduced drastically, but the umbo velocity is reduced less since the manubrium can still bend (Nakajima et al., 2005). As a consequence, the most substantial difference between incus and malleus-incus fixation can be found by evaluating the change in incus velocity. It shows the least overlap in standard deviations of both types of fixations. A considerable frequency region around 0.65 and 3 kHz has no overlap of the standard deviations intervals. The change in incus velocity, therefore, seems most suitable to distinguish between an incus and incus-malleus fixation.

Fixation of the stapes resulted in a reduction of the absolute velocities of both the incus and umbo and the incus-umbo velocity ratio. An incus fixation leads to a smaller change in incus velocity than stapes fixation. This is because we measure the velocity at the incus tip. The motion of the incus tip is orientated in the direction of the stapes piston movement. As a consequence, the stapes fixation has a more significant effect on incus tip velocity than incus fixation. The change in incus velocity allows again for distinguishing an incus fixation from a stapes fixation. In contrast, it is impossible to distinguish an incus-malleus fixation from a stapes fixation at low frequencies.

However, if one compares the change in velocity of the incus and umbo over the entire frequency range, malleus-incus fixations led to a substantial reduction in these absolute velocities over all frequencies. Stapes fixations, however, led to a smaller reduction in those absolute velocities where the higher frequencies (>2kHz) were less affected, similar to the effect of experimental and clinical stapes fixations measured by (Nakajima et al., 2005) and (Nakajima et al., 2012) respectively. In our previous study (Peacock et al., 2016), and others (Dai et al., 2007), fixation of the anterior ligament of the malleus showed a resulting reduction in umbo and incus velocities that were less significant in the higher frequencies. This shows that although both fixations occur in the attic, a fixation of the anterior mallear ligament and a bone-to-bone fixation, as in our study, can elicit different patterns with laser vibrometry. A thorough assessment of several types of fixations in several temporal bone studies would enable us to deduce a more consistent pattern.

An experimental study (Nakajima et al., 2005) assessed the umbo and stapes velocity for several types of fixations. The stapes velocity was correlated with the air-bone gap. If the stapes and umbo velocity were sufficient to differentiate between fixation types, then this differentiation could be done non-invasively by measuring the air-bone gap and the umbo velocity through the ear canal. The study showed that stapes fixations could clearly be distinguished from malleus fixations. In the same study on two temporal bone specimens, incus fixations were differentiated from stapes fixations through the greater loss in umbo velocity with incus fixations. This pattern at the umbo was not observed in our study. However, we found that there was an average difference of 9.8 dB change in incus velocity between stapes and incus fixations.

Distinguishing between malleus, malleus-incus, or malleus-stapes fixations is impossible using only stapes and umbo velocity data (Nakajima et al., 2005). Future experiments may show whether incus velocity measurements can aid to resolve this problem. Our measurements show that the change in incus velocity allows distinguishing between incus, incus-malleus, and stapes fixations. The most sensitive frequencies are 0.65 and 3 kHz. At 0.65 kHz, incus fixations show a change of only -8dB while incus-malleus and stapes fixations show changes of -30dB and -25dB respectively. Thus, a clear distinction can be made between incus fixations and incus-malleus or stapes fixations. To distinguish between incus-malleus and stapes fixation or incus fixation, one can observe the change in incus velocity at 3 kHz. A change of -4dB, -11dB and -28dB were measured for incus, stapes and incus-malleus fixation respectively, clearly separating incus-malleus fixations from the other fixations. However, it may prove in future studies that it is important to compare absolute velocities (Nakajima et al., 2005; Rosowski et al., 2008) and their ratios (Dobrev et al., 2016; Wales et al., 2018) at several sites in the ossicular chain over the whole frequency range to distinguish between different fixations.

A firm attachment of the FMT to the manubrium is essential. When the FMT is not firmly clamped, it requires a higher input voltage at specific high frequencies to mimic the acoustically induced vibrations obtained at 90dB SPL with an intact membrane. This could explain the results in sample D for which there was not sufficient power in the frequency range of 2.7-3.3 kHz.

Clinically, the MIVIB system would be useful to assess where a fixation is located, quality control in ossiculoplasty (Zahnert et al., 2016) or to assess new prosthesis systems (Gottlieb et al., 2016). Incus velocity could be used to discriminate between stapes, incus, and incus-malleus fixations. Distinguishing other types of fixations may require a combination of umbo velocity, incus velocity, and incus-umbo velocity ratio or other measurements. The inclusion of stapes velocity, for example, could be useful to differentiate between other fixation combinations (Nakajima et al., 2005). However, one should be careful to use strict quality control so as not to use a “tired” coupler. Although two frequencies (0.65 and 3 kHz) were suggested for which the change in incus velocity suffices to distinguish between incus, incus-malleus and stapes fixations, an observation of the absolute velocities over a large frequency range can easily reveal a “tired” or badly attached coupler. Therefore, we believe it is important to keep performing velocity measurements over a large frequency range.

A critique of laser vibrometry could be that adherent reflective patches are used to amplify the signal. This would result in glue contacting the ossicular chain. As this is an undesired effect intraoperatively, aluminum foil (from suture packaging) was used and shown to have the same reflective properties to enhance the laser signal. This allows for a more attractive process to be used clinically.

In cases where the eardrum is lifted entirely, the method is minimally invasive as the FMT is just clipped onto the manubrium without any adhesive substances and can be easily removed without leaving any trace. This method only uses licensed clinical products, which have been shown over several years to be safe. In an ongoing study we are working on the development of a more compact custom-made clip which will allow

positioning the FMT in the upper half of the manubrium, allowing maintaining the lower part of the TM and its connection to the manubrium intact. This can be achieved with a new clip design that will reduce the space occupied by the FMT-and-clip unit. It is also relevant that the procedure of making the acoustic stimulated measurement and achieving the equivalent umbo velocity using the FMT takes less than 4 minutes. Subsequent measurements are done quickly, taking less than 8 seconds, which is important for clinical applications. However, further in-vitro study and modifications of the procedure are necessary prior to an attempt in live patients.

8.3 Clinical implementation

8.3.1 Are acoustic measurements redundant?

In section 8.2.1, we described the measurement procedure used in our TB studies. It involved an umbo velocity response measurement using a sound stimulation of 90dB SPL. Subsequently, the TM was removed, and the FMT was placed on the manubrium. The voltage input to the FMT was then adjusted in order to obtain the same umbo velocity response as for the sound measurement. This ensures that the inner ear in patients is not overloaded since the ME stimulation is equivalent to that of a 90dB SPL sound. Is this useful in a clinical situation?

The TBs used in our studies were considered healthy. For this reason, adequate vibration levels were obtained, providing a high signal to noise ratio at an equivalent stimulation of 90dB SPL. For a clinical case, this is not true. Since the patients are on consultation, they have conductive hearing loss. As a consequence, a 90dB SPL sound stimulation can result in very low umbo vibration levels. Since we use the FMT to replicate the umbo response, we will obtain data with a low signal-to-noise ratio.

On top of that, the measurement using acoustic stimulation is one of the most time-consuming parts of the whole procedure. For the TBs we placed a cavity with a window on top of the ear canal and made it airtight. If this part of the procedure can be avoided, the easier it is for the surgeon to apply the method. Can we avoid the measurement using acoustic stimulation and still maintain safe vibration levels in order not to overload the cochlea?

During the TB experiments, we recorded what the input voltage to the FMT was after we adjusted it to obtain the same umbo velocity response as when using a sound stimulation at 90dB SPL. We can use this data to design new input voltage signals and can then calculate what the equivalent sound pressure level would have been. We can, for example, calculate an average of the FMT input voltage curves (Figure 8.12) to produce an equivalent stimulation of 90 dB SPL. By comparing this average input signal to that used for the individual TBs, we can evaluate its equivalent sound pressure level (Figure 8.13). We observe that for most frequencies, the equivalent sound pressure level stays within a range of 80 to 100 dB SPL. An alternative is using a constant voltage for all frequencies to drive the FMT. The amount of voltage requires careful consideration. In TBs, we used a 200 mV RMS input for which the equivalent sound pressure levels are shown in Figure 8.14. At mid frequencies, an equivalent sound pressure level of 106 dB is reached. At low

frequencies, we obtain equivalent SPLs of only 70dB. As long as the vibration levels are such that a good signal to noise ratio is obtained, these lower vibration levels are not a problem.

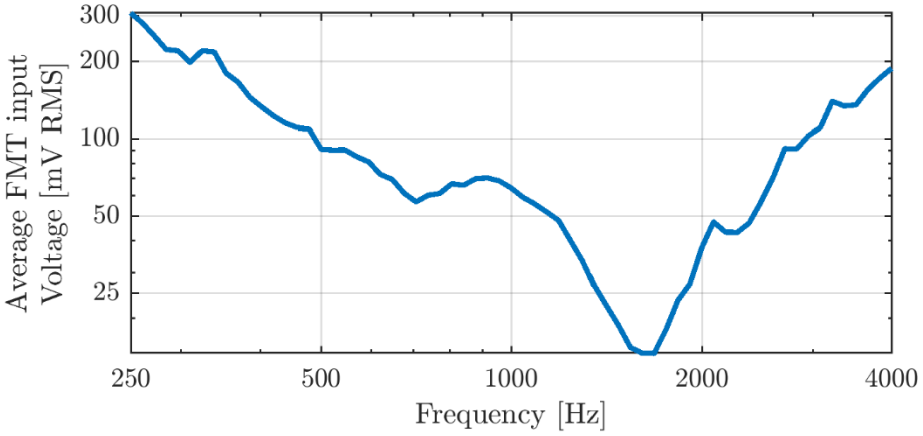

Figure 8.12: FMT input voltage signal determined by averaging the FMT input voltage signals generating an equivalent sound pressure level of 90 dB SPL in 12 temporal bones.

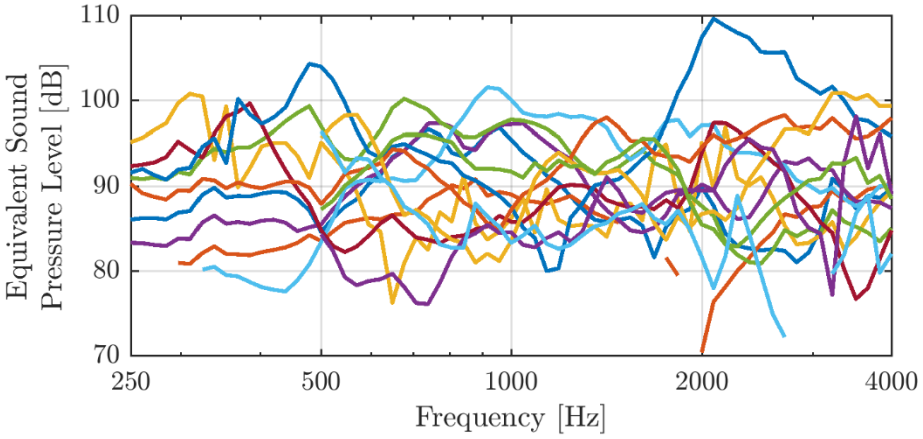

Figure 8.13: Predicted equivalent sound pressure level for 12 temporal bones if the average FMT input voltage signal were to be used instead of the individual FMT input voltage signal.

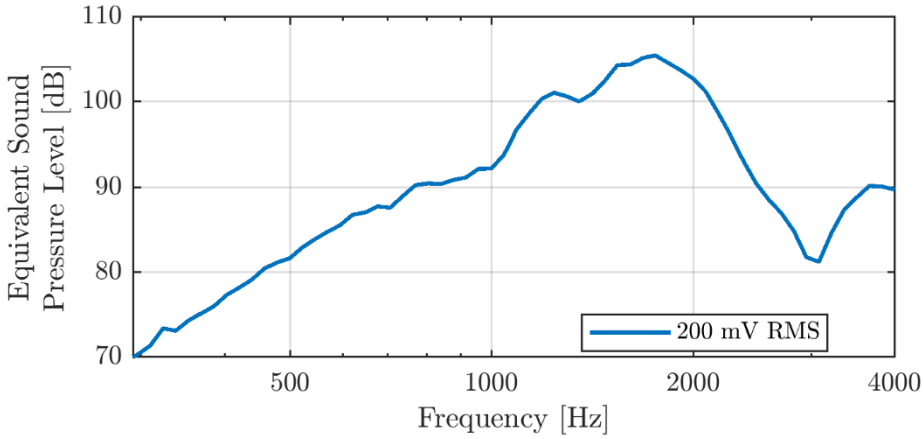

Figure 8.14: Calculated equivalent sound pressure level of one temporal bone when a constant 200 mV RMS signal was used to drive the floating mass transducer.

In the TB experiments, the ossicle vibration responses of the healthy ears were compared to those of the same ears with a fixation. In the clinical case, we do not have a healthy vibration response reference for the subject. As a consequence, we need a reference. This reference needs to be based on the type of stimulation signal which is going to be used since a constant voltage input signal would return a very different healthy vibration response compared to the calculated average FMT input signal mentioned earlier. Note that the average input signal should be calculated for identical measuring conditions. The sound measurements were performed in diverse manners for different sets of TBs. The sound measurements of TBA-D were done at the entrance of the ear canal, while the sound in TB1-8 was measured closer to the umbo. These discrepancies return different umbo response levels and consequently also different FMT input signals. Similar arguments can be made for FMT placement, sites of vibration measurements, angle of the laser. The approach has to be standardized, and reference data has to be gathered accordingly.

8.3.2 Real-time measurements using multisine stimulation

Surgeons can benefit from real-time measurements when performing operations on a patient. Micro adjustments can result in different outcomes, and it could, therefore, be useful to observe in real-time whether such adjustment improved the vibration levels in a patient. Single sine measurements using a frequency range of 250 to 4000 Hz with 16 lines per octave for 50 periods and a 0.1 s transient time can take up to 11 seconds. Adjusting the parameters above can reduce measurement time, but real-time measurements are out of order. The multisine provides a solution to this problem by stimulating at multiple frequencies simultaneously. The measurement time is mainly determined by the requested frequency resolution. A frequency resolution of 5 Hz should allow for five measurements per second. The main bottleneck will be the refresh rate of the software calculating and displaying the real-time vibration response.

However, using multisine stimulation poses other limits. The total amount of energy has to be divided over all frequency components. If we want to drive the FMT to obtain an equivalent sound pressure level of 90 dB SPL, each frequency component will have a lower equivalent sound pressure level.

8.3.3 FMT placement and evaluation sites

In the TB experiments, a full myringectomy was performed before the FMT was placed on the manubrium. In cases where the eardrum is lifted entirely, the method is minimally invasive as the FMT is just clipped onto the manubrium without any adhesive substances and can be easily removed without leaving any trace. In an ongoing study, we are working on the development of a more compact custom-made clip which will allow positioning the FMT in the upper half of the manubrium, allowing to maintain the lower part of the TM and its connection to the manubrium intact.

In one TB, the superior part of the TM was lifted and folded over to the inferior side, revealing the stapes, incus and a portion of the manubrium. The umbo is covered, and we are thus required to choose a different evaluation site than for previous measurements. We measured in the middle of the manubrium (halfway between the lateral process and umbo). And we measured the vibration levels in a quarter, close to the lateral process. Figure 8.15 shows that the change in velocity between both measurement spots is similar after full stapes fixation. The manubrium velocity barely changes at all. The change of the incus velocity deviates from previous measurements between 1-2 kHz (figure 8.6). Although only one TB was used here, we note that the different placement of the FMT might result in different changes in velocity amplitude after fixation. We stress again that the method has to be standardized, and then data has to be collected accordingly.

Previous experiments did not include a measurement of the stapes (shoulder). From Figure 8.15, we can conclude that such measurements can be useful. For stapes fixations, the change in stapes shoulder velocity amplitude is largest. This might facilitate distinguishing different type of fixations. Additional stapes measurements for different types of fixations should be made.

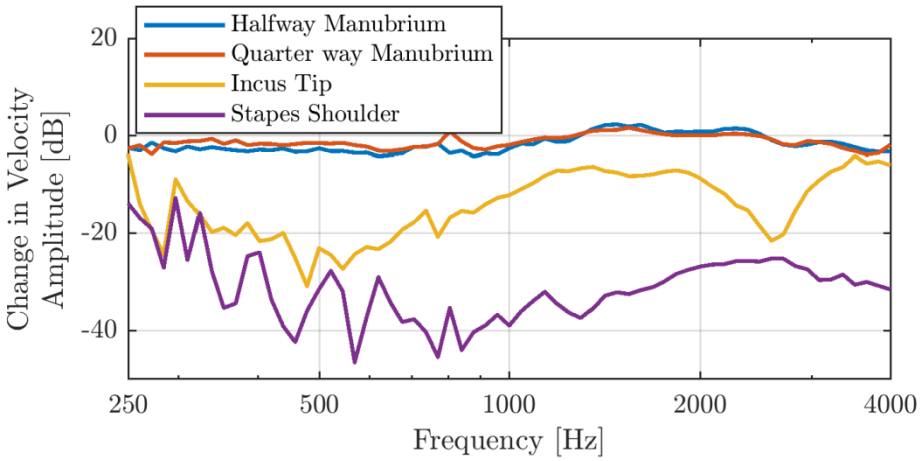

Figure 8.15: Change in velocity amplitude for different measurement points when only the superior region of the tympanic membrane has been lifted, and the floating mass transducer has been placed more superiorly on the manubrium.

8.4 Locating source(s) of nonlinearity

In section 5.2, we discussed how Dirckx and Decraemer (2001) investigated the effect of ME components on the quasi-static deformation in rabbits by sequentially removing ME components beginning with the cochlea and stapes, and working their way down the ME chain. We mentioned it would be interesting to use a similar approach when investigating dynamic nonlinear behavior. The floating mass transducer allows to invert the removal sequence. We can stimulate the ME by placing the FMT on the incus (or possibly the stapes) and start by removing the TM. This way, we remove the influence of the TM on the ME nonlinearity, and by using the FMT we can keep stimulating the ME, no sound source is needed. We can then find other possible sources of nonlinearity by measuring the nonlinear response of the remaining system like the upper limit of stapes displacement (Price, 1974).

8.5 Conclusion

The use of the MIVIB system can discriminate between a variety of fixations in the middle ear. We believe the use of this system would improve surgical planning to reduce the risk of doing an unnecessarily extensive operation in the middle ear and therefore improve surgical outcomes. However, some issues still have to be addressed. The method has to be standardized, and more data has to be collected.

Chapter 9:
AVERAGE MIDDLE EAR FREQUENCY RESPONSE CURVES WITH PRESERVATION OF CURVE MORPHOLOGY CHARACTERISTICS

Abstract

For the validation of modeling results, or the comparison of middle ear interventions, such as prostheses placement, average responses of middle ear vibrations are needed. One such response is the amplitude and phase of the vibration of the stapes footplate as a function of frequency. Average responses and their standard deviation are commonly obtained by calculating the mean of several measured responses at each frequency. A typical middle ear magnitude response curve shows several distinct peaks, and the location of these peaks varies between ears. By simply taking an average along the magnitude or phase response axis, the typical fine structure of the response curve is flattened out, delivering an average curve which no longer has the typical morphology of an individual response curve. This chapter introduces methods to avoid this problem by first aligning the typical curve features along the frequency axis before calculating the average along the magnitude or phase axis, resulting in average magnitude and phase curves which maintain the typical morphology of the curve obtained for an individual ear. In the method, landmark points on the response magnitude curves are defined, and the frequencies at which these points occur are averaged. Next, these average frequencies are used to align the landmark points between curves, before averaging values along the magnitude or phase axes. Methods for semi-automatic and manual assignment of landmark points and curve alignment are presented. After alignment, the correspondence between the original landmark frequencies and aligned frequencies is obtained together with the warping function, which maps each original magnitude curve to its aligned version. The phase curves are aligned using the warping functions determined from the corresponding magnitude curves. Finally, a method is proposed to compare the data set of an individual measurement or model result in an aligned average curve in terms of magnitude and frequency by applying the alignment procedure to the individual curve.

This chapter is based on:

Gladine, K., Dirckx, J.J.J. 2018b. Average middle ear frequency response curves with preservation of curve morphology characteristics. Hear Res 363, 39-48.

9.1 Introduction

Frequency response curves of ossicular vibrations provide important data for the validation of middle ear modeling results. As many models are built using average material parameters and shapes, it is common to compare the model outcome to average response curves (De Greef et al., 2017). The most common way to obtain such a response curve is to average magnitude and phase values for each measured (or interpolated) frequency. Such averages give a good representation of the general frequency response of the middle ear (e.g. Rosowski et al., 2007).

Each individual response curve has a specific morphology, with local maxima that can be attributed to some extent to specific physiologic parameters or characteristic properties of the system, such as the resonance frequency of the ear canal (Keefe et al., 1993; Stinson, 1990) or the first ossicular mode (Homma et al., 2009). As shapes, masses and other parameters of middle ear structures vary from one individual to the next, both the height and frequency location of local maxima differ. By averaging along the magnitude axis (or along the phase axis), the sharpness of these local maxima diminishes because for each individual specimen the frequency location of the maximum is slightly different. As a result, the average response curve taken over many specimens shows a much less detailed structure than an individual response curve, and the typically peaked morphology of the curve tends to flatten out towards a broadly spread maximum at a center frequency. These less-pronounced peaks/troughs could easily be misinterpreted by modelers to mean that the middle ear is more damped than it really is.

Therefore, it would be useful to generate average response curves which preserve the typical morphology of the individual response curve. In this chapter, we present a procedure to first align the typical morphologic features of response curves along the frequency axis before taking the cross-sectional average along with the magnitude or phase axis.

9.2 Materials and Methods

9.2.1 Input data

To demonstrate the new processing method, we used stapes vibration data obtained from human temporal bones in previous work (Niklasson, 2017). In these experiments, the stapes footplate velocity was measured from the medial side at the center of the footplate after removal of the inner ear, and sound stimulation was presented through the intact ear canal. Therefore, the response curves show the transfer function of the middle ear system without cochlear loading. Measurements were taken at 16 frequencies per octave in a frequency range of 0.125-8kHz. As the processing of the data benefits from using more densely sampled curves, the curves were resampled using smoothed spline approximation to obtain a set of 500 logarithmically spaced data points.

9.2.2 Assigning landmarks

The alignment algorithm makes use of landmark points, which are to be defined on individual curves (Kneip and Gasser, 1992). In this section, we describe two ways to assign such landmark points. These landmark points will be used to align the vibration magnitude and phase curves.

Manual landmark assignment (MLA)

The least complex way to assign landmarks to the response curves is by choosing them manually. This is done by visually inspecting the data curves, choosing a curve feature, and noting the frequency at which this feature occurs for each curve. This can be done for several features. If a feature is not present in an individual curve, the landmark point is not assigned.

Up to 5 landmark points were used, which will be described in detail in the results section.

Semi-automatic landmark assignment (SLA)

In the semi-automatic assignment, peaks in the curve are automatically detected. Then, conditions are set to filter the found peaks such that only the peaks of interest remain.

To find the peaks, we have used the MATLAB function *findpeaks*. We then applied mathematical conditions to limit the number of found peaks to three landmarks. The conditions for each landmark were:

- The peak frequency was required to be lower than 1.5 kHz. In addition the peak frequency was required to be close to 1 kHz and preferred to have a high peak prominence. These last two conditions were applied using weighting. This landmark is indicated by a circle in figure 9.2.
- The peak with the highest amplitude (indicated by an asterisk in figure 9.2).
- The peak frequency was required to be higher than that of the peak with the highest amplitude. In addition, the peak frequency was required to be the closest to 5 kHz (indicated by a diamond in figure 9.2).

The resulting landmarks are displayed in the results section in figure 9.2. And the corresponding frequencies are given in table 9.1.

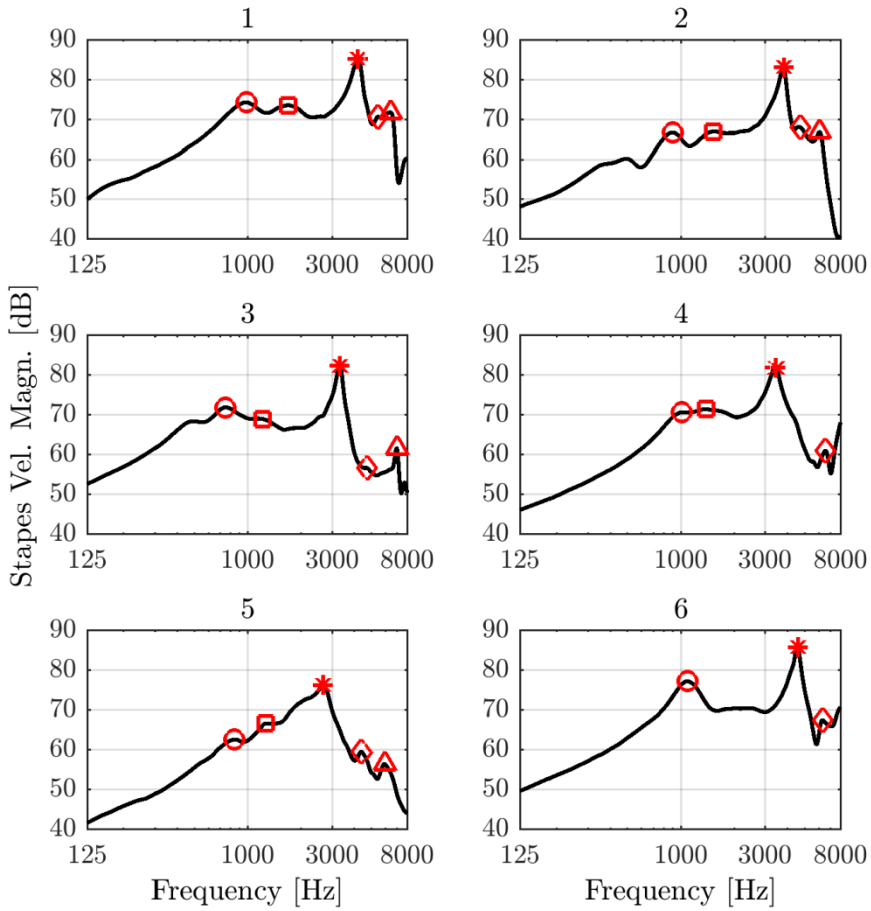

Figure 9.1: Manually assigned landmarks for each stapes velocity magnitude curve. Each corresponding landmark is denoted using the same symbol.

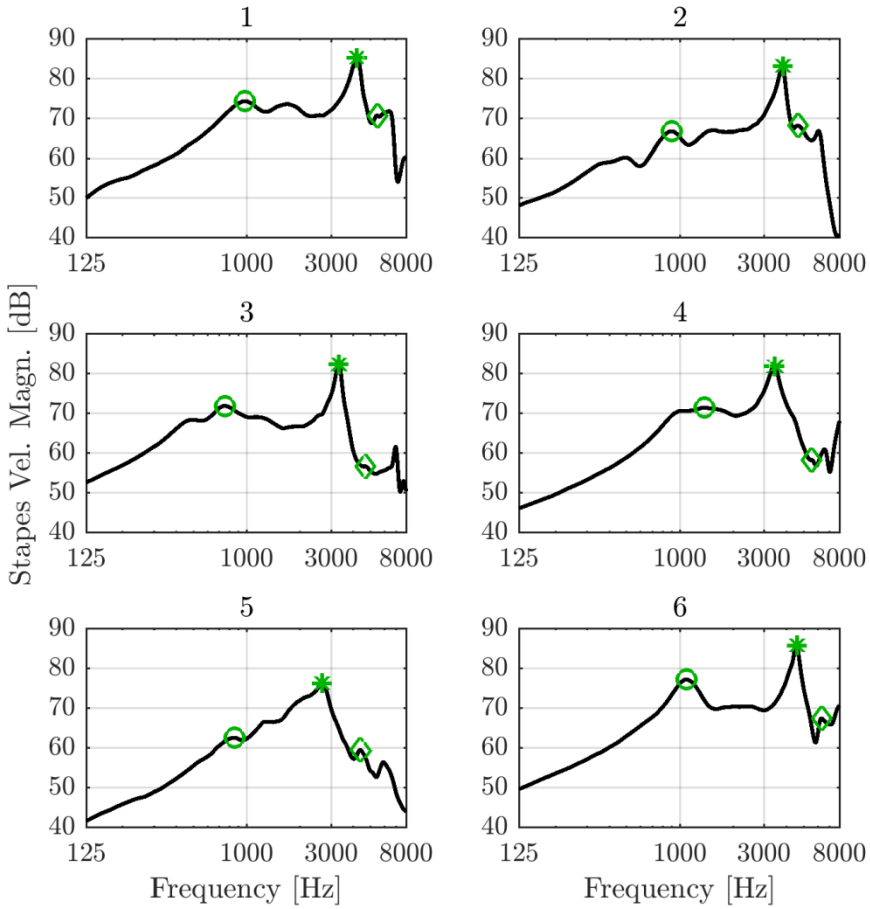

Figure 9.2: Semi-automatically assigned landmarks for each stapes velocity magnitude curve. Each corresponding landmark is denoted using the same symbol.

9.2.3 Curve alignment

Warping functions

In this section, we describe different warping functions and their properties. Warping functions are used to transform the data along the frequency axis. The original frequency-axis should be projected on a new frequency-axis such that the landmarks of all curves are aligned.

The warping function $X(f)$ needs to be monotonic because each frequency f needs to be projected onto a unique frequency, and the projected frequencies need to remain

monotonically increasing. In other words, aligning the curves could mean we either shift them and/or stretch/squeeze them, but we cannot change the order of curve segments. As an analogy, for time-related data, this criterion would imply the preservation of causality.

Several types of functions obey this criterion. A first example is the linear warping function.

$$X(f) = \alpha + \beta f \tag{9.1}$$

If $\alpha > 0$ the curve will shift to lower frequencies. When $\beta > 1$ the curve will be squeezed together; conversely, when $\beta < 1$, the curve will be stretched out. This type of warping function does not fix the endpoints of the curves, and thus warped frequencies can exceed the minimal and maximal value of the original frequency range. If this occurs, data has to be estimated for frequencies outside the measured frequency range. This is no problem if all curves converge to a constant value or a similar slope at the boundaries of the data set. For our data set, this is not the case. At the upper boundary of the measured frequency range, some curves go up, and some go down. Extrapolation of the data will result in very different values and curve shapes for different curves and thus the use of a linear warping function is not advisable.

A second class of warping functions, satisfying monotonicity, is

$$X(f) = \frac{(f_{MAX} - f_{MIN}) \int_{f_{MIN}}^{f} \exp\big(g(s)\big)\, ds}{\int_{f_{MIN}}^{f_{MAX}} \exp\big(g(s)\big)\, ds} + f_{MIN} \tag{9.2}$$

for which $g(s)$ is constructed using a finite-dimensional basis $g(s) = \sum_{i=0}^{q} \gamma_i w_i(s)$ with $w_i(s)$ a q-dimensional basis, γ_i the coefficients and s is a dummy variable which takes on the value of the frequencies determined by the integral boundaries, similar to James (2007).

In this chapter, we have chosen to use a b-spline functions for $g(s)$. Such a b-spline function is defined as a linear combination of control points γ_i and b-spline basis functions $w_i(s)$: $g(s) = \sum_{i=0}^{q} \gamma_i w_i(s)$, for this reason, we call the control points also coefficients. We make use of b-spline basis functions of the third order ($k = 3$). A lower-order results in a less smooth warping function. An example of a b-spline basis is shown in figure 9.3, for the sake of clarity $q = 5$ is used. The coefficients γ_i completely determine $g(s)$ and thus $X(f)$. For example, if all γ_i are chosen to be equal, $g(s)$ is a constant. As a consequence, the integral in equation (9.2) will be a linear function. Since $X(f)$ is normalized to fit the desired frequency range $[f_{MIN}, f_{MAX}]$, only one linear function holds, which is the automorphism $X = F$. Figure 9.4 shows the function $g(s)$ and the corresponding $X(f)$ for various values of the coefficients γ for $q = 5$. The MATLAB code for determining b-spline basis is available at the MATLAB file exchange website. To construct a b-spline basis, the order k of the basis functions and a knot vector T is required. The basis functions are defined on this knot vector T, which in our case spans the required frequency range. For a dimensionality of q, T contains $q + k + 1$

elements, but there are only q unique elements. The first and last element, f_{MIN} and f_{MAX} respectively, are repeated k times. The q unique elements were logarithmically spaced.

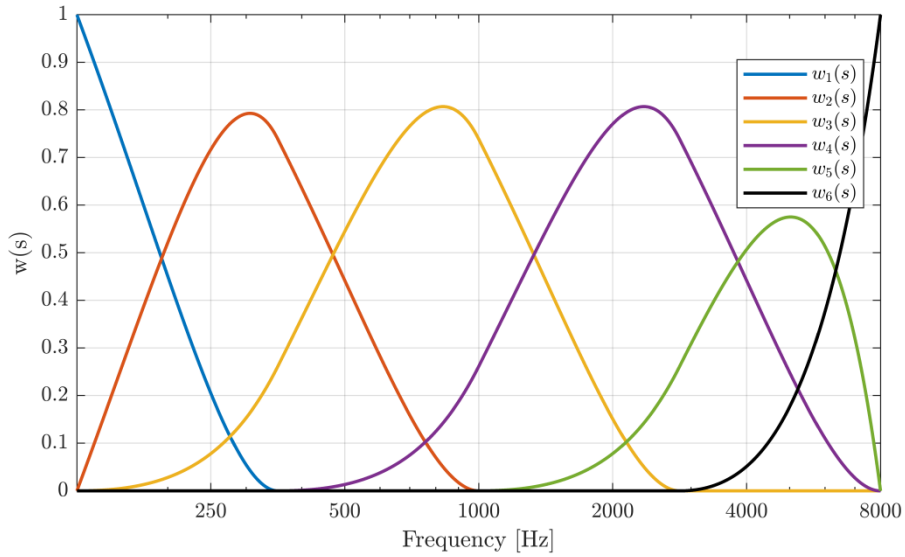

Figure 9.3: Example of a third order ($k = 3$) b-spline basis $w(s)$ with dimensionality $q = 5$ defined on the frequency range of the data sets using logarithmically spaced elements of the knot vector T.

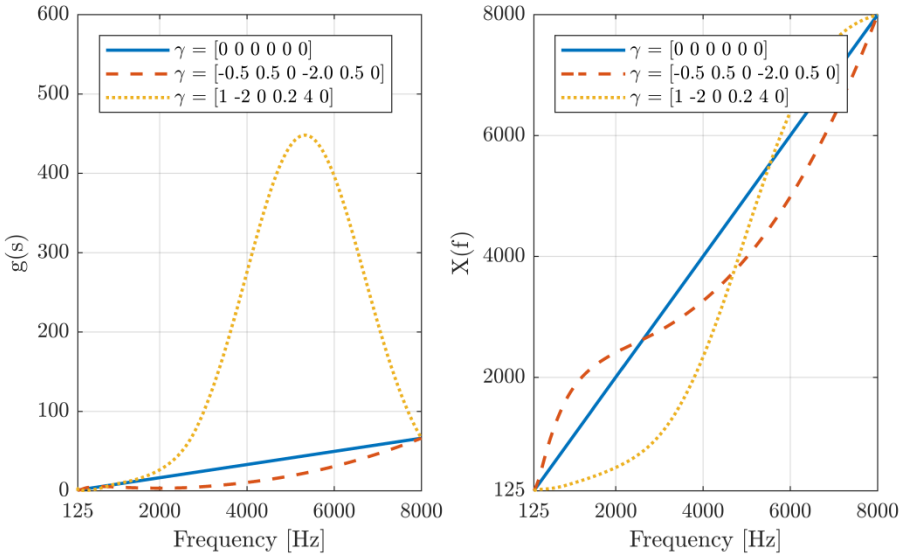

Figure 9.4: Example of the b-spline function $g(s)$ for different values of γ (left) using a third order b-spline basis ($k = 3$) and dimensionality $q = 5$ and the associated warping functions $X(f)$ (right).

This warping function has the properties of a cumulative distribution function, but it is scaled and shifted such that the boundary values of the frequency range are projected on themselves (i.e. $X(f_{MIN}) = f_{MIN}$ and $X(f_{MAX}) = f_{MAX}$). When the boundary values of the data range are fixed, the possible need for extrapolation of the data is ruled out. A disadvantage is that rigid translations are not possible, the curve will always be deformed unless all γ_i are zero, then the warping function reduces to $X(f) = f$ (i.e. an automorphism).

We used the type of warping function defined by equation (9.2) to achieve the results shown in this chapter. The q-dimensional basis was chosen to be constructed by third-order basis splines with a dimensionality q of 100. A higher dimensionality increases the warping function flexibility, allowing for local warping. Other types of warping functions which fix the frequency boundaries and have sufficient flexibility should return very similar results.

Alignment cost function

We consider the curves to be aligned when the landmarks of the curves are aligned. For each curve, we need to find the warping function that achieves this. When using warping functions of the type shown in equation (9.2), the problem is reduced to determining the coefficients γ_i.

The determination of the γ_i's is done by minimizing a cost function C similar to James (2007) consisting of a few components (Q, R, S).

$$C = \lambda_Q Q + \lambda_R R + \lambda_S S + \dots \tag{9.3}$$

The parameters λ_Q,λ_R and λ_S are weights put on the individual cost contributions. Q is defined by the deviation of each landmark frequency from the geometric mean frequency of that landmark calculated using all curves for which that landmark has been assigned.

$$Q = \sum_{j=1}^{P^i} |f_j^i - \bar{f}_j| \quad with\ \bar{f}_j = \left(\prod_{i=1}^{N^j} f_j^i \right)^{\frac{1}{N^j}} \tag{9.4}$$

In equation (9.4), the index i represents the ith curve from the total number of N^j curves for which landmark j was assigned and P^i is the number of landmarks assigned on curve i. Note that there is no summation over the number of curves in Q. The optimization procedure aligns one curve at a time. Thus Q only needs to contain landmark frequencies of one curve at a time. The average frequency was determined using the geometric mean since the frequency distribution of the landmark features more naturally fits a logarithmic distribution.

R is the average deviation of the warped frequencies $X(f_k)$ from their original frequencies f_k (eq. (9.5)). This term will ensure that the warping functions will not go to extremes and maintain the original shape of the curve as much as possible. It can also improve the convergence by forcing the algorithm to use smaller step sizes in the minimization.

$$R = \frac{1}{K} \sum_{k=1}^{K} |X(f_k) - f_k| \tag{9.5}$$

In equation (9.5), K is the total number of frequencies of each curve, not just the number of landmark frequencies. If the chosen warping function contains a shift term X_0, equation (9.5) can be adapted to $R = \frac{1}{K} \sum_{k=1}^{K} |X(f_k) - f_k - X_0|$. This would force the algorithm to achieve an alignment using mainly the shift term and thus minimizing the amount of curve deformation.

Conditional statements can also be used as shown in equation (9.6). The term S is a hard condition to avoid too strong local warping. When there is no warping, the derivative of the warping function $X'(f)$ is 1 for all frequencies.

$$S = \begin{cases} +\infty \ if\ |X'(f_k) - 1| > tolerance \\ 0 \quad if\ |X'(f_k) - 1| < tolerance \end{cases} \tag{9.6}$$

The weights $(\lambda_Q, \lambda_R, \lambda_S)$ can be set by experimentation and are dependent on the user. This dependency exists due to the goals of terms R and S. Which amount of (local) warping is *too much*? Additional cost terms can be used to increase control over the alignment procedure.

In this study, the convergence of the alignment of one curve using SLA landmarks was improved using $\lambda_R = 0.01$. The alignment of other curves did not pose any problems

regarding an excessive amount of (local) warping. For this reason, λ_S was set to zero. Parameter λ_Q was set to one.

Comparing a single data curve with an aligned average curve

In this section, we describe how we can compare a single curve with aligned average data. The curve features of the single curve are not necessarily aligned with those of the aligned average data. Comparing the magnitude of both datasets at each frequency individually would therefore be an unfair comparison. We can use the alignment procedure to align the curve features of the single curve to that of the aligned average data. It is important to note that only the single curve will be warped; the aligned average data remains untouched. We can then compare both datasets in terms of magnitude by comparing the aligned curves, but we can also compare them in terms of frequency by inspecting the warping functions.

To demonstrate this, we isolated curve number 5 from the six curves (see figure 9.1 for the numbering of the curves). Curve number 5 was chosen to be isolated as it was the most different in comparison with the other curves. A newly aligned average and standard deviation were calculated using only the five remaining curves. Next, a cross-sectional average and standard deviation of the five warping functions, originating from the alignment procedure of the five remaining curves, were calculated. Then, curve number 5 was aligned with the aligned average using landmarks determined by MLA. After this, the aligned curve number 5, and the aligned average were compared. The difference along the magnitude-axis was inspected using the aligned curves themselves, while the difference along the frequency-axis was inspected by comparing their warping functions.

9.3 Results

9.3.1 Assigned landmarks

The manually assigned landmarks are shown in figure 9.1. The first landmark (indicated by a circle in figure 9.1) was assigned to the local maximum after the initial increasing slope, ignoring local maxima below 600 Hz. The second landmark (square in figure 9.1) was the next local maximum between 1-2 kHz. This landmark was not clearly identifiable for curve number 6. The third landmark (asterisk in figure 9.1) was assigned to the global maximum. The fourth landmark (diamond in figure 9.1) was assigned to the first prominent local maximum after the downward slope after the global maximum. The fifth and last landmark (triangle in figure 9.1) was assigned to the local maximum at frequencies higher than the fourth landmark. For curve 4 and 6, this local maximum was not found. To avoid confusion, the landmarks will be referred to by their symbol only from this point on.

The semi-automatic assignment of three landmarks resulted in similar landmarks to those of manual assignment (figure 9.2). The landmark points of the SLA method, which correspond to the landmark points of the MLA method are indicated using the same

symbol. Only two significant differences are present; the circle landmark is placed at a higher frequency for curve 4 when using SLA as opposed to MLA, while the diamond landmark (◊) is assigned to a lower frequency. The numerical values of the landmark frequencies for both methods are given in table 9.1.

Method	Curve \ Landmark	o	□	*	◊	Δ
MLA	1	988	1698	4211	5452	6441
	2	901	1523	3810	4732	6076
	3	750	1216	3335	4732	7001
	4	1013	1390	3419	6550	-
	5	843	1268	2685	4390	5976
	6	1091	-	4577	6335	-
SLA	1	979	-	4211	5498	-
	2	901	-	3810	4654	-
	3	756	-	3335	4693	-
	4	1378	-	3419	5544	-
	5	857	-	2685	4390	-
	6	1091	-	4577	6335	-

Table 9.1: Frequencies in Hertz of the landmarks assigned using MLA and SLA. Landmarks that were not assigned are depicted as a dash (-). Landmarks that have been placed at a significantly different frequency for the MLA and SLA methods are shaded.

9.3.2 Curve alignment

Figure 9.5a shows the original magnitude response curves for all 6 specimens. The average response curve (blue line) is obtained by just averaging the magnitude values. Figure 9.5b shows the response curves after alignment of the landmark points determined by MLA. The aligned MLA average is shown in red. Figure 9.5c shows the result using SLA landmarks; the aligned SLA average is shown in green. The traditional cross-sectional, MLA aligned, and SLA aligned averages are shown again in figure 9.5d for comparison. After alignment of the landmarks assigned by either method, the average curve shows more distinct features which are also seen in the individual curves (figure 9.5a). The rising slope below 0.7 kHz is similar to that of the traditional cross-sectional average curve. A small difference is present at 0.6 kHz; the original average curve makes a slightly more noticeable dip. The first local maximum is less flat than that of the original average curve. This is also true for the local maximum in the 1-2 kHz region. The largest difference is seen at the global maximum. The MLA and SLA aligned averages show a distinctive peak for which the amplitude is higher than for the original average. For frequencies beyond the maximum response, the MLA and SLA aligned averages show two distinct peaks instead of one peak and a shoulder. All averages converge to the same

values at the boundaries of the measured frequency range due to the boundary conditions of the warping function (section 9.2.3). The difference between the MLA and SLA averages are small. There is a small discrepancy in the locations of the first and second local maximum of the SLA and MLA aligned averages (56 Hz and 73 Hz respectively) and a difference in amplitude of the last two local maxima (-0.8dB and -0.6dB respectively).

The warping functions associated with the MLA and SLA average are shown in figure 9.6. The MLA warping functions are a little more straight at the lower frequencies, but some of them are broader in the 4-6 kHz range.

The effect of applying the warping functions to the phase curves (figure 9.7) is less pronounced than for the magnitude curves. The most obvious change occurs again at around 4 kHz. The aligned averages show a steep phase jump. Between 1 and 2 kHz, the MLA and SLA aligned averages show small nuances indicating the local maxima. This is not the case for the original average for which the phase curve is almost a straight line in the 1-2 kHz range.

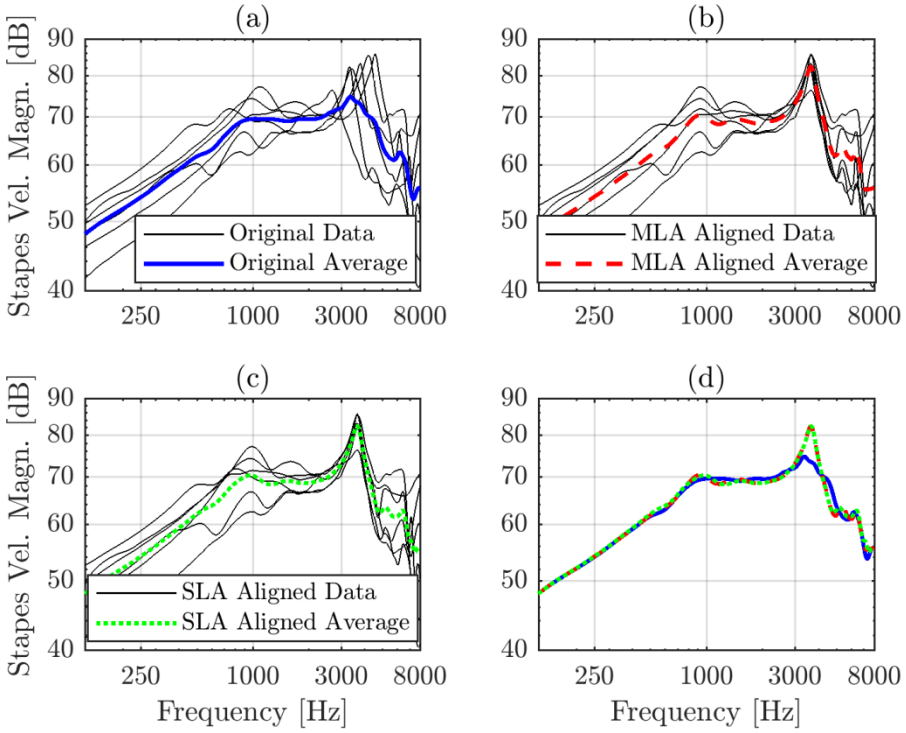

Figure 9.5: Individual and cross-sectional average frequency response magnitude of (a) original data, (b) aligned data using MLA, (c) aligned data using SLA. (d) Comparison of cross-sectional averages of (a), (b) and (c).

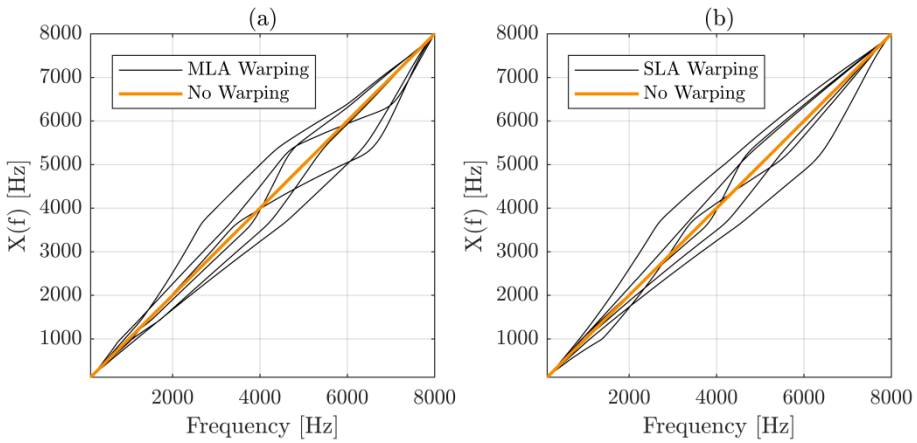

Figure 9.6: Warping functions when using MLA (a) and using SLA (b).

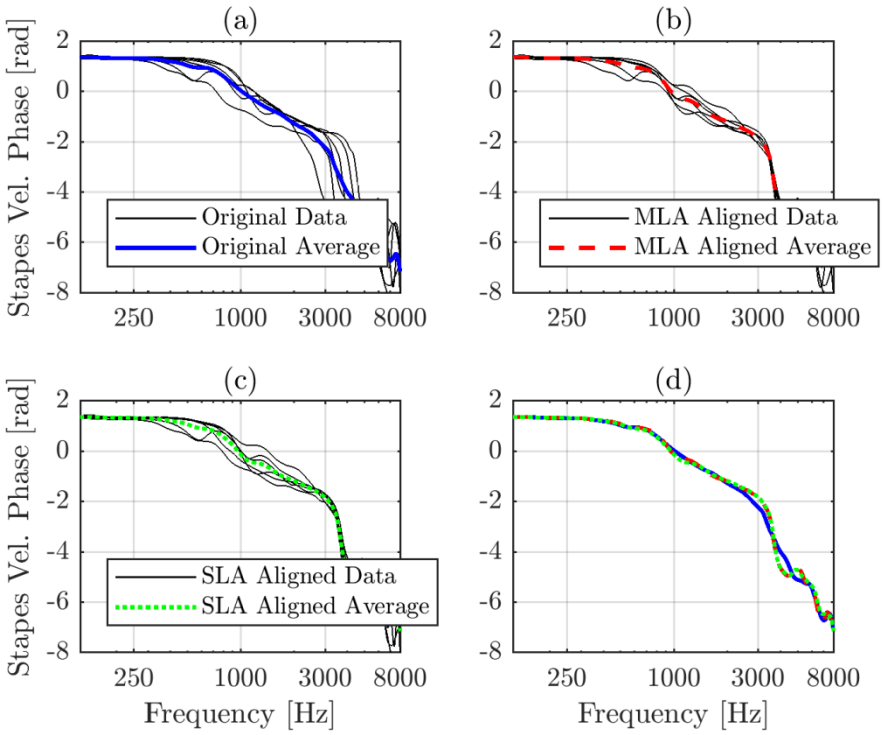

Figure 9.7: Individual and cross-sectional average frequency phase response of (a) original data, (b) aligned data using manual landmark assignment (MLA), (c) aligned data using semiautomatic landmark assignment (SLA). (d) Comparison of cross-sectional averages of (a), (b) and (c).

9.4 Discussion

9.4.1 Landmark assignment

The manual assignment of landmarks is robust and grants a lot of freedom to the user. It is relatively simple to visually recognize and mark features of the curves. The overall shape of each curve and the fact that all curves represent the same variable is taken into account. It can always be decided that a landmark, associated with a certain curve feature, will be assigned to a curve or not. If the associated curve feature is not present, the landmark is simply not assigned for that curve.

The semi-automatic assignment of landmarks offers speed as its main advantage. The biggest drawbacks are the lack of flexibility and that landmarks can easily be placed at locations which do not correspond with intuition. This was the case for two landmarks (O, ◊) of curve 4 (figure 9.2). The circle landmark of curve 4 was assigned to the resonance peak between 1-2 kHz, which is actually the square landmark between 1-2 kHz

for the manual landmark assignment. The cause is the prominence criterion set in the SLA algorithm. The prominence of the resonance between 1-2 kHz was higher than that of the resonance at 1 kHz; giving the 1-2 kHz resonance a higher weight in the SLA algorithm and thus making this resonance more likely to be chosen as the requested landmark. However, if prominence were not taken into account, the same would have happened for curve 3 instead, for which the resonance between 1-2 kHz is the closest to 1 kHz. This shows that it is hard to design SLA criteria that result in the same landmarks as the MLA method for all curves.

Overall, 16 out of 18 semi-automatic landmarks using SLA closely match with the corresponding landmarks using MLA. The SLA method performance is also less robust when looking for the two peaks at around 5 kHz. Additionally, it is very complicated to design criteria such that the SLA method can decide if a landmark is present or not. For this reason, the number of landmarks to be assigned using SLA was reduced from five to three.

More complicated methods to find corresponding data points that can be used as landmark points exist, such as the minimum description length (Thodberg, 2003). We also tested this method, but for our application, even the minimum description length method with the addition of curvature cost (Thodberg and Olafsdottir, 2003) did not seem to improve the results.

One could argue that the MLA method is subjective, and different people could obtain different results. In SLA, different algorithms can also result in different landmarks. The presented SLA method inherently includes subjectivity by utilizing user-defined criteria and criteria weightings. A fully automatic solution could be possible using machine learning. The use of machine learning could reduce or even completely remove the subjectivity. A large number of input data will be needed to train the decision algorithm. We believe that if a group of experts can agree on the chosen landmarks, and alignment result, then it does not matter if the landmarks were chosen manually or (semi-)automatically. To achieve this, it is advised not to assign many more landmarks than the amount that seems necessary. Preferably, the features chosen to determine the landmarks are features which are known to be existent for every curve. For our magnitude curves, this is the resonance peak at around 1 kHz, associated with a hinging ossicular motion (Homma et al., 2009) and the resonance of the ear canal at around 3-4 kHz (Keefe et al., 1993; Stinson, 1990). In contrary, resonances below 0.7 kHz are uncommon and not generally reported in literature. The most robust landmarks will be based on underlying knowledge of the physiology, which leads to the existence of the specific feature in the curve.

Landmarks close to the frequency range boundaries (e.g. Δ, figure 9.1) may not be ideal. For curve 4 and 6, the triangle landmark could perhaps be found just outside the measured frequency range. This reduces the validity of the averaged final local maximum. Four out of six data points are now averaged with two non-corresponding data points, which is similar to what happens with traditional cross-sectional averaging. The same applies to the data points at the fixed boundary frequencies.

If the data contains noise, choosing landmark features becomes more difficult. Using the MLA method, the most obvious landmark features (O,□,*) can still be easily determined. Distinguishing between the triangle and diamond landmark would be harder, even impossible. If these two landmarks would appear as one broad peak in most curves due to noise, the center of this broad peak can be used as a landmark feature. The SLA method will perform worse when noise spikes are present. By smoothing the original data, the noise spikes are reduced and performance can be increased.

It is important to note that other landmark features than local maxima can be used. Local minima in the data have also been linked to physical phenomena within the middle ear or experimental setup (e.g. resonance at around 2 kHz in chinchilla middle ear due to a hole drilled in bulla for experimental measurements, Rosowski et al. 2006). Such curve features can also be used for the alignment process.

9.4.2 Curve alignment

Comparison between the traditional average and the MLA and SLA aligned averages

Both landmark assignment methods show good results after alignment (figure 9.5). For the MLA and SLA aligned averages, a clear distinction can be made between the first and second resonance in the 0.9-2 kHz range. In contrary, the traditional cross-sectional average has a nearly constant value in that range because both resonant peaks occur at different frequencies for different curves.

Similarly, the traditional average showed a broad peak at the global maximum and just one local maximum and a shoulder at higher frequencies. This is due to the misalignment of the global maximum and overlap with the local maxima at higher frequencies. After alignment, this broad peak is resolved into one peak and two local maxima at higher frequencies, improving representation of the average curve shape and estimation of the average peak height. It should be noted that due to the frequency warping of the individual transfer functions the width of the curve peaks has been deformed and the aligned average curve does not show the mean width of the individual curve peaks and thus does not reflect the mean damping behavior.

Effect of dimensionality q

The dimensionality q of the basis used to construct the warping functions determines the flexibility of the warping functions. When q is large, the flexibility increases and local warping can be done. This can be observed in the warping functions; if they show multiple bending points, the flexibility is high (figure 9.6). When q is low (e.g. $q < 50$), finer details such as the last two resonances are harder to align. When q is high (e.g. $q > 200$), the optimization takes longer and may result in undesired strong local warping. Although this can be limited by the cost term S, which limits the amount of local warping. From experience, choosing $q \approx 100$ should suffice.

Figure 9.8 shows the effect of choosing different values of the dimensionality q on the aligned average. It is clear that lower flexibility will result in bad alignment. For $q = 1$, the alignment result is mediocre for every landmark feature, resulting in an increased number of resonance peaks. The average converges as q gets larger. Figure 9.9 shows the effect of q by displaying the aligned individual curves.

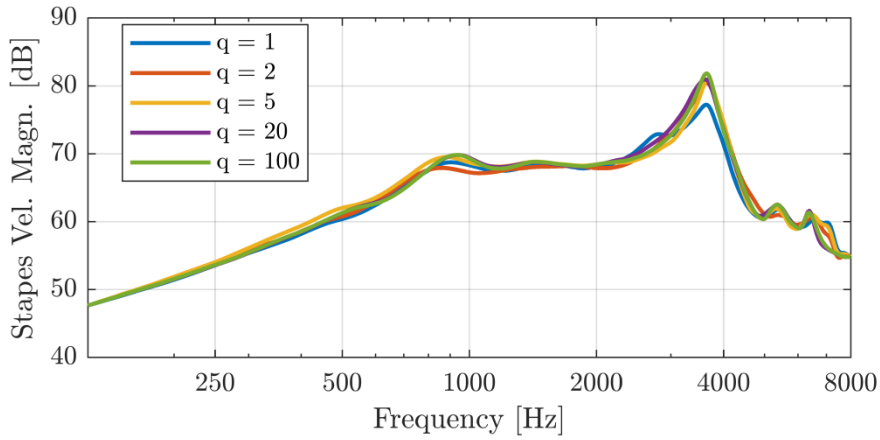

Figure 9.8: The effect of the dimensionality of the warping functions on the aligned magnitude average.

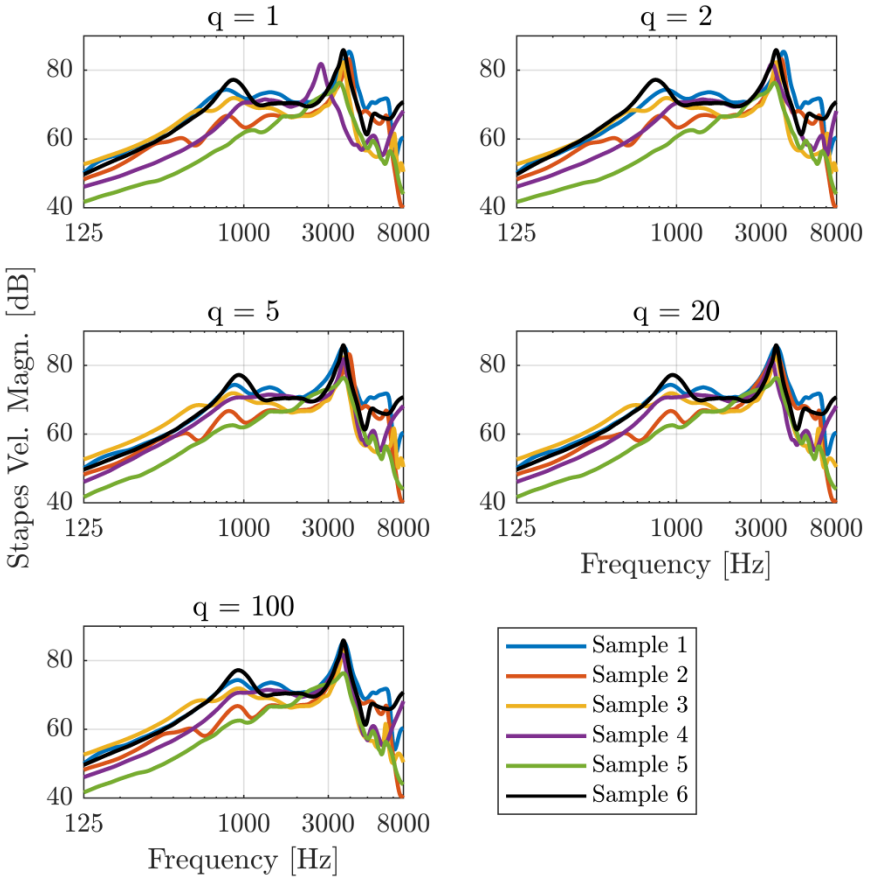

Figure 9.9: The effect of the dimensionality of the warping functions on the individual aligned magnitude curves.

Effect of fixed frequency boundaries

Fixing the frequency boundaries is necessary when no accurate extrapolation of the data can be done at one or both boundaries. In our case, the data at the 8 kHz boundary showed different slope directions for different curves, making extrapolation unsuitable. However, if the data is predictable (e.g. convergence to a constant value or slope) and similar for all curves, it can be considered to include a shift term in the warping functions. A shift term can produce a reasonable alignment without deforming the curve, resulting in an improved preservation of the original shape after full alignment.

Aligning phase curves

Aligning the phase curves using the warping functions associated with the aligned magnitude curves has two advantages. First, the average has improved with respect to the traditional cross-sectional average (figure 9.7). Although the difference is less drastic than for the magnitude curves, some details of the individual curve shapes are now preserved. The individual phase changes corresponding to local magnitude maxima between 1-2 kHz and around 5 kHz are a good example of this. Second, the correspondence between the phase and magnitude data points is restored. For example, the steep phase jump around 4 kHz occurs at the same frequency as the global maximum of the magnitude curve.

Other alignment methods

Other alignment methods such as Procrustes alignment (Ramsay and Li, 1998) and alignment by moments (James, 2007) were considered. However, the Procrustes method tries to align the curves by minimizing the square distance of the magnitudes to those of a target function. This target function is usually chosen to be the cross-sectional average of the curves. The focus on absolute magnitudes instead of the location of curve features results in large deformations of the magnitude curves, especially at the rising slope below 1 kHz.

The alignment by moments makes use of curve feature functions which are integrated over the entire frequency range to produce moments. These moments are then matched by a minimization procedure, similar to that presented earlier (section 9.2.3). Moments based on feature functions considering local maxima are mainly determined by the zero-crossings of the first and second derivative of the data. As a consequence, these moments are heavily dependent on the number of data points. Additionally, the moments are also dependent on the number of local maxima, which is not the same for all magnitude curves.

Additional remarks

The main purpose of the present chapter was to present the advantages of pre-aligned averaging over traditional cross-sectional averaging. We based our average on six measured curves as these are the data we have currently available. To generate a truly representative average, much more response curves will need to be gathered. In collaboration with other authors, we also hope to gather data of other response curves such as umbo vibration amplitude or stapes vibration amplitude in the presence of intact cochlear load, so that our method can be used to generate a set of standard reference curves. It is important to note that in order to generate a standard reference curve, the data sets which are used should all be obtained under the same experimental conditions. Specimens should, for instance, be prepared in the same way so that possible artifacts (e.g. an anti-resonance caused by making an access hole to the middle ear cavity) are taken into account in the same way between combined data sets.

9.4.3 Comparing data to aligned average data

For the purpose of demonstration, we compared one measured curve to the frequency-aligned average of the other measured curves and found that it significantly deviates from the average, possibly indicating it should be treated as an outlier. The same method of comparison can be used for validation of modeling results.

Figure 9.10 (top) shows the magnitude of curve 5 in both its original and aligned state compared with the aligned magnitude average and standard deviation band calculated using all curves excluding number 5. For frequencies up to 1.5 kHz, curve number 5 does not lie within the standard deviation band of the aligned average. The same holds for frequencies above 6 kHz and the magnitude at the global maximum. We can conclude that for frequency ranges 0.125-1.5 kHz, 3.9 kHz and 6-8 kHz the magnitude is significantly below average.

Similarly, the warping function used to align curve number 5 with the aligned average does not lie within the standard deviation band of the average of the warping functions, originating from the alignment procedure of the 5 curves, for a frequency range of 1-7.5 kHz, almost spanning the complete data range (figure 9.10bottom). It can be concluded that the warping function deviates far from an automorphism for a frequency range of 1-8 kHz. These observations possibly indicate that curve 5 should be treated as an outlier.

Finally, it needs to be noted that using standard deviation bands on the warping functions is not strictly correct and should be used with care. For example, the standard deviation band can violate the requirement of monotonicity of the warping functions. Still, it can be used as an indication of the agreement of frequency locations of curve features between the aligned average and an individual curve as shown in this example.

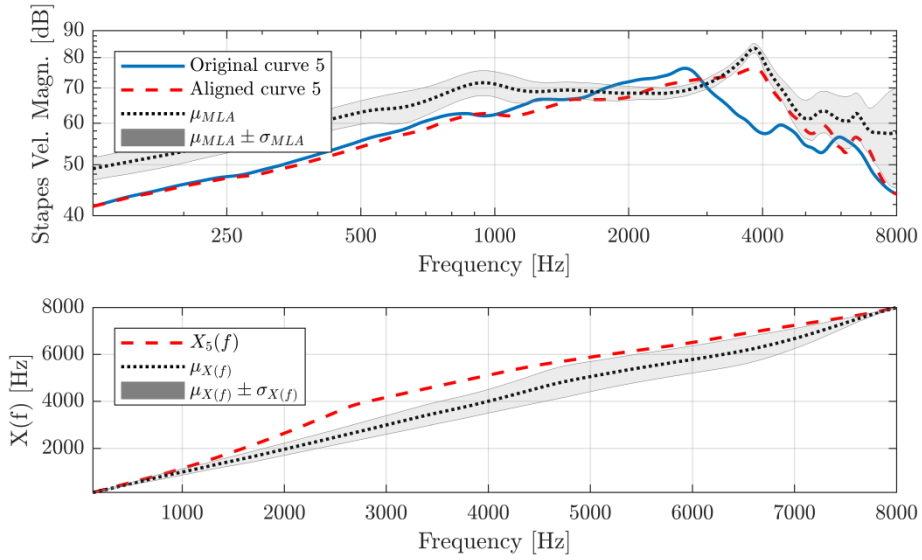

Figure 9.10: (top) Comparison of magnitude curve 5 before and after alignment with the average aligned curve μ_{MLA} (remaining 5 curves used) and its standard deviation band σ_{MLA}. (bottom) Comparison of the warping function of curve 5 with the average warping function $\mu_{X(f)}$and its standard deviation band $\sigma_{X(f)}$ of the 5 curves used to obtain the aligned average magnitude curve

9.4.4 In retrospect

We mentioned that the method used in this chapter deforms the curves. A side-effect is that the width of the resonances changes, which renders the obtained average unphysical. We propose another method which might circumvent this issue.

Each system can usually be characterized by evaluating the poles of the response data. If this done for each ear, one can calculate the average parameters of the characterized ME systems and construct a new frequency response curve based on this averaged theoretical model. Such model will also have the average resonance width incorporated.

The characterization of a system requires the poles/resonances to be nicely separated. Whether such separation is sufficiently present in ME systems should be investigated.

9.5 Conclusion

In this chapter, we have introduced a method for calculating average middle ear frequency response magnitude and phase curves with preservation of curve characteristics. We have demonstrated this method using stapes footplate velocity data obtained from human temporal bones with intact ear canal and removed cochlea. We have proposed a manual and semi-automatic method of generating landmark points on

individual magnitude curves. A warping function was chosen and employed to align individual magnitude curves. A minimization algorithm was implemented to optimize alignment of landmark points by frequency and additional terms to control the amount of warping were suggested. It was shown that the phase curves can be aligned accordingly using the warping functions determined from the corresponding aligned magnitude curves. We introduced a procedure to test if a data set lies within an acceptable range of the aligned average data on the magnitude (or phase) axis as well as on the frequency axis: this method can be used to validate models or to determine outliers in an experimental data set.

In future work, we plan to collect more data to improve this middle ear frequency response average. We will also collect data originating from temporal bones with intact inner ear and no ear canal, which are the conditions used in many models, to construct a frequency response average representing those conditions as well. We invite other researches to bring together data on middle ear vibrations to use the new averaging method for the generation of a set of reference curves.

GENERAL CONCLUSIONS AND FUTURE

In this dissertation, we explored the functionality of the middle ear under different circumstances.

In **chapter 5**, we investigated the behavior of the ME at high sound pressure levels. Experimentally, we discovered that the ME is weakly nonlinear. We found that dynamically, the TM would displace easier in the lateral direction than the medial direction, just like for high static pressures. As a consequence, the TM will oscillate at a lateralized position compared to its resting state. The oscillation pattern will be asymmetrical, and this is why the generated distortions will contain a higher level of even degree nonlinearities compared to odd degree nonlinearities. We also observed that the resonance frequency would decrease as the sound pressure levels increased, which means the ME is a softening system. By evaluating the results of FE models of curved and flat membranes, we found that the ME behavior correlated well with curved membranes. This observation led us to the conclusion that the nonlinear behavior of the ME was a consequence of the conical shape of the TM. However, the FE models lacked all the observed qualities we found experimentally. Therefore, there must be another cause for the nonlinear behavior of the ME.

In **chapter 6**, we encountered a similar problem. The results of our FE model did not match with experimental data. In this chapter, we investigated the transmission loss as a consequence of a malleus fracture. We found that the experimental data showed higher transmission at low frequencies, which could occasionally have increased after a fracture. The FE models did not show this unless we lowered the stiffness of the TM after a fracture. Experimentally, the TM lost its shape after fracture and seemed like it did not retain its elastic properties.

We repeated such observations in **chapter 7**. In rabbits, we found that after fracture, the TM is barely resisting to any force until it is forced into a shape similar to its resting position or an inversion of that. We concluded that the TM must be pre-tensioned in its normal state. This might explain the modeling problems we encountered in chapter 6 as no pre-tension was included in our models. We also found that when subjected to static pressures, the rabbit TM shows much higher negative strains when displacing laterally than positive strains when moving medially. If the shape of the TM is achieved by pre-strain, a lateral movement counters that pre-strain and makes the membrane less stiff. This provides an explanation for the nonlinear behavior we observed in chapter 5 and the lack of that behavior in our FE models, which again, did not include any pre-strain. Similar results were achieved in human TMs.

In **chapter 8**, we developed a diagnostic method to evaluate the location of ossicular fixations. The method is an improvement to the current method using manual palpation of the ossicles as we can objectively measure the mobility of the ossicles over a broad frequency range. On top of that, it is not more invasive than the current methods. The

TM is lifted in explorative surgery anyway. We just added a floating mass transducer, which originates from a clinically approved hearing aid. We found that the mobility of the incus can be a good indicator to distinguish incus, incus-malleus and stapes fixations from each other. However, more measurements are necessary to get statistically relevant data. The method has to be refined further to make it clinically applicable. A sound-induced measurement before lifting the TM and placing the FMT is impractical. The FMT must be stimulated with a standardized signal which allows high-quality measurements in any middle ear without damaging the inner ear.

In **chapter 9**, we solved an issue commonly encountered when averaging measured frequency responses of MEs. All ME frequency responses are similar but still unique. Not only the magnitudes differ, but also the resonance frequencies. Simply calculating the average at each frequency results in a mean curve, which does not represent the characteristics of the individual curves very well. We solved this by first aligning the curves such that the resonances are located at the average resonance frequency. In a second step, we calculated the average at each frequency as we would normally do. Due to the alignment, the curve characteristics can be preserved. The proposed averaging method will be useful to compare FE model data to average experimental data.

In future work, it would be interesting to evaluate the influence of other ME components on ME nonlinearity. This can be done by sequentially removing ME components and determining the nonlinear characteristics. There are two sequences that can be performed. Removing ME components starting from the medial side (cochlea first, malleus last) or from the lateral side (TM first). The latter option requires ME stimulation using the floating mass transducer as done during MIVIB in chapter 8.

The pre-strain and its source in human eardrums should be investigated and estimated, and the FE models should be updated accordingly. The models can be prestrained by applying a static load on the malleus and incus at the site of the superior mallear and incudal ligaments. Then the FE research on ME nonlinearity and malleus fractures can be continued.

The data on strains of intact TMs under static pressure should be used to further validate the FE models. This might improve anisotropic models which estimate the influence of the circular and radial fibers in the TM.

For the MIVIB project, more data on ME response after fixation(s) should be collected and be compared to averaged data of healthy ears. A statistically relevant dataset should be achieved such that the method can be validated before moving on to real-life patients. Other measurement points should be included such as the stapes. FE models might be used to reveal other relevant measurement points for different types of fixations.

It should be investigated whether it is possible to generate an average theoretical model of the ME based on the poles of measured frequency responses. This might return an averaged ME response even more accurate than the method proposed in this thesis.

NEDERLANDSTALIGE SAMENVATTING

Het gehoord behoort tot één van de vijf traditionele zintuigen en werkt omwille van een fantastisch biologisch ontwerp. In ons dagelijks leven, kunnen we drukverschillen in lucht waarnemen die maar liefst een miljoen keer kleiner zijn dan de atmosferische druk. De vibraties die hierdoor veroorzaakt worden in ons trommelvlies zijn slechts nanometers groot. Deze vibraties worden getransporteerd naar ons slakkenhuis met behulp van de gehoorsbeentjes, die zelf maar enkele milimeters groot zijn. De ingenieuze constructie van de cochlea laat die toe om de verschillende frequencies van een geluid te onderscheiden van elkaar en de gepaste neurale stimulaties uit te voeren. Dit laat ons dan uiteindelijk toe om te communiceren, naar muziek te luisteren, en veel meer.

Jammer genoeg, is ons gehoor vatbaar voor verschillende ziektes of zichzelf toegebrachte schade die gehoorverlies veroorzaken. Volgens cijfers van de wereld gezondheids organizatie zou 5% van de gehele wereldpopulatie gehoorverlies lijden. De twee hoofdzakelijke categoriën aan gehoorverlies zijn sensorneuraal and conductief gehoorverlies. De oorzaak van sensorneuraal gehoorverlies ligt bij de cochlea. In jonge indvidiuen wordt het vaak veroorzaakt door lange blootstelling aan geluiden met hoge intensiteit (of muziek) of korte blootstelling aan extreem intense geluiden zoals geweerschoten. Bij ouderen daarentegen komt het regelmatig voor en ligt de oorzaak bij de ouderdom. Sensorneuraal gehoorverlies is permanent maar kan verholpen worden met behulp van cochleaire implantaten die rechtstreeks de gehoorzenuwen stimuleren. In minder erge gevallen, kan een traditioneel gehoor apparaat ook soelaas bieden. De bron van conductief gehoorverlies is dan weer te vinden in het middenoor waar het trommelvlies en de gehoorbeentjes zich bevinden. Sommige van zulke gehoorverliezen zijn tijdelijk en zijn bijvoorbeeld het gevolg van een oorinfectie of een exuberantie aan vloeistof in het middenoor. Andere types zijn verkalking van de gehoorsbeentjes, waardoor ze minder mobiel worden, een breuk in één van de gehoorsbeentjes of een discontinuiteit in de gehoorketen. Het verhelpen van zulke problemen kan enerzijds met traditionele gehoorapparaten, middenoor implantaten of door een operatie. Deze scriptie focust zich op de mechanica van het middenoor. Bijgevolg zal elk gehoorverlies gerelateerd onderzoek handelen over conductief gehoorverlies.

Of er nu fundamenteel of toegepast middenoor onderzoek uitgevoerd wordt zal men vaak inzichten verkrijgen in beide velden. Enkele voorbeeldjes... Traditionele hoorapparaten versterken het geluid enorm, wat leidt tot de vraag: werkt het middenoor nog wel zo goed bij zulke hoge geluidsdrukken? Wanneer één van onze collega's de beste operatieprocedure onderzocht om het gehoorverlies ten gevolge van een gebroken gehoorbeentje te verhelpen ontdekte hij dat het trommelvlies na zulke breuk een gebrek aan elasticiteit vertoonde. Daardoor lijkt het alsof een trommelvlies in normale toestand eigenlijk onder constante spanning staat. Echter, in geen enkel computermodel van het middenoor wordt zo'n spanning ingebouwd. En kunnen onze modellen op hun beurt

chirurgen helpen om de beste meetlocaties te vinden om gehoorbeentjes fixaties te evalueren? De lijst kan nog even doorgaan.

De eerste 4 hoofdstukken dienen als een introductie tot de onderzoeksonderwerpen en meettechnieken die zullen gebruikt worden in deze scriptie. De 5 overblijvende hoofdstukken gaan meer in detail op elk onderwerp en de verkregen resultaten. De meeste van die hoofdstukken zijn sterk gebaseerd op gepubliceerd materiaal (hoofdstuk 6, 8 en 9) of papers die nog beoordeeld worden (hoofdstuk 7). Hoofdstuk 5 bevat vooral ongepubliceerd materiaal.

In hoofdstuk 1 geven we een introductie tot geluid en de morfologie en fysiologie van het zoogdieroor met focus op dat van de mens. In hoofdstuk 2 beschrijven we kort de verschillende onderzoeksonderwerpen van hoofdstukken 5-9 en leggen we uit welke type onderzoekstechnieken we nodig hebben om deze vragen op te lossen. In hoofdstuk 3 leggen we de theorie over (visco-)elasticiteit en vibraties uit, wat ons zal helpen voeling geven over hoe het middenoor werkt als een mechanisch system. In hoofdstuk 4 beschrijven we dan de technieken die we zullen gebruiken om bepaalde variabelen van het middenoor te evalueren en de problemen op te lossen die we in hoodfstuk 2 beschreven hebben.

In hoofdstuk 5 duiken we in het eerste onderzoeksonderwerp en verkennen we hoe de functionaliteit van het middenoor beïnvloed wordt door hoge geluidsdrukken. We doen dit aan de hand van optische meettechnieken en modellering. Experimenteel ontdekten we dat het middenoor zich lichtmatig niet-lineair gedraagt. We vonden dat het trommelvlies makkelijker te verplaatsen is naar de buitekant van het oor toe dan naar de binnenkant wanneer we deze met geluid stimuleren. Dit zien we ook wanneer het trommelvlies onderhevig is aan statische drukken. Als gevolg, zal het trommelvlies trillen rond een positie meer naar buiten toe dan haar rustpositie. Daardoor is het oscillatiepatroon asymmetrisch en zijn de gegenereerde distorties zowel van even als oneven graad. We zagen eveneens dat de resonantiefrequentie van het middenoor verlaagde wanneer de geluidsdruk toenam, wat wil zeggen dat het middenoor een ‘softening’ systeem is. Zulk gedrag is te associeren met membranen met zekere curvature, en daardoor concludeerde we dat de vorm van het trommelvlies de oorsprong was van de geobserveerde niet-lineariteit van het middenoor. De resultaten van onze eindige elementen modellen vertoonden echter niet hetzelfde niet-lineair gedrag als datgene we experimentaal waargenomen hadden. Daarom moest er nog een andere oorzaak zijn voor het niet-lineair gedrag van het middenoor.

In hoofdstuk 6 gebruiken we opnieuw modellering om beter te begrijpen wat exact het gehoorverlies veroorzaakt na een breuk van één van de gehoorbeentjes. Opnieuw hadden we het probleem dat de resultaten van onze simulaties niet overeenkwamen met experimentele data. De experimentele data toonde hogere geluidstransmissie bij lage frequenties na een malleusbreuk. De modellen deden dit niet tenzij we de stijfheid van he ttrommelvlies verlaagde na een breuk. Experimenteel was ook geobserveerd dat het trommelvlies haar vorm verloor na een breuk en dat de stijfheid en elasticiteit erg verminderd was. Dit was niet in ons model meegenomen.

In hoofdstuk 7 proberen we dan te zoeken wat er ontbreekt aan onze modellen. We zagen ook in konijnen, dat na een breuk, het trommelvlies geen stijfheid bevatte. Daarom

concludeerden we dat er een voorspanning van het trommelvlies is. Dit kan de problemen verklaren in hoofdstku 5 en 6, waar geen spanning geïncorporeerd was in de modellen. Met de digitale beeldcorrelatie vonden we eveneens dat het trommelvlies heel sterke negatieve rek (compressie) vertoonde wanneer het trommelvlies naar buiten werd geduwd. Dit is logisch wanneer een voorspannig bestaat, een laterale beweging werkt de voorspanning tegen. Dit zou ook kunnen verklaren waarom in hoofdstuk 5 het niet-lineair gedrag zo beperkt was. Het tegenwerken van de voorspanning zorgt voor niet-lineaire effecten.

In hoofdstuk 8 hebben we vooral experimenteel werk. We werkten een diagnostische methode uit om de locatie van beentjesfixatie te achterhalen. De methode is een verbetering op de huidige methode waarbij men op handgevoel afgaat. In onze methode, kunnen we objectief de mobiliteit van de beetnjes meten over een groot frequentiebereik. Bovendien is de methode niet heel invasief. De huidige methodes, liften het trommelvlies, wij doen hetzelfde maar voegen slechts een clinisch goedgekeurd apparaat toe afkomstig van een hoorapparaat. Dit apparaatje gebruiken we dan om de beentjes te stimuleren. We vonden dat de incus mobiliteit een goede indicator kan zijn om onderscheid te maken tussen incus, incus-malleus en stapes fixaties. Maar er zijn meer metingen nodig om een statistische relevante dataset the genereren.

In hoofdstuk 9 bekijken we data manipulatie methodes om een accurater gemiddelde te genereren van meetdata. Dit accuraat gemiddelde zou heel nuttig kunnen zijn om theoretische modellen te valideren. Alle middenoor frequentie responsfuncties zijn gelijkaardig, maar toch uniek. Niet enkel de magnitudes verschillen, maar ook de resonantiefrequenties. Wanneer er simpelweg een gemiddelde wordt genomen op elke frequentie, zal de gemiddelde curve niet de karakterisitieken van de individuele curves behouden. We lostten dit op door eerst de curves the aligneren op basis van de resonantiefrequenties. Daarna namen we het gemiddelde op elke frequentie zoals we normaal zouden doen. Door de alignering, bleven de meeste curvekarakersitieken bewaard.

In de toekomst, zou het interessant zijn om de invloed van andere middenoor componenten op het niet-lineair gedrag van het middenoor te onderzoeken. Dit kan door sequentieel componenten te verwijderen van de keten en telkens opnieuw de niet-lineaire karakterisitieken op te meten. We kunnen twee sequenties uitvoeren. We kunnen starten door aan de zijde van de cochlea (binnenoor) te beginnen. Of we kunnen eerst het trommelvlies weghalen. Voor dit laatste moeten we wel de floating mass transducer gebruiken om het middenoor te stimuleren aangezien het geluid niet meer kan opgevangen worden als we het trommelvlies verwijderen. Dit is een gelijkaardige werkwijze aan die in hoofdstuk 8.

De voorspanning in menselijke trommelvliezen zou moeten onderzocht en afgeschat worden zodat de eindige elementen modellen kunnen verbeterd worden. De modellen kunnen voorspanning gegeven worden door een kracht uit te voeren op de plaats van de superior mallear en incudal ligamenten. Het onderzoek met eindige elementen modellen rond niet-lineariteit van het middenoor en malleusbreuken kan dan hervat worden.

De data verzameld rond strains van een intact trommelvlies onderhevig aan statische drukken zou moeten gebruikt worden om eindige elementen modellen verder te valideren. Zij kunnen de anisotropische modellen verbeteren die momenteel slechts een beredeneerde gok maken van de invloed van de circulaire en radiele fibers in het trommelvlies.

Voor het MIVIB project zou er meer data moeten verzameld worden. Deze data moet dan vergeleken worden met een gemiddelde van de respons van gezonde oren. Een statistische relevante dataset moet verkregen worden voor men de methode kan toepassen op echte patiënten. Andere meetpunten zoals de stapes moeten toegevoegd worden aan de procedure en eindige elementen modellen kunnen inzicht leveren over andere mogelijke relevante meetpunten voor andere fixaties.

Er moet onderzocht worden of er een gemiddeld theoretisch model van het middenoor kan opgesteld worden op basis van de polen van de gemeten frequentie respons functies. Dit kan een gemiddelde middenoor respons opleveren die zelfs nog meer accuraat is dan diegene bezorgd door de methode voorgesteld in deze thesis.

BIBLIOGRAPHY

1. Aernouts, J., Aerts, J.R., Dirckx, J.J. 2012. Mechanical properties of human tympanic membrane in the quasi-static regime from in situ point indentation measurements. Hear Res 290, 45-54.
2. Aerts, J. 2010. Optical Measurement of the Weak Non-linearity in the Eardrum Vibration Response to Auditory Stimuli, University of Antwerp, UAntwerpen.
3. Aerts, J., Dirckx, J. 2007. A fast full frequency range measurement of nonlinear distortions in the vibration of acoustic transducers and acoustically driven membranes. Measurement Science and Technoogy 18, 3344-50.
4. Aerts, J.R.M., Dirckx, J.J.J. 2010. Nonlinearity in eardrum vibration as a function of frequency and sound pressure. Hearing Res 263, 26-32.
5. ANSI. 2014. F2504 – 05 (Reapproved 2014), Standard Practice for Describing System Output of Implantable Middle Ear Hearing Devices. American National Standards Institute.
6. Banks, H.T., Hu, S., Kenz, Z.R. 2011. A brief review of elasticity and viscoelasticity for solids. Adv. Appl. Math. Mech 3, 1-51.
7. Blanchard, M., Abergel, A., Verillaud, B., Williams, M.T., Ayache, D. 2011. Isolated malleus-handle fracture. Auris Nasus Larynx 38, 439-43.
8. Buunen, T.J., Vlaming, M.S. 1981. Laser--Doppler velocity meter applied to tympanic membrane vibrations in cat. J Acoust Soc Am 69, 744-50.
9. Cai, H., Jackson, R.P., Steele, C.R., Puria, S. 2010. A Biological Gear in the Human Middle Ear. Proceedings of the COMSOL Conference 2010.
10. Cheng, T., Gan, R.Z. 2007. Mechanical properties of stapedial tendon in human middle ear. J Biomech Eng-T Asme 129, 913-918.
11. Cheng, T., Gan, R.Z. 2008a. Experimental measurement and modeling analysis on mechanical properties of tensor tympani tendon. Med Eng Phys 30, 358-366.
12. Cheng, T., Gan, R.Z. 2008b. Mechanical properties of anterior malleolar ligament from experimental measurement and material modeling analysis. Biomech Model Mechan 7, 387-394.
13. Cheng, T., Dai, C., Gan, R.Z. 2007. Viscoelastic properties of human tympanic membrane. Ann Biomed Eng 35, 305-14.
14. Chien, W., McKenna, M.J., Rosowski, J.J., Merchant, S.N. 2008. Isolated fracture of the manubrium of the malleus. J Laryngol Otol 122, 898-904.
15. Claes, R., Muyshondt, P.G.G., Van Assche, F., Van Hoorebeke, L., Aerts, P., Dirckx, J.J.J. 2018. Eardrum and columella displacement in single ossicle ears under quasi-static pressure variations. Hear Res 365, 141-148.
16. Dai, C., Cheng, T., Wood, M.W., Gan, R.Z. 2007. Fixation and detachment of superior and anterior malleolar ligaments in human middle ear: experiment and modeling. Hear Res 230, 24-33.
17. Dalhoff, E., Turcanu, D., Zenner, H.P., Gummer, A.W. 2007. Distortion product otoacoustic emissions measured as vibration on the eardrum of human subjects. Proc Natl Acad Sci U S A 104, 1546-51.

18. De Greef, D., Pires, F., Dirckx, J.J. 2017. Effects of model definitions and parameter values in finite element modeling of human middle ear mechanics. Hear Res 344, 195-206.
19. De Greef, D., Goyens, J., Pintelon, I., Bogers, J.P., Van Rompaey, V., Hamans, E., Van de Heyning, P., Dirckx, J.J.J. 2016. On the connection between the tympanic membrane and the malleus. Hear Res 340, 50-59.
20. Delrue, S., De Foer, B., van Dinther, J., Zarowski, A., Somers, T., Casselman, J., Offeciers, E. 2015. Handling an Isolated Malleus Handle Fracture: Current Diagnostic Work-up and Treatment Options. Ann Otol Rhinol Laryngol 124, 244-9.
21. Dirckx, J.J., Decraemer, W.F. 1991. Human tympanic membrane deformation under static pressure. Hear Res 51, 93-105.
22. Dirckx, J.J., Decraemer, W.F. 1992. Area change and volume displacement of the human tympanic membrane under static pressure. Hear Res 62, 99-104.
23. Dirckx, J.J., Decraemer, W.F. 2001. Effect of middle ear components on eardrum quasi-static deformation. Hear Res 157, 124-37.
24. Dirckx, J.J., Buytaert, J.A., Decraemer, W.F. 2006. Quasi-static transfer function of the rabbit middle ear' measured with a heterodyne interferometer with high-resolution position decoder. J Assoc Res Otolaryngol 7, 339-51.
25. Dobrev, I., Ihrle, S., Roosli, C., Gerig, R., Eiber, A., Huber, A.M., Sim, J.H. 2016. A method to measure sound transmission via the malleus-incus complex. Hear Res 340, 89-98.
26. Farahmand, R.B., Merchant, G.R., Lookabaugh, S.A., Roosli, C., Ulku, C.H., McKenna, M.J., de Venecia, R.K., Halpin, C.F., Rosowski, J.J., Nakajima, H.H. 2016. The Audiometric and Mechanical Effects of Partial Ossicular Discontinuity. Ear Hear 37, 206-15.
27. Fletcher, N.H. 1992. Acoustic systems in biology Oxford University Press, New York.
28. Gaihede, M. 1999. Mechanical properties of the middle ear system investigated by its pressure-volume relationship. Introduction to methods and selected preliminary clinical cases. Audiol Neurootol 4, 137-41.
29. Gan, R.Z., Feng, B., Sun, Q. 2004. Three-dimensional finite element modeling of human ear for sound transmission. Ann Biomed Eng 32, 847-59.
30. Gladine, K., Dirckx, J. 2018a. 3D deformation and strain measurement of an intact eardrum using digital image correlation. Journal of Physics: Conference Series 1149, 1-6.
31. Gladine, K., Dirckx, J.J.J. 2018b. Average middle ear frequency response curves with preservation of curve morphology characteristics. Hear Res 363, 39-48.
32. Gladine, K., Dirckx, J. 2019. Strain distribution in rabbit eardrums under static pressure. Hear Res, (under review).
33. Gladine, K., Muyshondt, P.G.G., Dirckx, J.J.J. 2017. Human middle-ear nonlinearity measurements using laser Doppler vibrometry. Opt Laser Eng 99, 98-102.
34. Gladine, K., Muyshondt, P., De Greef, D., Dirckx, J. 2018. Effect of Malleus Handle Fracture on Middle Ear Sound Transmission: Laser Doppler Vibrometry Measurements and Finite Element Simulations. Proceedings 2018 2, 1-5.
35. Gladine, K., Wales, J., Silvola, J., Muyshondt, P., Topsakal, V., Van de Heyning, P., Dirckx, J., Von Unge, M. 2019. Evaluation of artificial fixation of the incus and

malleus with minimally invasive intraoperative laser vibrometry (MIVIB) in a temporal bone model. Otol Neurotol (under review).
36. Gladiné, K., Muyshondt, P., Dirckx, J. 2016. LDV measurement of small nonlinearities in flat and curved membranes. A model for eardrum nonlinear acoustic behaviour. . AIP Conference Proceedings Vol. 1740, 050005.
37. Gottlieb, P.K., Li, X., Monfared, A., Blevins, N., Puria, S. 2016. First results of a novel adjustable-length ossicular reconstruction prosthesis in temporal bones. Laryngoscope 126, 2559-2564.
38. Gray, H. 1918. Anatomy of the human body Lea & Febiger.
39. Greene, N.T., Jenkins, H.A., Tollin, D.J., Easter, J.R. 2017. Stapes displacement and intracochlear pressure in response to very high level, low frequency sounds. Hear Res 348, 16-30.
40. Guillermo, J., Gonzales, G., Gonzaléz, J.A.O., Freire, J., 2017. Analysis of Mixed-mode Stress Intensity Factors using Digital Image Correlation Displacement Fields, 24th ABCM International Congress of Mechanical Engineering.
41. Guinan, J.J., Jr., Peake, W.T. 1967. Middle-ear characteristics of anesthetized cats. J Acoust Soc Am 41, 1237-61.
42. Hato, N., Stenfelt, S., Goode, R.L. 2003. Three-dimensional stapes footplate motion in human temporal bones. Audiol Neurootol 8, 140-52.
43. Hato, N., Okada, M., Hakuba, N., Hyodo, M., Gyo, K. 2007. Repair of a malleus-handle fracture using calcium phosphate bone cement. Laryngoscope 117, 361-3.
44. Hernandez-Montes, M.D., Santoyo, F.M., Munoz, S., Perez, C., de la Torre, M., Flores, M., Alvarez, L. 2015. Surface strain-field determination of tympanic membrane using 3D-digital holographic interferometry. Opt Laser Eng 71, 42-50.
45. Homma, K., Du, Y., Shimizu, Y., Puria, S. 2009. Ossicular resonance modes of the human middle ear for bone and air conduction. J Acoust Soc Am 125, 968-79.
46. Homma, K., Shimizu, Y., Kim, N., Du, Y., Puria, S. 2010. Effects of ear-canal pressurization on middle-ear bone- and air-conduction responses. Hear Res 263, 204-15.
47. Iurato, S., Quaranta, A. 1999. Malleus-handle fracture: historical review and three new cases. Am J Otol 20, 19-25.
48. James, G.M. 2007. Curve Alignment by Moments. Ann Appl Stat 1, 480-501.
49. Johnson, D.H. 1980. Applicability of white-noise nonlinear system analysis to the peripheral auditory system. J Acoust Soc Am 68, 876-84.
50. Keefe, D.H., Bulen, J.C., Arehart, K.H., Burns, E.M. 1993. Ear-canal impedance and reflection coefficient in human infants and adults. J Acoust Soc Am 94, 2617-38.
51. Khaleghi, M., Furlong, C., Ravicz, M., Cheng, J.T., Rosowski, J.J. 2015. Three-dimensional vibrometry of the human eardrum with stroboscopic lensless digital holography. J Biomed Opt 20, 051028.
52. Kneip, A., Gasser, T. 1992. Statistical Tools to Analyze Data Representing a Sample of Curves. Ann Stat 20, 1266-1305.
53. Koike, T., Hiroshi, W., Kobayashi, T. 2001. Effect of Depth of Conical-Shaped Tympanic Membrane on Middle-Ear Sound Transmission. JSME International Journal 44, 1097-1102.
54. Koike, T., Wada, H., Kobayashi, T. 2002. Modeling of the human middle ear using the finite-element method. J Acoust Soc Am 111, 1306-17.

55. Kuypers, L.C., Decraemer, W.F., Dirckx, J.J. 2006. Thickness distribution of fresh and preserved human eardrums measured with confocal microscopy. Otol Neurotol 27, 256-64.
56. Kuypers, L.C., Dirckx, J.J., Decraemer, W.F., Timmermans, J.P. 2005. Thickness of the gerbil tympanic membrane measured with confocal microscopy. Hear Res 209, 42-52.
57. Ladak, H.M., Decraemer, W.F., Dirckx, J.J., Funnell, W.R. 2004. Response of the cat eardrum to static pressures: mobile versus immobile malleus. J Acoust Soc Am 116, 3008-21.
58. Ladak, H.M., Funnell, W.R.J., Decraemer, W.F., Dirckx, J.J.J. 2006. A geometrically nonlinear finite-element model of the cat eardrum. Journal of the Acoustical Society of America 119, 2859-2868.
59. Li, Y., Barbi, J., #269. 2014. Stable orthotropic materials, Proceedings of the ACM SIGGRAPH/Eurographics Symposium on Computer Animation. Eurographics Association, Copenhagen, Denmark. pp. 41-46.
60. Lindsay, P.H., Norman, D.A. 1977. Human information processing: An introduction to psychology Academic Press.
61. Merchant, G.R., Merchant, S.N., Rosowski, J.J., Nakajima, H.H. 2016. Controlled exploration of the effects of conductive hearing loss on wideband acoustic immittance in human cadaveric preparations. Hear Res 341, 19-30.
62. Muyshondt, P. 2018a. Mechanics of a single-ossicle ear: Optical measurements and finite-element modeling of the avian middle ear, University of Antwerp.
63. Muyshondt, P. 2018b. Mechanics of a single-ossicle ear: optical measurements and finite-element modeling of the avian middle ear, University of Antwerp, UAntwerpen.
64. Muyshondt, P.G.G., Aerts, P., Dirckx, J.J.J. 2018. The effect of single-ossicle ear flexibility and eardrum cone orientation on quasi-static behavior of the chicken middle ear. Hear Res.
65. Nakajima, H.H., Ravicz, M.E., Merchant, S.N., Peake, W.T., Rosowski, J.J. 2005. Experimental ossicular fixations and the middle ear's response to sound: evidence for a flexible ossicular chain. Hear Res 204, 60-77.
66. Nakajima, H.H., Pisano, D.V., Roosli, C., Hamade, M.A., Merchant, G.R., Mahfoud, L., Halpin, C.F., Rosowski, J.J., Merchant, S.N. 2012. Comparison of ear-canal reflectance and umbo velocity in patients with conductive hearing loss: a preliminary study. Ear Hear 33, 35-43.
67. Nedzelnitsky, V. 1980. Sound pressures in the basal turn of the cat cochlea. J Acoust Soc Am 68, 1676-89.
68. Niklasson, A. 2017. An optimal partial ossicular prosthesis should connect both to the tympanic membrane and malleus. A temporal bone study using Laser Doppler Vibrometry. Otol Neurotol (Accepted).
69. Niklasson, A., Tano, K. 2010. Self-inflicted negative pressure of the external ear canal: a common cause of isolated malleus fractures. Acta Otolaryngol 130, 410-6.
70. Niklasson, A., Ronnblom, A., Muyshondt, P., Dirckx, J., von Unge, M., Tano, K. 2016. Ossiculoplasty on Isolated Malleus Fractures: A Human Temporal Bone Study Using Laser Doppler Vibrometry. Otol Neurotol 37, 895-901.
71. Ozturk, O., Uneri, C. 2009. Isolated fracture of the malleus handle. Otolaryngol Head Neck Surg 141, 653-4.

72. Palanca, M., Tozzi, G., Cristofolini, L. 2016. The use of digital image correlation in the biomechanical area: a review. International Biomechanics 3, 1-21.
73. Peacock, J., von Unge, M., Dirckx, J. 2013. Magnetically driven middle ear ossicles for optical measurement of vibrations in an ear with opened tympanic membrane. Rev Sci Instrum 84, 121707.
74. Peacock, J., Pintelon, R., Dirckx, J. 2015. Nonlinear Vibration Response Measured at Umbo and Stapes in the Rabbit Middle ear. Jaro-J Assoc Res Oto 16, 569-580.
75. Peacock, J., Dirckx, J., von Unge, M. 2016. Intraoperative assessment of ossicular fixation. Hear Res 340, 99-106.
76. Pedersen, C.B. 1989. Traumatic middle ear lesions. Fracture of the malleus handle, aetiology, diagnosis and treatment. J Laryngol Otol 103, 901-3.
77. Price, G.R. 1974. Upper limit to stapes displacement: implications for hearing loss. J Acoust Soc Am 56, 195-9.
78. Punke, C., Pau, H.W. 2006. [Isolated fracture of the handle of malleus. A rare differential diagnosis in cases of conductive hearing loss]. HNO 54, 121-4.
79. Puria, S., Steele, C. 2008. Mechano-Acoustical Transformations, The senses: A comprehensive reference, Vol. 3. Academic Press, San Diego. pp. 165-202.
80. Puria, S., Peake, W.T., Rosowski, J.J. 1997. Sound-pressure measurements in the cochlear vestibule of human-cadaver ears. J Acoust Soc Am 101, 2754-70.
81. R. F. Coelho, Pyl, L. 2014. Structural Analysis and Finite Elements Université Libre de Bruxelles.
82. Ramsay, J.O., Li, X.C. 1998. Curve registration. J Roy Stat Soc B 60, 351-363.
83. Ronnblom, A., Gladine, K., Niklasson, A., Von Unge, M., Dirckx, J., Tano, K. 2019. A new, promising experimental ossicular prosthesis A human temporal bone study with laser Doppler vibrometry. Otol Neurotol, (under review).
84. Rosowski, J.J., Peake, W.T., Lynch, T.J., 3rd 1984. Acoustic input-admittance of the alligator-lizard ear: nonlinear features. Hear Res 16, 205-23.
85. Rosowski, J.J., Ravicz, M.E., Songer, J.E. 2006. Structures that contribute to middle-ear admittance in chinchilla. J Comp Physiol A Neuroethol Sens Neural Behav Physiol 192, 1287-311.
86. Rosowski, J.J., Nakajima, H.H., Merchant, S.N. 2008. Clinical utility of laser-Doppler vibrometer measurements in live normal and pathologic human ears. Ear Hear 29, 3-19.
87. Rosowski, J.J., Chien, W., Ravicz, M.E., Merchant, S.N. 2007. Testing a method for quantifying the output of implantable middle ear hearing devices. Audiol Neurootol 12, 265-76.
88. Rosowski, J.J., Davis, P.J., Merchant, S.N., Donahue, K.M., Coltrera, M.D. 1990. Cadaver middle ears as models for living ears: comparisons of middle ear input immittance. Ann Otol Rhinol Laryngol 99, 403-12.
89. Rosowski, J.J., Nakajima, H.H., Hamade, M.A., Mahfoud, L., Merchant, G.R., Halpin, C.F., Merchant, S.N. 2012. Ear-canal reflectance, umbo velocity, and tympanometry in normal-hearing adults. Ear Hear 33, 19-34.
90. Rothberg, S.J., Allen, M.S., Castellini, P., Di Maio, D., Dirckx, J., Ewins, D.J., Halkon, B.J., Muyshondt, P., Paone, N., Ryan, T., Steger, H., Tomasini, E.P., Vanlanduit, S., Vignola, J.F. 2016. An international review of laser Doppler vibrometry: Making light work of vibration measurement. Opt Laser Eng 99, 11-22.
91. Sadd, M. 2005. Elasticity: Theory, applicatoins and numerics. Elsevier.

92. Shaw, E.A.G. 1982. Localization of sound: theory and applications, chapter External ear response and lound localization Amphora.
93. Sivian, L.J., White, S.D. 1933. ON MINIMUM AUDIBLE SOUND FIELDS. The Journal of the Acoustical Society of America 4, 288-321.
94. Stinson, M.R. 1990. Revision of estimates of acoustic energy reflectance at the human eardrum. J Acoust Soc Am 88, 1773-8.
95. Sy A., R.E.J., Ndiaye M., Thill M.P. 2017. Isolated malleus handle fracture: Two case reports. . Egypt J Ear Nose Throat Allied Sci (2017) http://dx.doi.org/10.1016/j.ejenta.2017.02.001.
96. Tan M., U.N., Pearl MS, Carey JP 2015. Fracture of the Manubrium of the Malleus. Otology & Neurotology 37, 254-5.
97. Thodberg, H.H. 2003. Minimum description length shape and appearance models. Lect Notes Comput Sc 2732, 51-62.
98. Thodberg, H.H., Olafsdottir, H., 2003. Adding curvature to minimum description length shape models. In: Bangham, R.H.a.A., (Ed.), British Machine Vision Conference. BMVA Press. pp. 26.1-26.10.
99. Tuck-Lee, J.P., Pinsky, P.M., Steele, C.R., Puria, S. 2008. Finite element modeling of acousto-mechanical coupling in the cat middle ear. J Acoust Soc Am 124, 348-62.
100. Van der Jeught, S., Dirckx, J.J., Aerts, J.R., Bradu, A., Podoleanu, A.G., Buytaert, J.A. 2013. Full-field thickness distribution of human tympanic membrane obtained with optical coherence tomography. J Assoc Res Otolaryngol 14, 483-94.
101. Vlaming, M.S., Feenstra, L. 1986. Studies on the mechanics of the normal human middle ear. Clin Otolaryngol Allied Sci 11, 353-63.
102. Volandri, G., Di Puccio, F., Forte, P., Carmignani, C. 2011. Biomechanics of the tympanic membrane. J Biomech 44, 1219-36.
103. von Unge, M., Decraemer, W.F., Bagger-Sjoback, D., Dirckx, J.J. 1993. Displacement of the gerbil tympanic membrane under static pressure variations measured with a real-time differential moire interferometer. Hear Res 70, 229-42.
104. Voss, S.E., Rosowski, J.J., Merchant, S.N., Peake, W.T. 2000. Acoustic responses of the human middle ear. Hear Res 150, 43-69.
105. Wales, J., Gladine, K., Van de Heyning, P., Topsakal, V., von Unge, M., Dirckx, J. 2018. Minimally invasive laser vibrometry (MIVIB) with a floating mass transducer - A new method for objective evaluation of the middle ear demonstrated on stapes fixation. Hear Res 357, 46-53.
106. Zahnert, T., Metasch, M.L., Seidler, H., Bornitz, M., Lasurashvili, N., Neudert, M. 2016. A New Intraoperative Real-time Monitoring System for Reconstructive Middle Ear Surgery: An Experimental and Clinical Feasibility Study. Otol Neurotol 37, 1601-1607.

ABBREVIATIONS

(μ)CT	(Micro-)computed tomography
AML	Anterior mallear ligament
DIC	Digital image correlation
FE	Finite element
FMT	Floating mass transducer
HRTF	Head related transfer function
IE	Inner ear
ISJ	Incudo-stapedial joint
LDV	Laser Doppler vibrometry
LML	Lateral mallear ligament
ME	Middle ear
MIVIB	Minimally invasive vibrometry
MLA	Manually assigned landmarks
PF	Pars flaccida
PIL	Posterior incudal ligament
PT	Pars tensa
PTA	Posphotungstic acid
RMS	Root mean square
SAL	Stapedial annular ligament
SFP	Stapes footplate
SLA	Semi-automatically assigned landmarks
SM	Stapedius muscle
SPL	Sound pressure level

STL	Stereolithography file format
TB	Temporal bone
TM	Tympanic membrane
TT	Tendon tympani

LIST OF PUBLICATIONS

Journal publications with peer review

Gladine, K., Muyshondt, P.G.G., Dirckx, J.J.J. 2017. Human middle ear nonlinearity measurements using laser Doppler vibrometry. Opt Laser Eng 99, 98-102.

Gladine, K., Dirckx, J.J.J. 2018b. Average middle ear frequency response curves with preservation of curve morphology characteristics. Hear Res 363, 39-48.

Gladine, K., Wales, J., Van de Heyning, P., Topsakal, V., von Unge, M., Dirckx, J. 2018. Minimally invasive laser vibrometry (MIVIB) with a floating mass transducer - A new method for objective evaluation of the middle ear demonstrated on stapes fixation. Hear Res 357, 46-53.

Niklasson, A., Gladine, K., Ronnblom, A., von Unge, M., Dirckx, J., Tano, K. 2018. An Optimal Partial Ossicular Prosthesis Should Connect Both to the Tympanic Membrane and Malleus: A Temporal Bone Study Using Laser Doppler Vibrometry. Otol Neurotol 39, 333-339

Gladine, K., Dirckx, J. 2019. Strain distribution in rabbit eardrums under static pressure. Hear Res 381, https://doi.org/10.1016/j.heares.2019.107772.

Journal publications currently under peer review

Gladine, K., Wales, J., Silvola, J., Muyshondt, P., Topsakal, V., Van de Heyning, P., Dirckx, J., Von Unge, M. 2019. Evaluation of artificial fixation of the incus and malleus with minimally invasive intraoperative laser vibrometry (MIVIB) in a temporal bone model. Otol Neurotol (Accepted).

Ronnblom, A., Gladine, K., Niklasson, A., Von Unge, M., Dirckx, J., Tano, K. 2019. A new, promising experimental ossicular prosthesis A human temporal bone study with laser Doppler vibrometry. Otol Neurotol, (under review).

Conference papers

Gladiné, K., Muyshondt, P., Dirckx, J. 2016. LDV measurement of small nonlinearities in flat and curved membranes. A model for eardrum nonlinear acoustic behaviour. AIP Conference Proceedings Vol. 1740, 050005.

Gladine, K., Dirckx, J. 2018a. 3D deformation and strain measurement of an intact eardrum using digital image correlation. Journal of Physics: Conference Series 1149, 1-6.

Gladine, K., Muyshondt, P., De Greef, D., Dirckx, J. 2018. Effect of Malleus Handle Fracture on Middle Ear Sound Transmission: Laser Doppler Vibrometry Measurements and Finite Element Simulations. Proceedings 2018 2, 1-5.

Conference contributions

(P)Presenting author

Gladiné, K.(P), Dirckx, J. 2015. Time-domain model of the inner ear to study nonlinear responses. Comsol Conference, Grenoble, France, October 2015 (Presentation)

Gladiné, K.(P), Dirckx, J. 2016. Eardrum conical shape as source of non-linear response to sound pressure: Measurements and finite element modeling in human ears. IUTAM Symposium on Advances in Biomechanics of Hearing, Stuttgart, Germany, May 2016 (Presentation)

Gladiné, K.(P), Dirckx, J., 2016. Vibration measurements in the human middle ear. 15th Polytec Benelux Anniversary, Antwerp, Belgium, June 2016. (Presentation)

Gladiné, K.(P), Muyshondt P., Dirckx, J., 2016. LDV measurement of small nonlinearities in flat and curved membranes. A model for eardrum nonlinear acoustic behaviour. 12th International Conference on Vibration Measurements by Laser and Noncontact Techniques – AIVELA 2016, Ancona, Italy, June 2016. (Presentation)

Gladiné, K.(P), Dirckx, J., 2017. Middle ears and Chinese gongs: A striking resemblance. Nonlinear behavior of the middle ear at high sound pressure levels and the influence of eardrum shape. BNCPAP Colloquium at the Royal Academy: physics of the living systems, Brussels, Belgium, April 2017 (Poster)

Gladine, K.(P), Dirckx, J., 2018. 3D deformation and strain measurement of an intact eardrum using digital image correlation. 13th International Conference on Vibration Measurements by Laser and Noncontact Techniques – AIVELA 2018, Ancona, Italy, June 2018. (Presentation)

Gladine, K.(P), Muyshondt, P., Degreef, D., Dirckx, J. 2018. Effect of Malleus Handle Fracture on Middle Ear Sound Transmission: Laser Doppler Vibrometry Measurements and Finite Element Simulations. 18th international conference on experimental mechanics, ICEM, Brussels, Belgium, July 2018 (Presentation)

Gladine, K.(P), Dirckx, J., 2018. Average umbo vibration of the human ear using curve feature alignment. 8th International symposium on middle ear mechanics in research and otology, MEMRO, Shanghai, China, July 2018 (Presentation)

Gladine, K.(P), Wales, J., Silvola, J., Topsakal, V., Van De Heyning, P., von Unge, M., Dirckx, J., 2018. Average umbo vibration of the human ear using curve feature alignment. 8th International symposium on middle ear mechanics in research and otology, MEMRO, Shanghai, China, July 2018 (Presentation)

DANKWOORD-ACKNOWLEDGEMENTS

Ziezo, hier zijn we dan. Helemaal aan het einde. Graag neem ik even de tijd en ruimte om enkele mensen te bedanken.

Allereerst wil ik mijn promotor Joris Dirckx bedanken. Het doctoraat heeft misschien 'maar' vier jaar geduurd, maar eigenlijk kan je wel zeggen dat Joris me al veel langer begeleid. In de bachelorstudie ontdekte ik het projectpracticum holografie en was direct gebeten. In een lokaaltje dat zich nu recht tegenover mijn bureau bevindt maakte ik toen mijn eigen hologrammen. Dat vond ik uiteraard enorm cool ! Het was dan ook vanzelfsprekend dat een bachelorproef rond digitale holografie begeleid door Joris me wel zou liggen. En op die manier, zette ik een eerste stap binnen bij BIMEF. Ik ontdekte dat ze bij BIMEF rond het gehoor werkte. Een biomedische tak van de fysica, dat leek me uiterst interessant. Sinds toen was het zeker, ik zou graag nog enige tijd bij BIMEF vertoeven. Tijdens mijn doctoraat is de alwetende Joris telkens een grote hulp geweest, zijn kennis en duizende ideeën hebben me enorm vooruit geholpen. Bedankt Joris !

Tijdens de bachelor en masterthesis had ik ook Daniël de Greef en Joris Soons die me een handje toestaken. Hun kennis over programmeren en modelleren hebben me heel snel veel doen opsteken. Tesamen met Ortwin Leenaerts (a.k.a. Pico) en Sam Van Der Jeught werd ik ook snel geïntegreerd in de kaartclub tijdens de middag. Of het nu kleurenwiezen was of hartenjagen, er werd telkens veel geschaterd, gevloekt, gehuild of gezegevierd. Bedankt !

Nu we het toch over middag- en koffiepauzes hebben, wil ik ook Greet Eyckmans bedanken voor de lekkere cake die zij of Joris meebracht en die we vaak kunnen hebben verorberen. Af en toe kregen we ook gezellig bezoek van onze collega uit de biologie, Jana. Ik kwam haar af en toe eens tegen op een muziekconcert en het was dan heel fijn om een bekend gezicht te zien en een babbeltje te slaan in een ruimte vol onbekende metalheads of progrockers.

De start van mijn thesis was een opvolging van het werk van vroegere collega's Johan Aerts en John Peacock. Uit hun werk heb ik ook heel wat kunnen bijleren.

Voor het technische aspect van de thesis heb ik vaak beroep kunnen doen op Fred Wiese, Wim Huyge, en William de Blauwe, die aangename man die ik al had leren kennen tijdens het tweede jaar op de universiteit. Of het nu rubberen membraantjes maken was, complexe geluidsopstellingen of allerhande elektronische apparatuur; Op hen kon je altijd rekenen. Daarnaast zijn het nog eens toffe mensen ook ! 1+1 gratis. Eveneens wil ik graag het secretariaat bedanken. Op Hilde, Gert, Nathalie en Tessa kon je altijd rekenen voor elk stukje administratief werk waar je zelf niet aan uit kon.

Het magische duo, Arne Van Overloop en Tine Bosschaert mag zeker niet vergeten worden. Niet alleen waren ze grote hulp bij het organiseren van practica, maar ik zal ze

vooral herinneren voor alle leuke activiteiten die ze voor BIMEF georganiseerd hebben. De jaarlijkse BIMEF quiz op het uitmuntende kerstfeestje was altijd dikke fun !! Ik hoop er nog een keertje bij te zijn in de toekomst.

Een andere duo zijn Pieter Muyshondt en Pieter Livens (Pieter1 en Pieter2). Deze combi is nog maar recent gevormd, maar ze werkt wel heel goed. Soms komen ze zelf (onbewust) in matchende outfits werken. Met hen heb ik vele vruchtbare discussies gehad over onderzoek. Ik heb het genoegen gehad om met Pieter M. een beetje de wereld af te reizen voor verschillende congressen. Ons tripje door Shanghai en Peking was wel echt de moeite. Bedankt voor het aangename gezelschap.

Pieter L. is nog een kersverse doctoraatstudent en ik kan hem voldoende wijze raad geven over alle domme dingen die je kan doen in vier jaar tijd, of hoe ze beter kunnen. Maar ik zie nu al dat hij het heel goed zal doen. Net zoals zijn kompaan, Joaquim Sanctorum. De goedlachse en sympathieke drummer, boordevol verhalen voor tijdens de middagpauze. Het was leuk om met jou, Joris, en Adriaan Campo heel even in een fysica-band te zitten, de almachtige *Englert Bosons*. Ik wens jullie veel succes.

Of het nu over wetenschap, appartementen kopen, bitcoins, MMA of eender wat ging, bij Sam Van der Jeught kon je telkens terecht. Bovendien maakt Sam ook heerlijke lasagne en heb ik een snelcursus pool gekregen waar ik nog steeds de vruchten van pluk.

Dan hebben we de man van het zuiden, uit het verre Brazilië. Intussen kan hij dit vast en zeker lezen dankzij zijn intense cursus Nederlands. Felipe Pires is altijd iemand geweest waar ik wat naar opkeek. Het aanschouwen van zijn enthousiasme over eender wat kan ieder mens opwekken. Af en toe krijg je wel een pak slaag bij één van zijn eureka momenten, maar vergeet niet dat het slagen uit vreugde zijn. Dus die incasseer je met plezier.

We hadden dit jaar nog een nieuweling, Matthias Dillen. Het bleek al snel dat wij goed overeen gingen komen met elkaar. Op korte tijd hebben we veel gelachen en elkaar goed leren kennen, samen drones gekocht (die moeten we nog eens samen testen hè) en af en toe eens flink gaan feesten. Hij kan ook bijzonder goed tekenen, bekijk figuur 5.13 op pagina 70 nog een keer. Jullie dachten toch niet dat ik dat zelf gemaakt had zeker? Kortom een toffe vriendelijke jongeman, maar pas wel op als hij met zijn auto komt aangevlogen.

I also want to thank the members of my doctoral jury: Internal jury members prof. Dr. Paul Scheunders and prof. Dr. Bart Partoens, prof. Dr. Steve Vanlanduit and external members prof. Dr. Hanif Ladak, prof. Dr. Magnus von Unge. Thank you for reading and evaluating my work and providing a fruitful discussion during the defense.

I want to thank the reviewers and editors of all my published work for their critical view and helpful suggestions.

I want to thank our Swedish or Norwegian colleagues, Krister Tano, Anders Niklasson, Anton Rönnblom Juha Silvola, Magnus von Unge, Jeremy Wales for all the interesting work we did. In particular, I would like to thank Anders, Anton, and Krister for their hospitality. I had a great stay at Lulea and Gotland in April 2019.

Het laatste jaar was enorm druk. Het doctoraat afronden, soliciteren en een appartement inorde brengen. Bij alles kon ik rekenen op steun van mijn ouders. Zonder hun hulp en advies had het allemaal veel moeilijker geweest. Ik zeg het misschien te weinig, maar ik denk dat jullie wel weten hoezeer ik het apprecieer. En hetzelfde kan ik zeggen over broer en zus !

In het weekend kon ik vaak even ademhalen met vrienden. Rustig op café of gaan 'dansen' voor zover dat dat dansen genoemd kon worden. Maar altijd heel plezierig. Bedankt mannen, je weet wel wie je bent.

In februari heb ik dan toch nog eens de liefde gevonden. Ik leerde een mooie, fantastische jongedame kennen genaamd Maroucha. Bij haar kom ik helemaal tot rust. Ze is zo behulpzaam, lief en inspirerend dat je je in een sprookje waant waar alles altijd wel goed komt. Bedankt voor je steun in deze laatste gekke maanden allerliefste Maroucha.

En zoals ze zeggen, 'last but not least'. Partner in crime, al 9 jaar lang, William Keustermans. In één van de eerste weken leerde we elkaar kennen op de banken van de universiteit. 'Je moet naar station Mortsel fietsen, da's korter en heb je meer tijd om je trein te halen'. En zo geschiedde, elke dag samen op de fiets, de trein en in de les. Zelfde traject, zelfde passie, zelfde ongeloofelijk absurde humor. Veel lachen, maar ook serieus doen, het hoorde er allemaal bij. Een ware vriend en steun voor zo lang. Bedankt William.

Ik had nooit gedacht dat ik een dankwoord zo lang zou maken. Maar er moet toch een eind aan komen. Dus voor al wie nu nog niet vermeld is, een dikke merci !!